Design and Critical Evaluation of Permanent Magnet Wind Generator Technology for Small-scale Wind Energy Systems

by

Casper Jeremias Johannes Labuschagne

Dissertation presented for the degree of Doctor of Philosophy in Electrical Engineering in the Faculty of Engineering at Stellenbosch University

Supervisor:

Prof. M. J. Kamper

December 2022

Declaration

By submitting this dissertation electronically, I declare that the entirety of the work contained therein is my own, original work, that I am the sole author thereof (save to the extent explicitly otherwise stated), that reproduction and publication thereof by Stellenbosch University will not infringe any third party rights and that I have not previously in its entirety or in part submitted it for obtaining any qualification.

Date: 2022/02/21 .....

Abstract

Design and Critical Evaluation of Permanent Magnet Wind Generator Technology for Small-scale Wind Energy Systems

C. J. J. Labuschagne

Department of Electrical and Electronic Engineering,
Stellenbosch University,
Private Bag X1, Matieland 7602, South Africa.

Dissertation: Ph.D. Eng. (Electrical)

December 2022

Small-scale wind energy systems with energy storage offer an attractive electrification solution for rural stand-alone applications in Sub-Saharan Africa where utility grid connection is too expensive. However, small-scale wind energy systems need to be more cost-competitive and more reliable. Subsequently, lower installation costs, reduced operation and maintenance costs, durability, and improved performance are the critical aspects that must be improved. Therefore, the focus in this dissertation is to investigate the design of optimal wind generators for different front-end rectifier connected small-scale wind energy systems. The aim is then to critically evaluate the wind generator technology and to compare the different wind energy systems.

The uncontrolled passive wind energy system, where the wind generator is directly connected to the battery energy storage via a diode bridge rectifier, is identified as an ideal candidate for this application. However, designing the generator for good power matching with the wind turbine is difficult. Therefore, a method of external impedance matching is proposed, whereby an external inductance is added between the wind generator and the diode bridge rectifier. To calculate the necessary external impedance, a unique finite element analysis solution method is proposed that is more accurate than analytical calculations.

Following the above, methods of "building" the necessary impedance into the machine in the design optimisation process are investigated for the passive system's wind generator. This is done by changing the stator slot's structure to significantly increase leakage-flux, or by altering the placement and orientation of the permanent magnets in the rotor to increase the magnetic saliency of the machine. It is found that these are effective methods to design the wind generators for a natural impedance matching. Finally, permanent magnet Vernier generators are also investigated as an alternative wind generator technology for their novel use in uncontrolled passive systems. It is shown that Vernier generators are well suited for this application. However, conventional permanent magnet synchronous generators use less rare earth permanent magnet material, and are found to be more cost-effective.

Two wind energy systems with active control and maximum power point tracking are further investigated in this dissertation, namely (i) the DC-DC converter system, where

the generator is connected to the battery energy storage via an uncontrolled diode rectifier and a controlled DC-DC converter, and (ii) the active synchronous rectifier controlled wind energy system. For both of these controlled wind energy systems, conventional permanent magnet synchronous generators are investigated and optimised for the comparison with the uncontrolled passive system's optimum generator. In addition, wind generators with overlapping and non-overlapping windings are also compared for the DC-DC converter system. However, it is shown that there is essentially no trade-off between wind generators with either winding configuration.

In the final evaluation, the optimum wind generators for the different front-end rectifier connected wind energy systems are compared in terms of active mass and the estimated active material cost. The wind energy systems are also evaluated in terms of the system's annual energy production and the estimated sub-system component cost. It is shown in the comparison that even though the uncontrolled passive wind energy system's generators are heavier and more expensive, that the uncontrolled passive wind energy system is the most cost-competitive system, which is an unexpected result.

Uittreksel

Ontwerp en Kritiese Evaluering van Permanente Magneet Windgeneratortegnologie vir Kleinskaalse Windenergiestelsels

C. J. J. Labuschagne

Departement van Elektriese en Elektroniese Ingenieurswese,
Universiteit van Stellenbosch,
Privaatsak X1, Matieland 7602, Suid-Afrika.

Proefskrif: Ph.D. Ing. (Elektries)

Desember 2022

Die gebruik van kleinskaalse windenergiestelsels met energiebergingeenhede bied 'n aantreklike oplossing vir die elektrifisering van afgeleë alleenstaande toepassings en gemeenskappe in yl bevolkde landelike gebiede. Dit is veral van toepassing op Afrika lande suid van die Sahara waar die aanleg van, of aansluiting met, die hoof elektriese netwerk onbekostigbaar geag word. Dit is dus noodsaaklik vir hierdie kleinskaalse windenergiestelsels om meer koste mededingend te wees, asook om hierdie stelsels se betroubaarheid te verbeter. As sulks is die noodsaaklike gebiede vir verbetering: om 'n laer installasie koste te handhaaf, om die bedryfs- en onderhoudskoste te verminder, en om die stelsel se werking te verbeter. Die fokus in hierdie proefskrif is dus om die ontwerp van optimale windgenerators vir windenergiestelsels wat deur middel van verskeie gelykrigters bedryf word te ondersoek. Die doel is dan om hierdie windgeneratortegnologie krities te evalueer en om die verskillende windenergiestelsels met mekaar te vergelyk.

Die onbeheerde passiewe windenergiestelsel, waar die windgenerator direk aan die batterybank via 'n diodebrug-gelykrigter gekoppel word, is as die ideale kandidaat vir dié toepassing geïdentifiseer. Dit is egter nie so eenvoudig om die generator vir 'n goeie passing met die drywingskurwes van die windturbine te ontwerp nie. Om hierdie probleem op te los, word eksterne impedansie passing as metodiek voorgestel, i.e. om 'n eksterne induktor tussen die generator en die diodebrug-gelykrigter te koppel. Verder, om die nodige eksterne induktansie se waarde te bereken word 'n unieke eindige element oplossing gebaseerde metodiek voorgestel.

Met betrekking tot die bogenoemde, word verdere metodes om die nodige impedansie in die masjien "in te bou" ook as deel van die ontwerp en optimerings proses vir windgenerators in passiewe stelsels ondersoek. Sulke metodes word uitgevoer deur onder andere, die statorgleuwe se struktuur te verander om sodanig die masjien se spreivloed te vermeerder, asook die posisie en oriëntering van die permanente magnete in die rotor te verander en daardeur dan die magnetiese speek-eienskap te vergroot. Daar is bevind dat beide van die voorafgenoemde metodes doeltreffend gebruik kan word om die windgenerator vir 'n natuurlike impedansiepassing te ontwerp. As 'n alternatief, word permanente magneet Vernier-generators ook as 'n moontlike windgeneratortegnologie ondersoek. Vir

dié tegnologie om gebruik te word in onbeheerde passiewe stelsels is dan ook 'n oorspronklike toepassing. Die bevindinge dui daarop dat permanente magneet Vernier-generators besonders goed geskik is vir hierdie toepassing, maar dat konvensionele permanente magneet sinchroongenerators nogtans minder permanent magneet materiaal gebruik en meer kostedoeltreffend is.

Twee windenergiestelsels wat gebruik maak van aktiewe beheer om maksimum drywingspunt werking te bewerkstellig word ook in hierdie proefskrif ondersoek. Hierdie twee stelsels is dan (i) die GS-GS-omsetterstelsel, waar die generator gekoppel is aan die batterybank via 'n onbeheerde diodegelykrigter en 'n GS-GS-omsetter, en (ii) die aktief sinchroongelykrigter beheerde windenergiestelsel. Vir beide hierdie beheerde windenergiestelsels word konvensionele permanente magneet sinchroongenerators ondersoek. Hieride generators word ook geoptimeer, met die doel om dit met die generators van die onbeheerde passiewe stelsel te vergelyk. Daarbenewens word windgenerators met oorvleulende en nie-oorvleulende wikkelings vir die GS-GS-omsetterstelsel ook ondersoek. Maar dit word wel uitgewys dat daar klaarblyklik geen wesenlike voordeel gewin word deur een óf die ander wikkelingkonfigurasie in dié geval te gebruik nie.

Laastens, in die finale evaluering word die optimum generators van die verskeie windenergiestelsels dan in terme van die generators se aktiewe massa en die afgeskatte materiaalkoste vergelyk. Die jaarlikse energieproduksie deur elke stelsel en die beraamde substelselkomponentkoste word ook ge-evalueer om tot 'n finale gevolgtrekking te kom. Daar word bevind dat, alhoewel die onbeheerde passiewe stelsel se windgenerators beide swaarder en duurder is, dié stelsel nogsteeds meer kostemededingend is. Die laasgenoemde is 'n merkwaardige, en onverwagte uitkomste.

List of Publications

Journal Papers

C. J. J. Labuschagne and M. J. Kamper, "Wind Generator Impedance Matching in Small-scale Passive Wind Energy Systems," in *IEEE Access*, vol. 9, pp. 22558-22568, 2021.

C. J. J. Labuschagne and M. J. Kamper, "Design and Performance Evaluation of PM Vernier Generator Technology for a Small-scale Uncontrolled Passive Wind Generator System," in print at *IEEE Transactions on Industry Applications*, 2022.

C. J. J. Labuschagne and M. J. Kamper, "On the Design and Topology Selection of Permanent Magnet Synchronous Generators for Natural Impedance Matching in Small-scale Uncontrolled Passive Wind Generator Systems," in *Energies*, vol. 15, no. 5, pp. 1888, 2022.

International Conference Papers

C. J. J. Labuschagne and M. J. Kamper, "Performance and Cost Comparison of Conventional and Vernier Permanent Magnet Wind Generators for Small-scale Uncontrolled Passive Wind Energy Systems," in *2021 IEEE Energy Conversion Congress and Exposition (ECCE)*, Vancouver, Canada, 2021, pp. 4591-4597.

C. J. J. Labuschagne and M. J. Kamper, "Permanent Magnet Vernier Generator Design for a Small-scale Passive Wind Generator System," in *2021 IEEE International Electric Machines & Drives Conference (IEMDC)*, Hartford, CT, USA, 2021, pp. 1-7.

C. J. J. Labuschagne and M. J. Kamper, "Evaluation of PM Rotor Topologies for Impedance Matching of Small-Scale Passive DC-Connected Wind Generator Systems," in *2020 IEEE XIV International Conference on Electrical Machines (ICEM)*, Gothenburg, Sweden, 2020, pp. 690-696.

M. J. Kamper, C. Africa, C. J. J. Labuschagne and L. P. Mdakane, "Line Reactance Criteria for Minimizing Line Current Harmonic Content in Diode Rectifier Connected Wind Generator Systems," in *2020 IEEE International SAUPEC/RobMech/PRASA Conference*, Cape Town, South Africa, 2020, pp. 1-6.

C. J. J. Labuschagne and M. J. Kamper, "Design Optimisation and Comparison of Fractional-Slot Overlap and Non-Overlap Winding Direct-Drive PM Wind Generators for DC-connected Applications," in *2019 IEEE Energy Conversion Congress and Exposition (ECCE)*, Baltimore, MD, USA, 2019, pp. 724-731.

T. Kanda, L. P. Mdakane, C. J. J. Labuschagne and M. J. Kamper, "Dynamics of Maximum Power Point Wind Energy Battery Charging Systems," in *2019 IEEE Southern African Universities Power Engineering Conference/Robotics and Mechatronics/Pattern Recognition Association of South Africa (SAUPEC/RobMech/PRASA)*, Bloemfontein, South Africa, 2019, pp. 576-581.

C. J. J. Labuschagne and M. J. Kamper, "Performance Analysis of Direct-Drive PM Synchronous Wind Generator for Maximum Power Point Direct Battery Charging," in *2018 IEEE XIII International Conference on Electrical Machines (ICEM)*, Alexandroupoli, Greece, 2018, pp. 358-364.

C. J. J. Labuschagne and M. J. Kamper, "Design Optimisation and Comparison of Non-overlap Winding PM Wind Generators for Active and Passive Battery Charging Systems," in *2018 IEEE XIII International Conference on Electrical Machines (ICEM)*, Alexandroupoli, Greece, 2018, pp. 690-696.

National Conference Papers

C. J. J. Labuschagne and M. J. Kamper, "Coordinate Descent Method to Minimise Cogging Torque in Small-scale Wind Generators," in *2021 Southern African Sustainability Conference (SASEC)*, Stellenbosch, South Africa, 2020, pp. 182-187.

Industrial Research Report

C.J.J. Labuschagne, "Permanent Magnet Vernier Machines: Design and Feasibility Study for Railway Traction Applications," Siemens Mobility GmbH, R&D Motors and Generators, Nuremberg, Germany, Technical Report, 2020.

Acknowledgements

I would like to express my sincere gratitude to the following people and organisations:

My supervisor, Prof. M. J. Kamper, for his profound supervision and guidance throughout the course of this research, and also for his willingness and patience to support me beyond of what is expected.

The Centre for Renewable and Sustainable Energy Studies (CRSES) at Stellenbosch University, who funded this research.

My parents, Martin and Elena, for their love and support throughout the course of my studies. Also to my two younger brothers, Albert and Martin (Jnr.), who were always a helping hand when needed.

My fellow colleagues in the EMLab and faculty members at Stellenbosch University for their friendship and scientific exchanges. Dillan Ockhuis, Christoff Botha, Ore Olubamiwa, Marné Botha and Awie Botes for all the not-so-scientific exchanges (☕). A special mention to Dr. S. Gerber for his support with SEMFEM, and Dr. P. M. Tlali, for always being willing to assist and give advice.

To Dr. J. J. Germishuizen, who acted as my supervisor during the research exchange to Siemens Mobility in Nuremberg, Germany. Also to him and his family, Elke and Jan, for opening their home to me and many memorable weekends.

To Mr. K. Cloete and my brother Mr. A. W. Labuschagne, for their assistance with the mechanical design of the prototypes and the manufacturing thereof.

The workshop staff at the Department of Electrical Engineering who assisted with prototype manufacturing: Mr. A. Swart, Mr. H. Koopman, Mr. P. Petzer, Mr. M. Arendse and Mr. B. Gideons.

All of my close friends. Especially Gabriël Roux and Bernard Swart, a.k.a. the IT crowd, for their assistance with research related work.

To the colleagues at Siemens Mobility for their hospitality, their invaluable mentoring and interest in the project.

I would also like to thank Mr. S. H. Mullineux and Mr. J. M. Coetzer for the inspiration that set me on this career path.

Above all, I thank the Lord God Almighty.
For we are merely His machines, studying His work.

Dedications

Hierdie werk word opgedra aan

Liezl.

Om dankie te sê, vir alles.

Nomenclature

Abbreviations

2D	Two-dimensional
3D	Three-dimensional
AC	Alternating current
AEP	Annual energy production
C-PMVG	Conventional permanent magnet Vernier generator
CP-PMM	Consequent-pole permanent magnet machine
DC	Direct current
EMF	Electromotive force
E-PM	Embedded permanent magnet rotor
FE	Finite element
FEA	Finite element analysis
GCD	Greatest common divisor
FL	Full load
HAWT	Horizontal axis wind turbine
ICC	Installed capital cost
IG	Induction generator
LCM	Least common multiple
LCOE	Levelised cost of energy
MMF	Magneto-motive force
MPPT	Maximum power point tracking
NO-PMSG	Non-overlapping winding PM synchronous generator
NSGA-II	Non-dominated sorting genetic algorithm II
O&M	Operation and maintenance
O-PMSG	Overlapping winding PM synchronous generator
PF	Power factor
PM	Permanent magnet
PV	Photovoltaic
PMSG	Permanent magnet synchronous generator
PMSM	Permanent magnet synchronous machine
PMVG	Permanent magnet Vernier generator
PMVM	Permanent magnet Vernier machine
RMS	Root mean square

SP-PM	Spoke-type permanent magnet rotor
S-PM	Surface mounted permanent magnet rotor
ST-PMVG	Split-tooth permanent magnet Vernier generator
VAWT	Vertical axis wind turbine
WECS	Wind energy conversion system
WFSG	Wound field synchronous generator
WRSG	Wound rotor synchronous generator

Constants

$k_{\text{Cu}} =$	0.4
$\mu_{\text{Cu}} =$	$1.68 \times 10^{-8}\,\text{H/m}$
$\mu_0 =$	$4\pi \times 10^{-6}\,\text{H/m}$
$V_{\text{u}} =$	1040

Variables

α	Current angle	[deg]
δ	Load angle	[deg]
δ_{s}	Phase-displacement angle	[deg]
η	Generator efficiency	[%]
η_{system}	Total system efficiency	[%]
Λ_{uv}	Slot permeance factor	[ ]
Λ	Permeance	[Wb/A]
Λ_0	Average permeance	[Wb/A]
Λ_{v}	v^{th} harmonic permeance	[Wb/A]
λ_{PM}	PM flux linkage	[Wb]
λ	Flux linkage	[Wb]
λ_{t}	Tip speed ratio	[ ]
μ_x	Permeability of certain material denoted by x	[H/m]
ν	Harmonic order	[ ]
ω_{blade}	Wind turbine blade velocity	[rad/s]
ω_{m}	Mechanical turbine speed	[rad/s]
ω_{e}	Synchronous electrical speed	[rad/s]
ω_{r}	Mechanical rotor speed	[rad/s]
ρ_{air}	Air density	[kg/m^3]
ρ	Specified material's density	[kg/m^3]
σ	Electrical angle of a phase-band	[rad]
σ_{p}	Magnet pitch to pole pitch ratio	[ ]
σ_{t}	Slot opening to slot pitch ratio	[ ]
$\Delta\tau$	No-load cogging torque	[pu]
τ_{d}	Differential harmonic leakage-flux coefficient	[ ]
τ_{per}	Periodicity of a machine	[ ]

ξ	Magnetic saliency	[ ]
A_{blade}	Wind turbine blade area	[m^2]
A_{Cu}	Slot area per coil	[m^2]
A_ν	ν^{th} order machine constant	[ ]
B_{g}	Air gap flux density due to PMs	[T]
B_{aux}	Maximum auxiliary tooth flux density	[T]
B_{t}	Maximum stator tooth flux density	[T]
B_{lt}	Maximum lower tooth flux density	[T]
B_{ut}	Maximum upper tooth flux density	[T]
B_{yh}	Maximum stator yoke flux density	[T]
B_{r}	Remnant flux density	[T]
C_{f}	Wind site capacity factor	[pu]
C_{fs}	Wind site sub-system capacity factor	[pu]
C_{p}	Wind turbine power coefficient	[ ]
c, x, y	Steinmetz coefficients	[ ]
c_{p}	Coil pitch in terms of number of slots	[ ]
d_{i}	Air gap diameter	[m]
d_{o}	Outer diameter	[m]
E_{g}	Induced generator voltage	[V]
F_{ph}	Phase group MMF	[At]
F_ν	ν^{th} order 3-phase winding MMF harmonic	[At]
F_{PM}	Air gap MMF due to PM rotor	[At]
f_{e}	Synchronous electrical frequency	[Hz]
G_{r}	Harmonic coupling factor or magnetic gearing ratio	[ ]
g_{air}	Mechanical air gap	[mm]
g'_{air}	Effective air gap	[mm]
I_{rms}	RMS current	[A]
I_{s}	Generator current	[A]
I	Peak phase current	[A]
$i_{a,b,c}$	Instantaneous phase current	[A]
J_{rms}	Current density	[A/mm^2]
K_{f}	Fringing end-effect factor	[ ]
K_{s}	Saturation factor	[ ]
k_{c}	Carter's factor	[ ]
k_{Cu}	Copper fill factor	[%]
k_{e}	Stator end-winding factor	[ ]
k_{w}	Winding factor	[ ]
k_{d}	Coil distribution factor	[ ]
k_{p}	Coil pitch factor	[ ]
L_{c}	Transmission cable inductance	[mH]
L_{e}	End-winding inductance	[mH]

L_{ext}	External inductance	[mH]
L_{i}	Internal synchronous inductance	[mH]
L_{m}	Magnetisation inductance	[mH]
L_{sl}	Slot-leakage inductance	[mH]
L_{s}	Synchronous inductance	[mH]
l_{coil}	Average length of a coil turn	[m]
l_{e}	End-winding length	[m]
l_{Fe}	Axial stack length	[m]
l_{o}	End-winding overhang length	[m]
M_{active}	Active generator mass	[kg]
M_{PM}	PM mass	[kg]
M_{aux}	Auxiliary tooth iron mass	[kg]
M_{t}	Stator tooth iron mass	[kg]
M_{lt}	Lower tooth iron mass	[kg]
M_{ut}	Upper tooth iron mass	[kg]
M_{yh}	Stator yoke iron mass	[kg]
M_{s}	Number of machine sections	[ ]
m	Number of phases	[r/min]
N_{c}	Number of coils per phase	[ ]
N_{L}	Number of coil layers	[ ]
N_{s}	Number of turns per coil	[ ]
N_{sc}	Number of stator coils	[ ]
N_{ph}	Number of series turns per phase	[ ]
n_{c}	Cut-in speed	[r/min]
n_{r}	Rated speed	[r/min]
P_{air}	Total available power in the wind	[kW]
P_{bat}	Power delivered to the battery storage	[kW]
P_{Cu}	Copper losses	[kW]
P_{Fe}	Iron core losses	[kW]
P_{g}	Generated power	[kW]
P_{out}	Generator output power	[kW]
P_{t}	Turbine power	[kW]
P_{trans}	Transmission losses	[kW]
p	Number of pole pairs	[ ]
p_{p}	Number of poles	[ ]
p_{fm}	Flux-modulating poles	[ ]
p_{r}	Rotor pole pairs	[ ]
p_{s}	Stator pole pairs	[ ]
Q_{s}	Number of stator slots or teeth	[ ]
q	Number of slots per pole per phase	[ ]
R_{ac}	Referred AC battery resistance	[Ω]

R_{bat}	Internal battery resistance	[Ω]
R_c	Combined resistance of brush-slip-rings and transmission cable	[Ω]
R_e	End-winding resistance	[Ω]
R_{ext}	External inductor resistance	[Ω]
R_i	Internal resistance	[Ω]
R_s	Synchronous resistance	[Ω]
R_{st}	Equivalent per phase resistance	[Ω]
r_{blade}	Wind turbine blade tip radius	[m]
T_g	Generated torque	[Nm]
$\Delta T_{no\text{-}load}$	Peak to peak no-load torque	[Nm]
ΔT_{cog}	No-load cogging torque	[%]
ΔT_r	Full load torque ripple	[%]
t	Time	[s]
u	Number of coils in a phase group	[ ]
v_w	Wind velocity	[m/s]
V_{bat}	Battery terminal voltage	[V]
V_b	Battery terminal voltage referred to ac-side of diode rectifier	[V]
V_{diode}	Forwarde voltage drop across diode	[V]
V_{rms}	RMS voltage	[V]
V_u	End-winding constant	[ ]
W_s	Number of winding sections	[ ]
X_e	End-winding reactance	[Ω]
X_{ext}	External reactance	[Ω]
X_i	Internal synchronous reactance	[Ω]
X_m	Magnetisation reactance	[Ω]
X_{sl}	Slot-leakage reactance	[Ω]
X_s	Synchronous reactance	[Ω]
y_q	Coil span in slot pitches	[ ]
Z_c	Combined impedance of brush-slip-rings and transmission cable	[Ω]
Z_s	Synchronous impedance	[Ω]
Z_{ext}	External impedance	[Ω]
z	Number of parallel circuits	[ ]

Currency

$	United States Dollar
CNY	Chinese Yuan
R	South African Rand

Subscripts

d	Direct axis
q	Quadrature axis
ν	ν^{th} order harmonic ...

Contents

List of Figures

List of Tables

Chapter 1

Introduction

Energy generation for, and the electrification of, rural communities and farms are still some of the main socio-economic issues in developing countries. Especially for Sub-Sahara African countries, where a relatively small percentage of the rural population is estimated to currently have access to electricity. In this context of rural energy generation, and with the goal of climate change mitigation, wind and hybrid photovoltaic (PV) energy systems with battery storage are attractive options for ac or dc microgrids in remote communities where there is no utility grid connection. However, with the relatively inexpensive PV systems available nowadays, reports have shown that small-scale wind generator systems need to be more cost effective [1] [2] and there are current incentives to make small-scale distributed wind energy technology more competitive, e.g. [3] and those outlined in [4].

> *So, what are the challenges for small-scale wind energy systems and what can be done to make these wind energy systems more competitive?*

Recurring themes discussed in [4–8] indicate that the critical challenges that need to be addressed for small-scale wind energy systems are:

- To reduce installation costs
- To reduce operation and maintenance (O&M) costs
- To increase the system's performance (annual energy yield or capacity factor)

1.1 Background

1.1.1 Installation Costs

The first one of these challenges, albeit intuitive, is to reduce installation costs to attract new owners and to increase market penetration. Installation costs encompasses the costs of the whole system; thus the cost of the turbine tower, the blades, nacelle, yaw-system, electric hardware, energy storage and the wind generator. This may also include transportation and labour costs to install the wind energy system at the site. From a wind generator design perspective, it is possible to reduce installation costs by minimising the wind generator's active mass. This not only reduces the generator's material costs, but also reduces the turbine's top tower mass. Reducing the turbine's top tower mass is an attractive prospect, because this in turn may result in a smaller turbine tower structure being required. Furthermore, the most popular wind generator technology for small-scale

wind are permanent magnet synchronous generators (PMSGs) [9–11]. Given China's monopoly on expensive rare-earth materials (NdFeB) and the volatile cost thereof [12], it is also desired to reduce the amount of PM material used in the generator. Using less PM material could result in less expensive wind generator units and reduce the manufacturer's import costs.

1.1.2 Operation and Maintenance Costs

For small-scale wind energy systems, operation costs differ from maintenance costs. Operational costs would typically be insurance or a remote monitoring system. Maintenance costs on the other hand are more relevant and include labour, travel expenses and new components for repairs. In the case of remote standalone systems, extreme distances and the unavailability of components can result in prolonged downtime. Therefore, reliability and durability are essential. According to [13] and [14], the most common cause of failures in small-scale wind energy systems are the failure of the power electronic converters. Thus, deploying wind energy systems that use minimal power electronics could increase reliability and make the system more durable. Power electronics also add significantly to the installation cost. Mechanical failure in the drive train is another issue that often leads to downtime [13]. For wind turbines this is mostly failure of the gearbox [7], and as a result, the use of direct-drive wind generators are preferred [15].

1.1.3 System Performance

In [16] a study was conducted where the energy yield of different commercially available small-scale wind energy systems are compared. These systems were all installed at the same wind site. It was found that all of the wind energy systems produced a lower energy yield than what was predicted by the manufacturer's data. The main reason for this being poor power matching between the wind generator and the wind turbine power at low wind speeds. Unlike utility scale wind farms, small-scale wind energy systems are deployed according to need and not at the optimal wind site. The findings in [16] highlight the importance of designing small-scale wind energy systems for good power matching at low wind speeds and emphasises the importance of the generator's performance at the cut-in speed operating point.

Similarly, in the Distributed Wind Market Report: 2021 Edition for the U.S. Department of Energy [4], the low capacity factor[1] of small-scale wind energy systems is identified as a critical issue. Geographical differences of wind resources and installations near obstacles in complex terrain all contribute to a lower energy yield. This then further emphasises that good power matching with the wind turbine at low wind speeds should form part of the wind generator's design criteria. Downtime due to the wind turbine not operating for extended periods of time, caused by a lack of wind resources or system failure, is also identified in [4] as a contributing factor to poor performance. The latter ties in with the discussion on reliability in the previous subsection.

[1]Capacity factor is the system's actual annual energy production divided by its annual potential energy production if it were to operate at full capacity. Capacity factor is sometimes used as a measure of annual energy yield.

1.1.4 Introductory Remarks

From the above discussion on the challenges for small-scale wind energy systems, the design criteria pertaining to wind generator technology can be summarised by the following points:

1. Small-scale wind generators need to be designed to reduce material costs, especially rare earth PM material, and to minimise top tower mass.
2. It is imperative that the wind generator matches well with the available power from the wind turbine. This is necessary, not only at the rated operating point, but also at low wind speeds.
3. To make the system more reliable, minimal power electronics should be used. This however affects the control method, and thus the design methodology of the wind generator.

1.2 Small-scale Wind Energy Systems

Consider the single line diagrams of the small-scale wind energy systems shown in Fig. 1.1 where the wind generators are connected to the battery storage via different front end-rectifiers: Fig. 1.1(a) is an uncontrolled passive wind energy system that only makes use of a diode bridge rectifier between the wind generator and the battery storage. An actively controlled system is shown in Fig. 1.1(b), where an actively controlled synchronous rectifier is used for maximum power matching with the wind turbine. In Fig 1.1(c) a DC-DC system is shown, which uses an uncontrolled diode bridge rectifier and a controlled DC to DC converter for maximum power matching. The list of electric components for each of the wind energy systems in Fig. 1.1 are summarised in Table 1.1. The rectification method used for each of the systems in Fig. 1.1 has a direct effect on the size of the necessary wind generator for the same operating specifications. It is important to take this into consideration. Hence, a more comprehensive discussion on these systems and on relevant literature are given in the following subsections.

1.2.1 Passive Uncontrolled System

It is recognisable from Fig. 1.1 and Table 1.1 that uncontrolled passive wind energy systems are in many ways ideal for remote standalone applications due to the system's simplicity. Minimal power electronics are used in the system, and is therefore potentially more reliable and cost-effective. However, because the wind generator is uncontrolled, it is much more difficult to design the generator for good power matching with the wind turbine. The latter is most probably the reason why these systems aren't all that popular with industry in developed countries, but the former being the reason why they are

Table 1.1: Summarised list of electric components for the wind energy systems in Fig. 1.1.

System	External Inductance	Sensorless Control		High frequency filter
		Shaft encoder	V & I sensors	
Passive	✓/ ✗	✗	✗	✗
AC-DC	✗	✓/ ✗	✓	✓/ ✗
DC-DC	✗	✓/ ✗	✓/ ✗	✓

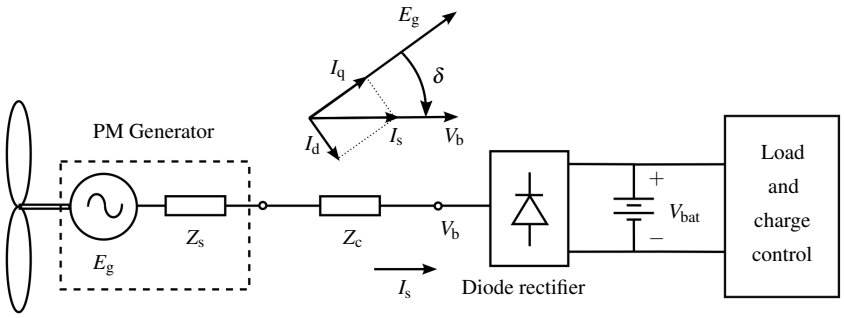

(a) Uncontrolled passive system

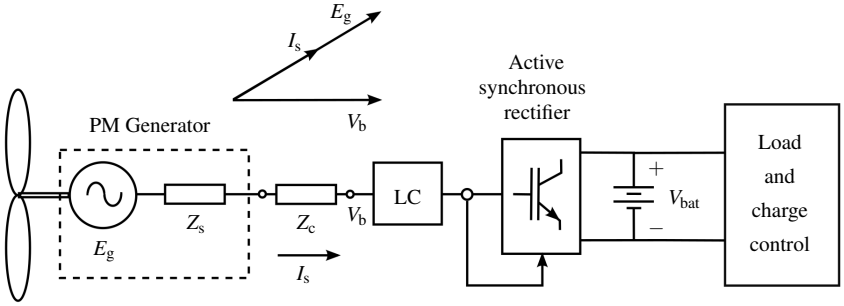

(b) Active synchronous rectifier controlled system

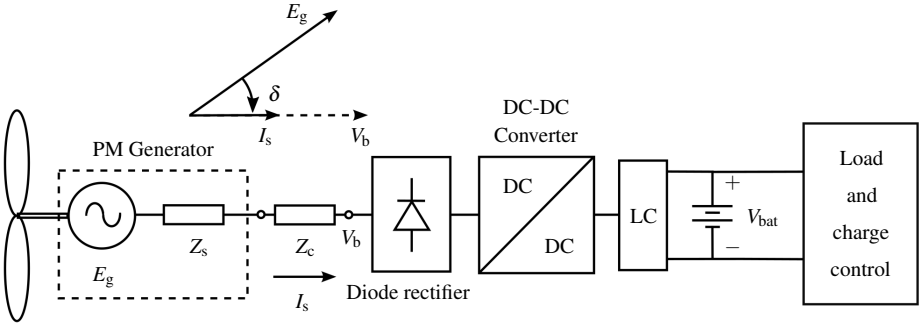

(c) DC-DC converter system

Figure 1.1: Simplified single line diagrams of PM wind generators connected to different front end-rectifiers with battery storage systems.

popular in developing countries, especially for rural areas. In most cases the generator will also be oversized, which is not ideal for a low top tower mass.

To shed more light on the generator design: An example of the wind turbine power versus turbine speed curves for a small-scale wind turbine is shown in Fig. 1.2. Power curve A in Fig. 1.2 shows the desired power matching for the passive system. The wind generator cuts in at the specified speed, n_c, and matches the maximum power of the wind turbine at the rated wind and turbine speed, indicated by n_r. Because no control method is used, the wind generator's internal impedance, Z_s in Fig. 1.1(a), needs to match correctly with the load voltage to ensure that the wind generator's power matches with the available power from the wind turbine at the maximum power point. Thus, the generator needs to be designed for a type of *natural impedance matching*. It is later shown with a theoretical estimation in Section 1.3.2, that for such a *natural impedance matching*, the required internal impedance of the generator is very large. For reference, power curve

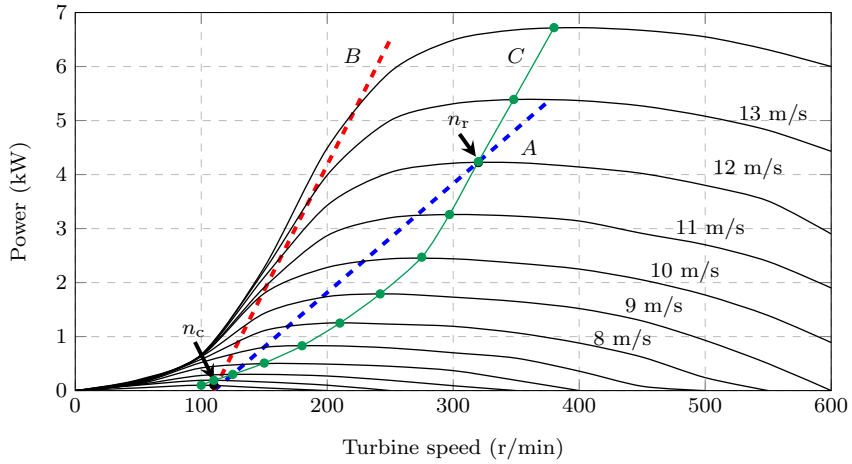

Figure 1.2: Wind turbine power versus turbine speed curves with wind speed a parameter. Examples of passive uncontrolled (curves A and B), and an actively and DC-DC controlled system (curve C).

B in Fig. 1.2 shows an example of the typical power curve of a surface mounted PM rotor permanent magnet synchronous generator (PMSG), with non-overlapping stator windings, and much smaller internal impedance.

Various approaches and generator design methodologies for uncontrolled passive wind generator systems are found in literature in [17–23]. In [17], the PMSG is designed for the desired performance and then the wind turbine's parameters are adjusted for better power matching. However, changing the wind turbine's parameters is not always desirable and it is standard practice to match the generator to the wind turbine. In [18–21], the PMSGs are designed by optimising the generator's power matching with the wind turbine for the potential power capture of a perceived "typical wind cycle". However, this approach to designing the wind generator neglects to design it for a specified cut-in speed. Through this approach the PMSG's operating power curve, curve B in Fig. 1.2, is essentially shifted to the right. Therefore, this approach does not necessarily guarantee good power matching at low wind speeds. The wind generators in these cases will have to be site-specific, seeing as small-scale wind energy systems are deployed according to need as opposed to at the optimal wind site. Ultimately, both the aforementioned design approaches are not optimal for a universal or geographically independent design, making it unsuited for small-scale distributed wind energy applications.

In [22] and [23] a method of external impedance matching is used, whereby an external impedance inductance is added between the wind generator and the diode bridge rectifier in Fig. 1.1(a). This method of impedance matching ensures that the generator matches with the wind turbine power and the power curve resembles curve A in Fig. 1.2. With the correct inductance added for external impedance matching, effectively any generator can be matched with any wind turbine, provided that the generator's rated power is sufficient. This also complements research on recycling electric machines for small-scale wind energy systems [24], [25]. Another additional advantage of the externally connected inductance is that it inadvertently addresses the issue of discontinuous current due to commutation [26] and ensures sinusoidal generator line currents flowing into the diode rectifier [27]. The latter is important, because this improves the torque quality and reduces the noise of the PMSG [28].

In [22] and [23], the external impedance matching was done for a passive wind energy

system with an *air cored* PMSG. However, when using an *iron cored* PMSG the necessary external inductance calculation is much more challenging. With iron-cored PMSGs the effect of saturation and armature reaction must be taken into account very accurately. More so in this case, with the relatively large demagnetisation d-axis current in the generator, as shown in Fig. 1.1(a). This makes the use of analytical models and calculations much more difficult. In [21], an analytical model is used to design the PMSG for the passive wind generator system, however substantial errors of 17% and 24% for the generated torque and back-EMF are reported. Therefore, to calculate the performance of the PMSGs, it is much better to use finite element analysis (FEA) methods. Considering all this, *there is a need to develop an accurate solution method to calculate the required external inductance for external impedance matching in passive wind energy systems.* The full extent to which this method can be practically applied also requires further investigation.

Although the forgoing external impedance matching method can be used effectively, as is done in [22] and [23], the additional external inductance to the system is still an unwanted component. If the wind generators can be designed to have a *natural impedance matching*, that would certainly make the passive system even more attractive. Therefore, *methods to design the PM generators to have the required internal impedance must also be investigated.*

1.2.2 Controlled Wind Energy Systems

The alternative to the uncontrolled system in the previous subsection are the controlled systems in Figs. 1.1(b) and (c). In these cases, maximum power point tracking (MPPT) of the system can be obtained by using power electronic converters as indicated in Fig. 1.1 and Table 1.1, along with rather complex MPPT algorithms [29–31]. The main advantage of using a controlled system with MPPT is that it is possible to extract the maximum available power from the wind turbine at all wind speeds; the wind generator's operating power curve would resemble that of power curve C in Fig. 1.2.

1.2.2.1 Active Synchronous Rectifier Controlled System

The actively controlled system shown in Fig. 1.1(b) is a popularly used system for small-scale wind energy, as well as utility scale wind energy systems. As mentioned, the advantage of an actively controlled wind energy system is that maximum power matching is achieved between the generator and the wind turbine for all wind speeds. Furthermore, the generator design is uncomplicated. This is due to only q-axis current flowing, as shown in Fig. 1.1(b), that is controlled by means of the active synchronous rectifier. The active synchronous rectifier can either be placed in the nacelle or at ground level. If the rectifier is placed in the nacelle, a larger nacelle structure is required and it would be very difficult to do repairs to the system. However, if the rectifier is placed at ground level, a high frequency LC-filter, shown in Fig. 1.1(b), must be connected between the generator and the active synchronous rectifier to prevent high switching frequency voltages along the transmission connection. When taking the LC-filter into account, the use of an active synchronous rectifier is complex in terms of position sensorless operation [32].

1.2.2.2 DC-DC Converter System

The DC-DC converter system shown in Fig. 1.1(c) is also a very attractive system for small-scale wind energy systems. The system somewhat resembles that of the Enercon

wind turbines [33], except that a PMSG is used instead of an electrically excited wound field/rotor synchronous generator (WFSG/WRSG).

In Fig. 1.1(c), the diode bridge rectifier can be placed on top of the tower in the wind turbine's nacelle. The advantage of this system is that it uses dc transmission between the generator and the battery bank, and can be utilised to minimise transmission losses in the system. A DC-DC buck step-down converter is used and is connected to the battery storage via an LC-filter. A further advantage, is that the control for this system need not be as difficult as for the active synchronous rectifier controlled system in Fig. 1.1(b). A simple robust MPPT control strategy can be implemented, as is done in [34–36], which makes use of a pre-calculated duty cycle function to implement a type of control method using gain scheduling.

1.2.2.3 On Generator Design and Additional Remarks

As mentioned, the generator design for the active synchronous rectifier controlled system in Fig. 1.1(b) is straight forward and uncomplicated. However, for the DC-DC converter system in Fig. 1.1(c), the generator design is more difficult due to the uncontrolled diode bridge rectifier that is connected between the generator and the DC-DC converter. Because of the uncontrolled diode bridge rectifier, the generator current and terminal voltage will be in phase, as shown in Fig. 1.1(c). Therefore, it is desired that the load angle, δ in Fig. 1.1(c), be as small as possible to maximise the generated torque. Thus, the wind generator needs to be designed for a small reactance. The choice of wind generator topology will therefore also be a factor that needs to be considered. Therefore, *the optimal choice of wind generator topology for the DC-DC controlled system in* Fig. 1.1(c) *needs to be investigated.*

In [37], an economic evaluation is done between an uncontrolled passive wind energy system and an active synchronous rectifier controlled wind energy system, both using an air-cored PMSG. It is found that the uncontrolled passive wind energy system is more cost-effective. Other than in [37], *there aren't any studies that specifically focus on comparing wind generator technology in passive uncontrolled wind energy systems to that in controlled wind energy systems for small-scale wind energy.*

1.3 Impedance Matching Requirements

In this section a theoretical estimation of the necessary impedance for the desired power matching in uncontrolled passive wind energy systems is given. This section then, serves as a theoretical problem statement and introduction to the requirements of passive wind energy systems. For the theoretical estimation a 4.2 kW passive wind energy system is used as an example.

1.3.1 4.2 kW System Specifications

The wind turbine power versus speed curves for the 4.2 kW wind turbine are shown in Fig. 1.2. It is desired that the wind generator start generating power at the indicated cut-in speed, n_c, and match with the maximum wind turbine power at rated speed, n_r, as indicated in Fig. 1.2. The specifications and desired operating points are summarised in Table 1.2. The wind generator is connected to a 48 V battery bank, via the diode bridge rectifier.

Table 1.2: Summary of specified operating points.

	$n_{\mathbf{c}}$	$n_{\mathbf{r}}$
Wind speed	3 m/s	12 m/s
Turbine speed	110 r/min	320 r/min
Generated power, P_{g}	0 kW	4.2 kW
Battery storage voltage, V_{bat}	48 V	

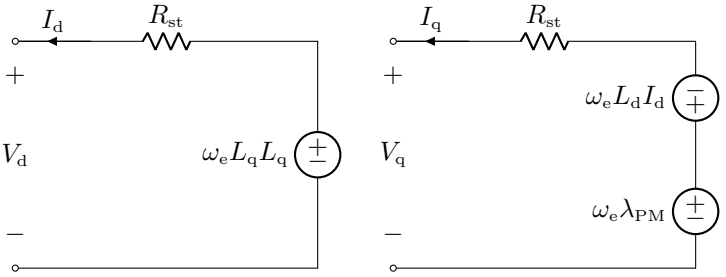

Figure 1.3: Per-phase dq-equivalent circuit diagram of PMSG.

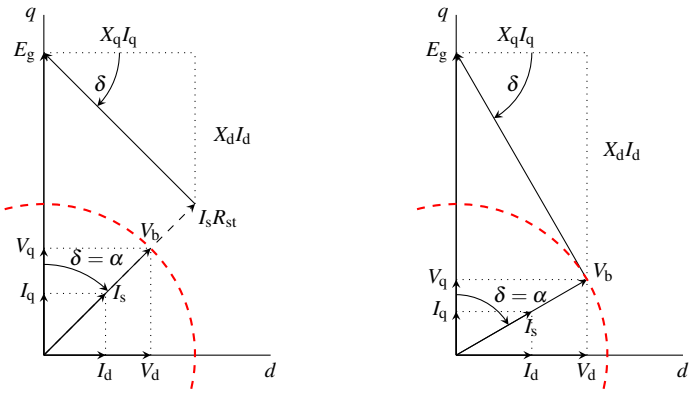

(a) **(b)**

Figure 1.4: Passive system phasor diagrams.

1.3.2 Equivalent Per Unit *dq*-modelling

The PMSG in Fig. 1.1(a) is modelled in the dq-reference frame. From the dq-equivalent circuits in Fig. 1.3, the steady-state dq-equations are

$$\begin{aligned} V_{\mathrm{q}} &= -R_{\mathrm{st}} I_{\mathrm{q}} - \omega_{\mathrm{e}} L_{\mathrm{d}} I_{\mathrm{d}} + \omega_{\mathrm{e}} \lambda_{\mathrm{PM}} \\ &= -R_{\mathrm{st}} I_{\mathrm{q}} - \omega_{\mathrm{e}} L_{\mathrm{d}} I_{\mathrm{d}} + E_{\mathrm{g}} \\ V_{\mathrm{d}} &= -R_{\mathrm{st}} I_{\mathrm{d}} + \omega_{\mathrm{e}} L_{\mathrm{q}} I_{\mathrm{q}}. \end{aligned} \tag{1.3.1}$$

In (1.3.1) and Fig. 1.3, ω_{e} is the synchronous electrical speed, λ_{PM} is the PM flux linkage, E_{g} is the induced generator voltage and R_{st} is the total per phase resistance of the passive system. The resulting phasor diagram for the passive system is shown in Fig. 1.4(a). In Fig. 1.4(a), the constrained terminal voltage, V_{b}, is the fixed fundamental per phase voltage on the ac-side of the diode rectifier. Due to the diode rectifier, the passive system will always operate at a unity displacement power factor [26], i.e. I_{s} and V_{b} are in phase.

For simplification, it is further assumed that R_{st} in (1.3.1) and Fig. 1.3 is negligible. Subsequently, we now have the phasor diagram in Fig. 1.4(b), and the dq-voltage equa-

tions of (1.3.1) can be rewritten as

$$\begin{aligned} V_{\mathrm{q}} &= -\omega_{\mathrm{e}} L_{\mathrm{d}} I_{\mathrm{d}} + E_{\mathrm{g}} = -X_{\mathrm{d}} I_{\mathrm{d}} + E_{\mathrm{g}} \\ V_{\mathrm{d}} &= \omega_{\mathrm{e}} L_{\mathrm{q}} I_{\mathrm{q}} = X_{\mathrm{q}} I_{\mathrm{q}}. \end{aligned} \tag{1.3.2}$$

At rated power, E_{g} can be calculated using

$$E_{\mathrm{g}} = a V_{\mathrm{b}} \tag{1.3.3}$$

with

$$a = \frac{n_{\mathrm{r}}}{n_{\mathrm{c}}} = \frac{320}{110} = 2.91. \tag{1.3.4}$$

From Fig. 1.4(b), we also have

$$\cos(\delta) = \frac{V_{\mathrm{b}}}{E_{\mathrm{g}}} = \frac{1}{a} \Rightarrow \delta = \cos^{-1}\left(\frac{1}{a}\right) \tag{1.3.5}$$

and

$$\tan(\delta) = \frac{V_{\mathrm{d}}}{V_{\mathrm{q}}} = \frac{I_{\mathrm{d}}}{I_{\mathrm{q}}} = \frac{X_{\mathrm{d}} I_{\mathrm{d}}}{X_{\mathrm{q}} I_{\mathrm{q}}} \Rightarrow \frac{X_{\mathrm{d}}}{X_{\mathrm{q}}} = 1.0. \tag{1.3.6}$$

Subsequently, by substituting a into (1.3.5) and then δ into (1.3.6) we have

$$\frac{I_{\mathrm{d}}}{I_{\mathrm{q}}} = \tan(69.9^{\circ}) = 2.73 \tag{1.3.7}$$

With $V_{\mathrm{b}} = I_{\mathrm{s}} = 1.0$ pu, the per unit values at rated power can be calculated and are summarised in Table 1.3.

Of course, R_{st} in Fig. 1.4(a) cannot be ignored. Nonetheless, the estimated per unit results in Table 1.3 are remarkable in terms of how high the per unit reactance must be to have the desired power matching. The required reactance at base speed is $X_{\mathrm{d}} = X_{\mathrm{q}} = 2.73/2.91 = 0.94$ pu, whereas surface mounted PMSGs with non-overlapping windings have per unit reactance values that are typically between 0.2 to 0.4 pu. Therefore, it is often necessary to add an external inductance, L_{ext}, between the PMSG and the diode rectifier, as shown in Fig. 1.5 ($Z_{\mathrm{ext}} = j\omega_{\mathrm{e}} L_{\mathrm{ext}}$).

Table 1.3: Predicted PMSG dq values at rated power.

$P = 1.0$ pu	$V_b = 1.0$ pu	$I_s = 1.0$ pu	$E_g = 2.91$ pu
$V_d = 0.94$ pu	$I_d = 0.94$ pu		$X_d = 2.73$ pu
$V_q = 0.344$ pu	$I_q = 0.344$ pu		$X_q = 2.73$ pu

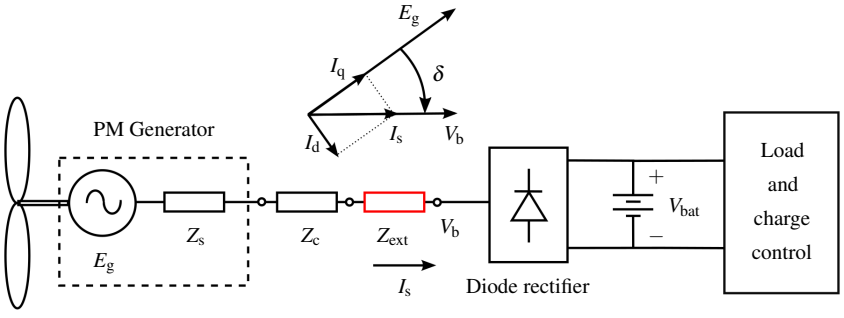

Figure 1.5: Single line diagram of the passive wind generator system with an external impedance added between the wind generator and the diode rectifier.

1.4 Main Research Question

It is evident that the uncontrolled passive wind energy system in Fig. 1.1(a) possesses many attractive attributes for rural and standalone distributed small-scale wind energy applications. However, designing the wind generator is difficult. The system also has drawbacks in terms of optimal power matching. So, there are questions such as "How to design the generator?" and whether the uncontrolled system is actually better than the controlled wind energy systems shown in Fig. 1.1.

Hence, a comprehensive study should be undertaken to give more perspective to industry on what the trade-offs are between these small-scale wind energy systems from a generator perspective. The main research question in this dissertation is then formulated as follows:

> **Can wind generators in small-scale uncontrolled passive wind energy systems be designed to make the system more competitive, and which properties make it a better alternative for the small-scale wind energy industry?**

1.5 Research Sub-questions

The main research question can be categorically sub divided into two parts:

Part 1 - Designing wind generators for uncontrolled passive wind energy systems.

Part 2 - Comparing them to those that are designed for controlled wind energy systems.

Similarly, this dissertation is also divided into two parts. However, for each of these parts in the dissertation there are aspects that require more in-depth investigation. To answer the main research question conclusively, the following additional research sub-questions need to be investigated and addressed:

Part 1: Uncontrolled Passive Wind Energy System

1. Are analytical methods to calculate the external inductance for external impedance matching sufficient or is there a more accurate solution method?
2. To what extent can external impedance matching be applied in small-scale passive wind energy systems to improve power matching?
3. Can PMSGs be designed for a *natural* impedance matching with the wind turbine? (i.e. there is no external inductance)
4. What are the alternative wind generator technologies, other than the widely used PMSG, and are there any benefits to using these technologies instead?
5. How does the uncontrolled passive system compare at different power levels in the small-scale power region?

Part 2: Controlled Wind Energy Systems

5. What is the optimal wind generator technology for the DC-DC controlled wind energy system?
6. What are the trade-offs from a generator perspective when using the different wind energy systems?

1.6 Dissertation Layout

A visual representation of the dissertation and its relation to the research sub-questions is given in Fig. 1.6.

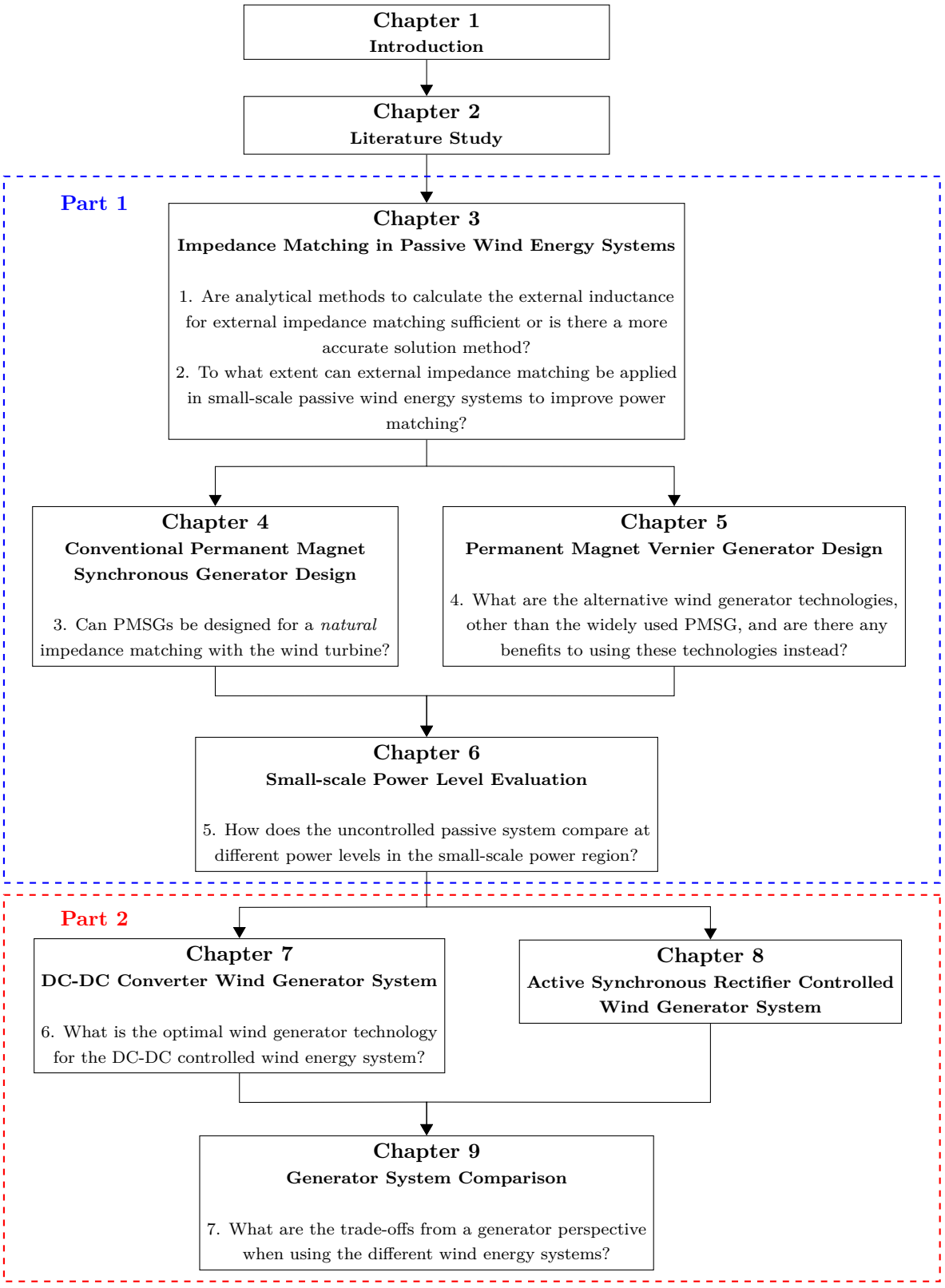

Figure 1.6: Visual representation of the dissertation.

1.7 Scope of the Dissertation

In this dissertation the focus is solely on the electromagnetic design and analysis of wind generators for small-scale wind turbines.

- Wind turbine and blade design are not within the scope. The wind generators in this dissertation are designed for the turbine power versus speed curves of two existing wind turbines. Mechanical and structural analysis of the generators are not included in the dissertation. However, basic mechanical design constraints form part of the electromagnetic design.

- In terms of electrical components: all power electronics, converters and wind generator control are not within the scope. Only the necessary requirements are taken into account in the generator design.

- A good method for comparing and determining the viability of renewable energy systems is to do a levelised cost of energy (LCOE) calculation. However, due to a lack of data this is not included in the dissertation.

1.8 Notes to the Reader

1.8.1 Definition of Small-scale

For the purpose of this dissertation, it is necessary to properly distinguish between the different power level ratings of wind turbines and their respective classifications. The classification used in this dissertation is given in Table 1.4.

There is often confusion in distinguishing between micro wind turbines and small-scale wind turbines. Various sources consider this transition to be at power levels that are either 1 kW, 2 kW or even 5 kW. In this dissertation, any wind turbine rated < 1 kW is considered to be a micro wind turbine. Thus, when referring to *small-scale* systems in this dissertation, it is implied that the power level of the wind turbine is between 1 kW and a 100 kW.

Table 1.4: Classification of power ratings for wind turbines.

Wind Turbine	Power rating
Micro	$0 - 1$ kW
Small	$1 - 100$ kW
Distributed	$0.1 - 1$ MW
Large	> 1 MW

1.8.2 Wind Generator and Turbine Control

For cases where an active synchronous rectifier or a DC-to-DC converter are used, ideal control of the generator and maximum power point tracking (MPPT) is assumed.

For more information on the dynamics of the DC-DC converter system the reader may refer to [27] and [34], and for the control thereof to [35] and [36]. The work done in [27] and [34] were investigated in the broader context of this study. However, this work is excluded from this dissertation and is rather cited in text in order to stay within the scope of the dissertation.

1.8.3 Finite Element Analysis Software

1.8.3.1 2D FEA

Unless otherwise specified, all static 2D FEA solutions and electrical machine designs were done with the in-house finite element package SEMFEM [38]. The commercial FE package, Infolytica MagNet, was also used for certain 2D FEA solutions. This is mainly to verify cogging torque values. Infolytica MagNet can also be used to generate informative plots for irreversible demagnetisation calculations and is used in this dissertation to present these results.

1.8.3.2 3D FEA

3D FEA is also used throughout this dissertation to verify certain generator designs. 3D FEA is very accurate and takes into account fringing end-effects, end-winding inductance etc.; design aspects that 2D FEA do not, that need to be added manually to the 2D FEA analysis. All 3D-transient solutions were done with the commercial FE package from Ansys Maxwell.

1.8.4 Optimisation Tools

Mutli-objective optimisation is used for the various generator designs. To facilitate the design optimisation the VisaulDOC package from Vanderplaats R&D is used in conjunction with the finite element package SEMFEM.

1.8.5 Repetition of Figures and Diagrams

For better continuity, and to enhance the reader's experience, certain figures or variations thereof are sometimes repeated throughout this dissertation. These figures are mostly given to indicate machine structures with dimensions that are relevant to the text. For reference, the wind energy systems in Fig. 1.1 are also repeated in the respective chapters where they are relevant.

1.8.6 Current Density Specification in Chapter 3

The maximum allowed current density in a machine is typically specified as a thermal constraint. In Chapter 3, a maximum *peak* value of $J = 6.5$ A/mm^2 is specified. Later on through the course of this dissertation, it was decided to change the maximum allowed current density specifications to $J_{\text{rms}} = 5$ A/mm^2. These values are nearly the same and the results in Chapter 3 were kept unchanged to keep them consistent with those published by the author in [39]. Ultimately, within the context of the research objectives this has no effect on the conclusions.

1.8.7 Material Costs

Material costs are difficult to account for, seeing that they vary with time and depend on the provider. They are also difficult to come by. If their costs were available from a reliable source, all of the material prices that are used in the cost evaluation are that of 1 December 2021.

1.9 Difficulties Encountered

1. Unforeseen mechanical difficulties, that were not under the author's control, delayed prototype construction.

2. The effect that the PM's dimensional tolerances have on the performance of the various generator prototypes was initially underestimated and not accounted for. Since rare earth neodymium magnets must be ordered from China, there was not enough time to rectify this oversight given the manufacturing and shipping timeline. This is later discussed in the relevant chapters.

Historical circumstances that had a significant impact on the research are:

3. The Covid-19 pandemic had an impact on various aspects that ultimately delayed the research. PMs had to be ordered from China for the generator prototypes, manufacturing thereof was delayed due to factories closing for extended periods of time. The same applied for specially machined mechanical components for the various prototype assemblies. Access to the faculty and laboratory were also restricted at times during the pandemic.

4. In South Africa, the government has implemented a controlled countrywide load shedding policy. During load shedding the electrical power to specific regions or communities are switched off for prolonged periods of time, according to a timetable that is stage dependent (extremity determined by the national energy provider). This directly affected the design optimisation done in this dissertation; optimisation algorithms are expensive in terms of computational time and can take multiple days to complete.
   (Ironically, this emphasises the importance of this research.)

1.10 Research Exchange

During 2020, the author worked as an intern researcher at Siemens Mobility GmbH, at the department for Research and Development of Motors and Generators in Nuremberg, Germany. The purpose was to investigate alternative electric machine technology for railway traction applications. In this case, focussing specifically on Vernier machines. At the time, the author had no prior experience in designing or working with Vernier machines. The agreement was that while being employed at Siemens Mobility, the author would study Vernier machines with the purpose of implementing Vernier machines thereafter in this dissertation. Some of the work presented in Appendix C is then from the industrial research report listed priorly under the "List of Publications" and cited in text as [40].

Chapter 2

Literature Study

2.1 Small Wind Generators: State of the Art

From a generator perspective, the PMSG and the squirrel cage induction generator are identified by [10] as distinctively suitable generators for small-scale wind energy systems. However, despite the volatile cost of PM material, the use of PMSGs in small-scale wind generator applications are far more popular with industry [9] [11]. Ultimately, PM machines are superior to electrically excited machines in terms of their efficiency and energy yield, their reliability and higher torque density [15]. PMSGs are also ideal wind generators for direct-drive implementation, which omits the gearbox and other mechanical transmission components in the wind generator drive train. By using a direct-drive wind generator system, the overall reliability of the system is increased and leads to lower maintenance cost [15] [41].

PMSGs can be classified into different types according to their structure, the orientation of the magnetic flux path, the winding type etc. Each PMSG variation has certain attributes that make them suitable for small-scale wind generator systems. In the following subsections, the main advantages and disadvantages are discussed. The discussion is mainly focussed on the following:

- **PM material -** Certain PMSG structures inherently use more rare-earth PM material. The cost of NdFeB over time is shown in Fig. 2.1. The current high price, shown in Fig. 2.1, emphasises the importance of using minimal PM material.
- **Specific torque -** For this application, a high specific torque is more important than a high torque density; a generator with a high torque per mass ratio is desired for potentially lowering the top tower mass.
- **Torque quality -** Wind generators with low cogging torque and torque ripple are very attractive for small-scale wind energy applications. Good torque quality reduces mechanical vibrations and noise. Moreover, low generator cogging torque is *essential* for the wind turbine to start spinning and generating power.
- **Manufacturing aspects -** The generator must be suitable for mass-production and not have a complex mechanical structure. Ease of manufacturing and insensitivity to manufacturing tolerances are an advantage.
- **Performance -** It is always desired to have a high generator efficiency.

Figure 2.1: Cost of rare earth Neodymium material over time [12].

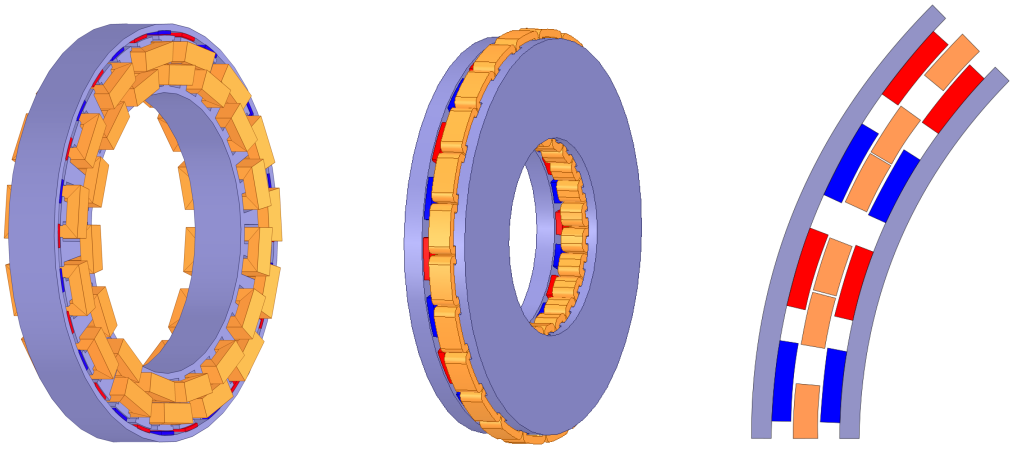

(a) Radial-flux **(b)** Axial-flux **(c)** Air-cored PMSG [45]

Figure 2.2: Examples of different PMSG topologies and structures.

2.1.1 Axial-flux vs Raidal-flux Generators

When classifying PMSGs as either axial-flux or radial-flux, the term refers to the orientation of the PMSG's magnetic flux path. Examples of a radial-flux and axial-flux PMSG are shown in Figs. 2.2(a) and (b) respectively. Axial-flux permanent magnet machines have the advantage of a short axial length, a simple winding layout, low cogging torque and a higher torque per volume ratio than radial-flux permanent magnet machines [42]. Some of the disadvantages are that they use a large amount of PM material, they are prone to have structural instability and have manufacturing difficulties such as to maintain the air gap over a large diameter due to high attraction forces. However, the main drawback is the lower torque per mass ratio (specific torque) when compared to radial-flux permanent magnet machines [42–44], which makes radial-flux permanent magnet machines more suitable for small-scale wind generator systems.

2.1.2 Air-cored vs Iron-cored Generators

The use of air-cored permanent magnet generators in wind turbines offers an alternative to iron-cored PMSGs. Air-cored PMSGs can also be used in direct-drive applications and have been investigated for small-scale wind turbines in [23] and [46]. For reference, the partial cross-section of a radial-flux double-sided air-cored PMSG is shown in Fig. 2.2(c).

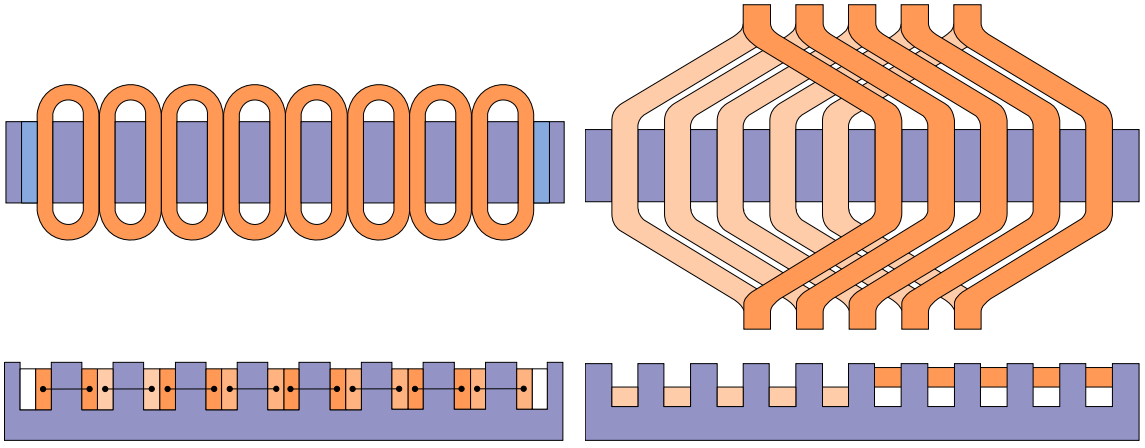

(a) Non-overlapping **(b)** Overlapping

Figure 2.3: Winding types. (Figures adapted from [48])

In [45], a comparison between air-cored and iron-cored radial-flux direct-drive PMSGs was done for small-scale actively controlled wind energy systems. The most appealing aspect pointed out in [45], is the superior torque quality of the air-cored PMSG which is important for start-up and low noise. Although the air-cored generator had a far greater volume than the iron-cored generator, its active mass was found to be almost the same. But in terms of cost, the excessive amount of PM material in the air-cored generator is its greatest disadvantage.

2.1.3 Winding Aspects and Considerations

Windings can generally be classified as either overlapping or non-overlapping windings. Examples are shown in Fig. 2.3. Windings can then further be sub categorised as either fractional-slot or integral-windings. If the number of stator slots per pole per phase is an integer number, the machine's winding is an integral winding. Integral winding PMSGs in general have a high torque ripple [47] and are not suited for wind generator applications. Therefore, only fractional-slot distributed overlapping windings and fractional-slot non-overlapping windings are considered in this dissertation for the PMSG design. Non-overlapping windings are also sometimes referred to as fractional-slot concentrated windings or tooth-concentrated windings.

PMSGs with non-overlapping windings (NO-PMSGs) are very attractive due to their short end-winding length. This makes it possible for the generator structure to be more compact and is ideal for direct-drive applications [49]. The NO-PMSG's shorter end-winding length also implies that it is possible to have less copper losses in the machine. The latter is very attractive for small-scale wind generators, since copper losses typically dominate the core losses in small machines. NO-PMSGs typically have a larger internal synchronous reactance than overlapping winding PMSGs (O-PMSGs). For the wind generator to achieve a *natural* impedance matching in an uncontrolled passive wind energy system, the NO-PMSG topology's larger internal synchronous reactance could be advantageous.

NO-PMSGs do however have a high space harmonic content in the air gap distribution [50]. These unwanted sub MMF harmonics may lead to additional losses in the rotor and can have a significant effect on the generator's performance [51] [52]. In terms of the manufacturing of the generator, the generator's iron yokes will have to be constructed

from segmented laminations to reduce core losses. These unwanted harmonics also result in eddy-current losses in the PMs. Therefore, the PMs must also be segmented. Contrarily, fractional-slot distributed overlapping windings have very little sub MMF harmonic content in the air gap distribution, which is considered to be an advantage. Furthermore, single-layer windings are prone to have larger sub MMF harmonics than double-layer windings and it has been shown in [53] that opting to use double-layer windings can reduce the rotor core losses. Therefore, only double-layer winding configurations are considered in this dissertation.

For both overlapping and non-overlapping windings, it is possible to use preformed coils in the manufacturing process. However, the non-overlapping coils with a slot pitch of one are considered to be more practical and easier to form by using simple moulds.

2.1.4 Discussion

From the preceding literature comparison, it is apparent that the radial-flux iron-cored PMSG is the most practical generator choice for direct-drive small-scale wind energy systems. NO-PMSGs with preformed coils are also considered easier to manufacture. Therefore, the NO-PMSG topology is investigated in Chapters 3 and 4 for the uncontrolled passive wind energy system and relates to research sub-questions 1, 2 and 3 in Chapter 1.5.

For the DC-DC converter system, the lower internal reactance of the O-PMSG topology might be an advantage over NO-PMSGs. However, the long end-winding lengths of the O-PMSG is not that good in terms of generator efficiency. Thus, to conclusively answer sub-question 5 in Chapter 1.5, "What is the optimal wind generator technology for the DC-DC controlled wind energy system?", a comparison between the NO-PMSG and O-PMSG needs to be done.

2.2 Alternative Generator Technology

There are other generator technologies that might offer a better alternative to PMSGs for the uncontrolled passive wind energy system in terms of impedance matching. In this section, the relevant literature on these alternative generator technologies are evaluated. This section is aimed at sub-question 5 in Chapter 1.5: "What are the alternative wind generator technologies, other than the widely used PMSG, and are there any benefits to using these technologies instead?"

2.2.1 Permanent Magnet Vernier Generator

Permanent magnet Vernier machines (PMVM) are very much at the forefront of current research on alternative wind generator technologies [15], with power levels ranging from small- to large-scale applications [54–56]. The extensive review on PMVMs in [57], highlights that PMVMs are paricularly suited for low speed direct-drive applications and have the potential for a high torque density. The PMVM's torque producing capability is especially attractive for wind generator technology. However, the practicality of PMVMs for industry are hindered by their characteristic of poor power factors, which increases the cost of the power converter. This can predominantly be attributed to the excessive leakage flux in PMVMs and to inherently high operating frequencies due to machine selection, with both factors contributing to a large reactance. Complex design structures have

been proposed to improve the PMVM's power factor [58] [59], but from a manufacturing perspective, these proposals are not always ideal for wind generator applications.

As mentioned, the preferred generator technology in small-scale wind generator systems are PM synchronous generators (PMSG), but the torque producing capability of PMVGs may further reduce generator cost and mass. This was shown in the direct comparison between a PMSG and PMVG for a small-scale *actively controlled* wind generator system in [55]. However, the compromise for the larger inverter due to the PMVG's low power factor is still the levelling trade-off. As of yet, the design of a PMVG for an uncontrolled passive wind generator system has not been done. The argument then, for using a PMVG in a passive wind generator system, is that for this application the PMVG's large internal reactance is not considered to be a drawback.

2.2.2 Wound Rotor Synchronous Generator

The wound rotor synchronous generator (WRSG) is another candidate for small-scale wind energy systems. The volatile cost of rare-earth PM material, and the scarceness thereof, does make a strong case for the WRSG to be considered as a possible machine technology. However, there are two main issues with implementing this generator technology in small-scale wind energy systems:

1. The WRSG requires a method of self excitation. Which makes it very impractical for the uncontrolled passive system and for standalone applications in general. Although it is not impossible to do an uncontrolled passive system with a WRSG, e.g. self excitation can be done using a small brushless exciter, investigating such a system is considered to deviate too far from the focus of this dissertation and is therefore out of the scope.

2. The lack of expensive PM material could possibly result in a cheaper wind generator. However, the WRSG would still have a lower torque density and therefore inevitably have a higher top-tower mass than the PM generators.

2.2.3 Induction Generators

Induction generators (IGs) also do not use any PM material and are therefore an attractive alternative. In the comparison/review in [10], IGs are considered to be better than PMSGs for small-scale wind generators. However, weighting tables are used in [10] to compare the different generator technologies. Weighting tables are subjective and do not necessarily reflect a technically conclusive outcome. Thus, they may not penalise or promote certain aspects fairly. For instance, IGs require a gearbox, which is undesired and increases O&M costs [13, 14]. Moreover, nearly all of the small-scale wind generators used in industry are PM generators [11]. Therefore, PM generators are noticeably more suited for small-scale wind energy systems.

2.2.4 Consequent-pole Permanent Magnet Generators

The consequent-pole PM machine (CP-PMM) topology is a variation on conventional PMSGs and PMVGs, and has recently gained a lot of interest because it uses less PM material. An example of a CP-PMM rotor is shown in Fig. 2.4. In [60] it was found that the CP-PMSG used 33.3% less PM material than a conventional NO-PMSG. Which is a

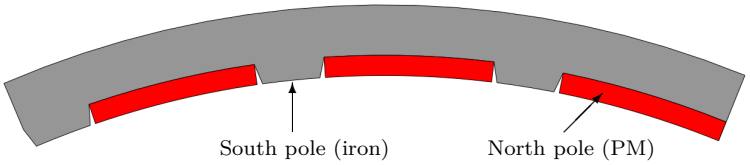

Figure 2.4: Partial cross-section of a consequent-pole rotor.

remarkable reduction considering the current rare-earth material price shown in Fig. 2.1. However, the problem with CP-PMMs is that they are sensitive to having a high torque ripple [61]. Various methods to reduce the torque ripple in CP-PMMs exist, such as pole shaping [61] and magnet shifting [62]. However, the problem is that even if the torque ripple is minimised, these CP-PMMs are still very sensitive to manufacturing tolerances. Within the context of this dissertation, the shaping of PMs and sensitive manufacturing tolerances are not ideal when one of the objectives is to simplify the manufacturing process.

2.2.5 Discussion

It is evident that WRSGs and IGs are not such a good generator choice for this application and are therefore not considered as viable generator technologies. CP-PMMs on the other hand are very attractive. However, the CP-PMM's torque quality is an issue.
The use of a PMVG in an uncontrolled passive wind energy system is a new and unknown concept. PMVGs may offer a better alternative to PMSGs and are investigated in Chapter 5 as an alternative generator technology.

2.3 Small-scale Wind Energy

In this section the focus is to address the relevance of small-scale wind energy and why it is important to strive for the advancement of this technology.

2.3.1 South African and Sub-Saharan Context

Although wind energy is mostly applied for large on- and offshore wind farms, small-scale wind energy offers a feasible solution for standalone systems and microgrids with energy storage. In a South African context, standalone systems with energy storage are an attractive option for farms and rural areas without access to the utility grid.

In Figs. 2.5(a) and (b), wind resource maps of the annual mean wind speed in South Africa at 20 m and 50 m above the ground are given. Additionally in Table 2.1, a breakdown of the electrification status of each South African province is given. It is shown in Table 2.1 that there is a serious demand for electrification, especially in provinces like the Eastern Cape and KwaZulu Natal. Both of whom, merely have 80% of households with reliable electricity. Although the data in Table 2.1 is for 2013, more recent data from The World Bank on rural access to electricity, given in Table 2.2, puts these figures more into

Table 2.1: Electrification status of South African provinces in 2013 (%). [63]

Provinces are numbered according to Fig. 2.5					
1. Northern Cape	89.7	4. North West	88.3	7. Gauteng	83.6
2. Western Cape	89.3	5. Free State	91.7	8. Mpumalanga	89.3
3. Eastern Cape	81.3	6. Limpopo	90.3	9. KwaZulu Natal	80.0

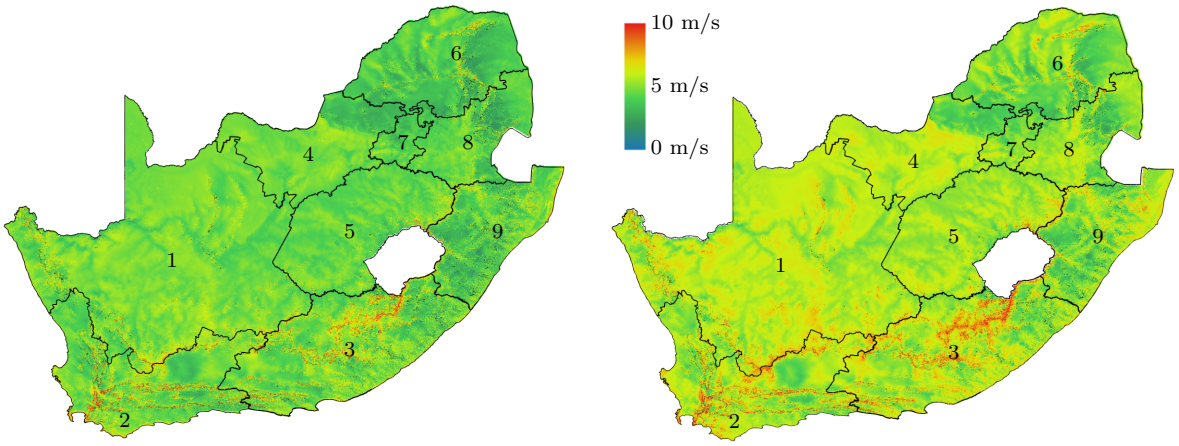

(a) 20 m **(b)** 50 m

Figure 2.5: Wind resource maps of South Africa. Data obtained from [64].

Table 2.2: Rural access to electricity in Sub-Saharan African countries 2019 (%). [65]

Angola	-	Ethiopia	36.3	Niger	12.6
Benin	17.4	Gabon	24.2	Nigeria	25.6
Botswana	27.6	Gambia, The	27.6	Rwanda	26.2
Burkina Faso	-	Ghana	70.0	São Tomé and Príncipe	75.2
Burundi	3.1	Guinea	16.4	Senegal	47.8
Cabo Verde	81.3	Guinea-Bissau	12.9	Seychelles	80.0
Cameroon	2.2	Kenya	61.7	Sierra Leone	1.5
Central African Rep.	1.5	Lesotho	32.2	Somalia	11.1
Chad	8.4	Liberia	7.6	**South Africa**	**79.2**
Comoros	78.2	Madagascar	-	South Sudan	5.1
Congo, Dem. Rep. of	1.0	Malawi	4.1	Sudan	39.0
Congo, Rep. of	12.7	Mali	15.3	Tanzania	19.0
Cote d'Ivoire	41.9	Mauritania	-	Togo	23.6
Equatorial Guinea	2.2	Mauritius	100.0	Uganda	31.8
Eritrea	36.7	Mozambique	4.9	Zambia	13.9
Eswatini	72.9	Namibia	35.0	Zimbabwe	20.1

perspective. It is shown in Table 2.2 that only 79.2% of rural households in South Africa currently have access to electricity. Therefore, from Fig. 2.5 it can objectively be pointed out that there are a lot of wind resources that can be harnessed to electrify these rural communities and farms. Especially in provinces like the North West province, and the Northern-, Eastern- and Western Cape.

For the rest of Sub-Saharan Africa, the percentages in Table 2.2 are a lot more detrimental. It is shown that for a lot of these countries, far less than 70% of the people in rural areas have access to electricity. From a humanitarian perspective, the percentages in Table 2.2 are particularly worrying and pose a great challenge. Furthermore, a lot of these communities are geographically isolated from utility grids and lack proper transportation infrastructure. Often in these remote areas the electricity consumption is too low to justify any new investment for the necessary infrastructure to connect to the main grid. Small-scale wind energy systems with energy storage therefore offer an excellent solution, however, the latter reiterates the need for these small-scale wind energy systems to be as durable and cost-effective as possible. In this context of cost-effective wind energy systems for Sub-Saharan Africa, even the recycling of an automotive alternator as a wind generator has been investigated in [11].

Of course, wind energy systems do not have to be deployed on their own. Various renewable energy resources can be integrated in a hybrid renewable energy system with battery storage. This way the different renewable resources can compensate for one another in periods of low generation. Nonetheless, small-scale wind energy can play a vital role in the electrification of South Africa and Sub-Saharan Africa. Particularly the uncontrolled passive system in Fig. 1.1(a), which is ideal for these applications given the techno-economic criteria.

2.3.2 Global Context

In the more global context, it is difficult to formulate an all encompassing picture of the small-scale wind energy market due to inconsistent data and the lack of reporting on new installations. The Distributed Wind Market Report: 2021 Edition for the U.S. Department of Energy [6] is probably the most detailed source available on this topic. The global cumulatively installed small-scale wind energy capacity is estimated to be approximately 1.8 GW [6]. A summary of the small-scale wind energy capacity for different countries is given in Table 2.3. It is shown in Table 2.3 that there were 25.65 MW of newly installed small-scale wind energy systems in China during 2020, which accounts for 84% of the global installations. Thereby completely dominating the current global market. Other countries, such as Denmark, Italy, the United Kingdom and the U.S.A also account for a significant proportion of the globally installed capacity.

It can be observed from Table 2.3 that the newly installed capacity of small-scale wind energy systems is very inconsistent, varying from country to country, year by year. The reason for this, is that at present, new small-scale wind energy installations are very dependant on government funded schemes and policies [4]. There is however increasing attention due to climate change awareness, and there are new incentives for deploying small-scale wind energy. Multiple studies have also been conducted in different countries to determine the feasibility thereof (even for urban deployment), such as those in [66–68]. However, for an uptake in the global small-scale wind energy market the challenges that are outlined in Chapter 1 must first be addressed.

It is definitely worth noting that the majority of small wind installations reported by companies in the U.S.A. for 2020 were refurbishments [6]. Refurbishments in this case meaning: existing installations were upgraded, where the existing towers were retrofitted

Table 2.3: Global small-scale wind energy capacity (MW). [4]*

Country	2013	2014	2015	2016	2017	2018	2019	2020	**Cumulative capacity**
				(MW)					
Australia	-	0.02	0.03	-	0.02	-	0.01	0.0	1.47
Brazil	0.03	0.02	0.11	0.04	0.11	0.29	0.44	0.07	1.11
Canada	-	-	-	-	-	-	-	-	13.47
China	72.25	69.68	48.60	45.00	27.70	30.76	21.4	25.65	610.61
Denmark	11.04	7.50	24.78	14.64	2.58	0.40	0.18	0.05	610.88
Germany	0.02	0.24	0.44	2.25	2.25	1.00	0.25	2.50	35.75
Italy	7.00	16.27	9.81	57.90	77.46	-	-	0.65	190.08
Japan	-	-	-	-	-	-	-	-	12.88
New Zealand	-	-	-	-	-	-	-	-	0.19
South Korea	0.01	0.06	0.09	0.79	0.08	0.06	0.0	-	4.08
United Kingdom	14.71	28.53	11.72	7.73	0.39	0.42	0.43	-	141.51
U.S.A.	5.70	3.67	4.32	2.43	1.74	1.51	1.3	1.55	152.65
Global	110.75	126.01	99.90	130.75	112.32	34.43	26.25	30.46	1774.68

*Refer to source for more detail on data.

with new generators, blades and power converters. As more small-scale wind energy systems are tending to reach the end of their lifetime, retrofitting of these systems are expected to continue and even increase. This is a very interesting trend, and bodes well for the argument for using uncontrolled passive wind energy systems; not only in a Sub-Sahara African context, but in the global context. Generators can effectively be recycled while limited power electronics are needed, making the refurbishment less expensive.

2.4 Implementation

Although the focus of this study is on wind generator design and not on the specifics of the load- or grid side, more information on the application is given in this section. The aim is to clarify the extent and limitations to which the direct battery connected wind energy systems, like the ones shown in Fig. 1.1, can be applied.

2.4.1 Energy Storage

In the past, diesel generators were often used for energy generation in standalone applications. Nowadays, single or various renewable energy sources can be used to replace diesel generators. However, microgrids and standalone energy systems require a form of back-up to ensure stability and to ensure continuous power supply with the imbalance between generation and demand. Therefore energy storage is a vital component in these systems. Battery technology, flywheels, super capacitors and super conducting magnetic energy storage are some of the energy storage technologies that are available, to name but a few.

Of the available energy storage technologies, battery energy storage offers clear advantages such as uninterrupted power supply, controllability, long term energy management and is geographically independent [69]. Compared to NiCd, NiMH and Li-ion batteries, the lead-acid battery is the most affordable battery for renewable applications [70]. Li-ion battery technology is on the uptake, with large scale MW capacity battery banks currently being installed. However, for Li-ion batteries each cell must be individually monitored for overcharge and therefore requires a sophisticated charge controller. With lead-acid batteries this is not an issue and the charge control can be implemented on the load side, as is shown in Fig. 1.1. Note that Li-ion batteries can still be used, but for rural small-scale applications lead-acid batteries are deemed more practical.

2.4.2 Microgrid and Standalone Applications

Regarding microgrids: At the moment there are numerous microgrid configurations, with no standardised regulations or guidelines on the system architecture (a thorough review on state of the art microgrid technology is given in [71]). Standalone energy systems are also technically a type of isolated dc microgrid. In this dissertation, it is proposed that the small-scale wind energy systems are implemented in a microgrid as shown in Fig. 2.6.

The proposed implementation shown in Figs. 2.6(a) and (b) resembles that of distributed energy storage system. In Fig 2.6, each renewable energy source is connected to an independent battery storage system that is then connected to a dc or ac bus. Thus, the state of charge for each battery storage system is also monitored separately. Furthermore, sizing of the battery storage for each renewable energy source can be done independently, which might be advantageous. In terms of the voltage level specifications, there aren't

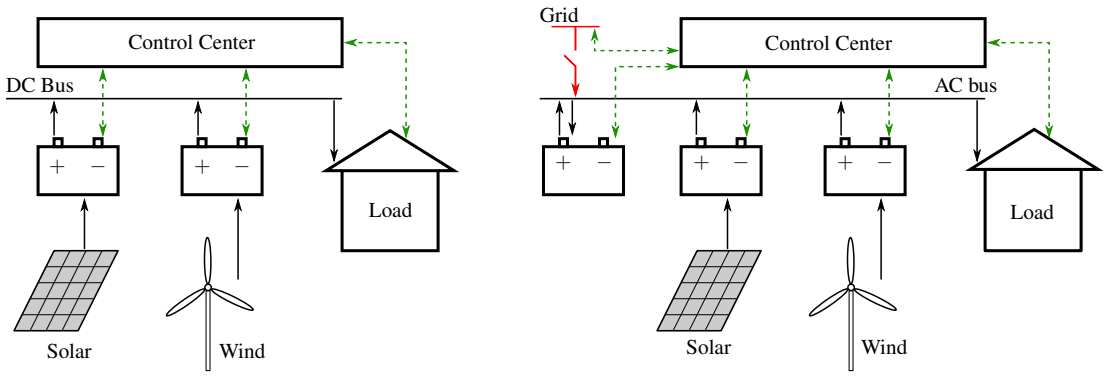

(a) Standalone **(b)** Microgrid

Figure 2.6: Diagrams illustrating the concept of the proposed implementation in a hybrid system. (For simplicity the converters are omitted from the schematic.)

any standardised regulations. However, in [71] some of the preferred voltage levels for dc power applications are given as:

- PV installation - 48V
- Energy storage system (Batteries) - 110V/220V

In the broader context and for real-world applications, the standalone and microgrid configurations shown in Figs. 2.6 are not fixed and ultimately just portray the concept. Other variations to the microgrid configuration will also work, as long as the directly connected wind energy system is implemented with a separate battery storage system.

2.5 Wind Turbine Technology

In this section, an overview of the different wind turbine technologies and the wind turbines that are used in this dissertation are given.

2.5.1 Wind Power

In short, the mechanical power that can be extracted from the wind by a wind turbine can be calculated using

$$\begin{aligned} P_{\mathrm{t}} &= C_{\mathrm{p}} P_{\mathrm{air}} \\ &= \frac{1}{2} C_{\mathrm{p}} \rho_{\mathrm{air}} v_{\mathrm{w}} A_{\mathrm{blade}}, \end{aligned} \tag{2.5.1}$$

where ρ_{air} is the air density, v_{w} is the wind velocity, A_{blade} is the area swept by the blades and C_{p} is the power coefficient that is less than the Betz limit of 0.59 [72]. The Betz limit is the maximum fraction of the available wind power that can be extracted by any ideal wind turbine. For small-scale wind turbines, the blades will almost always be fixed and not make use of blade-pitch control. Therefore, to maximise the wind turbine's efficiency, it is necessary to optimise the tip speed ratio of the turbine, λ_{t}. The tip speed ratio is calculated as

$$\lambda_{\mathrm{t}} = \omega_{\mathrm{blade}} \frac{r_{\mathrm{blade}}}{v_{\mathrm{w}}}, \tag{2.5.2}$$

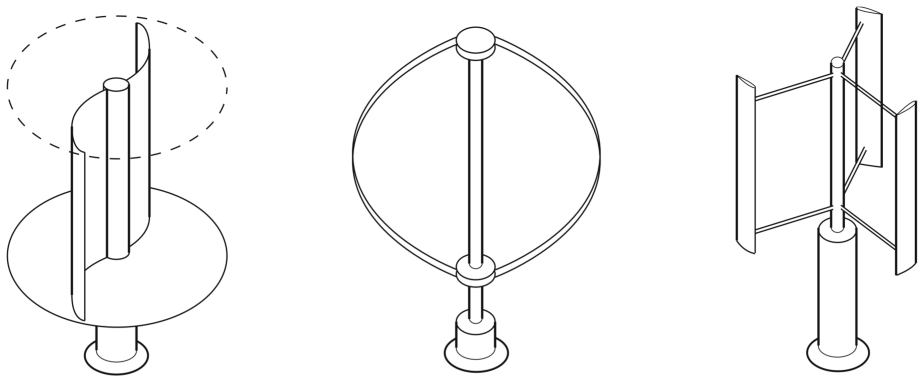

(a) Savonius **(b)** Darrieus **(c)** H-Darrieus

Figure 2.7: Vertical axis wind turbine topologies [73].

where ω_{blade} is the angular velocity of the wind turbine blades and r_{blade} is the turbine blade's radius. The aim is to match the angular velocity of the wind turbine to the incoming wind velocity, in order to optimise the power coefficient, C_{p}, in (2.5.1). A higher tip speed ratio will result in a better power coefficient, however, it will also result in the wind turbine having a low starting torque.

Wind turbine design is not within the scope of this dissertation. However, the brief theory on wind turbine design is relevant regarding the argument in Chapter 1.2.1 against the uncontrolled passive wind generator design in [17], where the wind turbine's power characteristics are unconventionally matched to the wind generator. Wind turbine and blade design can be intricate and computationally expensive [73]. Therefore, it is deemed impractical to have unstandardised wind turbines.

2.5.2 Vertical Axis Wind Turbines

There are two main types of wind turbines, namely the vertical axis wind turbine (VAWT) and the horizontal axis wind turbine (HAWT). Both aptly named according to the orientation of their drive-axis with relation to the incoming wind.

Different topology VAWTs are shown in Fig. 2.7. Some of the advantages for using VAWTs in small-scale wind energy systems are that they don't require a yaw system, and that the wind generator can be placed on the ground; making most components easily accessible for maintenance [74]. The latter also applies to the gearbox (if a gearbox were to be used in the drive train). The disadvantage of using VAWTs, is that they are less efficient compared to HAWTs [67]. VAWTs are typically placed lower to the ground, where wind speeds are also lower. However, they still offer a feasible solution for urban areas where they can be placed on the rooftops of office buildings or residential houses, as proposed in [75].

2.5.3 Horizontal Axis Wind Turbines

The preferred wind turbine technology for both small- and large scale wind turbines are HAWTs. These wind turbines have to be aligned with the wind direction and can further be sub categorised into upwind- and downwind turbines. Typically, for large scale wind turbines, an active yaw mechanism at the top of the tower is used to align the nacelle and blades with the direction of the wind. For small-scale wind turbines it is possible to

(a) 4.2 kW **(b)** 15 kW

Figure 2.8: Wind turbine structures.

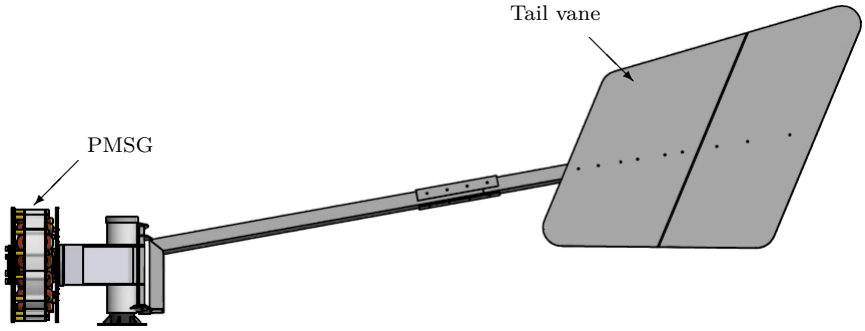

(a) Side view.

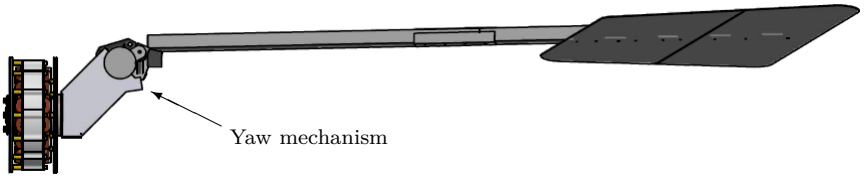

(b) Top view.

Figure 2.9: Schematic of the off-centre wind generator and tail vane assembly.

have a yaw system that passively aligns the turbine with the wind. Such is the case for the wind turbines used in this dissertation.

The erected 4.2 kW and 15 kW upwind turbines are shown in Fig. 2.8. The wind turbine data used in this dissertation are for these two respective wind turbines. A schematic of the nacelle's assembly is shown in Fig. 2.9. In Figs. 2.8 and 2.9, the nacelle has an full degree of rotation and the tail vane is used to align the nacelle's rotational

axis with the direction of the wind. Using a passive yaw mechanism instead of an active yaw mechanism has certain advantages in this case, such as reduced cost and a lower top tower mass. The 4.2 kW wind turbine in Fig. 2.8(a) has a blade radius of $r_{\text{blade}} = 1.9$ m, while the 15 kW wind turbine in Fig. 2.8(b) has a blade radius of $r_{\text{blade}} = 3.6$ m.

Regarding system protection: The wind turbine's blades and the PMSG are mounted off-centre in relation to the tower and tail vane as shown in Fig. 2.9(b). Under extreme conditions the wind pushes the turbine and generator out of the wind and against the tail mechanism that stays in line with the wind direction. In this way, the input power from the wind turbine is lowered, and system protection is provided.

Also, the HAWT's nacelle has an uncontrolled full degree of rotation and therefore requires brush-slip-rings for power transmission. The resistance of these brush-slip-rings need to be taken into account when designing the wind generators for the respective wind energy systems in Fig. 1.1. Note however, that results presented in this dissertation are not limited to this type of wind turbine technology.

Part 1

Uncontrolled Passive Wind Generator System

Chapter 3

Impedance Matching in Passive Wind Energy Systems

The theoretical estimation for the required impedance in passive wind energy systems in Chapter 1.3.2, shows why external impedance matching is often necessary for good power matching between the wind generator and the wind turbine. However, as outlined in Chapter 1.2.1, calculating the precise inductance value is difficult. Hence, the aim of this chapter is to address the following research sub-questions:

1. Are analytical methods to calculate the external inductance for external impedance matching sufficient or is there a more accurate solution method?

2. To what extent can external impedance matching be applied in small-scale passive wind energy systems to improve power matching?

Therefore in this chapter, first, an analytical method to calculate the external inductance is presented. Then, a new proposed solution method, that is more accurate, is given. Case studies for the 4.2 kW and 15 kW wind turbines are then presented to evaluate the two solution methods. The results are then verified with experimental measurements.

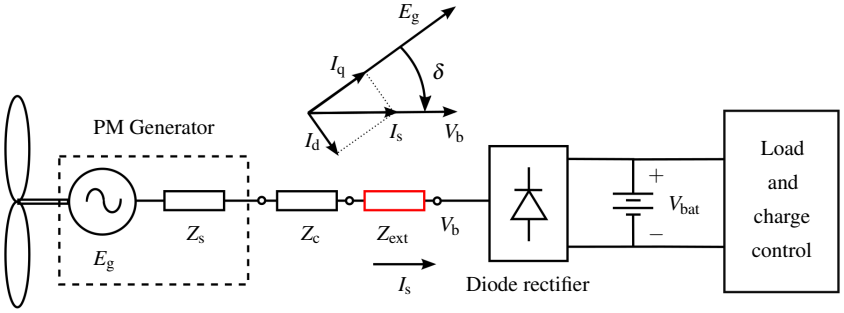

Figure 3.1: Single line diagram of the passive wind generator system with an external impedance added between the wind generator and the diode rectifier.

3.1 Analytical Method

In this section, the analytical calculation for the external inductance, L_{ext}, in Fig. 3.1 is given. The per phase equivalent and ac-equivalent circuits of the passive system in Fig. 3.1 are given in Figs. 3.2(a) and (b) respectively.

3.1.1 Battery Storage

For the passive system's analysis, the battery storage in Fig. 3.1 is typically modelled as a dc voltage, V_{bat}, in series with an internal resistance, R_{bat}, as shown in Fig. 3.2(a) [22]. The dc voltage, V_{bat}, and the forward voltage drop across a diode in the diode rectifier, V_{diode}, are used to calculate the fundamental phase voltage on the ac side of the diode rectifier as

$$V_{\text{b}} = \frac{\sqrt{2}(V_{\text{bat}} + 2V_{\text{diode}})}{\pi}, \tag{3.1.1}$$

and is shown in Fig. 3.2(b). The internal battery resistance is also referred to the ac side of the diode bridge rectifier as an ac-equivalent resistance, using

$$R_{\text{ac}} = \frac{6R_{\text{bat}}}{\pi^2}. \tag{3.1.2}$$

3.1.2 System Inductance

The per phase synchronous inductance of the PMSG in Fig. 3.2 is calculated as

$$\begin{aligned} L_{\text{s}} &= L_{\text{i}} + L_{\text{e}} \\ &= L_{\text{m}}(1 + \tau_{\text{d}}) + L_{\text{sl}} + L_{\text{e}}, \end{aligned} \tag{3.1.3}$$

where L_{m} is the magnetisation inductance, τ_{d} is the differential harmonic leakage flux coefficient, L_{sl} is the slot-leakage inductance and L_{e} is the end-winding inductance. The

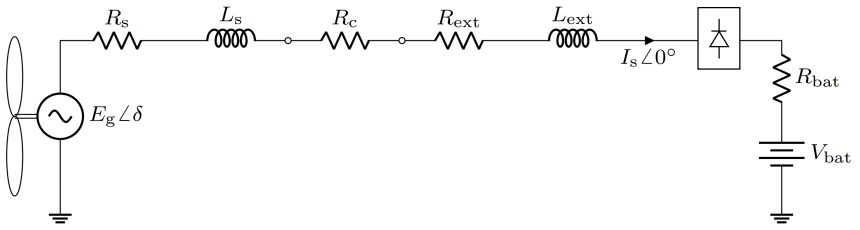

(a) Per phase equivalent circuit diagram.

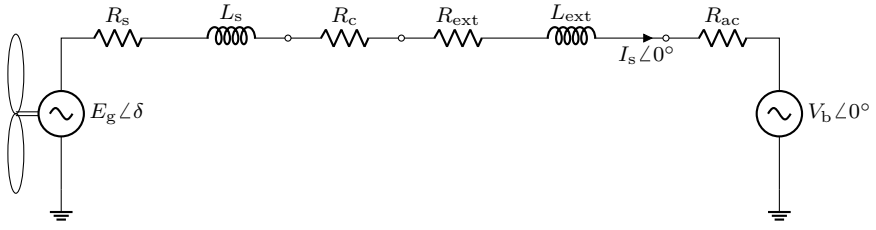

(b) Per phase ac-equivalent circuit.

Figure 3.2: Analytical modelling of the passive wind generator system.

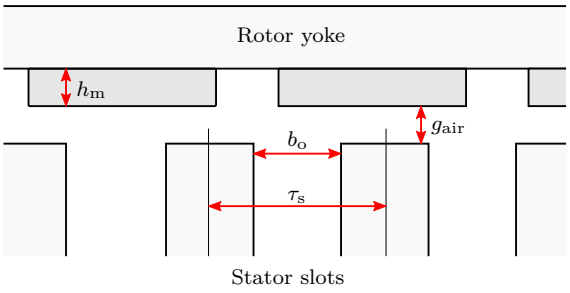

Figure 3.3: Linearised geometry of a typical PMSG with surface mounted PMs.

passive system's cable inductance, L_c, is considered negligible in the analysis, but can be incorporated if significant.

3.1.2.1 Magnetisation Inductance

The magnetisation inductance in (3.1.3) is given by

$$L_m = \frac{m(N_{ph}k_{wj})^2 d_i l_{Fe}\mu_0}{\pi p_p^2 g'_{air} K_s}, \tag{3.1.4}$$

where m is the number of phases, N_{ph} is the number of turns in series per phase, k_{wj} is the winding factor of the generator's working harmonic, d_i is the air gap diameter, l_{Fe} is the axial stack length, p_p is the number of pole pairs and K_s is the saturation factor. In (3.1.4), g'_{air} is the resultant air gap length taking Carter's factor, k_c, into account

$$g'_{air} = g_{air} + (k_c - 1)\left(g_{air} + \frac{h_m}{\mu_{PM}}\right). \tag{3.1.5}$$

Here, h_m is the PM height as shown in Fig. 3.3 and μ_{PM} is the relative permeability of the PM material. Carter's factor is calculated as in [76] using

$$k_c = \frac{\tau_s}{\tau_s - \gamma g_{air}}, \tag{3.1.6}$$

where γ is a function of the length of the slot opening, b_o, and the air gap, g_{air}, and is given by

$$\gamma = \frac{4}{\pi}\left(\frac{b_o}{2g_{air}}\tan^{-1}\frac{b_o}{2g_{air}} - \ln\sqrt{1+\left(\frac{b_o}{2g_{air}}\right)^2}\right). \tag{3.1.7}$$

3.1.2.2 Differential Harmonic Leakage Flux Coefficient

The differential harmonic leakage flux coefficient, τ_d in (3.1.3), is calculated from the harmonic analysis as in Appendix A, and is given by

$$\tau_d = \frac{\sum_{n\neq j}\left(\frac{k_{wn}}{n}\right)^2}{\left(\frac{k_{wj}}{j}\right)^2}. \tag{3.1.8}$$

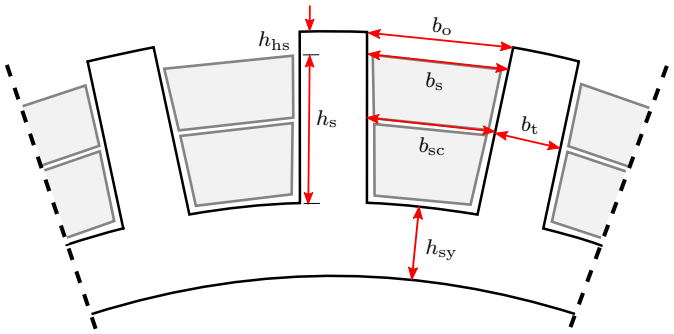

Figure 3.4: Stator slot structure with open slots and rectangular teeth.

3.1.2.3 Slot-leakage Inductance

The slot-leakage inductance, L_{sl}, is calculated using

$$L_{sl} = \frac{4m}{Q_s}\mu_0 l_{Fe} N_{ph}^2 \Lambda_{uv} \tag{3.1.9}$$

as in [77] and [78]. Here, Λ_{uv} is the slot permeance factor given in [77] for a double-layer non-overlapping winding with a vertical coil side arrangement (top bottom arrangement), and is given by

$$\Lambda_{uv} \approx z_1 \frac{h_s}{3b_s} + z_2 \frac{h_{hs}}{b_o}. \tag{3.1.10}$$

In (3.1.10), z_1 and z_2 are given by

$$\begin{aligned} z_1 &= 1 - \frac{3}{16}\frac{|y_q - c_p|}{q} \\ z_2 &= 1 - \frac{|y_q - c_p|}{4q} \end{aligned} \tag{3.1.11}$$

as in [77]. An example of the stator structure with a vertical coil side arrangement is shown in Fig. 3.4.

3.1.2.4 End-winding Inductance

The per phase end-winding inductance is calculated using the analytical approximations for non-overlapping winding PM machines in [79], as

$$L_e = \frac{N_s^2 N_c}{z^2}\left(\frac{3.9478 r_c^2 + 1.257 r_c(b_o + b_{sc})}{b_{sc}}\right)(K_1 + K_2). \tag{3.1.12}$$

In (3.1.12), N_s is the number of turns per coil, N_c is the number of coils per phase and z is the number of parallel circuits. The dimensions r_c, b_o and b_{sc} are defined in Fig. 3.5. The constants K_1 and K_2 are both given by

$$K_i = k_1 - k_2. \tag{3.1.13}$$

To calculate k_1, the following series formula can be used

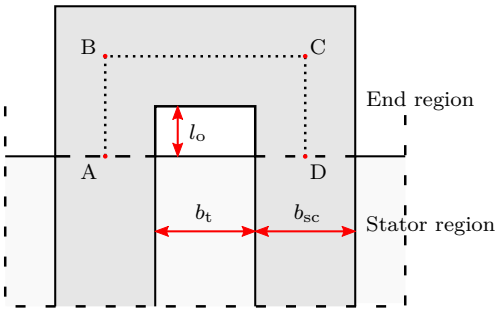

(a) Approximation of the end-winding path length.

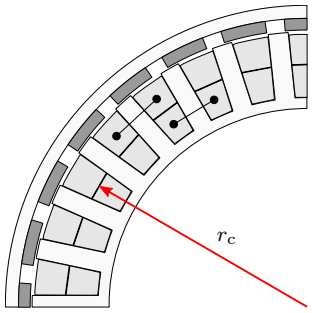

(b) Partial cross-section of a PMSG.

Figure 3.5: Dimensions for the non-overlapping end-winding calculations.

$$k_1 = \frac{2\beta}{\pi}\left[\left(\log_e\frac{4}{\beta}-\frac{1}{2}\right)+\frac{\beta^2}{8}\left(\log_e\frac{4}{\beta}-\frac{1}{8}\right)\right] - \frac{2\beta}{\pi}\left[\frac{\beta^2}{64}\left(\log_e\frac{4}{\beta}-\frac{2}{3}\right)+\frac{5\beta^6}{1021}\left(\log_e\frac{4}{\beta}-\frac{109}{120}\right)\ldots\right], \tag{3.1.14}$$

where β is equal to $b_{sc}/2r_c$ for K_1, and b_{sc}/r_c for K_2. The first three terms in (3.1.14) will yield an accurate enough value for k_1 [80]. The corresponding values for k_2 can be found in the lookup tables in Appendix B.

3.1.3 Equivalent Resistance

The generator's combined internal and end-winding per phase resistance can be calculated using

$$\begin{aligned} R_s &= R_i + R_e \\ &= \frac{2N_c N_s^2 \mu_{Cu}(l_{Fe}+l_e)}{zA_{Cu}k_{Cu}}, \end{aligned} \tag{3.1.15}$$

where A_{Cu} is the slot area per coil and k_{Cu} is the copper fill factor. For non-overlapping windings the end-winding length, l_e, is approximated as

$$l_e = 2l_o + 2b_s + 2b_t, \tag{3.1.16}$$

by the path ABCD in Fig. 3.5.

In Fig. 3.2, R_c is the resistance of the brush-slip-rings in the nacelle and transmission cable. Typical resistance values for the brush-slip-rings are between 0.2 and 0.3 Ω. Also in Fig. 3.2, R_{ext} is the resistance of the external inductance.

3.1.4 External Inductance Calculation

The resulting phasor diagram from the equivalent circuits in Fig. 3.2 is shown in Fig. 3.6, and is used for the analytical calculation of L_{ext}. Due to the diode rectifier, the passive system will operate at a unity displacement power factor [26]. As shown in Fig. 3.6, the generator current, I_s, is in phase with the fundamental component of the terminal voltage, V_b, at the diode rectifier. Hence the current angle, α, is equal to the load angle, δ,

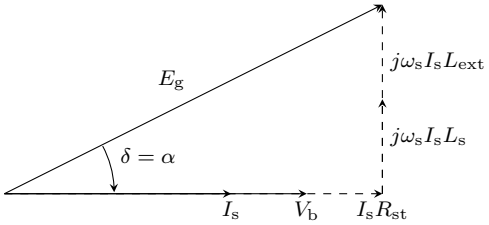

Figure 3.6: Equivalent per phase phasor diagram.

between the induced generator voltage E_g and the terminal voltage V_b, shown in Fig. 3.6. In Fig. 3.6, R_{st} is the equivalent per phase resistance given by

$$\begin{aligned} R_{st} &= R_s + R_c + R_{ext} + R_{ac} \\ &= R_i + R_e + R_c + R_{ext} + R_{ac}. \end{aligned} \tag{3.1.17}$$

The induced generator voltage at the rated operating point can be calculated using the relationship between E_g and the turbine speed, as given in (3.1.18). Since V_b is equal to the induced generator voltage at cut-in speed n_c, the induced generator voltage at rated speed n_r is given by

$$E_{g(r)} = V_b \frac{n_r}{n_c}. \tag{3.1.18}$$

As it is a small-scale wind generator, the core and windage-and-friction losses of the generator are further ignored. Thus, the generated power, P_g, is assumed equal to the known turbine power, P_t:

$$P_g = 3E_{g(r)} I_s \cos\delta \approx P_t. \tag{3.1.19}$$

From Fig. 3.6, $\cos\delta$ is calculated as

$$\cos\delta = \frac{V_b + I_s R_{st}}{E_{g(r)}}. \tag{3.1.20}$$

By substituting (3.1.20) into (3.1.19) and solving the quadratic equation, the rated current is given by

$$I_s = \frac{\sqrt{V_b^2 + \frac{4}{3} R_{st} P_g} - V_b}{2R_{st}}. \tag{3.1.21}$$

With I_s known, the load angle δ can now be calculated from (3.1.20). Also from Fig. 3.2(b),

$$\sin\delta = \frac{I_s \omega_e (L_s + L_{ext})}{E_{g(r)}}. \tag{3.1.22}$$

Subsequently, L_{ext} is calculated analytically by rewriting (3.1.22) as

$$L_{ext} = \left(\frac{60 V_b}{\pi p n_c}\right) \frac{\sin\delta}{I_s} - L_s, \tag{3.1.23}$$

where p is the number of poles and L_s is calculated analytically from (3.1.3).

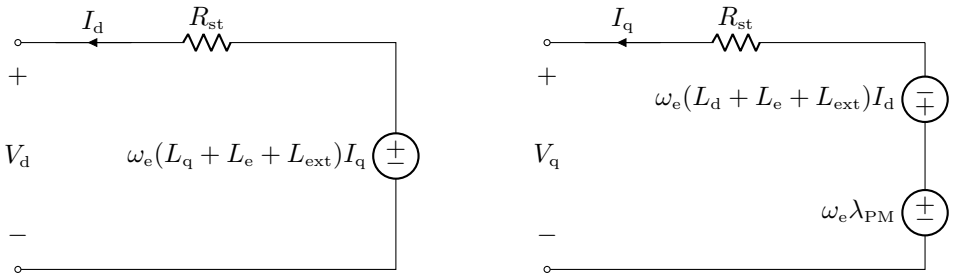

Figure 3.7: Per-phase *dq*-equivalent circuit diagram.

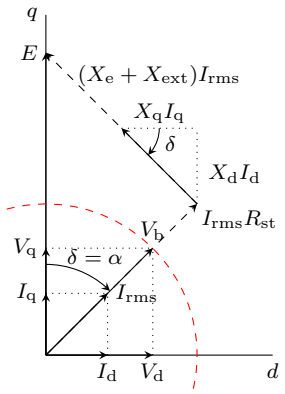

Figure 3.8: Equivalent vector diagram.

3.2 Equivalent Passive System Modelling

In the previous section, an approximated per phase model is used to analytically estimate L_{ext}. However, a more detailed model of the machine is necessary for an accurate calculation of L_{ext}. In this section, the equivalent modelling used for the proposed FEA based solution method in Section 3.3 is discussed.

3.2.1 Equivalent Circuit *dq*-modelling

The PMSG modelling for the static FEA is done in the steady-state and with the *dq*-reference frame fixed to the PM rotor. Fig. 3.7 shows the *dq*-equivalent circuits and the resulting vector diagram for the passive system is shown in Fig. 3.8.

The steady-state *dq*-equations can be derived from the *dq*-equivalent circuits in Fig. 3.7, as

$$V_q = -R_{st}I_q - \omega_e(L_d + L_e + L_{ext})I_d + \omega_e\lambda_{PM} \tag{3.2.1}$$

$$V_d = -R_{st}I_d + \omega_e(L_q + L_e + L_{ext})I_q, \tag{3.2.2}$$

where ω_e is the synchronous electrical speed and R_{st} is the same as in (3.1.17). The *dq*-inductances, L_q and L_d, are given by (3.2.3) and (3.2.4) respectively.

$$L_q = \frac{\lambda_q}{-I_q} \tag{3.2.3}$$

$$L_d = \frac{\lambda_d - \lambda_{PM}}{-I_d} \tag{3.2.4}$$

The general relations of voltage and current are given by

$$\begin{bmatrix} V_{\mathrm{q}} \\ V_{\mathrm{d}} \end{bmatrix} = \sqrt{2} V_{\mathrm{rms}} \begin{bmatrix} \cos\delta \\ \sin\delta \end{bmatrix} \\ \begin{bmatrix} I_{\mathrm{q}} \\ I_{\mathrm{d}} \end{bmatrix} = \sqrt{2} I_{\mathrm{rms}} \begin{bmatrix} \cos\alpha \\ \sin\alpha \end{bmatrix}, \tag{3.2.5}$$

where V_{rms} is the RMS value of the fixed voltage on the ac side of the uncontrolled diode rectifier, i.e. $V_{\mathrm{rms}} = V_{\mathrm{b}}$ of (3.1.1).

3.2.2 Performance

The developed torque and the electrical power generated by the PMSG are calculated using (3.2.6) and (3.2.7) respectively.

$$T_{\mathrm{g}} = \frac{3}{2} p_{\mathrm{p}} [(L_{\mathrm{q}} - L_{\mathrm{d}}) I_{\mathrm{d}} I_{\mathrm{q}} + \lambda_{\mathrm{PM}} I_{\mathrm{q}}] \tag{3.2.6}$$

$$P_{\mathrm{g}} = T_{\mathrm{g}} \omega_{\mathrm{m}} \tag{3.2.7}$$

The efficiency of the PMSG is calculated using

$$\eta = \frac{P_{\mathrm{g}} - P_{\mathrm{Cu}}}{P_{\mathrm{g}} + P_{\mathrm{Fe}}}, \tag{3.2.8}$$

where P_{Cu} is the copper losses and P_{Fe} is the iron core losses in the stator. To simplify the efficiency calculation, windage-and-friction losses are ignored. The copper losses are calculated as

$$P_{\mathrm{Cu}} = 3 {I_{\mathrm{rms}}}^2 R_{\mathrm{s}}. \tag{3.2.9}$$

The core losses are calculated by a semi-analytical method, expressed as

$$P_{\mathrm{Fe}} = c {f_{\mathrm{e}}}^x ({B_{\mathrm{t}}}^y M_{\mathrm{t}} + {B_{\mathrm{yh}}}^y M_{\mathrm{yh}}), \tag{3.2.10}$$

using Steinmetz coefficients and static FEA. B_{t} and B_{yh} are static FEA calculated maximum flux densities in the teeth and the yoke of the PMSG stator respectively. M_{t} and M_{yh} are the respective tooth- and yoke iron masses. The calculation is done at the PMSG's electrical frequency f_{e}, at the rated turbine operating speed n_{r}. The Steinmetz coefficients c, x and y are predetermined coefficients.

To account for fringing end-effects in the 2D FEA, the remnant flux density of the PM material, B_{r}, is multiplied by a correction fringing end-effect factor of $K_{\mathrm{f}} = 0.95$; as is done in [79] for NO-PMSGs with a similar aspect ratio.

3.3 Static FEA Solution Method

To calculate the PMSG's performance from the equivalent modelling discussed in the previous section, a solution method is necessary: The PMSG is connected to an uncontrolled passive system and thus the current-loading of the PMSG at a certain speed is unknown. The addition of an unknown external inductance, L_{ext}, for maximum power matching, further complicates the solution method. In order to calculate the machine performance at rated speed, as given in Section 3.2, the PMSG's current and load angle are solved iteratively using multiple static FEA solutions, as explained in the following subsections.

3.3.1 Rewriting Steady-state Equations

The steady-state dq-equations of the PMSG need to be rewritten in order to solve the unknowns that are necessary to calculate the PMSG performance. Equations (3.2.1) and (3.2.2) are rewritten by substituting the dq-values for voltage and current with their equivalent RMS values from (3.2.5). Then, by rewriting (3.2.1) and (3.2.2) in terms of I_{rms}, it gives

$$I_{\text{rms}} = \frac{\sqrt{2}V_{\text{rms}}\cos\delta - \omega_{\text{e}}\lambda_{\text{PM}}}{\sqrt{2}(-R_{\text{st}}\cos\delta - \omega_{\text{e}}(L_{\text{q}} + L_{\text{e}} + L_{\text{ext}})\sin\delta)} \tag{3.3.1}$$

and

$$I_{\text{rms}} = \frac{\sqrt{2}V_{\text{rms}}\sin\delta}{\sqrt{2}(-R_{\text{st}}\sin\delta + \omega_{\text{e}}(L_{\text{d}} + L_{\text{e}} + L_{\text{ext}})\cos\delta)}. \tag{3.3.2}$$

Equations (3.3.1) and (3.3.2) are used to numerically solve for δ and I_{rms}.

3.3.2 External Inductance Calculation

If the value of L_{ext} in (3.3.1) and (3.3.2) is known, then the PMSG's static FEA solutions can be used to evaluate its performance at the rated speed. By choosing three values for L_{ext} (L_1, L_2, L_3) and calculating the PMSG's performance for these three values, a second degree polynomial of the Newton form

$$f_2(y) = c_1 + c_2(y - y_1) + c_3(y - y_1)(y - y_2) \tag{3.3.3}$$

can be determined in terms of the generated power P_{g} and L_{ext}. The second degree polynomial of (3.3.3) is thus rewritten as

$$P_{\text{g}}(L_{\text{ext}}) = c_1 + c_2(L_{\text{ext}} - L_1) + c_3(L_{\text{ext}} - L_1)(L_{\text{ext}} - L_2). \tag{3.3.4}$$

Using the three generated power values $P_{\text{g}}(L_1)$, $P_{\text{g}}(L_2)$, $P_{\text{g}}(L_3)$, and their corresponding external inductance values L_1, L_2, L_3, the coefficients in (3.3.4) are calculated as

$$\begin{aligned} c_1 &= P_{\text{g}}(L_1), \\ c_2 &= \frac{P_{\text{g}}(L_1) - P_{\text{g}}(L_2)}{L_1 - L_2}, \\ c_3 &= \frac{c_2}{L_1 - L_3} - \frac{P_{\text{g}}(L_2) - P_{\text{g}}(L_3)}{(L_2 - L_3)(L_1 - L_3)}. \end{aligned} \tag{3.3.5}$$

An example of the calculated second degree polynomial is illustrated in Fig. 3.9(b). L_{ext} is calculated by substituting the rated generator power at rated speed into (3.3.4), i.e. $P_{\text{g}}(L_{\text{ext}})$. For the solution to be valid, the values for L_1 and L_3 have to bracket the solution value of L_{ext}. To estimate values for L_1, L_2 and L_3, the analytical calculation in (3.1.23) is used, whereby it is taken that $L_2 = L_{\text{ext(3.1.23)}}$ and then choosing values for L_1 and L_3 such that $L_1 < L_{\text{ext(3.1.23)}} < L_3$.

3.3.3 Solution Method Procedure

To externally match the impedance of the PMSG with the load in Fig. 3.1, the solution method in Fig. 3.10 can be used. This method implements the L_{ext} calculation in Fig. 3.9 by using static FEA iterations to calculate the PMSG's performance. The following steps are done:

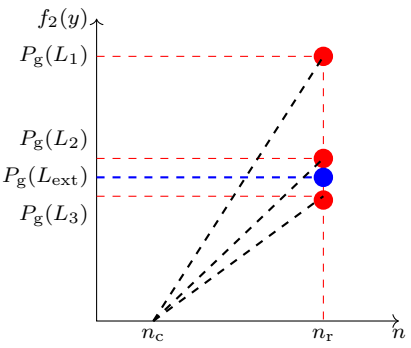

(a) Generated power, calculated at rated speed, with L_1, L_2 and L_3 added to the system. Collectively this brackets $P_g(L_{ext})$ and ensures accuracy.

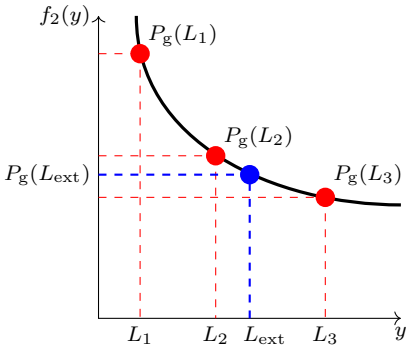

(b) Second degree polynomial curve fitting through three power points, from which L_{ext} is calculated knowing the rated power $P_g(L_{ext})$.

Figure 3.9: Visual representation of the external inductance calculation.

1. The induced generator voltage at cut-in speed n_c needs to be equal to the voltage at the battery terminals, V_b, with zero generator current flowing. The dq-equations (3.2.1) and (3.2.2) at n_c are thus, $V_q = \omega_e \lambda_{PM}$ and $V_d = 0$. It is thus necessary to alter λ_{PM} by calculating the number of turns per coil N_s that produces the desired value for λ_{PM}. This is done with the first static FEA solution.

2. Estimate L_1, L_2 and L_3 analytically using (3.1.23).

3. The external inductance is set equal to the first predetermined value, $L_{ext} = L_1$. For a starting point, the first static FEA iteration is run with δ and I_{rms} set to the analytically calculated values using (3.1.20) and (3.1.21).

4. Using the results from the previous static FEA iteration, equations (3.3.1) and (3.3.2) are solved simultaneously to calculate I_{rms} and δ, knowing that $0° \leq \delta \leq 90°$. Two static FEA iterations are now run to determine more accurate values for I_{rms} and δ by solving (3.3.1) and (3.3.2). These two static FEA iterations are deemed acceptable and accurate for current I_{rms} convergence.

5. Step 4 is now repeated for $L_{ext} = L_2$ and $L_{ext} = L_3$ (thus obtaining points $P_g(L_1)$, $P_g(L_2)$ and $P_g(L_3)$ as illustrated in Fig. 3.9(a)).

6. The calculated performance results are then used to determine the second degree polynomial of (3.3.4) and (3.3.5). By inspecting the obtained second degree polynomial, the final value for the added external inductance L_{ext} is calculated using the specified rated power (this step is also shown in Fig. 3.9(b)).

7. The generator's rated current, I_{rms}, and load angle, δ, are once more solved as in step 4. From this final solution, the performance evaluation of the generator is done using equations (3.2.6)-(3.2.8) to determine if it complies with the design specifications.

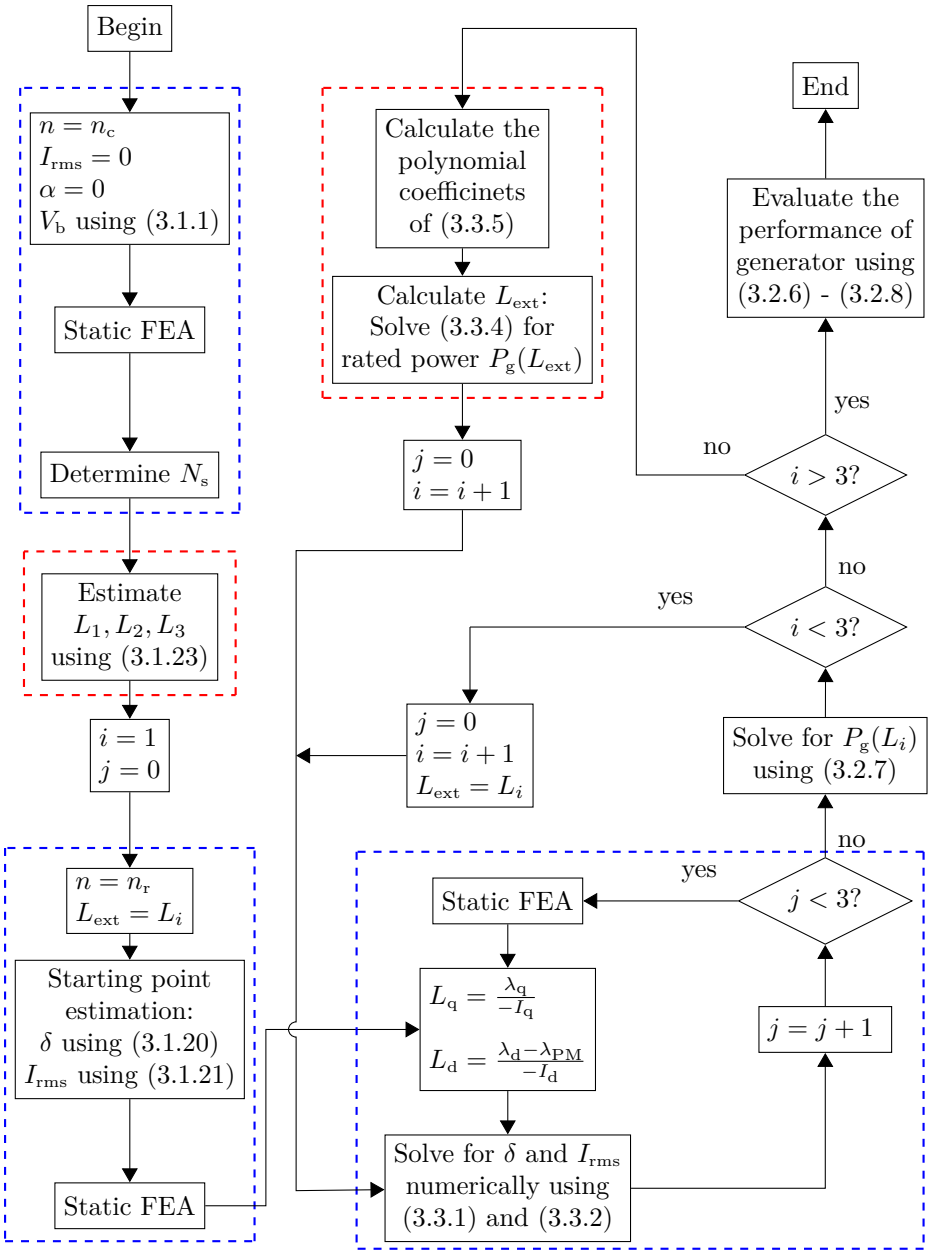

Figure 3.10: Static FEA solution method used to calculate L_{ext} for impedance matching and to evaluate the PMSG's performance. i = changing L_{ext} values [$L_{ext} = L_i$ with $i = 1, 2, 3$]. j = for solving current iteratively.

3.4 Static FEA Solution Method Results

In this section, two case studies are presented to investigate the application of external impedance matching as a method to improve power matching in passive wind energy systems. Two direct-drive NO-PMSGs, G_1 and G_2, are considered. Generator G_1 is for a 4.2 kW passive wind energy system and G_2 for a 12.5 kW passive passive wind energy system. The cross sections of the NO-PMSGs are shown in Fig. 3.11, with some design detail given in Table 3.1. The desired operating points for the respective wind turbines are summarised in Table 3.2.

Table 3.1: NO-PMSG data.

PMSG	G_1	G_2	G_3
Outer diameter, mm	384	655	361
Axial length, mm	70	125	54
slots-poles	$30-28$	$48-40$	$30-28$
M_{active}	22.6	83.8	16.1
M_{PM}	2.6	7.0	0.96

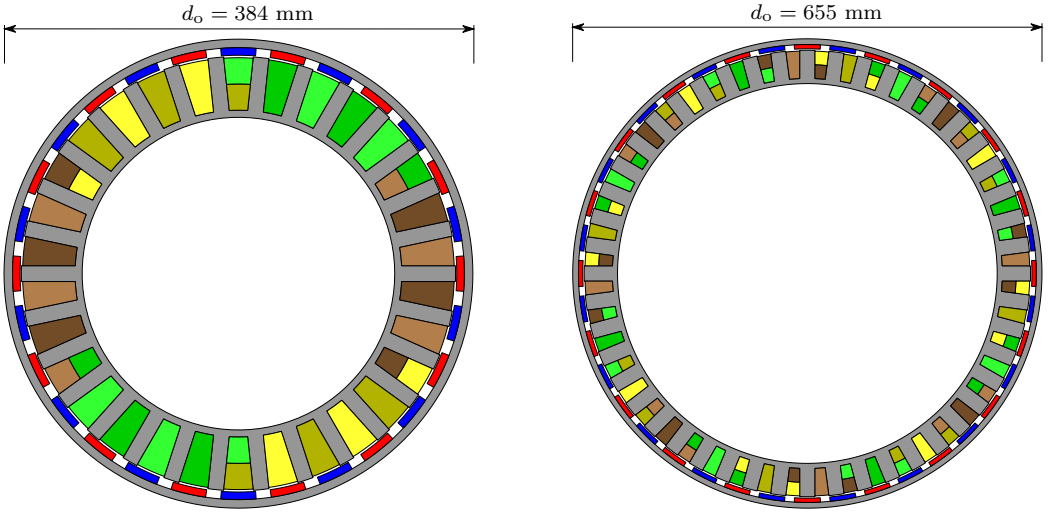

(a) G_1 **(b)** G_2 [81]

Figure 3.11: NO-PMSG cross sections (not to scale).

Table 3.2: Specified PMSG operating points for passive wind energy system case studies.

PMSG	G_1, G_3		G_2	
Operating point	n_c	n_r	n_c	n_r
Power, kW	0	4.2	0	12.5
Wind speed, m/s	3	12	3	10
Turbine speed, r/min	110	320	80	150
V_{bat}, V	48		240	

3.4.1 4.2 kW NO-PMSG Impedance Matching (G_1)

For generator G_1, the outer dimensions in Table 3.1 are according to the dimensional constraints of the wind turbine (turbine shown in Fig. 2.8(a), in Chapter 2.5.3). The other relevant generator dimensions were determined using initial sizing estimations.

The static FEA solution results for the impedance matching of G_1 are summarised in Table 3.3. It is shown in Table 3.3 that, with the calculated L_{ext} added to the passive wind energy system, G_1 matches with the rated generated power P_g at the specified operating point in Table 3.2.

To better illustrate the impedance matching results in Table 3.3, consider G_1's power curves in Fig. 3.12:

1. *Curve A* - This is G_1's power curve with zero external inductance added for impedance matching, but with N_s adjusted for the specified cut-in speed at $n_c = 110$ r/min. The generated power increases steeply with turbine speed and shows poor generated power performance compared to the available wind turbine power.

Table 3.3: Static FEA solution method results at rated operating point, n_r.

PMSG	G_1	G_2	G_3
P_g, kW	4.19	12.40	4.16
L_{ext}, mH	2.39	11.74	0.67
X_s, p.u.	0.48	0.39	1.47
X_{ext}, p.u.	1.71	0.94	0.47
X_{ext}/X_s	3.61	2.42	0.32
f_e, Hz	74.67	50.0	74.67
Turns per coil, N_s	13	19	22
V_{rms}	24.2	119.2	24.0
J, A/mm^2	5.1	6.3	6.5
δ	57.3°	51.6°	55.0°
η, %	92.8	93.0	90.0

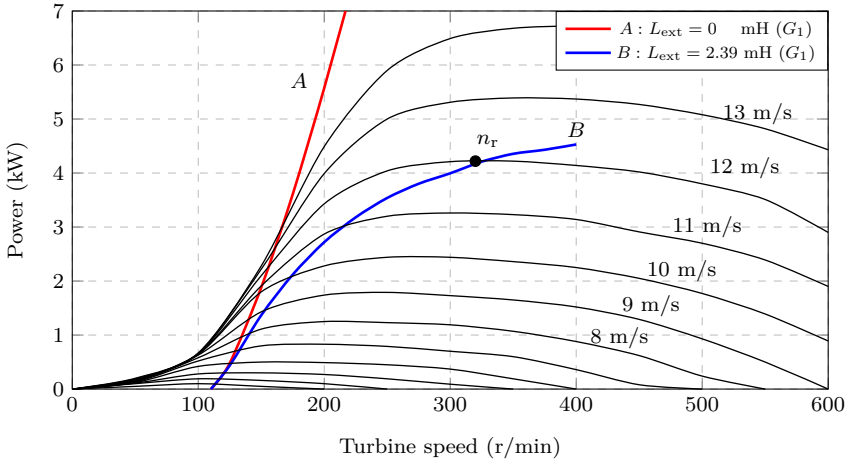

Figure 3.12: Power matching of G_1 with L_{ext} a parameter.

2. *Curve B* - This is G_1's power curve with the necessary L_{ext} in Table 3.3 connected between the generator and the diode rectifier. The power curve shows that the generated power now almost exactly matches the available turbine power at the specified maximum power point n_r, and that with the calculated $L_{ext} = 2.39$ mH added to the passive system a substantial improvement in power matching is obtained.

In Fig. 3.12 it is shown that, by adding L_{ext}, impedance matching can be used effectively as a method to improve power matching between the wind turbine and the wind generator in order to utilise more of the available wind power. The wind generator matches well with the turbine at low wind speeds, which is critical for the application, and still operates at the desired operating point at high wind speeds.

Incorporating external impedance matching into a site-specific design can also be done, similar to what is done in [18] for a specified wind cycle. In this case, the rated operating point, n_r, would then be determined using the specific site's annual wind profile. This will ensure that the wind generator achieves good power matching at low wind speeds and will increase annual energy harvesting.

3.4.2 12.5 kW NO-PMSG Impedance Matching (G_2)

To investige the impedance matching of a 12.5 kW passive wind energy system, the NO-PMSG in [81] is used. The NO-PMSG cross-section is shown in Fig. 3.11(b) and was

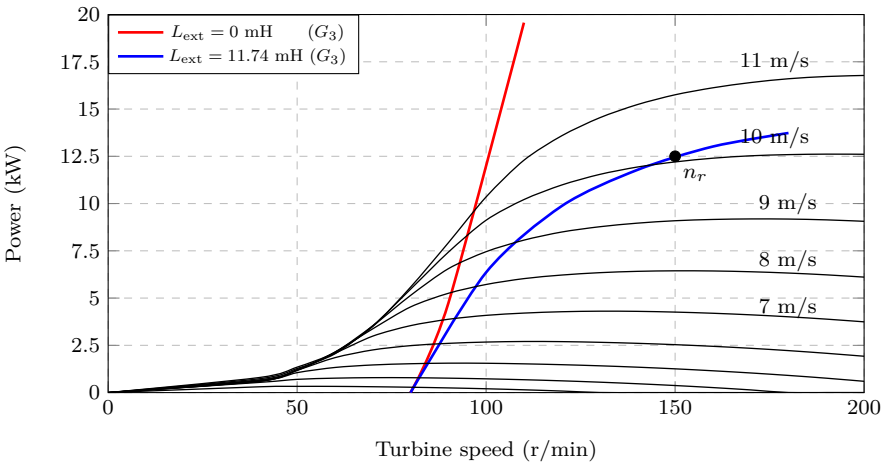

Figure 3.13: Power matching of G_3 with L_{ext} a parameter.

initially designed in [81] as a directly grid-connected 15 kW PM wind generator. The aim is to convert/recycle the existing machine for the 12.5 kW passive system.

The static FEA solution method is used to calculate the new N_s for the desired cut-in speed and also L_{ext} for maximum power point operation, as specified for G_2 in Table 3.2. The summarised results in Table 3.3 show that, with the calculated L_{ext} added to the 12.5 kW passive wind energy system, G_2 now matches with the rated generated power P_g at the specified operating point. The generator's power matching is shown in Fig. 3.13. Again, both operating power curves are given for the cases where $L_{ext} = 0$ mH and the calculated $L_{ext} = 11.74$ mH are added to the passive wind energy system.

Generator G_2's results show that by rewinding the existing machine and adding L_{ext}, as calculated with the static FEA solution method, impedance matching can be used effectively to "recycle" machines for small-scale uncontrolled passive wind energy systems. Moreover, by considering the results of both PMSGs G_1 and G_2, for small-scale passive wind energy systems it is shown that any generator can be matched with any wind turbine (provided that the generator's rated power is sufficient).

3.5 Wind Generator Design Optimisation

The static FEA method described in Section 3.3 can also be used when designing wind generators specifically for small-scale passive wind energy systems: Designing the wind generator for a desired performance whilst reducing the generator's total cost and mass is particularly of interest. However, the design process is significantly more complicated when still trying to achieve good power matching with the wind turbine at all wind speeds. Using external impedance matching with the proposed solution method can simplify the design process.

Note that in this section the design optimisation and results are not discussed in that much detail, because the focus is merely to demonstrate the usefulness of external impedance matching (Chapters 4 and 5 will focus on generator design).

3.5.1 4.2 kW NO-PMSG (G_3)

The proposed solution method is used together with an optimisation algorithm to optimally design the NO-PMSG topology in Fig. 3.11(a) for the 4.2 kW passive system. Here,

the NSGA-II optimisation algorithm is used with a multi-objective function to create a Pareto front of all the non-dominated design solutions. The aim of the multi-objective function is to minimise the active mass, M_{active}, and the permanent magnet mass, M_{PM}, of the NO-PMSG, whilst still adhering to the design constraints. The multi-objective function is given by

$$\min_{\mathbf{X}} \mathbf{F}(\mathbf{X}) = \min_{\mathbf{X}} \begin{bmatrix} M_{\text{active}}(\mathbf{X}) \\ M_{\text{PM}}(\mathbf{X}) \end{bmatrix}, \tag{3.5.1}$$

where $\mathbf{X}$ is the PMSG's dimensional array. For calculating M_{active}, all of the components shown in Fig. 3.11 are included, apart from the copper mass of the end-windings. The design constraints are chosen as

$$\mathbf{U} = \begin{bmatrix} P_{\text{g}} \\ \eta \\ J \end{bmatrix} = \begin{bmatrix} 4.2 \text{ kW} \\ \geq 90\% \\ \leq 6.5 \text{ A/mm}^2 \end{bmatrix}, \tag{3.5.2}$$

where J is the maximum allowed rated generator current density.

The design optimisation process aims to achieve the multi-objective function in (3.5.1) by varying the dimensions of the NO-PMSG and uses the proposed static FEA method to calculate the performance and to ensure maximum power matching. In this way, the cost of the generator is effectively minimised for the correct L_{ext}.

3.5.2 Results Discussion

Generator G_3 in Table 3.1 and Table 3.3 is one of the pareto front solutions obtained from the multi-objective optimisation. It is shown that the generator achieves maximum power matching at the rated operating point and that the performance constraints in (3.5.2) are met. Furthermore, M_{active} and M_{PM} are considerably reduced compared to generator G_1, showing that the proposed static FEA method can be used as an effective tool in the design optimisation process.

3.6 Calculation Method: Analytical vs Static FEA

The analytically calculated L_{ext} using (3.1.23) and the calculated L_{ext} using the proposed static FEA solution method for generators $G_1 - G_3$'s power matching are compared in Table 3.4. It is shown in Table 3.4 that the analytically calculated L_{ext} is overestimated and that, as a result, the generated power P_{g} is less than the rated maximum power. This can be attributed to the lower analytically calculated L_{s} in Table 3.4. Also shown is the difference between L_{d} and L_{q} of the surface mounted PMSG due to saturation. Generator $G_1 - G_3$'s power curves, with the respective L_{ext} values from Table 3.4, are given in Fig. 3.14 to show the overall power matching errors. All this confirms the necessity of the proposed static FEA method for precise power matching calculation using iron-cored PMSGs.

It is also important that the static FEA method be computationally efficient, since it requires a total of 10 static FEA solutions. The static FEA solutions were performed on a 3.20 GHz Intel(R) Core i7 CPU with 32 GB RAM. The computer solution time to complete the method in Fig. 3.10, for G_1, is on average 26 s; note that this is for full cross-section static FEA solutions of G_1 in Fig. 3.11(a).

Table 3.4: Analytical versus static FEA results.

PMSG	G_1		G_2		G_3	
	Anal.	FEA	Anal.	FEA	Anal.	FEA
P_g, kW	3.90	4.19	11.39	12.40	3.77	4.16
L_{ext}, mH	2.57	2.39	13.32	11.74	0.96	0.67
L_s, mH	0.67	0.81	4.44	5.49	2.05	2.48
L_q, mH	-	0.73	-	5.28	-	2.14
L_d, mH	-	0.58	-	4.43	-	2.04
L_e, mH	0.15	0.15	0.63	0.63	0.36	0.36

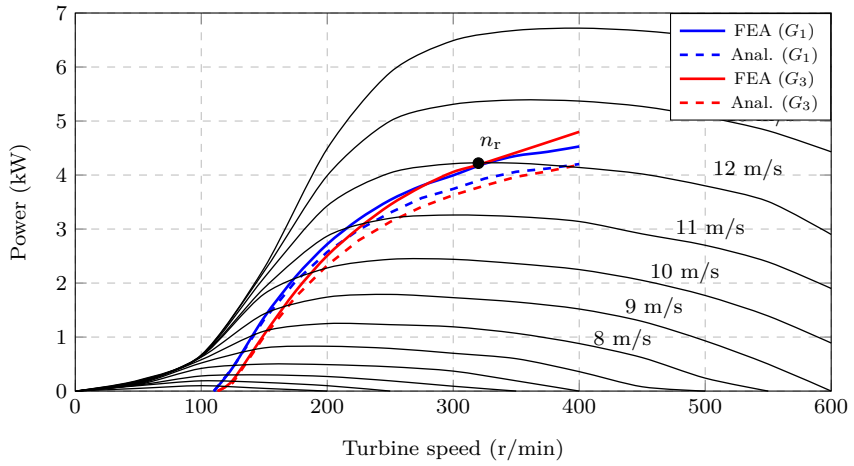

(a) Power curves of G_1 and G_3.

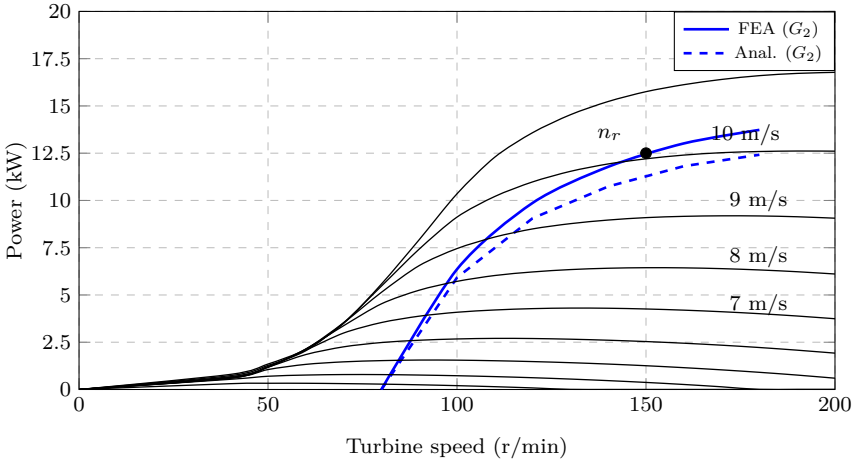

(b) Power curves for G_2.

Figure 3.14: Power matching curves comparing the analytical calculation and static FEA solution method, with the L_{ext} values from Table 3.4 a parameter.

3.7 Experimental Results

In this section, the accuracy of the proposed static FEA method for calculating L_{ext} and the improved power matching between the wind generator and wind turbine are verified through test results.

The test bench setup in Fig. 3.15(a) shows a manufactured NO-PMSG prototype that is connected via a torque sensor to a geared induction motor drive that emulates the wind turbine. The torque sensor is used to measure the input power. The NO-PMSG prototype has the same dimensions as G_1 in Table 3.3, only it was designed for a cut-in speed $n_{\text{c}} = 100$ rpm ($N_{\text{s}} = 14$) and has a lower copper fill factor due to the manufacturing of the preformed coils. To emulate the uncontrolled passive wind energy system in Fig. 3.1, the NO-PMSG's phase terminals are connected to a 48 V battery bank, shown in Fig. 3.15(b), via an external inductance L_{ext} (not connected in Fig. 3.15(b)), a resistance R_{c} that is equivalent to the resistance of the cable and brush-slip-rings, and a diode bridge rectifier. For the external inductance, an available inductor in the laboratory is used. The available external inductor used in the tests is measured as $L_{\text{ext}} = 3.8$ mH, and is shown in Fig. 3.16(b).

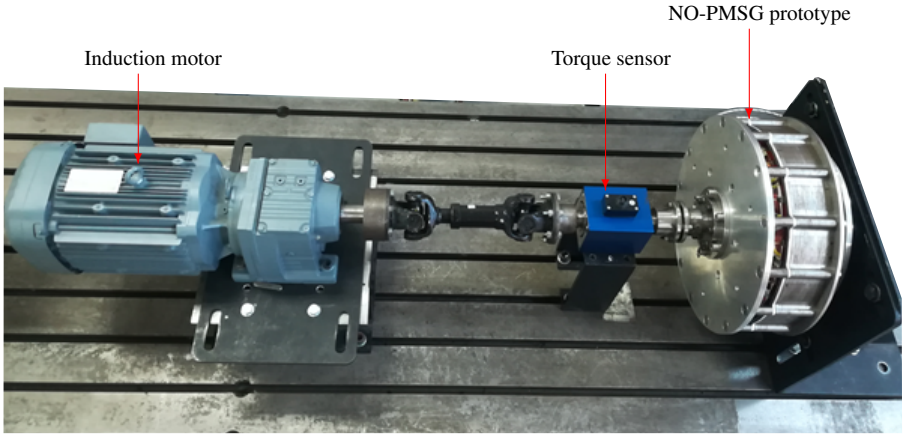

(a)

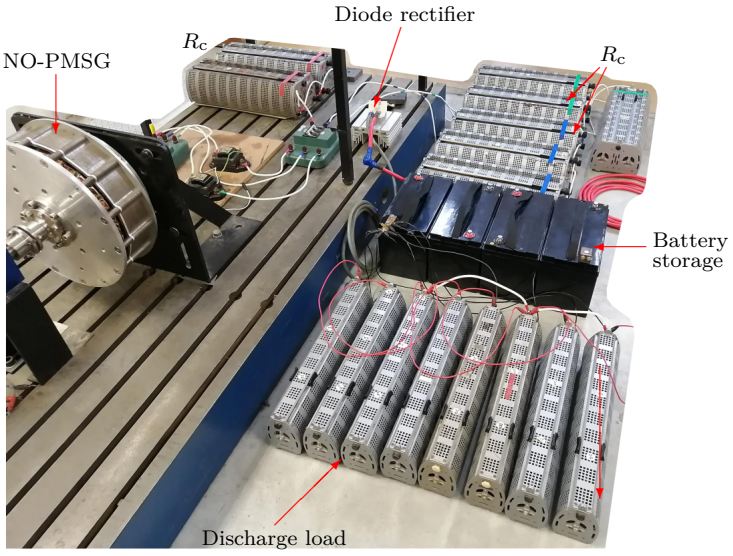

(b)

Figure 3.15: Experimental test bench setup of the manufactured NO-PMSG prototype.

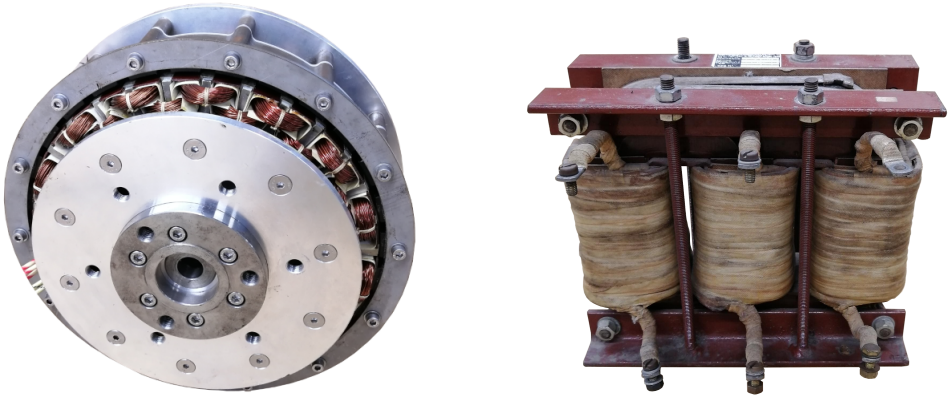

(a) NO-PMSG **(b)** External inductor.

Figure 3.16: NO-PMSG prototype and inductor used for experimental validation.

3.7.1 No-load and Short Circuit Measurements

The no-load open circuit and short circuit measurements are done to verify the NO-PMSG's static FEA calculated parameters.

The no-load open circuit voltage measurements are shown in Figs. 3.17 and 3.18. The values for the measured no-load open circuit voltage and FEA calculated voltage at $n_r = 320$ r/min are also summarised in Table 3.5. The measured no-load open circuit voltage versus FEA calculated results in Fig. 3.17 and Table 3.5 show good correlation.

The internal synchronous inductance of the NO-PMSG prototype is measured by means of a number of short circuit tests to get an average value. The average measured L_s and FEA calculated value are given in Table 3.5, and show a good comparison.

3.7.2 Load Tests

For the load tests, power measurements are taken at various turbine speeds with, and without, the external inductance connected between the NO-PMSG and the diode rectifier. The measured operating power curves are plotted in Fig. 3.19. The much improved power matching measured between the NO-PMSG and the wind turbine with $L_{ext} = 3.8$ mH is clearly shown in Fig. 3.19. The results prove that external impedance matching can be used effectively in uncontrolled passive wind energy systems to improve power matching. In practice, the battery terminal voltage is not constant and marginally increases due to the battery's state of charge. The equivalent modelling in Section 3.1.1 takes this ac-

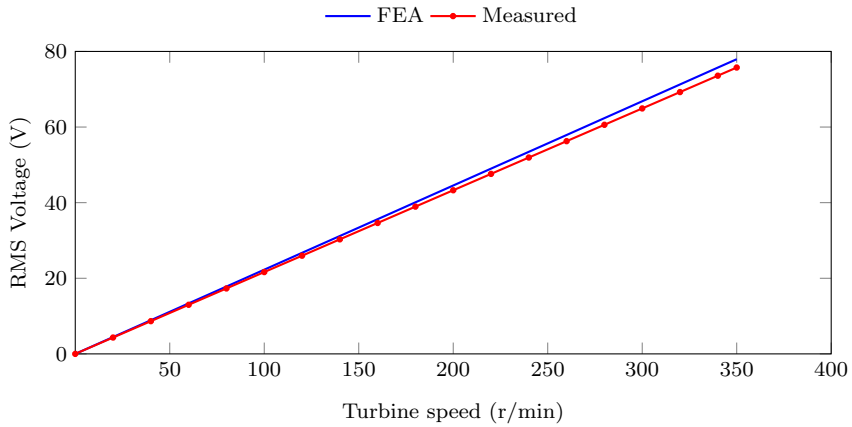

Figure 3.17: Measured open circuit voltage versus FEA calculated voltage.

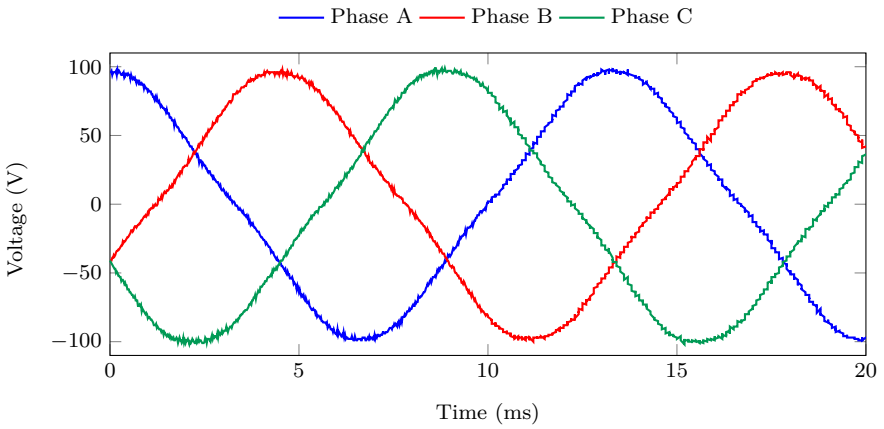

Figure 3.18: Measured no-load open circuit voltage waveforms.

Table 3.5: Measured and the corresponding static FEA solution method results.

Parameter	Measured	Static FEA solution
E_g, V	69.25	71.27
R_s, Ω	0.134	0.14
L_s, mH	1.04	0.95
n_r, r/min	320	320
L_{ext}, mH	3.8	3.77
P_g, kW	3.05	3.06

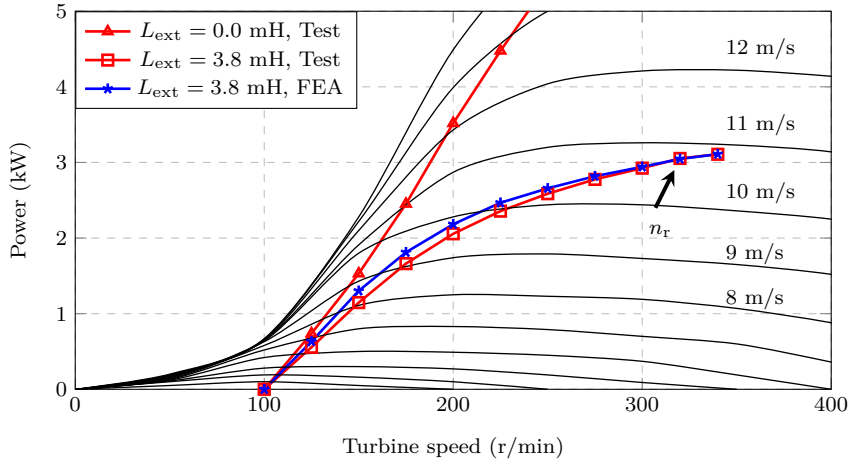

Figure 3.19: Measured and static FEA calculated power matching of the NO-PMSG prototype in the experimental passive system setup.

curately into account, with the measured battery terminal voltage varying between the predicted 48 V and 52 V.

To validate the equivalent modelling in Section 3.2 and the static FEA solution results in Sections 3.4 to 3.6, the NO-PMSG prototype's generated power at the same turbine speed intervals are calculated using the static FEA solution method with $L_{ext} = 3.8$ mH. The static FEA calculated operating power curve is plotted in Fig. 3.19. The slight difference between the measured and predicted power curves at certain turbine speeds can be attributed to slight inaccuracies in the battery model, however, the difference is negligible. Furthermore, the measured voltage and current waveforms at the diode rectifier under rated operating conditions are shown in Fig. 3.20. It is shown that the

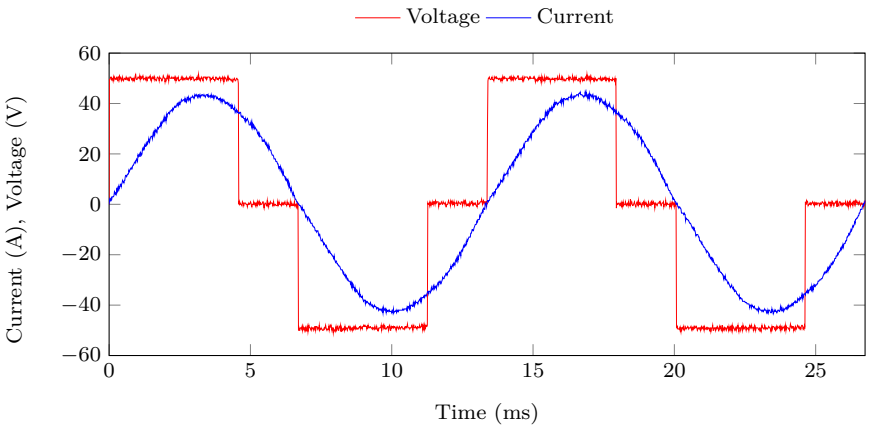

Figure 3.20: Measured current and line voltage waveforms at the diode bridge rectifier of the prototype passive generator system at 320 r/min and $L_{\text{ext}} = 3.8$ mH.

generator current is close to sinusoidal and validates the proposed ac-equivalent system modelling where sinusoidal generator currents are assumed.

To validate the accuracy of the proposed solution method in Section 3.3, that calculates the necessary L_{ext} for impedance matching, the following is done: The measured power value in Fig. 3.19 at a turbine speed of 320 r/min is taken as the NO-PMSG prototype operating point for which L_{ext} must be calculated. This operating point is at $n_{\text{r}} = 320$ r/min and $P_g = 3.05$ kW. Solving L_{ext} with the static FEA solution method in Fig. 3.10 yields $L_{\text{ext}} = 3.77$ mH, and the generated power at $n_{\text{r}} = 320$ r/min is $P_{\text{g}} = 3.06$ kW. The results are summarised in Table 3.5. By comparison, the results in Table 3.5 are almost exact and validate the accuracy of the proposed static FEA solution method.

3.8 Chapter Summary

In this chapter external impedance matching in small-scale passive wind energy systems is investigated for improved power matching. A fast and accurate solution method is proposed to calculate the necessary external inductance. From the results the following conclusions are drawn:

- It is shown with 4.2 kW and 12.5 kW passive system case studies that the external impedance matching method can be used effectively to improve power matching between the wind generator and the wind turbine. Furthermore, this can be applied to any existing wind generator with a sufficient rated power and wind turbine.
- The proposed method to calculate the required L_{ext} is shown to be accurate and computationally efficient. It is also shown that analytical methods to calculate L_{ext} can be inaccurate when iron-cored PMSGs are used and that the proposed method, using static FEA solutions, is necessary.
- Including the proposed calculation method in the design optimisation of the generator works excellently. The method can also be included in wind site-specific design optimisation, maximising annual wind energy harvesting and minimising generator and external inductance sizes.
- The accuracy of the proposed static FEA solution method and the improved power matching are confirmed by measured results.

Chapter 4

Conventional Permanent Magnet Synchronous Generator Design

In the previous chapter it was shown that external impedance matching can be used effectively to improve the power matching between the wind generator and the wind turbine. However, the external impedance inductance is an unwanted component to the passive wind energy system. Hence, the aim of this chapter is to address the research sub-question:

3. Can PMSGs be designed for a *natural* impedance matching with the wind turbine? (i.e. there is no external inductance necessary)

For the theoretical estimation in Chapter 1.3.2, it was shown that the required internal synchronous impedance for a *natural* impedance matching, such as shown in Fig. 4.1, is quite significant. Therefore, in this chapter various methods of designing the PMSG to have an increased synchronous inductance are investigated. Essentially to "build" the inductance into the PMSG. These methods include, altering the placement and the orientation of the PMs in the rotor to change the magnetic saliency of the PMSG, as well as the stator slot's structure to increase leakage flux. Furthermore, the various PMSG structures are designed and optimised for the 4.2 kW passive wind energy system. The results are then validated with experimental results of a designed PMSG prototype.

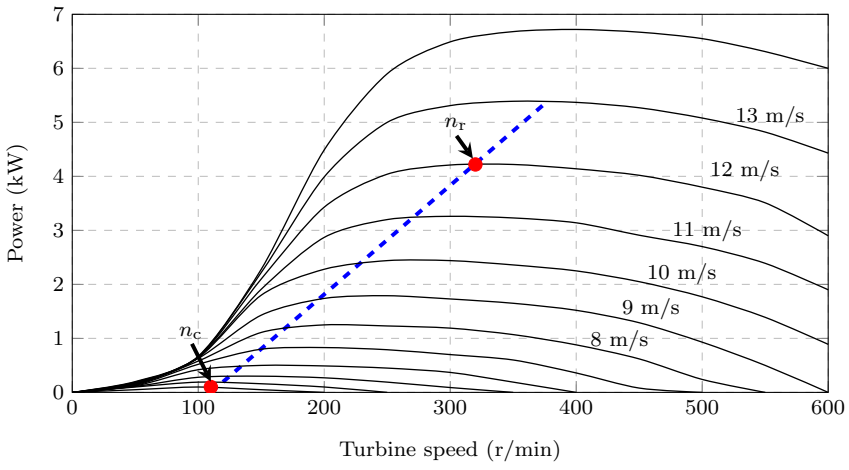

Figure 4.1: Wind turbine power versus speed curves with 4.2 kW wind generator specifications.

Table 4.1: Summary of specified operating points.

	n_c	n_r
Wind speed	3 m/s	12 m/s
Turbine speed	110 r/min	320 r/min
Generated power, P_g	0 kW	4.2 kW
Battery storage voltage, V_{bat}	48 V	

4.1 4.2 kW System Specifications

The design specifications for the PMSG are the same as for the 4.2 kW passive system in Chapter 3. The specifications and desired operating points are summarised in Table 4.1. It is desired that the wind generator start generating power at the cut-in speed, n_c, and match with the maximum wind turbine power at rated speed, n_r, as indicated in Fig. 4.1. The wind generator is connected to a 48 V battery bank via the diode bridge rectifier.

4.2 Generator Selection

Seeing that the machine selection is for a low speed direct-drive application, PMSGs with non-overlapping (fractional-slot concentrated) windings are very attractive. As outlined in the extended literature study in Chapter 2, PMSGs with non-overlapping windings have shorter end-winding lengths, resulting in less copper losses and a more compact mechanical structure.

Possible PMSG slot-pole combinations for the NO-PMSG are 36-30, 36-32 and 30-28. The MMF harmonic analysis of Appendix A is done for each of these slot-pole combinations and the results of the MMF harmonic analysis are given in Fig. 4.2. The magnitudes of the harmonics given in Fig. 4.2 are marginalised to the working harmonic and are given in per unit values. From the results in Fig. 4.2, the working harmonic winding factor for each generator can be calculated as in Appendix A. The working harmonic winding factors for each of the respective NO-PMSGs are summarised in Table 4.2.

As shown in (3.1.3), for calculating the internal synchronous inductance

$$L_s = L_m(1 + \tau_d) + L_{sl} + L_e,$$

it is possible to have a generator with a larger internal synchronous inductance by selecting one with a large differential harmonic leakage flux coefficient, τ_d. Typically, NO-PMSGs have much larger τ_d-values than O-PMSGs , which is another reason for using NO-PMSGs for passive wind generator systems. The τ_d-values for the different slot-pole combination NO-PMSGs are calculated from the results in Fig. 4.2 with (3.1.8), and are given in Table 4.2. It is shown in Table 4.2, that in this case, the τ_d-values do not differ by much and either one of these slot-pole combinations would be suitable in this regard.

In terms of torque quality, it is important that the generator has a low cogging torque. The wind turbine torque at the low cut-in wind speed (3 m/s) has to overcome this cogging torque for the generator to start generating power. A good indicator to predict whether a PMSG will have a small no-load cogging torque is the least common multiple (LCM) between the number of stator slots, Q_s, and the number of poles, p. Although the LCM does not directly relate to the amplitude of the cogging torque, it generally holds true that the larger the value of the PMSG's LCM, the smaller the no-load cogging torque will be [82]. The LCM values for the respective NO-PMSGs are given in Table 4.2.

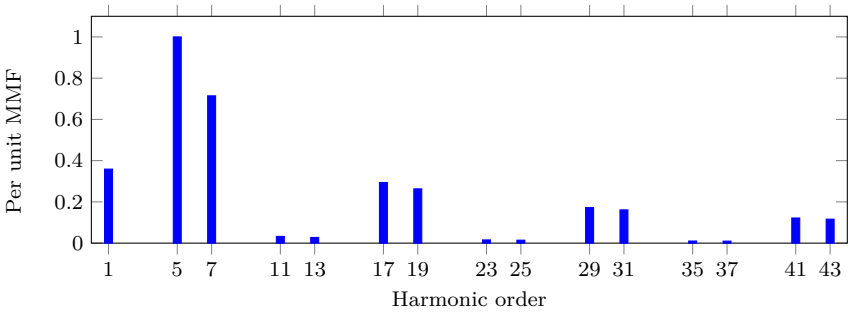

(a) 36-30 slot-pole

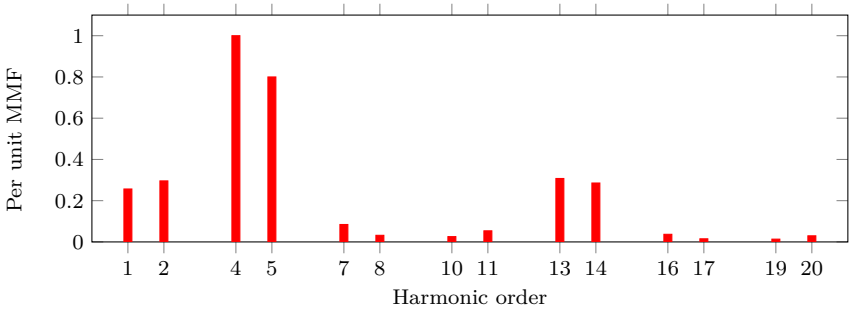

(b) 36-32 slot-pole

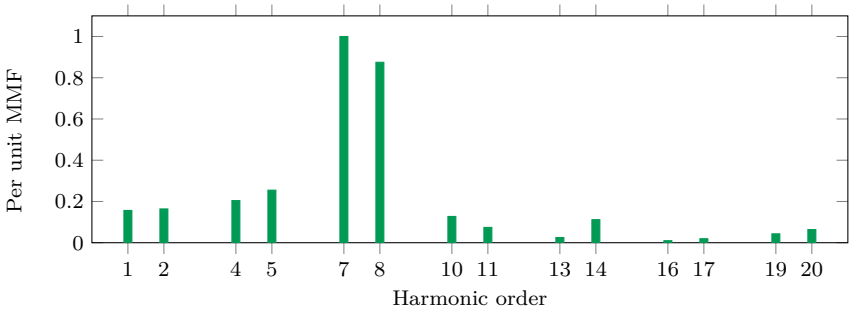

(c) 30-28 slot-pole

Figure 4.2: Per unit MMF harmonic content of potential NO-PMSGs.

Table 4.2: Comparison of potential slot-pole combinations for machines with fractional-slot concentrated windings.

Slot-Pole	36-30 (6-5)	36-32 (9-8)	30-28 (15-14)
Winding			
k_w, working harmonic winding factor	0.933	0.945	0.951
τ_d, differential harmonic leakage flux coefficient	1.48	1.43	1.40
Torque quality			
LCM(Q_s, p)	180	288	420

From Table 4.2, the optimal generator choice is the 30-28 PMSG. This particular combination has the highest working harmonic winding factor, with $k_{\mathrm{w}} \approx 0.951$, and a large LCM($Q_{\mathrm{s}}$, p) compared to the other slot-pole combinations.

4.3 Stator Design

For the stator's structure, it is advantageous to have open slots with rectangular teeth as shown in Fig. 4.3(a). This allows for preformed coils to be used that are easier to manufacture. However, with the focus on increasing the PMSG's per phase synchronous inductance, L_{s}, for improved power matching, this might not be the optimal slot shape. Alterations can be made to the stator structure in an attempt to increase L_{s}. Using rectangular semi-closed slots, as shown in Fig. 4.3(b), is one way to increase the PMSG's synchronous inductance:
Once more, consider the formula for calculating the slot-leakage inductance, given by

$$\begin{aligned} L_{\mathrm{sl}} &= \frac{4m}{Q_{\mathrm{s}}}\mu_0 l_{\mathrm{Fe}} N_{\mathrm{ph}}^2 \Lambda_{\mathrm{uv}} \\ &= \frac{4m}{Q_{\mathrm{s}}}\mu_0 l_{\mathrm{Fe}} N_{\mathrm{ph}}^2 \left(z_1 \frac{h_{\mathrm{s}}}{3b_{\mathrm{s}}} + z_2 \frac{h_{\mathrm{hs}}}{b_{\mathrm{o}}} \right). \end{aligned} \tag{4.3.1}$$

as in [77]. From (4.3.1), and the geometry definitions in Fig. 4.3, it is theoretically shown that L_{sl}, and therefore L_{s}, can be increased by closing the stator slots and using a rectangular slot shape: The slot-leakage inductance is inversely proportional to the stator slot width, b_{s}, and the stator slot tooth opening width, b_{o}. PMSGs with a semi-closed stator slot structure are therefore more likely to meet the desired impedance matching requirements.

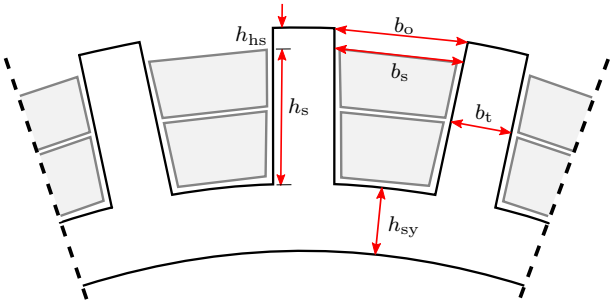

(a) Open slot with rectangular teeth.

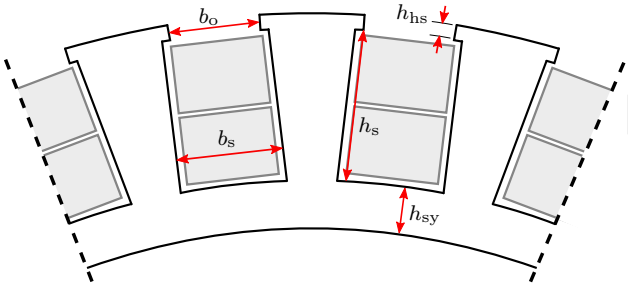

(b) Semi-closed slot.

Figure 4.3: Stator slot structures and dimensions.

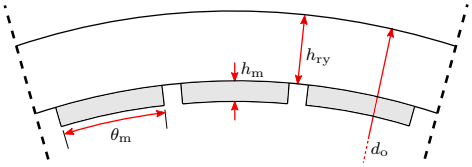

(a) Surface mounted PM rotor.

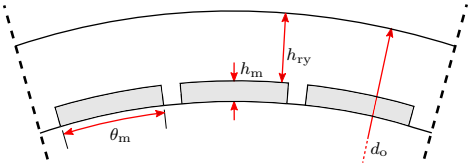

(b) Embedded PM rotor.

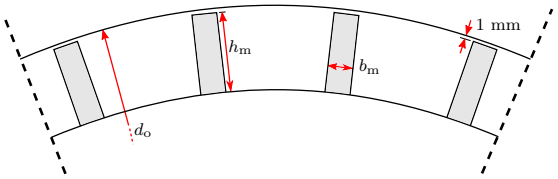

(c) Interior PM spoke-type rotor.

Figure 4.4: Rotor structures and dimensions.

4.4 Rotor Design

In terms of the PM rotor structure, it is possible to increase the synchronous inductance by altering the placement and the orientation of the PMs in the rotor. Thus, effectively "building" the necessary external inductance into the PMSG. The different rotor structures considered in this investigation are shown in Fig. 4.4. Fig. 4.4(a) shows the surface mounted PM (S-PM) rotor, Fig. 4.4(b) shows the embedded PM (E-PM) rotor and Fig. 4.4(c) the interior spoke-type PM (SP-PM) rotor. As a result of using interior PM rotors, there is a significant increase in stator magnetisation flux compared to that of an S-PM rotor. It also results in a larger difference between the direct-axis and quadrature-axis inductances of the machine (also referred to as the magnetic saliency) [78]. Typical machine saliency properties for the different rotor topologies in Fig. 4.4 are summarised in Table 4.3.

Opting to use either surface (S-PM) or interior PM (E-PM and SP-PM) rotor structures has certain trade-offs when it comes to manufacturing and machine performance. In the case of an S-PMSG the PMs are exposed, whereas for the interior PM rotors, the PMs are protected and at a low risk of being damaged. Embedding the PMs in the rotor also has the additional advantage that the PMs are well protected against demagnetisation. It is also apparent from Fig. 4.4 that the S-PMSG is more likely to use less iron material than the E-PMSG and SP-PMSG. The latter is an important design aspect, considering the need for a low top-tower mass.

Designing the SP-PMSG rotor like the one in [83] or with a modular rotor could reduce the active mass, however, it could also compromise the structural integrity of the PMSG. For the structural integrity of the SP-PM rotor in Fig. 4.4(c), the yoke needs support on at least one side of the interior embedded PM. It is shown in Fig. 4.5 that the support section on the rotor yoke adds an additional path for stray leakage flux from the PMs.

Table 4.3: Typical saliency properties of different rotor structures and relative slot-leakage inductance of different stator slot openings.

Rotor structure	**Saliency**, ξ	**Stator structure**	$L_{\mathbf{sl}}$
Surface mounted PM	$L_q \approx L_d$	Open slot	smaller L_{sl}
Interior Embedded PM	$L_q > L_d$	Semi-closed slot	larger L_{sl}
Interior spoke-type PM	$L_q > L_d$		

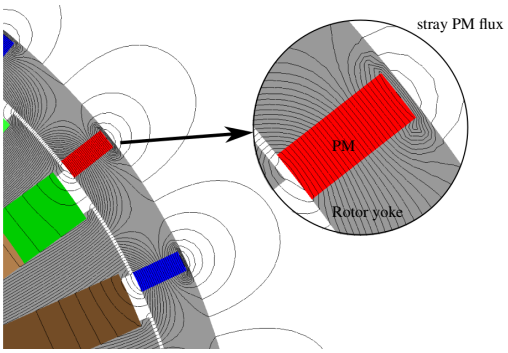

Figure 4.5: Enlarged section of an SP-PMSG, showing the PM flux paths and leakage flux in the rotor.

Also shown in Fig. 4.5, there is a large component of leakage flux to the exterior air region of the rotor. The effect of the outer air region was not initially taken into account in [84] and [85], and was later found by comparison to have a significant effect on the SP-PMSG's performance. The outer air region is then taken into account in this dissertation.

4.5 Design and Optimisation

In this section, the design approach and methodology for the different PMSG topologies outlined in Sections 4.3 and 4.4 is discussed. The PMSG topologies then, are the S-PMSG, E-PMSG and SP-PMSG with open slots; and the S-PMSG, E-PMSG and SP-PMSG with semi-closed rectangular slots. The results in Chapter 3 and in [21] confirm that it is better to use FEA solutions to design PMSGs in passive wind generator systems. Therefore, the performance of the respective PMSGs are solved using 2D static FEA as in Chapter 3.2.

4.5.1 Methodology

The population based NSGA-II (non-gradient genetic algorithm II) [86] is used in conjunction with the 2D static FEA solutions to optimise the PMSGs. The design optimisation work flow is shown in Fig. 4.6.

In Fig. 4.6, the PMSG topology and search space are first initialised. The static FEA solver then takes the relevant machine dimensions as an input vector to solve and to calculated the PMSG's performance. In turn, an output vector is created, containing the values of the specified objectives and performance constraints, and is given as feedback to the NSGA-II algorithm. The NSGA-II's elitist search algorithm then creates a Pareto optimal front from a diverse set of non-dominated solutions that satisfy the specified constraints and converge near a true Pareto-optimal set. After the optimisation results have converged, the optimum solution can be selected directly from the Pareto front by evaluating the trade-off between the objectives.

This design optimisation process is done for each of the respective PMSG topologies. Thereafter, a thorough evaluation of each selected optimum PMSG is done for comparison. The selected PMSGs' performance are then verified using 3D FEA solutions.

4.5.2 Multi-objective Function and Constraints

Reducing the PMSG's cost and minimising the top tower mass are important for small-scale wind generators. Therefore, the first two objectives of the multi-objective function

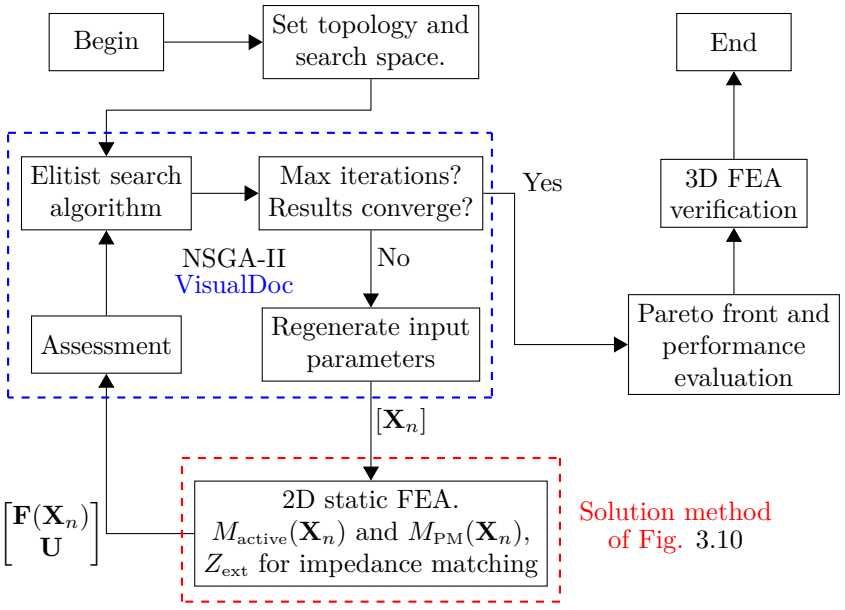

Figure 4.6: Design and optimisation flow diagram.

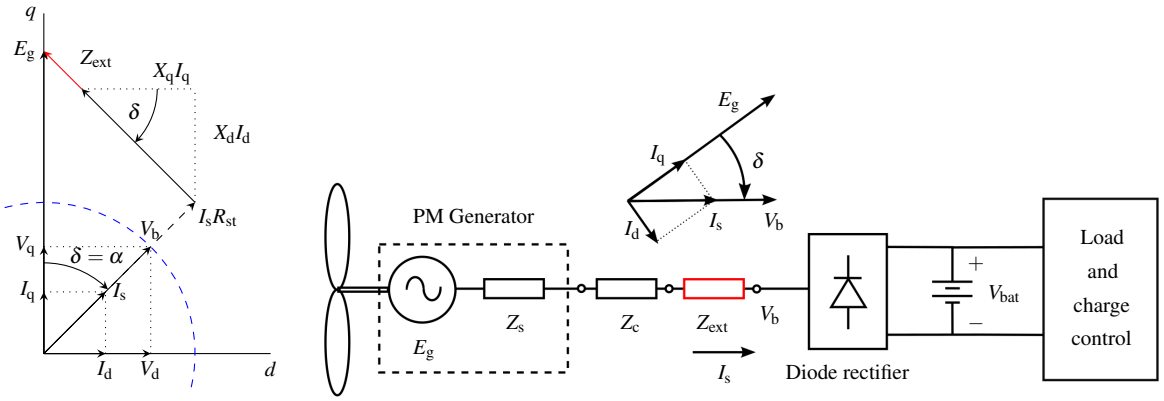

Figure 4.7: (a) Passive system phasor diagram with external impedance matching, Z_{ext}. (b) Single-line diagram of PM wind generator with external inductance for impedance matching connected in passive wind turbine system. The optimisation (4.5.1) accordingly minimises Z_{ext} to be zero if possible.

given in (4.5.1), are to minimise the PMSG's active mass, M_{active}, and the generator's PM mass, M_{PM}. Minimising M_{active} has the dual purpose of reducing the generator's cost and the top tower mass. The generator's PM mass M_{PM} is the most expensive material, and given its volatile cost, needs to be minimised as a separate objective.

$$\min_{\mathbf{X}_n} \mathbf{F}(\mathbf{X}_n) = \min_{\mathbf{X}_n} \begin{bmatrix} M_{\text{active}}(\mathbf{X}_n) \\ M_{\text{PM}}(\mathbf{X}_n) \\ Z_{\text{ext}}(\mathbf{X}_n) \end{bmatrix}. \tag{4.5.1}$$

The PMSG's active mass in (4.5.1) is calculated as

$$M_{\text{active}} = M_{\text{Fe}} + M_{\text{PM}} + M_{\text{Cu}}, \tag{4.5.2}$$

where M_{Fe} is the collective mass of the stator- and rotor iron laminations, and M_{Cu} is the total copper winding mass that includes the end-winding mass.

The other objective in (4.5.1), is to minimise the impedance error, Z_{ext}. This is the required difference in generator impedance, if not zero, to match the generator's power with the turbine at the rated operating point as shown in Fig. 4.7(a). The impedance error is visually illustrated in Fig. 4.7(b), as a physical external impedance component ($Z_{\text{ext}} = j\omega_{\text{e}} L_{\text{ext}}$) that is added, if necessary, to the passive generator system between the generator and the diode bridge rectifier. As shown in Fig. 4.6, the impedance error is calculated with the solution method for external impedance matching given in Fig 3.10. The impedance error is then given as feedback to the optimisation algorithm. This way, the optimisation algorithm finds non-dominated PMSG solutions where $Z_{\text{ext}} = 0$, i.e. where the PMSGs are designed for the correct synchronous impedance Z_{s} that matches *naturally* with the maximum wind turbine power. Or alternatively, where the PMSGs match with the wind turbine power with the correct external impedance added to the system.

The design constraints for the PMSGs at the rated operating point are given by

$$\mathbf{U} = \begin{bmatrix} P_{\text{g}} \\ \eta \\ J_{\text{rms}} \end{bmatrix} = \begin{bmatrix} 4.2 \text{ kW} \\ \geq 90\% \\ \leq 5 \text{ A/mm}^2 \end{bmatrix}. \tag{4.5.3}$$

In (4.5.3), P_{g} is the rated power, η is the generator efficiency and J_{rms} is the maximum allowed RMS current density. The constraint on P_{g} is imposed to ensure that the desired power matching between the PMSG and the wind turbine is achieved. The constraint on J_{rms} is a thermal constraint and is a typical value for small-scale machines of this power rating [78].

4.5.3 Parameterised Geometry

In (4.5.1), $\mathbf{X}_n$ is the input vector generated by the NSGA-II algorithm containing the relevant dimensions for each topology. The input vector, $\mathbf{X}_n$, is then defined as

$$\mathbf{X}_n = \begin{bmatrix} \mathbf{Y}_{\text{r}} \\ \mathbf{Y}_{\text{s}} \\ l_{\text{Fe}}. \end{bmatrix} \tag{4.5.4}$$

In (4.5.4), $\mathbf{Y}_{\text{r}}$ is the vector containing the relevant rotor structure's dimensions, as defined in Fig. 4.4, and is given by either

$$\mathbf{Y}_{\text{S-PM}} = \mathbf{Y}_{\text{E-PM}} = \begin{bmatrix} d_{\text{o}} & h_{\text{ry}} & h_{\text{m}} & \theta_{\text{m}} \end{bmatrix}^{\text{T}} \qquad \text{or} \qquad \mathbf{Y}_{\text{SP-PM}} = \begin{bmatrix} d_{\text{o}} & h_{\text{m}} & b_{\text{m}} \end{bmatrix}^{\text{T}} \tag{4.5.5}$$

for the S-PM, E-PM or SP-PM rotor structures respectively. In (4.5.4), $\mathbf{Y}_{\text{s}}$ is the vector containing the stator structure's dimensions, as defined in Fig. 4.3, and is given by either

$$\mathbf{Y}_{\text{os}} = \begin{bmatrix} h_{\text{hs}} & h_{\text{s}} & b_{\text{t}} & h_{\text{sy}} \end{bmatrix}^{\text{T}} \qquad \text{or} \qquad \mathbf{Y}_{\text{sc}} = \begin{bmatrix} b_{\text{o}} & h_{\text{hs}} & h_{\text{s}} & b_{\text{s}} & h_{\text{sy}} \end{bmatrix}^{\text{T}} \tag{4.5.6}$$

for the respective open slot and semi-closed slot stator structures.

Parameterised geometry is used to maintain a realistic optimisation search space and four geometric boundaries are imposed: the outer diameter is limited to that of the wind turbine's nacelle $d_{\text{o}} < 400$ mm; the relevant rotor- and stator yoke heights have to be $h_{\text{ry}}, h_{\text{sy}} > 6$ mm to maintain structural integrity; as a precaution for demagnetisation and for manufacturing ease (brittle PMs) of the S-PMSG, the minimum allowed PM height is $h_{\text{m}} > 3$ mm. For all the PMSG designs the mechanical air gap is kept constant at

$g_{\text{air}} = 1$ mm. For the SP-PMSGs, the rotor yoke support, as shown in Fig. 4.4(c), is kept constant at 1 mm.

4.6 Design Results and Evaluation

4.6.1 Optimisation Results

The multi-objective optimisation Pareto front results are shown in Fig. 4.8. The Pareto fronts in Fig. 4.8 show the trade-off between M_{active} and M_{PM} and provide insight into how the different PMSG topologies compare to one another. For the third objective in (4.5.1), to minimise Z_{ext}, the PMSG solutions where $Z_{\text{ext}} = 0$ are also indicated in Fig. 4.8. For these solutions, the internal impedance of the PMSG is sufficient for near maximum power matching. It is shown in Fig. 4.8(a), that for the S-PMSG with open stator slots, none of the solutions meet the desired *natural* impedance matching and require an external inductance for good power matching. Moreover, the Pareto front results in Fig. 4.8 confirm that altering the stator slot and rotor structure, to increase

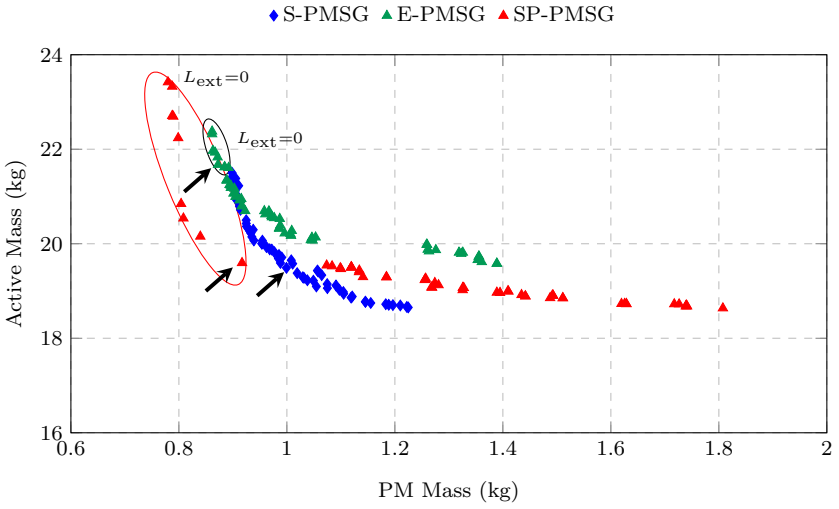

(a) Open slots

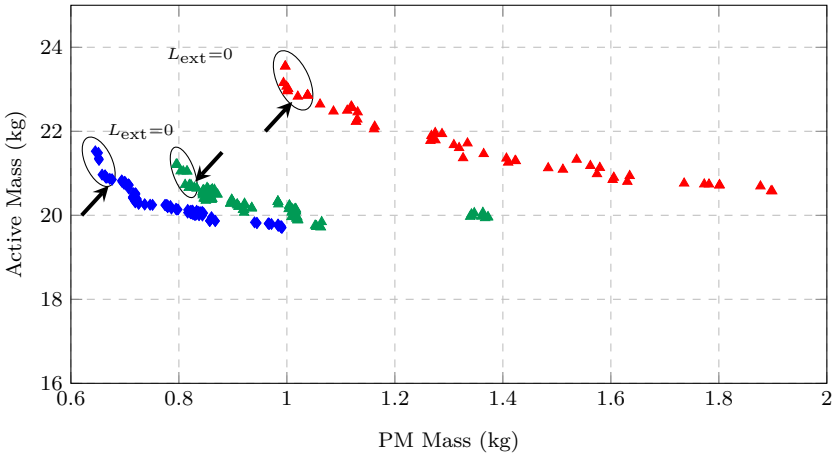

(b) Semi-closed slots

Figure 4.8: Multi-objective optimisation Pareto front results.

Table 4.4: Comparison of selected Pareto front PMSG solutions.

Open slot	S-PMSG	E-PMSG	SP-PMSG
M_{PM} (kg)	1.0	0.87	0.92
M_{active} (kg)	19.49	21.67	19.60
Z_{ext} (Ω)	0.36	0	0
P_{g} (kW)	4.18	4.16	4.17
η (%)	89.1	89.8	89.8
J_{rms} (A/mm^2)	5.0	4.93	4.97
L_{q} (mH)	2.71	3.90	3.43
L_{d} (mH)	2.58	2.94	3.00
ξ	1.05	1.33	1.14
X_{s} (pu)	1.6	2.48	2.28
d_{o} (mm)	376	375	383
l_{Fe} (mm)	40	47	39

Semi-closed slot	S-PMSG	E-PMSG	SP-PMSG
M_{PM} (kg)	0.72	0.82	0.99
M_{active} (kg)	21.33	20.72	23.15
Z_{ext} (Ω)	0	0	0
P_{g} (kW)	4.26	4.10	4.10
η (%)	89.8	89.9	89.8
J_{rms} (A/mm^2)	5.0	5.0	4.9
L_{q} (mH)	3.12	4.25	3.95
L_{d} (mH)	2.95	3.01	2.69
ξ	1.06	1.41	1.41
X_{s} (pu)	1.95	2.52	2.37
d_{o} (mm)	376	376	384
l_{Fe} (mm)	48.5	48	42

L_{sl} and the magnetic saliency ξ, are both viable methods to increase L_{s} for a natural impedance matching.

For each PMSG topology, the optimum design is selected at the optimal trade-off between the design objectives, as indicated in Fig. 4.8. The performance results are summarised in Table 4.4. Although the efficiency values in Table 4.4 are slightly lower than specified, they are still deemed acceptable. Altogether, the results in Table 4.4 confirm that the performance constraints in (4.5.3) are met. In terms of M_{active} and M_{PM}, the SP-PMSG with open slots and the S-PMSG with semi-closed slots are the best options. This is also evident from the Pareto fronts shown in Fig. 4.8. However, the difference between these two PMSG topologies is not that significant. The S-PMSG with open slots is also competitive in terms of M_{active} and M_{PM}. However, this topology can be discarded due to the necessary external inductance.

4.6.2 Power Matching

To illustrate the natural impedance matching of the respective PMSGs in Table 4.4, the FEA predicted power curves are plotted against the wind turbine's power curves in Fig. 4.9. The PMSGs start generating power at the specified cut-in speed and achieve good power matching at low wind speeds, which is essential for this application. The

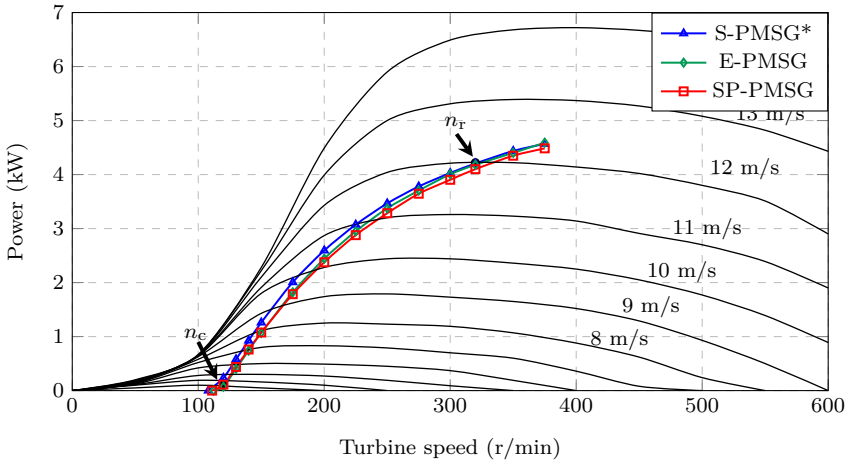

(a) Open slots

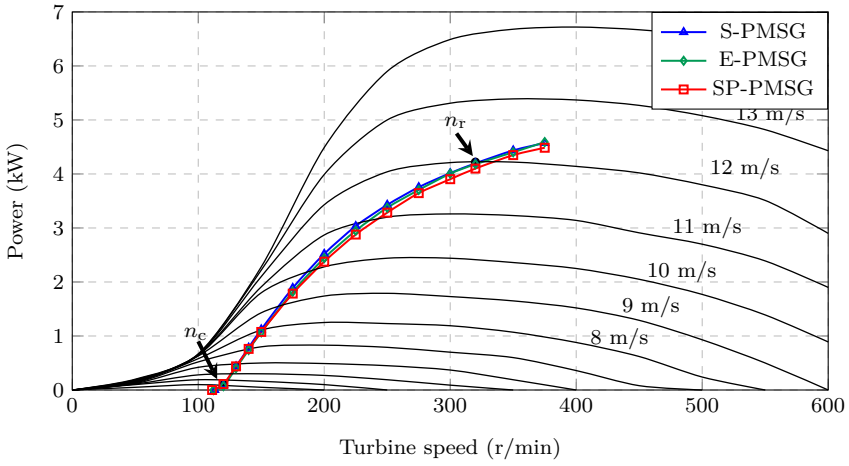

(b) Semi-closed slots

Figure 4.9: Power curves of the selected PMSGs in Table 4.4.

respective PMSGs also match with the wind turbine at the rated operating speed. Overall, the power matching plots in Fig. 4.9 are desirable; with the respective E-PMSGs and SP-PMSGs, as well as the S-PMSG with semi-closed slots, matching naturally with the wind turbine.

4.6.3 Torque Quality

Good torque quality is essential for small-scale wind generators, specifically the generator's cogging torque, since the wind turbine has to overcome this to start generating power. The cogging torque, ΔT_{cog}, and rated torque ripple, ΔT_r, results for the respective PMSGs in Table 4.4 are summarised in Table 4.5. All of the PMSGs have a very low cogging torque, with $\Delta T_{cog} < 2.1\%$ for all of the PMSGs. However, the torque ripple results for the interior embedded PMSG topologies in in Table 4.5 are undesired ($\Delta T_r > 10\%$). For comparison, the FE predicted ΔT_{cog} and ΔT_r for the semi-closed rectangular slot S-PMSG and the open slot SP-PMSG are shown for the mechanical rotation of one rotor pole pair (360 electrical degrees) in Fig. 4.10.

Table 4.5: Comparison of PMSG Torque Quality.

Open slot	S-PMSG	E-PMSG	ST-PMSG
ΔT_{cog}, (%)	1.2	1.2	2.0
ΔT_{r}, (%)	6.6	12.4	12.5

Semi-closed slot	S-PMSG	E-PMSG	ST-PMSG
ΔT_{cog}, (%)	1.5	1.9	2.1
ΔT_{r}, (%)	4.9	13.0	17.1

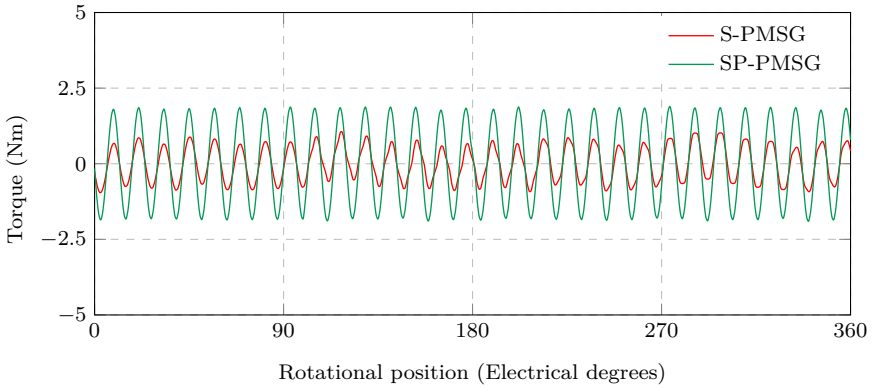

(a) Cogging torque, ΔT_{cog}

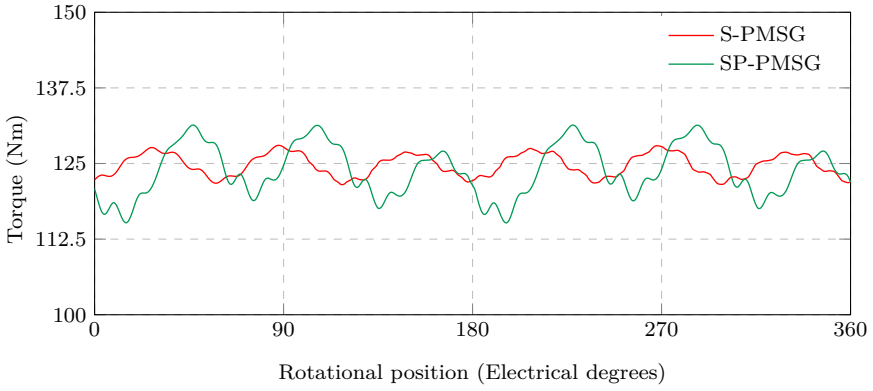

(b) Torque ripple, ΔT_{r}

Figure 4.10: FE predicted cogging torque and torque ripple of the S-PMSG with semi-closed slots and the SP-PMSG with open slots in Table 4.4.

4.6.4 Demagnetisation

Irreversible demagnetisation in small-scale PM wind generators can occur during short-circuit fault conditions or at high PM temperatures. Furthermore, at the full-load rated operating point, the PM generator in an uncontrolled passive wind generator system will operate with a relatively large d-axis current. This causes a strong magnetic field that opposes that of the PMs, which in turn may cause demagnetisation to occur. The geometric constraint on h_{m} in the design optimisation, is imposed to reduce the risk of demagnetisation. However, the PMSG designs in Table 4.4 still need to be evaluated for irreversible demagnetisation to determine the risk thereof.

It is evident from the power curves in Fig. 4.9 that the power in the passive wind

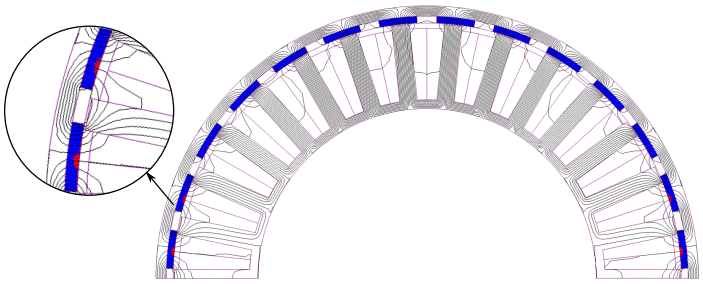

(a) S-PMSG open slots, 50°C PM temperature.

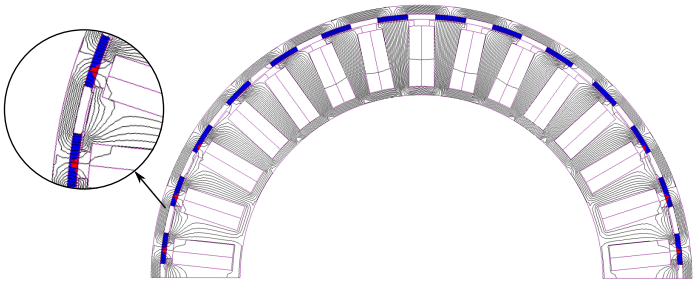

(b) S-PMSG semi-closed slots, 80°C PM temperature.

Figure 4.11: Demagnetisation prediction at different temperatures (indication by red colour in the magnets) for the S-PMSGs in Table 5.2 at rated conditions, 320 r/min and full load, using NdFeB N48.

generator system is limited independent of wind speed. Therefore, PM demagnetisation in the PMSGs is analysed at the generator's rated speed, n_r (thus at rated load). The demagnetisation prediction plots for the two S-PMSGs, using NdFeB N48 grade PMs, are shown in Fig. 4.11. It is shown in Fig. 4.11(a) that for the open-slot S-PMSG, demagnetisation will start occurring at PM temperatures > 50°C. However, the temperature of the PMs during operation are not expected to surpass 50°C. In Fig. 4.11(b), it is shown that the PMs in the semi-closed slot S-PMSG are at very low risk of demagnetising, with demagnetisation only occurring at > 80°C. Similarly, for the embedded interior PMSG topologies, E-PMSG and SP-PMSG, it is found that the PMSGs are at low risk of demagnetising, with slight demagnetisation only starting to occur at PM temperatures > 80°C. To nullify the risk of irreversible demagnetisation, NdFeB N48H grade PMs can be used.

4.6.5 3D FEA Performance Validation

To validate the 2D FEA solutions and optimisation results, the performance of the respective PMSGs in Table 4.4 are also solved using 3D FEA. The 3D models of the semi-closed slot S-PMSG and the open slot SP-PMSG are shown in Figs. 4.12(a) and (b) respectively. The 2D versus 3D FEA results are summarised in Table 4.6.

It is shown in Table 4.6, that the 3D FEA generated torque, T_g, and generator efficiency, η, at rated speed n_r, correlate well with the 2D FEA results. Also given in Table 4.6, are the calculated iron losses, P_{Fe}, at both n_r and n_c. The iron losses at n_c are important, because the wind turbine needs to overcome the PMSG's open circuit losses (predominantly P_{Fe}) up to the cut-in speed, n_c, to start generating power. It is shown in Table 4.6, that the 2D and 3D FEA core losses at n_c compare well. For the interior embedded PMSG topologies, the 2D FEA calulated core losses at n_r are lower than the 3D FEA calulated core losses. However, the effect on the PMSGs' performance at n_r is shown to be minor.

Table 4.6: 2D versus 3D FEA PMSG performance comparison.

Open slot	S-PMSG		E-PMSG		SP-PMSG	
	2D	3D	2D	3D	2D	3D
T_g, (Nm)	124.9	128.8	124.3	131.6	122.8	113.7
η, (%)	89.1	89.4	89.8	90.0	89.8	88.7
P_{Fe} at n_r, (W)	25.1	28.5	21.9	37.5	20.7	31.8
P_{Fe} at n_c, (W)	10.7	12.6	10.0	12.3	11.4	10.5

Semi-closed slot	S-PMSG		E-PMSG		SP-PMSG	
	2D	3D	2D	3D	2D	3D
T_g (Nm)	127.1	126.7	122.2	118.9	122.4	115.4
η, (%)	89.8	89.9	89.8	89.2	89.8	89.0
P_{Fe} at n_r, (W)	31.3	33.9	29.4	49.8	26.5	35.0
P_{Fe} at n_c, (W)	13.9	12.5	12.4	13.7	11.6	11.8

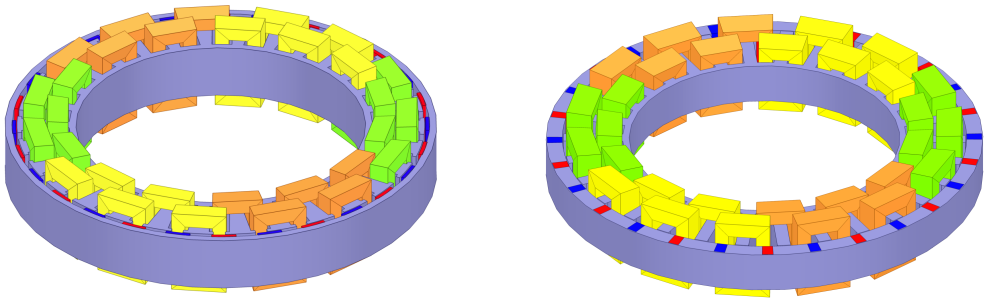

(a) S-PMSG, semi-closed slots. **(b)** SP-PMSG, open slots.

Figure 4.12: 3D FEA models for some of the PMSGs in Table 5.2.

4.6.6 Discussion

Considering all aspects of the performance evaluation done in the previous subsections, it is evident that the S-PMSG with semi-closed slots is the best generator topology. The results in Table 4.4 indicate that this PMSG is competitive in terms of active material costs and the generator's active mass. Furthermore, this PMSG has good power matching with the wind turbine, achieving the desired *natural* impedance matching, as well as having superior torque quality.

4.7 Prototype and Experimental Validation

The manufactured prototype of the S-PMSG with semi-closed slots in Table 4.4, is shown in Fig. 4.13(a). It is shown in Fig. 4.13(b), that the overhang of the end-winding length, l_o, is larger than what was designed for. In the 2D FEA this length was taken as $l_o = 5$ mm, however, the actual measured value is $l_o = 20$ mm [1]. For the experimental validation, this length is taken into account in the 2D FEA.

The experimental setup on the test bench is shown in Fig. 4.14. In Fig. 4.14, the S-PMSG prototype is mechanically connected to a geared induction motor drive that emulates the wind turbine. The torque sensor in Fig. 4.14 is used to measure the input power. The S-PMSG prototype is electrically connected to the battery bank via a resistor,

[1] This is an error by the winder. It is possible to wind the machine for the designed overhang length.

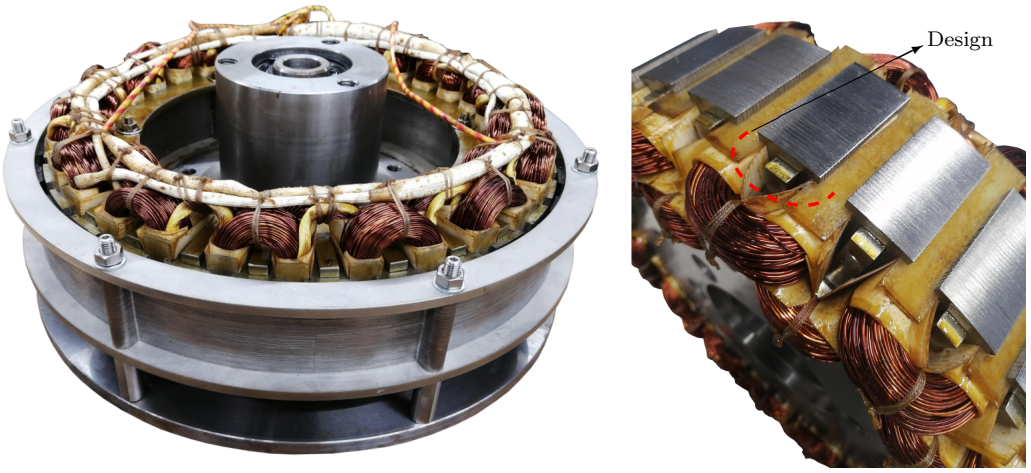

(a) NO-PMSG

(b) Design versus actual end-winding overhang length.

Figure 4.13: S-PMSG prototype with semi-closed stator slots.

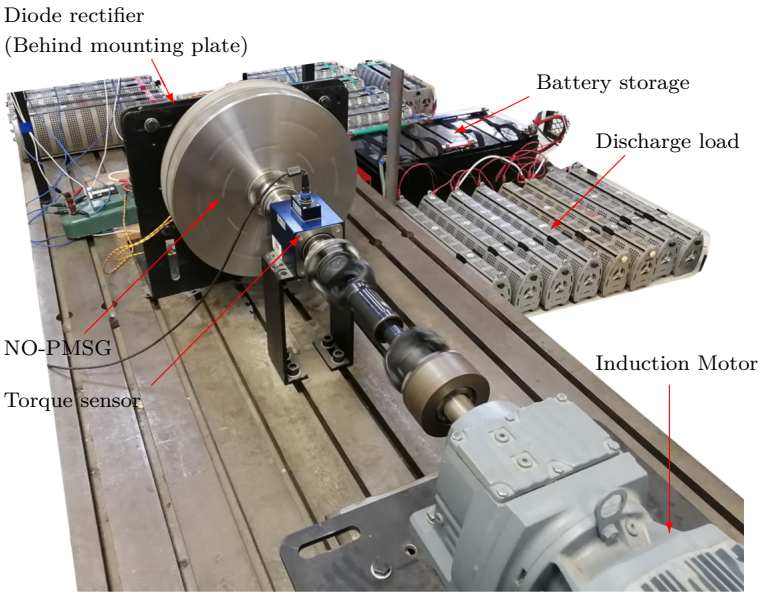

Figure 4.14: Experimental test bench setup of the manufactured NO-PMSG prototype.

equivalent to the resistance of the brush-slip-rings, and via the diode bridge rectifier. The 48 V battery bank energy storage and discharge load are also shown in Fig. 4.14.

4.7.1 Power Matching Measurements

The measured results for the S-PMSG prototype's generated power, P_g, and output power, P_{out}, are shown in Fig. 4.15. It is shown that the P_g power measurements are much lower than what were designed for (green FEA curve). The following explanation accounts for the measured results in Fig. 4.15:

The manufacturer of the prototype's PMs could only guarantee certain dimensional tolerances on the PMs. Initially these tolerances were considered insignificant. However, Fig. 4.16 shows that the S-PMSG's performance is very sensitive to these manufacturing tolerances, i.e. the magnet height h_m and the magnet pitch angle θ_m. It is shown in Fig. 4.16 that the PMSG's generated torque is particularly sensitive to h_m, seeing as a

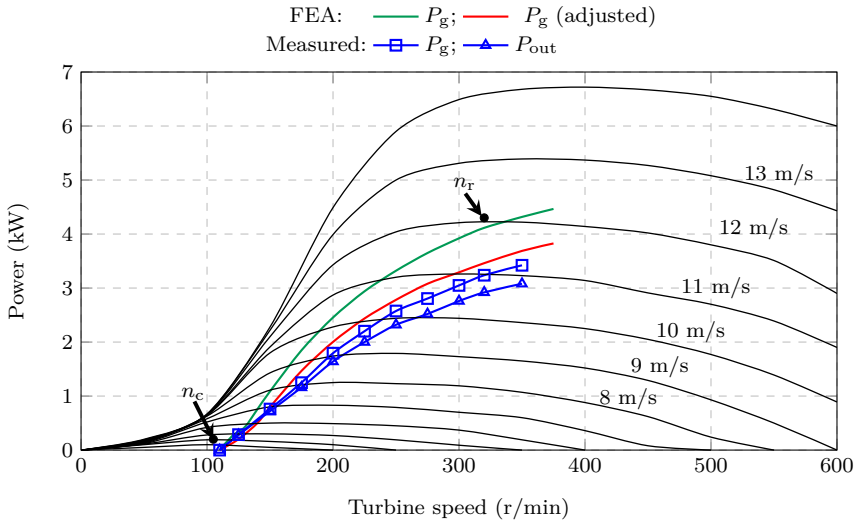

Figure 4.15: Measured power matching results of the S-PMSG prototype.

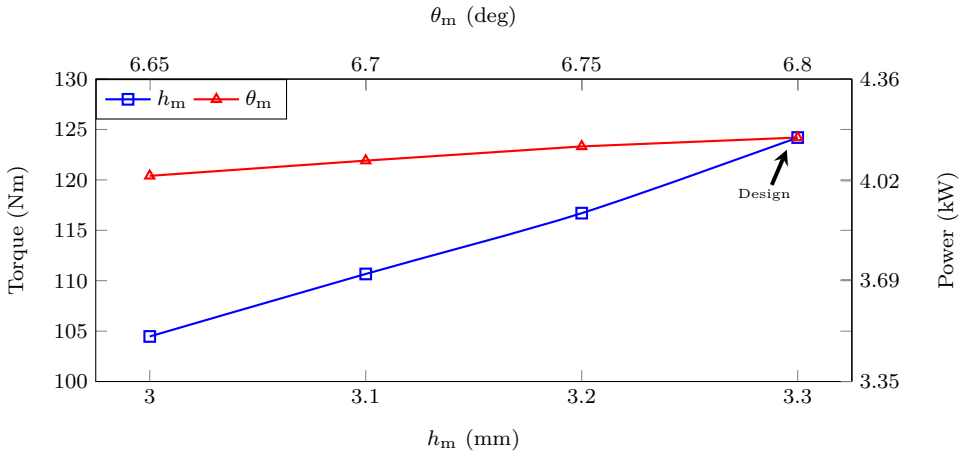

Figure 4.16: Effect of PM manufacturing tolerances on the generated torque and power at $n_r = 320$ r/min

smaller magnet height also results in a larger air gap. Attempts to measure the height and width of the PMs with a digital caliper are shown in Fig. 4.17. In Figs. 4.17(a) and (b) it is shown that the average PM height is $h_m \approx 3.1$ mm, instead of the $h_m = 3.3$ mm for which the PMs were designed. Also shown in Figs. 4.17(c) and (d), are that the magnet pitch angle and PM length are also slightly below the designed values of $\theta_m = 6.8$ deg and $l_{Fe} = 48.5$ mm.

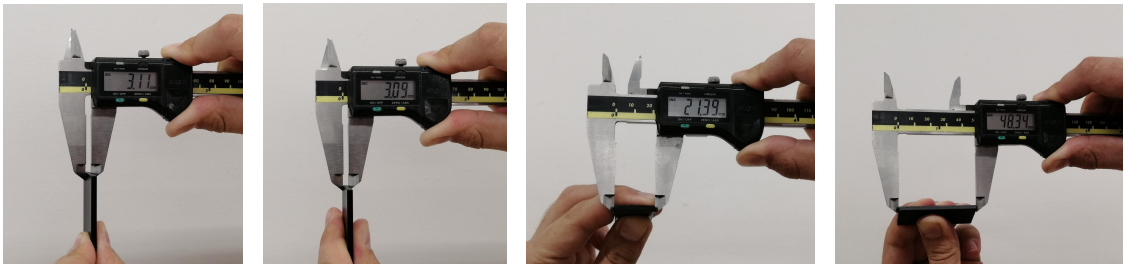

(a) $h_m = 3.11$ mm **(b)** $h_m = 3.09$ mm **(c)** $\theta_m < 6.8$ deg **(d)** $l_{Fe} < 48.5$ mm

Figure 4.17: Measuring of PM dimensions.

Table 4.7: Summary of PMSG prototype measurements.

	FEA		Measured
	2D	3D	
Parameters			
- PM height, h_m (mm)	3.1		3.1
- PM angle, θ_m (deg)	6.75		6.75
- PM length, l_{Fe} (mm)	48.35		48.35
- Phase resistance, R_s (Ω)	0.133	0.133	0.130
- Synchronous inductance, L_s (mH)	3.23	3.46	3.48
Performance at $n_r = 320$ r/min			
- P_g (kW)	3.43	3.46	3.26
- η (%)	89.3	88.6	86.5
- E_g (V)	61.4	60.6	60.9
Cogging torque			
- ΔT_{cog} (Nm)	1.31		5.60

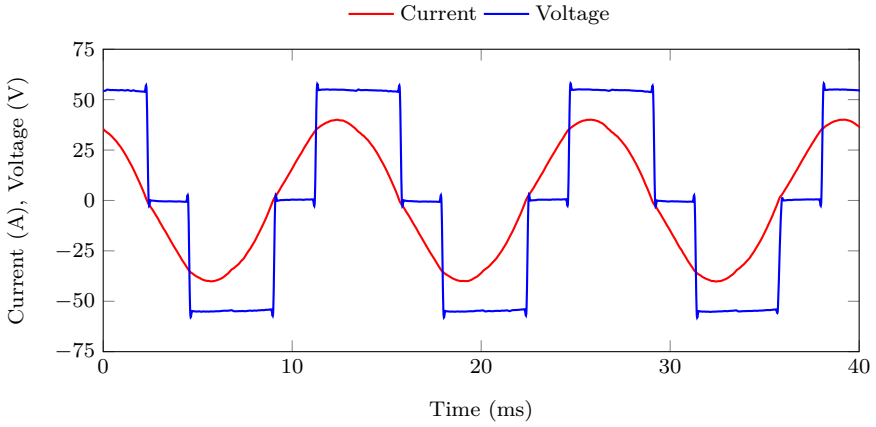

Figure 4.18: Measured phase current and line voltage at $n_r = 320$ r/min, showing operation at unity displacement power factor.

It is shown in Fig. 4.15, that if the PMs' dimensions are adjusted in the FEA accordingly, a better correlation between the measured power matching and the FEA (red curve) predicted power matching is obtained. The measured and FEA results are also summarised in Table 4.7. The 2D and 3D FEA results with the adjusted PMs are both included in Table 4.7. The error between the measured and FEA predicted P_g in Table 4.7 at $n_r = 320$ r/min is 5%. The measured generator efficiency in Table 4.7 is addressed in the next subsection.

The measured current and voltage waveforms are shown in Fig. 4.18. The current waveform in Fig. 4.18 shows to be sinusoidal, and also correctly 30 deg out of phase with the fundamental line voltage, i.e. the PMSG is operating at a unity displacement power factor.

4.7.2 No-load and Short Circuit Measurements

The no-load open circuit voltage measurements are shown in Figs. 4.19 and 4.20. The values for the measured no-load open circuit voltage at $n_r = 320$ r/min are also summarised in Table 4.7. The measured versus FEA results in Fig. 4.19 show good correlation. This

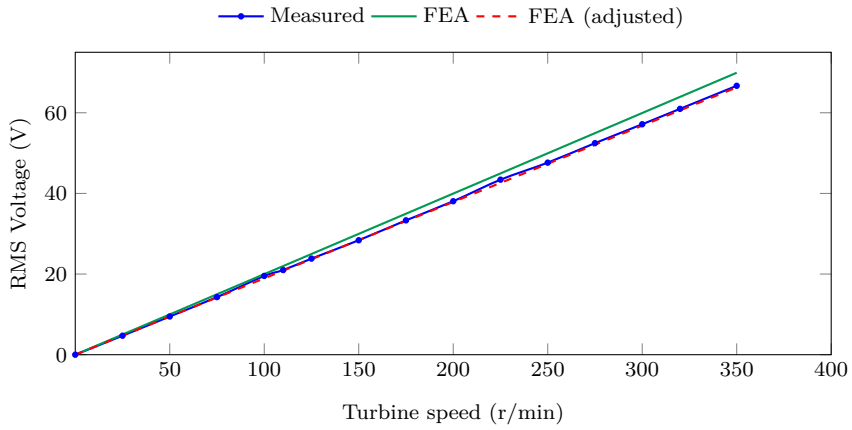

Figure 4.19: Measured open circuit voltage versus FEA calculated voltage.

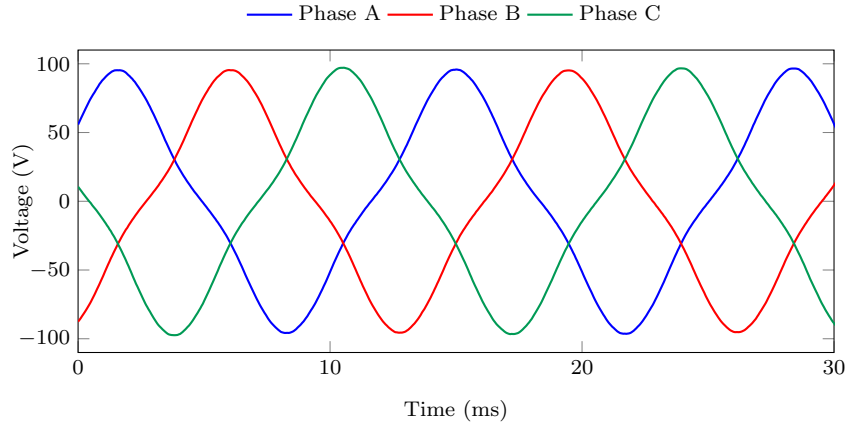

Figure 4.20: Measured no-load open circuit voltage waveforms at $n_r = 320$ r/min.

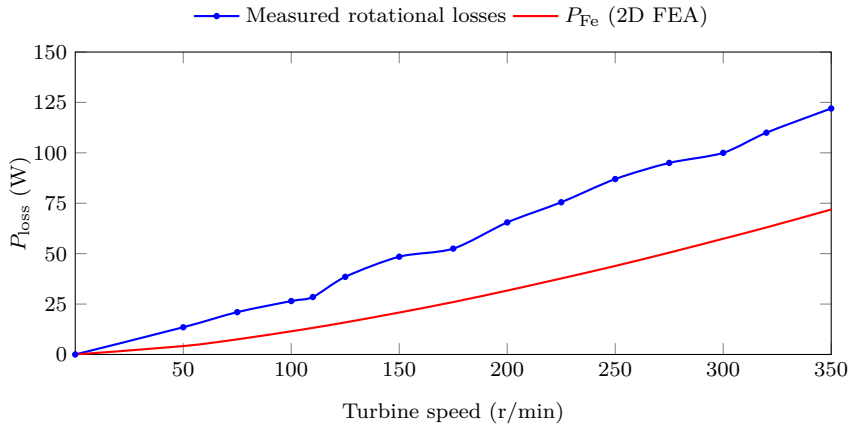

Figure 4.21: Measured no-load open circuit losses versus no-load FEA calculated iron losses.

verifies the results in the previous subsection and the effect of the manufacturing tolerances of the PMs.

The measured no-load rotational losses are also plotted in Fig. 4.21, and are compared to the no-load 2D FEA predicted iron losses P_{Fe}. The difference can be attributed to windage and friction losses that were not accounted for in the design process. The additional windage and friction losses then also account for a portion of the 5% difference between the measured and FEA predicted P_g in Fig. 4.15 and Table 4.7, as well as the difference in efficiency η. The measured rotational losses at n_r and rated load is 118 W.

As shown in the no-load measurements in Fig. 4.21, windage and friction losses account for approximately half of this. The latter indicates that the iron losses P_{Fe} at rated load are slightly higher than what is predicted in the FEA solutions and would account for the lower efficiency measurements in Table 4.7.

The internal synchronous inductance of the PMSG prototype is measured by means of a number of short circuit tests to get an average value. The average measured value is given in Table 4.7 and is shown to be very close to the FEA calculated value.

4.7.3 Cogging Torque

A schematic showing the experimental setup to measure the prototype's cogging torque is shown in Fig. 4.22. In Fig. 4.22, the PMSG is connected to a torque beam via the torque sensor. The method then, for measuring the cogging torque, is similar to that of [87]. The PMSG's rotor position is varied by adjusting the angle of the torque beam. Torque measurements are then taken at discrete angular displacements over one pole pair (360 electrical degrees). The measured cogging torque results are shown in Fig. 4.23 and ΔT_{cog} is given in Table 4.7. The results in Fig. 4.23 and Table 4.7 show that the prototype's cogging torque is higher than the predicted value. However, the measured cogging torque waveform in Fig. 4.23 indicates that either the prototype's air gap is not uniform or that there might be a mechanical imbalance. For the most part, the cogging torque pulses in Fig. 4.23 coincide with the FEA predicted cogging torque peaks. In Fig. 4.23 it seems that the "disturbance" repeats every 180 electrical degrees, indicating the presence of some low order harmonic. Furthermore, taking precise measurements is

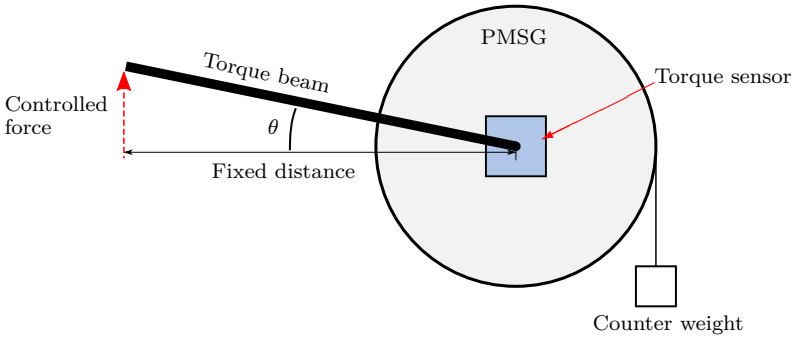

Figure 4.22: Schematic illustrating the experimental setup for cogging torque measurement.

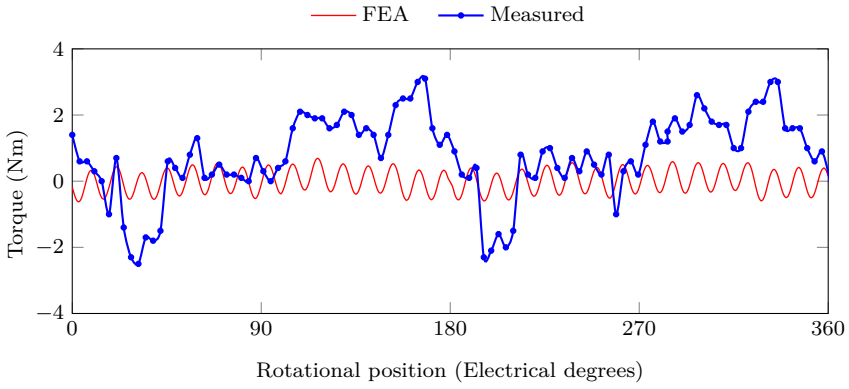

Figure 4.23: FEA calculated- and measured cogging torque versus the mechanical rotation of one pole pair (360 electrical degrees).

difficult given the sensitivity of the measurement and the available equipment. A torque sensor rated with a maximum of 200 Nm was used to measure the cogging torque. Using smaller torque sensor, with a more precise calibration, will give a more accurate reading.

4.8 Chapter Summary

In this chapter, different topology PMSGs are considered in the design process of wind generators for small-scale uncontrolled passive wind generator systems. This is done to investigate whether the resulting higher internal impedance of the generator, from either using an interior PM rotor or a different stator slot structure, is sufficient to achieve the desired power matching with the wind turbine. The respective PMSGs are designed using a multi-objective design optimisation approach. The following main conclusions are drawn from the investigation:

- For PMSGs with surface mounted PMs on the rotor, it is shown that the required impedance for a natural impedance matching with the wind turbine can be attained by changing the stator structure. Using semi-closed slots, as opposed to open slots, is shown to be a better design choice. Using semi-closed slots reduces the risk of PM demagnetisation and does not compromise the generator's torque quality. The S-PMSG with semi-closed slots is also the most cost effective generator and therefore, ultimately, the optimal generator choice.
- Altering the rotor structure and the orientation of the PMs in the rotor to increase the magnetic saliency, is shown to be another viable method to achieve the desired impedance matching. However, in this case, it is clear that an open slot stator structure should be used. The E-PMSG and SP-PMSG topologies also have poor torque quality compared to the S-PMSG generators. Therefore, it is not recommended that these topologies be used for small-scale wind generators. Careful attention should also be brought to the leakage- and end-effects of SP-PMSGs, as this can have a significant impact on the generator's performance if ignored.
- The results presented in this chapter are validated by a good comparison between calculated and measured results of a prototype S-PMSG with semi-closed stator slots. However, it is shown that when the PM material is minimised to the extreme in the design optimisation, that the manufacturing tolerances on the PMs can have a significant effect on the power matching results. This is a very important outcome, showing that manufacturing tolerances should be accounted for in the design and manufacturing process, especially the PM height.

Chapter 5

Permanent Magnet Vernier Generator Design

PMSGs are predominantly used in small-scale uncontrolled passive wind energy systems [17–23]. It is shown in Chapter 4 that it is possible to design PMSGs for a natural impedance matching in passive systems. However, the PMSG might not necessarily be the most suited generator technology for this application. Hence, the aim of this chapter is to address the research sub-question:

4. What are the alternative PM wind generator technologies, other than the widely used PMSG, and are there any benefits to using these technologies instead?

Permanent magnet Vernier generators are known to have excessive leakage flux compared to conventional PMSGs and inherently have high operating frequencies due to machine selection criteria. Both of the aforementioned factors result in a large internal reactance. Considering the arguments and results in the previous chapters, it becomes more clear why the PMVG might be a more suitable machine technology and why the PMVG's large internal reactance is not considered to be a drawback for this application (as opposed to the controlled wind energy systems in Figs. 1.1(b) and (c)).

5.1 PM Vernier Generators

5.1.1 Working Principle

The Vernier machine's potential for a higher torque density is due to the fact that Vernier machines have two torque producing components, as opposed to conventional machines that only have one. The two torque producing components are the result of "harmonic coupling" taking place; i.e. between the PM rotor's working harmonic and a higher order stator winding-MMF harmonic, as well as the resulting flux-modulated harmonic with the fundamental stator winding-MMF harmonic [88]. Therefore, Vernier machine selection is subject to the relationship given by

$$p_{\mathrm{s}} = p_{\mathrm{fm}} \pm p_{\mathrm{r}} \Rightarrow p_{\mathrm{s}} = p_{\mathrm{fm}} - p_{\mathrm{r}}, \tag{5.1.1}$$

where p_{s} is the number of stator pole pairs, p_{fm} is the number of flux-modulating poles and p_{r} is the number of PM rotor pole pairs. For an in-depth explanation of the harmonic coupling effect and Vernier machine working principle, refer to Appendix C.

The ratio of the number of rotor- to stator pole pairs, G_r, is referred to as the harmonic coupling factor or the magnetic gearing ratio:

$$G_r = \frac{p_r}{p_s} \tag{5.1.2}$$

Analytical equations for the generated torque and fundamental magnetisation reactance, obtained from [55], are given in (5.1.3) and (5.1.4) respectively. The magnetic gearing ratio of (5.1.2) is present in both (5.1.3) and (5.1.4), and highlights the fundamental trade-off for Vernier machine selection: a larger G_r results in better torque producing capability, but at the potential cost of a poorer power factor due to the large increase of X_{m1} with the increase in magnetic gearing ratio.

$$T_g = k_w N_s I_s d_i l_{Fe} \left[B_{PM0} + G_r \frac{B_{PM1}}{2} \right] \tag{5.1.3}$$

$$X_{m1} = \omega_r p_r L_{m1} = \omega_r G_r \frac{m(N_{ph} k_{w1})^2 l_{Fe} d_i \mu_0}{\pi p_s g'_{air}} \tag{5.1.4}$$

5.1.2 PMVG Topologies

The two Vernier machine topologies considered in this paper are the conventional topology (C-PMVG) with overlapping windings and the split-tooth topology (ST-PMVG) with non-overlapping windings. In the case of the C-PMVG with overlapping windings, the structure is similar to that of a conventional PMSG and the stator teeth act as the flux-modulating poles. For the C-PMVG the number of flux-modulating poles is therefore equal to the number of stator slots, Q_s. In the case of the ST-PMVG, auxiliary teeth on the stator teeth act as flux-modulating poles. These auxiliary teeth are shown in Fig. 5.1. For wind generator applications the ST-PMVG's shorter end-winding length is an advantage. This makes the wind generator more compact and easier to manufacture. However, ST-PMVGs are more prone to excessive leakage flux [57] and generally have worse power factors compared to C-PMVGs [55]. Using (5.1.1) and (5.1.2), the possible PMVG slot-pole combinations are summarised in Table 5.1.

Note that it is possible to select magnetic gearing ratios other than those in Table 5.1 by opting for a non-overlapping winding PMVG with a very low G_r, or a two-slot pitch winding PMVG as in [89–91]. However, the selection in Table 5.1 is deemed sufficient for this application. There are also promising topology variations in literature that use Halbach PM arrays, dual spoke-type PM rotors [57] or a consequent pole rotor with additional assist PMs on the stator [92]. However, due to the novelty of using PMVGs for this application, the focus in this chapter is confined to typical PMVG topologies with known structures.

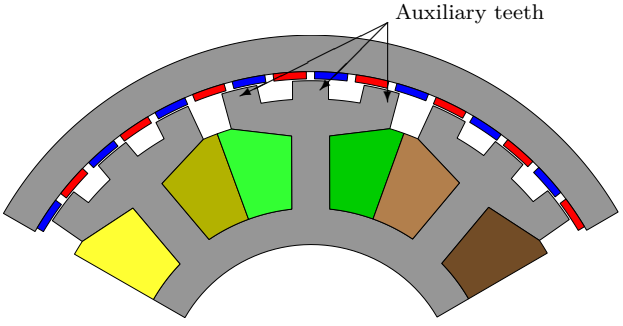

Figure 5.1: ST-PMVG topology with auxiliary teeth.

Table 5.1: Vernier machine selection with imposed frequency constraint at rated speed, n_r.

G_r	5			8			11			14		
p_s	p_{fm}	p_r	f_e (Hz)	p_{fm}	p_r	f_e (Hz)	p_{fm}	p_r	f_e (Hz)	p_{fm}	p_r	f_e (Hz)
1	6	5	26.67	9	8	42.67	12	11	58.67	15	14	74.67
2	12	10	53.33	18	16	85.53	24	22	117.33	30	28	149.33
3	18	15	80.0	27	24	128.0	36	33	176.0	45	42	224.0
4	24	20	106.67	36	32	170.67	48	44	234.67	60	56	298.67
5	30	25	133.33	45	40	213.33	60	55	293.33	75	70	373.33
6	36	30	160.0	54	48	256.0	72	66	352.0	90	84	448.0
q	1			1.5			2			2.5		

5.1.3 PMVG Selection

For small-scale wind generator systems, the wind generator needs to overcome both generator cogging torque and -open circuit losses (predominantly core losses) up to the system's cut-in speed, n_c, to start generating power.

Core losses increase with an increase in electrical frequency. Therefore, a maximum allowed electrical frequency of $f_e = 135$ Hz at the rated operating point is imposed on the machine selection. This constraint is indicated in Table 5.1 and three selected PMVG combinations, with $G_r = 5, 8$ and 11 respectively, are also indicated with a darker highlight. These machine selections are at the maximum frequency constraint and also have a realistic number of stator slots for manufacturing the winding.

As mentioned in Chapter 4, a good indicator to predict whether a PM machine will have a small no-load cogging torque is the least common multiple (LCM) between Q_s and $2p_r$. Generally, the larger LCM(Q_s,$2p_r$) is, the smaller the no-load cogging torque. The selected PMVGs in Table 5.1 for $G_r = 5, 8$ and 11, have corresponding LCM values of 120, 432 and 264 respectively. This indicates that the PMVG in Table 5.1 with $G_r = 8$ is best suited in terms of no-load cogging torque. Nonetheless, seeing as there are other factors to also consider, all three of the selected PMVG combinations indicated in Table 5.1 are further considered in the design for the passive system to ensure an all-encompassing investigation.

5.2 Equivalent Modelling

For the most part, the equivalent modelling of PMVGs are the same as in Chapter 3 for PMSGs. In this section, the main differences that need to be accounted for are highlighted.

5.2.1 Overlapping Windings

The C-PMVG topology has overlapping windings. Therefore, the semi-analytical end-winding calculations given in Chapter 3 for the static 2D FEA are no longer valid and can only be used for the ST-PMVG topology. The following alterations are implemented in the 2D FEA for the overlapping winding's end-winding calculations.

5.2.1.1 End-winding Length

Calculating the end-winding length for electrical machines with overlapping windings can be inexact. Nonetheless, this is a very important dimension, since it directly influences the machine's performance in terms of efficiency and the overall cost in terms of copper mass.

There are multiple formulae available in literature for calculating a machine's overlapping end-winding length such as in [40, 93, 94]. However, these formulae are merely estimations and can depend on manufacturing methods and the machine's size or power rating. For low-voltage machines, Pyrhönen et al. [78] gives an approximation for the average length of a coil turn as

$$l_{\text{coil}} = 2l_{\text{Fe}} + 2.4\tau_{\text{coil}} + 0.1. \tag{5.2.1}$$

In (5.2.1), τ_{coil} is the length of the coil pitch. Since l_{Fe} is the machine's axial stack length, the end-winding length can therefore be approximated as

$$l_{\text{e}} = \frac{2.4\tau_{\text{coil}} + 0.1}{2}. \tag{5.2.2}$$

In comparison to the respective end-winding length calculations in [40, 93, 94], it is found that the approximation in (5.2.2) gives the most consistent and realistic end-winding length.

5.2.1.2 End-winding Inductance

The end-winding inductance for a machine with overlapping windings can be calculated as in [95], using

$$L_{\text{e}} = \frac{mV_{\text{u}}d_{\text{i}}}{2\pi}\left(\frac{N_{\text{ph}}k_{\text{w}}}{p_{\text{s}}}\right)^2 k_{\text{e}}(p_{\text{s}}) \times 10^{-8}. \tag{5.2.3}$$

In (5.2.3), V_{u} is a constant for the elliptically shaped form of the stator end-windings with $V_{\text{u}} = 1040$, k_{w} is the working harmonic winding factor calculated as in Appendix A, $k_{\text{e}}(p_{\text{s}})$ is the stator end-winding factor for a machine with p_{s} pole pairs, as given in [95].

5.2.2 Performance

The developed torque and the electrical power generated by the PMVG are calculated using (5.2.4) and (5.2.5) respectively. Note here that the torque is calculated with the number of PM rotor pole pairs.

$$\begin{aligned} T_{\text{g}} &= \frac{3}{2}p_{\text{s}}G_{\text{r}}[(L_{\text{q}} - L_{\text{d}})I_{\text{d}}I_{\text{q}} + \lambda_{\text{PM}}I_{\text{q}}] \\ &= \frac{3}{2}p_{\text{r}}[(L_{\text{q}} - L_{\text{d}})I_{\text{d}}I_{\text{q}} + \lambda_{\text{PM}}I_{\text{q}}] \end{aligned} \tag{5.2.4}$$

$$P_{\text{g}} = T_{\text{g}}\omega_{\text{m}} \tag{5.2.5}$$

The efficiency of the PMVG is calculated using

$$\eta = \frac{P_{\text{g}} - P_{\text{Cu}}}{P_{\text{g}} + P_{\text{Fe}}}, \tag{5.2.6}$$

where P_{Cu} is the copper losses and P_{Fe} is the iron core losses in the stator. To simplify the efficiency calculation, windage and friction losses are ignored. The core losses for the C-PMVG topology are calculated by the same semi-analytical method as for the PMSGs using (3.2.10). Similarly, the core losses for the ST-PMVG topology are calculated as

$$P_{\text{Fe}} = cf_{\text{e}}^{x}(B_{\text{lt}}^{y}M_{\text{lt}} + B_{\text{ut}}^{y}M_{\text{ut}} + B_{\text{sy}}^{y}M_{\text{sy}} + B_{\text{aux}}^{y}M_{\text{aux}}), \tag{5.2.7}$$

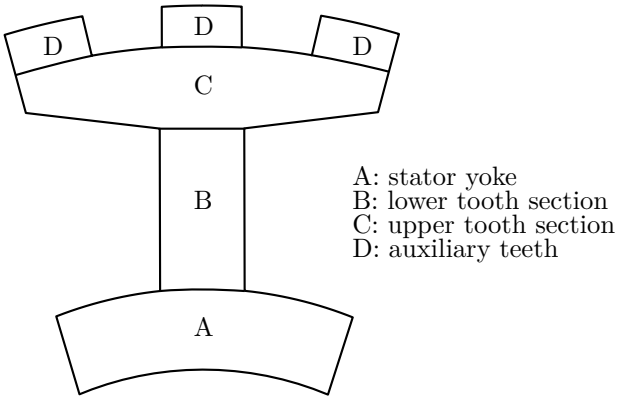

Figure 5.2: ST-PMVG stator area breakdown for core loss calculations.

using Steinmetz coefficients and static FEA. For the split-tooth topology's core loss calculation, the stator is subdivided into the stator-sections shown in Fig. 5.2. The maximum flux densities in the respective sections and their corresponding iron mass are then used in (5.2.7). The core loss calculation is done at the PMVG's electrical frequency f_{e}, at the rated turbine operating speed n_{r}. The Steinmetz coefficients c, x and y are predetermined coefficients.

5.3 Design and Optimisation

Using a multi-objective optimisation approach in the design process is inevitable. The PMVGs need to be designed with the correct reactance to achieve the desired impedance matching with the turbine, while taking the other design objectives and performance constraints into account. In this section the design approach and methodology for the PMVGs is discussed.

5.3.1 Methodology

As with the PMSG design process described in Chapter 4, the population based NSGA-II [86] is used for the design optimisation. The optimisation algorithm is used in conjunction with static 2D FEA that solves the PMVG's performance. The design and optimisation flow diagram is illustrated in Fig. 5.3.

In Fig. 5.3, the PMVG topology and search space are first initialised. The static FEA solver then takes the relevant machine dimensions as an input vector to solve and to calculate the PMVG's performance. The optimisation process then repeats itself as described in Chapter 4.5.1, with the NSGA-II algorithm creating a Pareto front from a diverse set of non-dominated solutions that satisfy the specified constraints and converge near a true Pareto-optimal set. After the optimisation results have converged, the optimum solution can be selected directly from the Pareto front by evaluating the trade-off between the objectives.

This design optimisation process is done for each of the respective PMVG topologies and combinations. Thereafter, a thorough evaluation of each PMVG is done for comparison, and the selected PMVGs' performance are verified using 3D FEA solutions.

5.3.2 Multi-objective Function and Constraints

The multi-objective function for the PMVG design optimisation, is given by

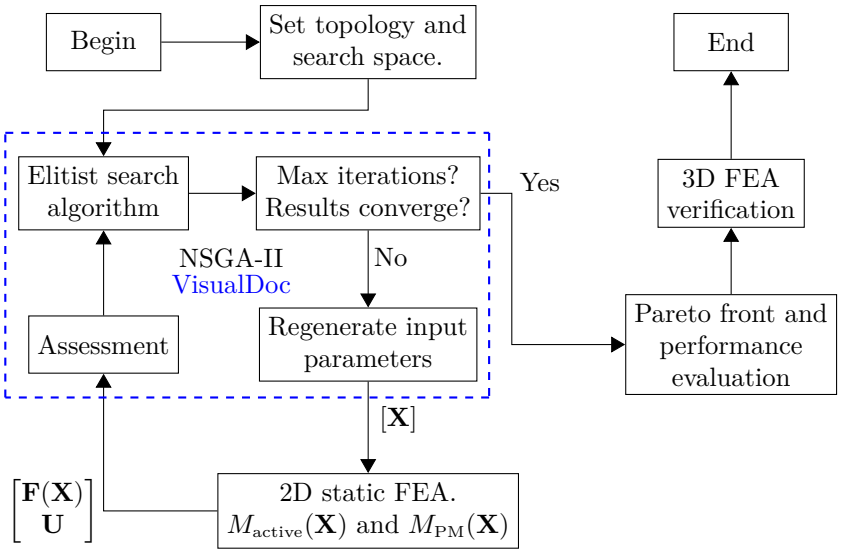

Figure 5.3: Design and optimisation flow diagram.

$$\min_{\mathbf{X}_n} \mathbf{F}(\mathbf{X}_n) = \min_{\mathbf{X}_n} \begin{bmatrix} M_{\text{active}}(\mathbf{X}_n) \\ M_{\text{PM}}(\mathbf{X}_n) \end{bmatrix}. \tag{5.3.1}$$

The objectives in (5.3.1) are once more to minimise the PMVG's active mass, M_{active}, and PM mass, M_{PM}. The active mass is calculated as in (4.5.2) by also taking the overlapping or non-overlapping end-winding mass into account.

The PMVGs in the design optimisation are subject to the performance constraints at the rated operating point, given by

$$\mathbf{U} = \begin{bmatrix} P_{\text{g}} \\ \eta \\ J_{\text{rms}} \end{bmatrix} = \begin{bmatrix} 4.2 \text{ kW} \\ \geq 90\% \\ \leq 5 \text{ A/mm}^2 \end{bmatrix}. \tag{5.3.2}$$

In (5.3.2), P_{g} is the rated power, η is the generator efficiency and J_{rms} is the maximum allowed RMS current density. The constraint imposed on P_{g}, is to guarantee that the desired power matching between the generator and the wind turbine is achieved. In the multi-objective function of (4.5.1), for the PMSG design, and in the initial paper on PMVGs published by the author [96], an "impedance error" is added to the multi-objective function in (5.3.1) to minimise and to ensure that the desired power matching is achieved. However, it was found in [96] that for PMVGs this is not necessary and that the constraint on P_{g} is sufficient, unlike for PMSGs. The generator efficiency in (5.3.2) is calculated using (5.2.6). The constraint on J_{rms} is imposed as a thermal constraint and is a typical value for small-scale machines of this power rating [78].

5.3.3 Parameterised Geometry

The dimensional vector $\mathbf{X}_n$ in (5.3.1), is the input vector generated by the NSGA-II algorithm in Fig. 5.3. The input vector, $\mathbf{X}_n$, is then either defined as

$$\mathbf{X}_1 = \begin{bmatrix} d_{\text{o}} & h_{\text{ry}} & h_{\text{m}} & \theta_{\text{m}} & b_{\text{o}} & h_{\text{hs}} & h_{\text{s}} & b_{\text{s}} & h_{\text{sy}} & l_{\text{Fe}} \end{bmatrix}^{\text{T}} \tag{5.3.3}$$

or

$$\mathbf{X}_2 = \begin{bmatrix} d_{\text{o}} & h_{\text{ry}} & h_{\text{m}} & \theta_{\text{m}} & w_{\text{at}} & w_{\text{st}} & \alpha_1 & \alpha_2 & \alpha_3 & h_{\text{s}} & h_{\text{sy}} & l_{\text{Fe}} \end{bmatrix}^{\text{T}}, \tag{5.3.4}$$

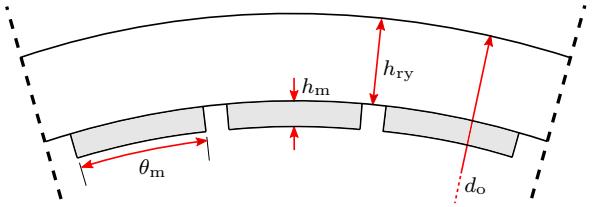

(a) Surface mount PM rotor

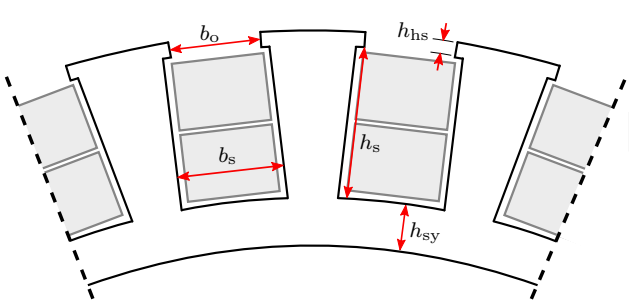

(b) Stator with semi-closed slots

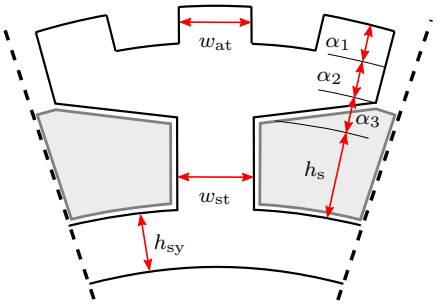

(c) Split-tooth stator

Figure 5.4: PMVG structural dimensions.

where the subscript n denotes the PMVG topology. The geometric variables in (5.3.3) and (5.3.4), are defined in Fig. 5.4, and l_{Fe} is the axial stack length. To maintain a realistic optimisation search space, parameterised geometry is used and four geometric boundaries are imposed: the outer diameter is limited to that of the wind turbine's nacelle, with $d_o < 400$ mm; to maintain structural integrity, the rotor- and stator yoke heights have to be $h_{ry}, h_{sy} > 6$ mm; as a precaution for demagnetisation and for manufacturing ease (brittle PMs) the minimum allowed PM height is $h_m > 3$ mm. For all of the PMVG solutions the height of the mechanical air gap is kept constant at $g_{air} = 1$ mm.

5.4 Design Results and Evaluation

In the following subsections, the optimisation results are evaluated to determine the optimum PMVG design.

5.4.1 Pareto Front Results

The Pareto front solutions for the respective PMVGs with different magnetic gearing ratios, are given in Fig. 5.5. The Pareto fronts in Fig. 5.5 give valuable insight in terms of M_{active} and M_{PM}, showing the trade-off in these objectives between the PMVGs with different magnetic gearing ratios. The performance results of five selected PMVGs, that are indicated in Fig. 5.5, are summarised in Table 5.2. These generators were selected for each case near the optimal trade-off between M_{active} and M_{PM}. In terms of the objectives in (5.3.1), it is shown in Fig. 5.5 that for both the C-PMVGs and the ST-PMVGs, M_{active} and M_{PM} is considerably lower as the magnetic gearing ratio of the machine decreases. It is unexpected that the PMVGs with a lower G_r would do better in this regard. However, a similar trend for PMVGs with a higher number of stator pole pairs, p_s, is found in [55] and [97].

Only considering the C-PMVG results in Fig. 5.5: On average the $G_r = 8$ PMVG uses approximately 20% more PM material than the $G_r = 5$ PMVG. For the $G_r = 11$ PMVG

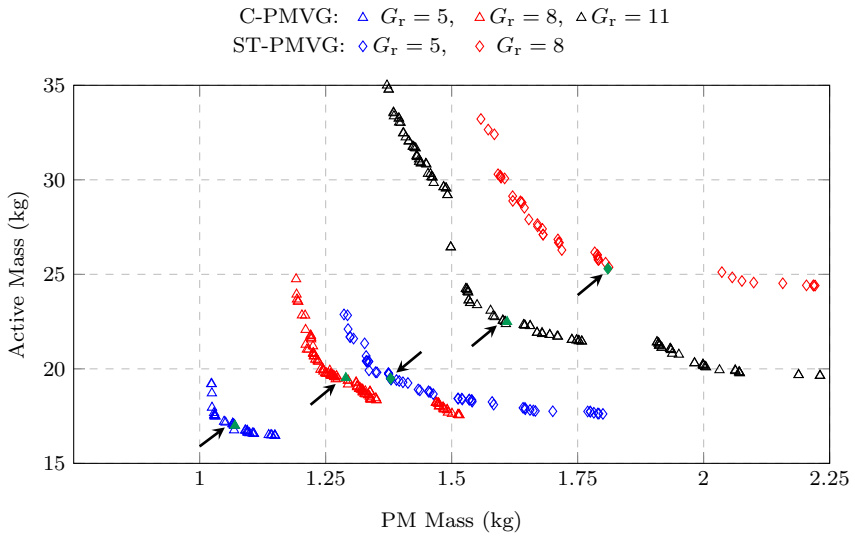

Figure 5.5: Pareto front results for the respective topologies and gearing ratios.

Table 5.2: Comparison of selected front solutions.

C-PMVG	$G_r = 5$	$G_r = 8$	$G_r = 11$
p_s	5	3	2
Q_s	30	27	24
p_r	25	24	22
M_{PM} (kg)	1.07	1.29	1.61
M_{active} (kg)	17.00	19.52	22.49
P_g (kW)	4.10	4.14	4.10
η (%)	90.7	91.8	93.5
J_{rms} (A/mm^2)	4.85	4.88	3.98
d_o (mm)	336	314	276
l_{Fe} (mm)	61	82	109

ST-PMVG	$G_r = 5$	$G_r = 8$	$G_r = 11$
p_s	5	3	-
p_{fm}	30	27	-
p_r	25	24	-
M_{PM} (kg)	1.38	1.81	-
M_{active} (kg)	19.48	25.38	-
P_g (kW)	4.09	4.09	-
η (%)	93.4	94.0	-
J_{rms} (A/mm^2)	4.92	4.97	-
d_o (mm)	360	343	-
l_{Fe} (mm)	76	92	-

it is approximately 50% more PM material. In terms of active mass, M_{active} increases by approximately 17% with the same trend. This increase in M_{active} and M_{PM}, for the PMVGs in Table 5.2, is also shown in Fig. 5.6. The same trend can also be observed in Fig. 5.5 and Fig. 5.6 for the ST-PMVG topology. In comparing the C-PMVG topology with the ST-PMVG topology: it is shown that opting for the ST-PMVG topology results in a larger M_{active} and M_{PM} for the same G_r. Hence, the C-PMVG topology is clearly the

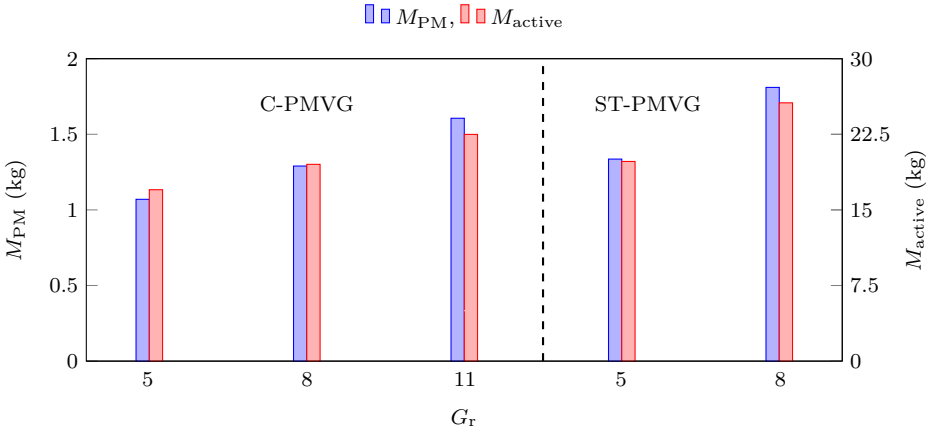

Figure 5.6: Visual comparison of M_{active} and M_{PM} for the PMVGs in Table 5.2.

better generator choice in terms of the design optimisation objectives.

All of the Pareto front results in Fig. 5.5 did converge. However, for the C-PMVG with $G_r = 11$ and the ST-PMVGs with $G_r = 5$ and $G_r = 8$, the limiting factor is the power constraint at the rated operating point, P_g in (5.3.2). The aforementioned PMVGs, especially the ST-PMVGs, are more prone to excessive leakage flux and subsequently a larger synchronous reactance. Although a large generator reactance is required for this application, as explained in Chapter 1.3.2, NSGA-II's elitist search algorithm struggles to find solutions that adhere to the P_g design constraint. For the $G_r = 11$ C-PMVG, neither of the other constraints are close to their allowed maximum or minimum, as shown in Table 5.2, and is the case for all other solutions in Fig. 5.5. The optimisation algorithm therefore increases generator size, to increase P_g. Also resulting in a larger η and a lower J_{rms} than the imposed constraints.

5.4.2 Power Matching

To show that the PMVGs achieve the desired power matching, the respective operating power curves for the PMVGs in Table 5.2 are plotted against the wind turbine power versus speed curves in Fig. 5.7. It is shown in Fig. 5.7 that the PMVGs achieve good power matching with the wind turbine at low wind speeds, which is essential for this application, and match with the turbine at the rated operating speed n_r.

The overall performance and power matching results are desirable. The power of the PMVGs match *naturally* with the near-to-maximum power of the wind turbine, i.e. no method of external impedance matching is necessary. The latter is a potential advantage over the conventional PMSGs in Chapter 4.

5.4.3 Torque Quality

Low generator cogging torque is essential for small-scale wind turbines since the wind turbine has to overcome this to start generating power. The cogging torque, ΔT_{cog}, and torque ripple, ΔT_r, results for the respective PMVGs in Table 5.2 are summarised in Table 5.3. The FE predicted cogging torque of the respective PMVGs are also shown for the mechanical rotation of one rotor pole pair (360 electrical degrees) in Fig. 5.8.

The extremely low cogging torque results for the $G_r = 8$ C-PMVG in Table 5.3 is ideal. The PMVG has almost zero cogging torque and negligible torque ripple at the

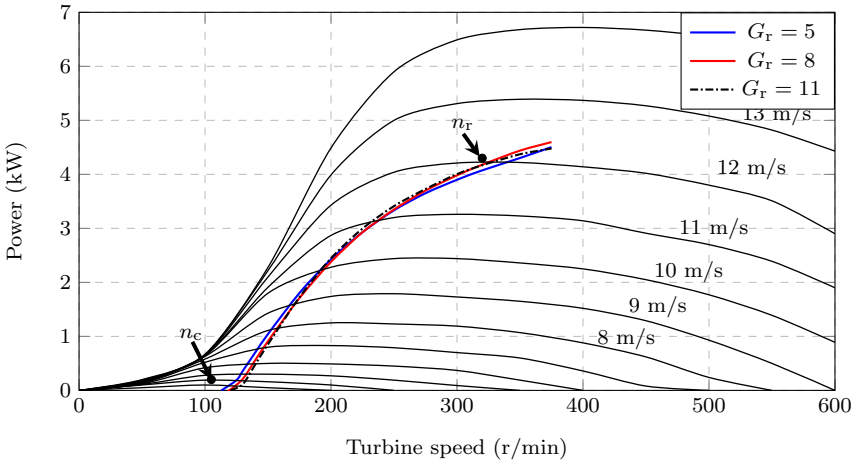

(a) C-PMVG

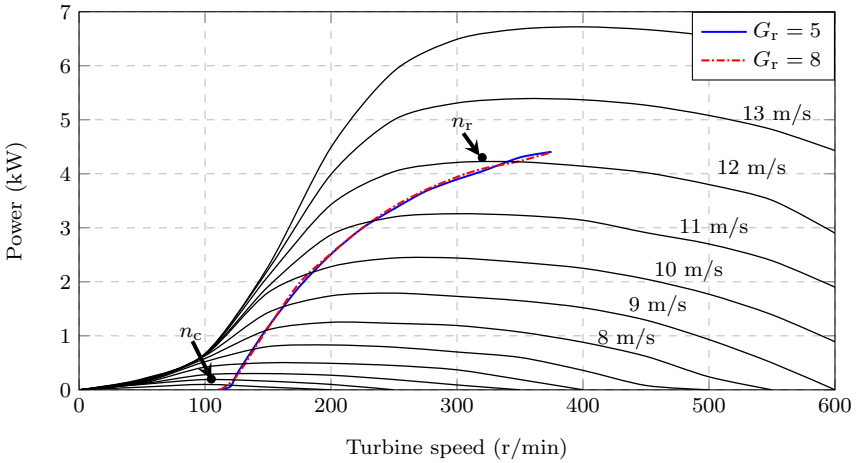

(b) ST-PMVG

Figure 5.7: Power curves of the selected PMVGs in Table 5.2.

Table 5.3: Torque quality comparison.

C-PMVG	$G_r = 5$	$G_r = 8$	$G_r = 11$
ΔT_{cog} (%)	8.94	1.1	0.7
ΔT_r (%)	30.1	1.3	1.4
ST-PMVG	$G_r = 5$	$G_r = 8$	$G_r = 11$
ΔT_{cog} (%)	26.4	2.9	-
ΔT_r (%)	29.3	3.9	-
LCM(Q_s,$2p_r$)	120	432	264

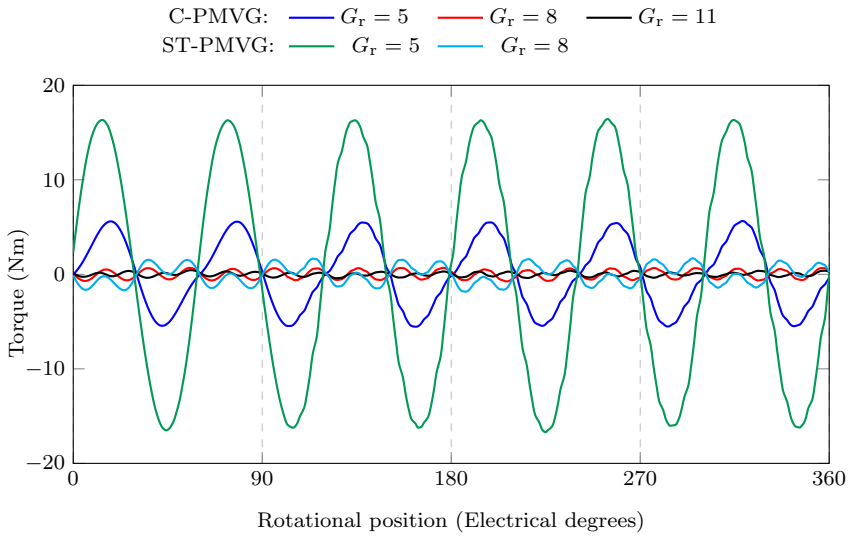

Figure 5.8: FE predicted cogging torque, ΔT_{cog}.

rated operating point. These results are attractive, because no special design steps were taken to minimise the PMVG's cogging torque. On the other hand, the cogging torque and torque ripple results for the C-PMVG and ST-PMVG with $G_r = 5$, indicate that they are unsuited for this application. The high cogging torque for the PMVGs with $G_r = 5$ correlates with that which is theoretically expected, because of the relatively small least common multiple (LCM) between the stator slots, Q_s, and the PM rotor poles, $2p_r$. The LCM values for the respective PMVGs are indicated in Table 5.3.

The torque quality results for the $G_r = 11$ C-PMVG in Table 5.3 are also very attractive, however, not all of the Pareto front solutions in Fig. 5.5 have a low cogging torque. In some cases the cogging torque can be as high as 5%. For the ST-PMVG with $G_r = 8$, the cogging torque is also still reasonably low and can even be further reduced in the design process. However, in terms of mass, the results in Fig. 5.5 show that these PMVGs are not an option. The C-PMVG with $G_r = 8$ is just superior in terms of M_{active} and M_{PM} and inherently has near ideal torque quality, which is important for this application.

Since some of the PMVGs in Table 5.3 have such undesired ΔT_{cog} values, and because cogging torque is such an important design aspect for small-scale wind generators, a cogging torque minimisation technique was also investigated and is presented in Appendix D.

5.4.4 2D FEA versus 3D FEA

All of the designs in the optimisation were done with 2D static FEA. To verify the design results, the selected PMVGs in Table 5.2 are also solved with 3D FEA models. Partial 3D FEA models for the C-PMVG with $G_r = 8$ and the ST-PMVG with $G_r = 5$, are shown in Fig. 5.9(a) and (b) respectively. The generated torque and generator efficiency results at the rated operating point, n_r, are summarised and compared in Table 5.4. Also compared in Table 5.4, are the PMVGs' per unit reactance values calculated with 2D and 3D FEA. The results show very good correlation between the 2D and 3D FEA solutions and verify that the obtained results are accurate. More specifically, the comparison in Table 5.4 indicates that the end-winding calculations and the accounting for end-effects, done in the 2D FEA, are sufficient.

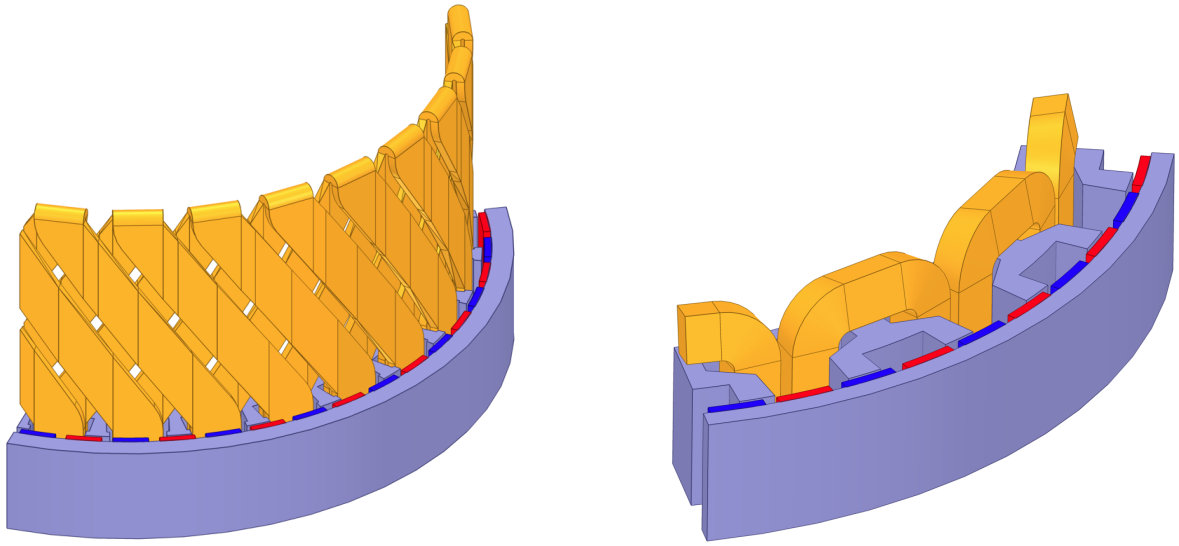

(a) C-PMVG, $G_r = 8$ **(b)** ST-PMVG, $G_r = 5$

Figure 5.9: Partial 3D FEA models for some of the PMVGs in Table 5.2.

Table 5.4: 2D versus 3D FEA comparison at n_r.

C-PMVG	$G_r = 5$		$G_r = 8$		$G_r = 11$	
	2D	3D	2D	3D	2D	3D
T_g (Nm)	122.2	123.3	123.6	122.0	122.5	117.0
η (%)	90.7	90.6	91.8	91.9	93.5	93.2
X_s (pu)	2.09	2.09	2.04	1.92	2.06	1.94

ST-PMVG	$G_r = 5$		$G_r = 8$		$G_r = 11$	
	2D	3D	2D	3D	2D	3D
T_g (Nm)	122.1	129.1	122.2	118.5	-	-
η (%)	93.4	93.5	94.0	93.5	-	-
X_s (pu)	2.22	2.45	2.17	2.30	-	-

5.4.5 Cut-in Speed Evaluation and PMVG Selection

In addition to the evaluation done in the previous subsections, the PMVGs in Table 5.2 are also evaluated at cut-in speed. For the passive system to start generating power, the wind generator needs to overcome the core losses up to n_c. The 2D and 3D FEA calculated core losses at the no-load cut-in speed, n_c, are given in Fig. 5.10. The 2D and 3D FEA results show good correlation and P_{Fe} at n_c is deemed sufficiently low; limiting the maximum allowed electrical frequency in Table 5.1, for machine selection, is shown to be an effective method to limit P_{Fe} up to n_c. Also shown in Fig. 5.10 are the respective PMVGs' cogging torque results from Table 5.3.

It is evident from the results presented in Fig. 5.10 and in the previous subsections that the $G_r = 8$ C-PMVG in Table 5.2 is the optimum PMVG for this application. This PMVG is superior in terms of torque quality, meets all of the desired power matching- and design constraints, and is competitive in terms of M_{active} and M_{PM}.

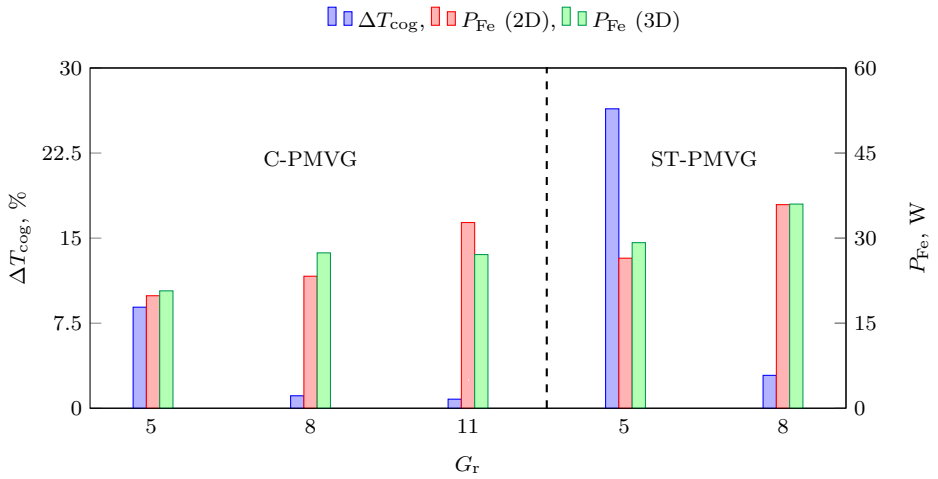

Figure 5.10: Comparison of cogging torque and core losses at n_c.

5.5 Optimum PMVG Demagnitisation Analysis

As in Chapter 4, the risk of irreversible demagnetisation is an important aspect that needs to be evaluated for the PMVGs. Only the $G_r = 8$ PMVG is investigated, since this is the optimum PMVG wind generator choice for this application. It is evident from the power matching results in Fig. 5.7 that the power in the passive system is limited independent of wind speed. Therefore, demagnetisation is investigated at the rated turbine speed of 320 r/min, with the PMVG operating at full load.

To evaluate whether demagnetisation will occur, various cases are investigated for two different NdFeB magnet grades, namely N48 and N48H. It is shown in Fig. 5.11(a) and (b), that when using N48 grade PMs, demagnetisation will start occurring at a magnet temperature of 60°C. However, the temperature of the magnets during operation are not expected to exceed 50°C. Nonetheless, it is shown in Fig. 5.11 that the risk of demagnetisation can be nullified by using N48H grade PMs, where demagnetisation will only occur at a magnet temperature > 100°C.

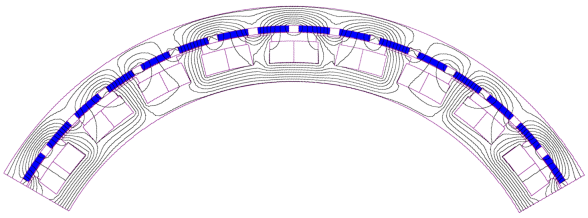

(a) N48, 40°C PM temperature.

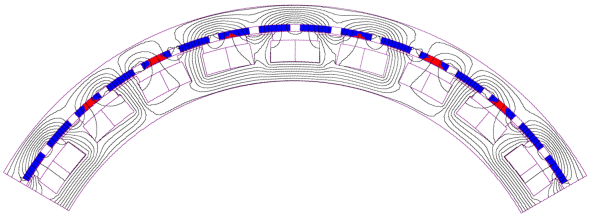

(b) N48, 60°C PM temperature.

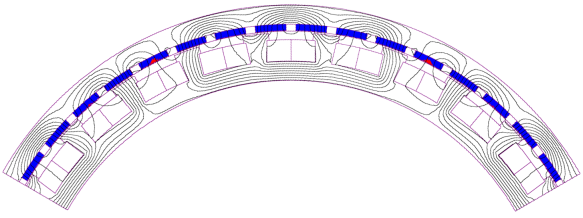

(c) N48H, 100°C PM temperature.

Figure 5.11: Demagnetisation prediction of the $G_r = 8$ C-PMVG at rated conditions, $n_r = 320$ r/min and full load, using NdFeB N48 and N48H.

5.6 Prototype and Experimental Validation

The manufactured prototype of the $G_r = 8$ C-PMVG in Table 5.2, is shown in Fig. 5.12. Although the C-PMVG designs in Section 5.4 had double layer top-bottom (vertical coil) winding layouts, the prototype in Fig. 5.12 has a double layer side-by-side (horizontal coil) winding layout. This was changed to make the manufacturing of the prototype easier. This is accounted for in the experimental validation done in this section. Altogether, the effect thereof on the performance is negligible and the designs in Section 5.4 are still valid.

The experimental setup on the test bench is shown in Fig. 5.13. In Fig. 5.13, the PMVG prototype is mechanically connected to a geared induction motor drive that emulates the wind turbine. The torque sensor in Fig. 5.13 is used to measure the input power. The PMVG-prototype is electrically connected to the battery bank via a diode bridge rectifier and a resistance equivalent to that of the brush-slip-rings.

5.6.1 Power Matching Measurements

The measured results for the PMVG prototype's generated power, P_g, and output power, P_{out}, are shown in Fig. 5.14. It is shown that the power measurements are lower than what were designed for. The following explanation accounts for the measured results in Fig. 5.14:

The manufacturer of the prototype's PMs could only guarantee certain dimensional tolerances on the PMs. Initially, these tolerances were considered insignificant (as was the case for the PMSG prototype in Chapter 4.7). However, Fig. 5.15 shows that the PMVG's performance is very sensitive to these manufacturing tolerances, i.e. the magnet height h_m and the magnet pitch to pole pitch ratio σ_m. It is shown in Fig. 5.15, that the PMVG's generated torque is particularly sensitive to h_m, seeing as a smaller h_m also results in a larger air gap. Attempts to measure the heights of the PMs showed that the average PM height is $h_m \approx 2.9$ mm, with the lowest being measured at $h_m = 2.85$ mm.

It is shown in Fig. 5.14, that if h_m is adjusted in the FEA accordingly, that the measured power matching correlates with the FEA predicted power matching. The measured and FEA results are also summarised in Table 5.5. The FEA results where $h_m = 3$ mm

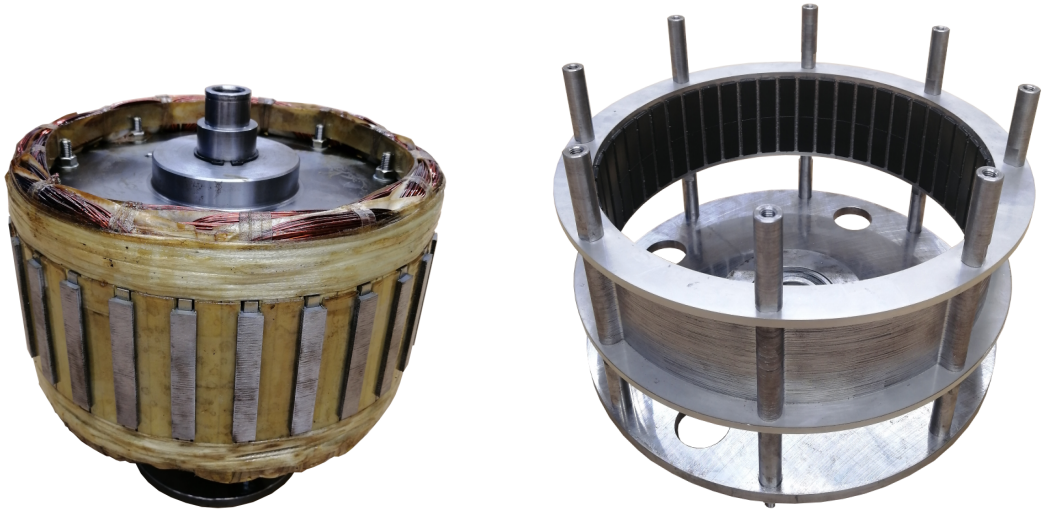

(a) Stator **(b)** PM rotor

Figure 5.12: Manufactured $G_r = 8$ C-PMVG prototype.

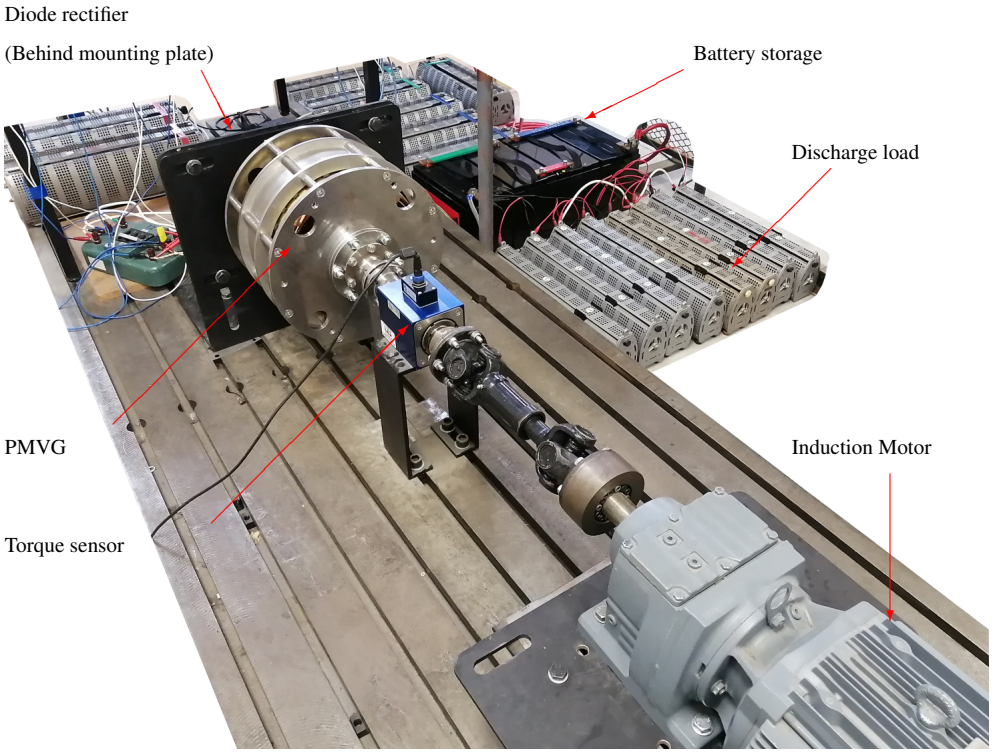

Figure 5.13: Experimental setup with PMVG prototype.

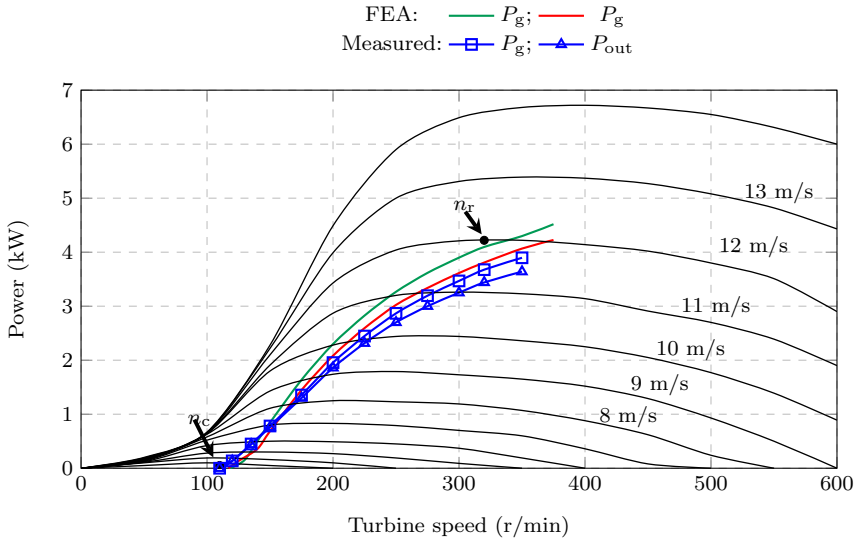

Figure 5.14: Measured power matching results of the PMVG prototype.

and 2.9 mm are both included in Table 5.5. The error between the measured and FEA predicted P_g in Table 5.5 is less than 4%.

The measured current and voltage waveforms are shown in Fig. 5.17. The current waveform in Fig. 5.17 shows to be sinusoidal, and also correctly 30 deg out of phase with the fundamental line voltage, i.e. the PMVG is operating at a unity displacement power factor. An additional experimental measurement, where the PMVG was run at near-maximum power for more than an hour until steady-state temperature is reached, was conducted to measure the PM temperature. The temperature measurement taken with the heat gun is shown in Fig. 5.18. The maximum measured PM temperature afterwards did not exceed 40°C, which also confirms that the PMVG is at low risk of demagnetisation.

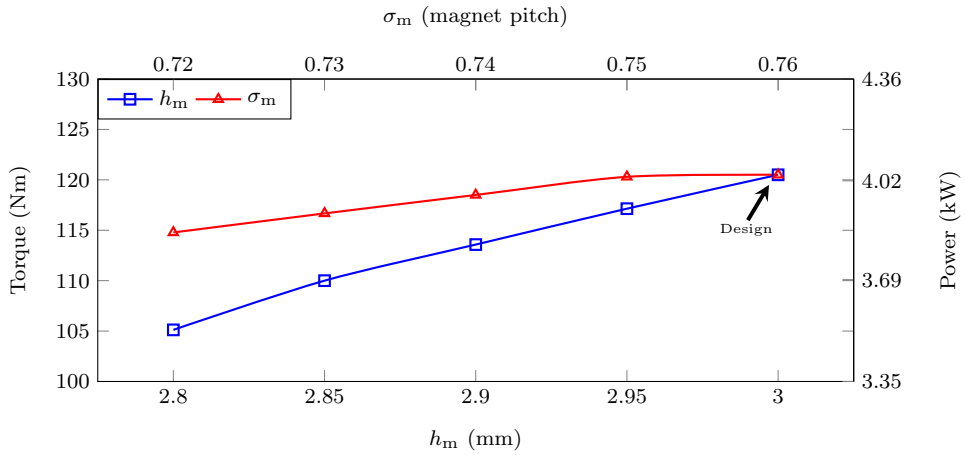

Figure 5.15: Effect of PM manufacturing tolerances on the generated torque and power at $n_r = 320$ r/min.

(a) $h_m = 2.85$ mm **(b)** $h_m = 2.9$ mm **(c)** $\sigma_m \approx 0.76$

Figure 5.16: Measuring of PM dimensions.

Table 5.5: Summary of C-PMVG prototype measurements.

	FEA		**Measured**
Parameters			
- PM height, h_m (mm)	3.0	2.9	2.9
- Phase resistance, R_s (Ω)	0.068	0.068	0.072
- Synchronous inductance, L_s (mH)	1.62	1.63	1.77
Performance at $n_r = 320$ r/min			
- P_g (kW)	4.04	3.83	3.68
- η (%)	92.8	93.0	91.5
- E_g (V)	59.6	57.9	58.1
Cogging torque			
- ΔT_{cog} (Nm)	1.14	1.14	1.80

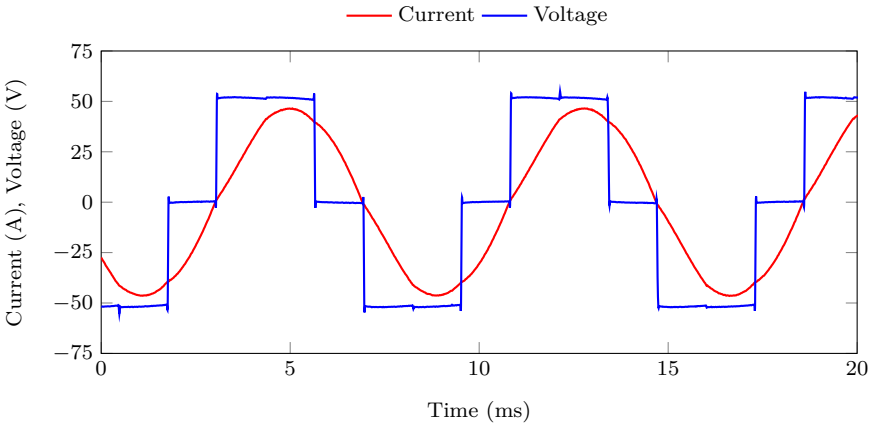

Figure 5.17: Measured phase current and line voltage at $n_r = 320$ r/min, showing operation at a unity displacement power factor.

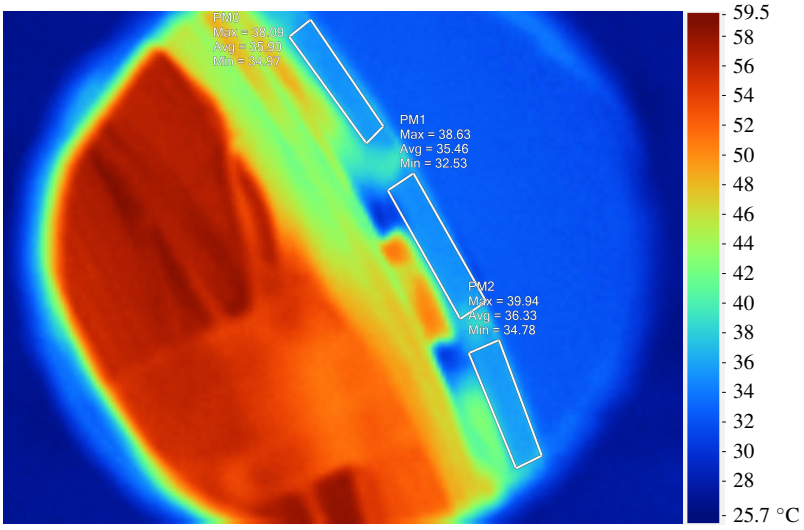

Figure 5.18: Steady-state PM temperature measurement.

5.6.2 No-load and Short Circuit Measurements

The no-load open circuit voltage measurements are shown in Figs. 5.19 and 5.20. The values for the measured no-load open circuit voltage at $n_r = 320$ r/min are also summarised in Table 5.5. The measured versus FEA results in Fig. 5.20 show good correlation. Furthermore, the FEA results with $h_m = 2.9$ mm, compared to the measured voltage, support the results in the previous subsection and confirms the effect of the manufacturing tolerance on h_m.

The measured no-load rotational losses are also plotted in Fig. 5.21, and are compared to the no-load 2D FEA predicted iron losses P_{Fe}. The measured and FEA predicted results in Fig. 5.21 show a good comparison. The difference can be attributed to windage and friction losses, that were not accounted for in the design process.

The internal synchronous inductance of the PMVG prototype is measured by means of a number of short circuit tests to get an average value. The measured L_s is given in Table 5.5 and is shown to be very close to the FEA calculated value.

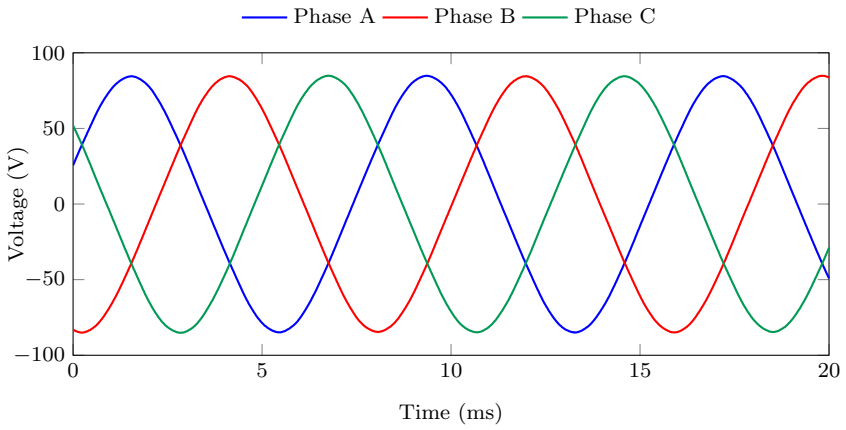

Figure 5.19: Measured no-load open circuit voltage at $n_r = 320$ r/min.

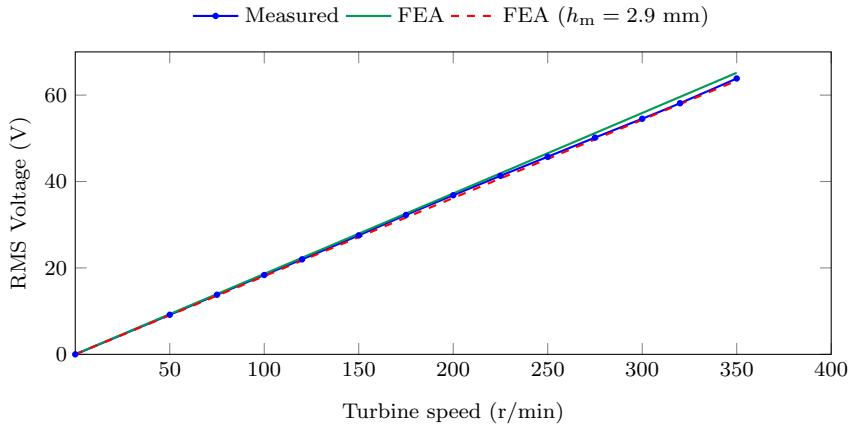

Figure 5.20: Measured open circuit voltage versus FEA calculated voltage.

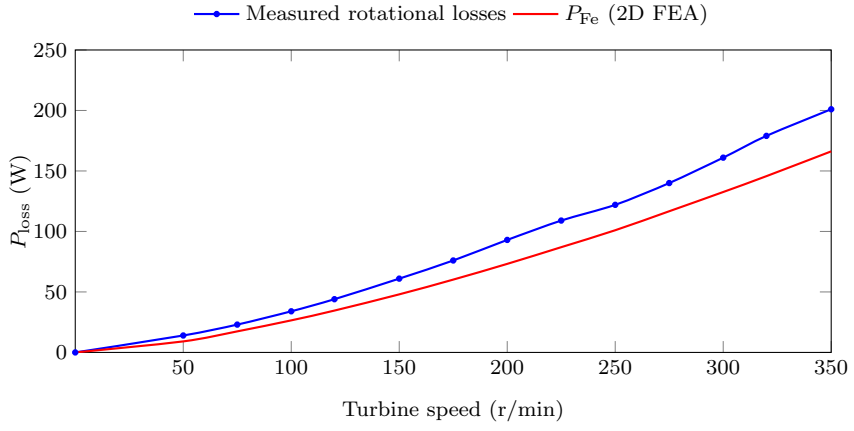

Figure 5.21: Measured no-load open circuit losses versus no-load FEA calculated iron losses.

5.6.3 Cogging Torque

The experimental setup to measure the PMVG's cogging torque is shown in Fig. 5.22. In Fig. 5.22, the PMVG is now disconnected from the induction motor and connected to a torque beam via the torque sensor. This setup is the same as shown in the schematic in Fig. 4.22, and the same method is used for measuring the cogging torque. The PMVG's rotor position is varied by adjusting the angle of the torque beam. Torque measurements are then taken at discrete angular displacements over one pole pair (360 electrical degrees).

The measured cogging torque results are shown in Fig. 5.23 and ΔT_{cog} is given in Table 5.5. As explained in Chapter 4.7.3, taking precise cogging torque measurements is difficult given the sensitivity of the measurement and the available equipment. Nonetheless, the peak to peak cogging torque values in Table 5.5 confirms that the PMVG has a very low cogging torque. Furthermore, the measured cogging torque in Fig. 5.23 is close to the FEA predicted cogging torque. Note that the slight "disturbance" measured in

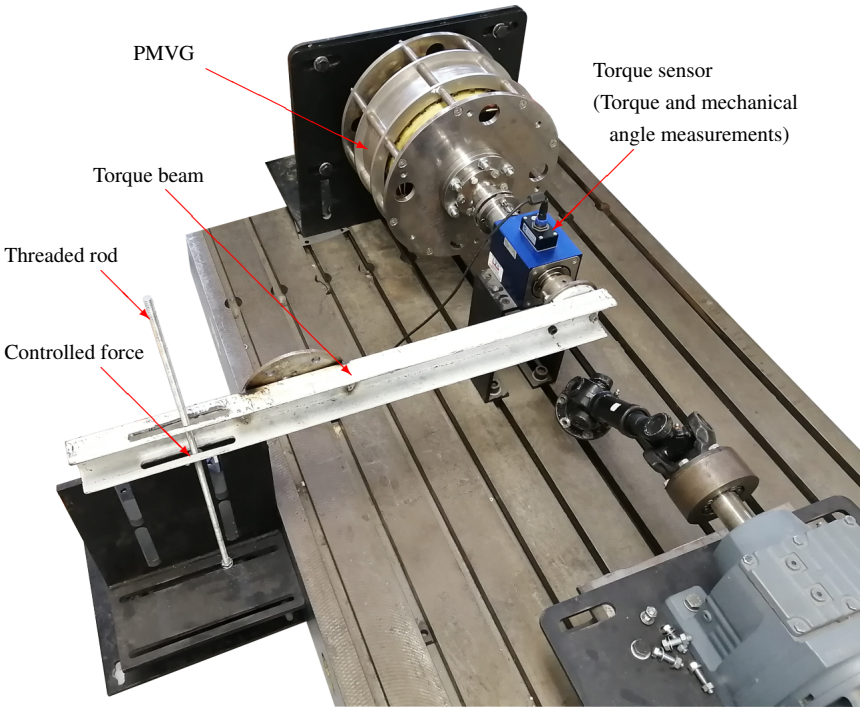

Figure 5.22: Experimental setup for cogging torque measurements.

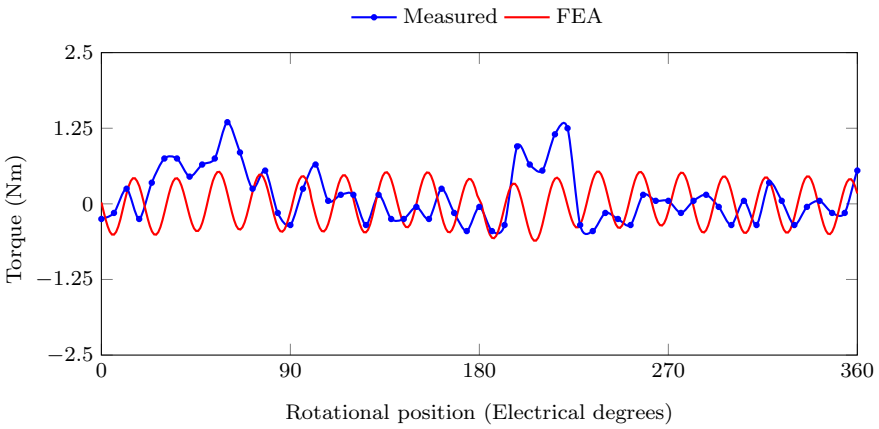

Figure 5.23: FEA calculated- and measured cogging torque versus the mechanical rotation of one pole pair (360 electrical degrees).

Fig. 5.23 repeats every 180 electrical degrees, as was the case in Chapter 4.7.3 for the PMSG prototype's cogging torque measurement. Thus, indicating that the disturbance might be in the experimental setup.

5.7 Chapter Summary

In this chapter the design of a PMVG for a small-scale uncontrolled passive wind generator system is done. Since this is an unknown application for PMVGs, a comprehensive design of different conventional and split-tooth vernier generators are done. The PMVG designs are then compared by evaluating various performance aspects that are critical to this application. Ultimately, an optimum generator design is determined. The following main conclusions are drawn:

- It is shown that PMVGs are excellently suited for passive wind generator systems. The inherently high internal reactance of PMVGs, which is typically considered to be its main drawback, is found to be advantageous for this application. As a result, all of the PMVG designs, that are uncontrolled and operate at a unity displacement power factor, naturally achieve the desired power matching with the wind turbine.
- In terms of the optimal topology, it is found that conventional PMVGs with overlapping windings are superior to split-tooth PMVGs. Furthermore, careful consideration should be taken for the PMVG selection; it is shown that PMVGs with certain gear ratios are unsuited for this application. The PMVG with $G_r = 8$ is a very attractive generator choice. This PMVG has excellent power matching and performance results, and near ideal torque quality. Furthermore, the $G_r = 8$ C-PMVG design is competitive in terms of active mass and the amount of PM material used.
- For validation purposes, a prototype of the $G_r = 8$ C-PMVG was constructed and successfully tested. Although there were manufacturing tolerances that affected the PMVG prototype's performance, the test results conclude that the FEA results presented in the chapter are valid. Furthermore, the experimental results confirm that PMVGs are an excellent generator choice for this application.

Chapter 6

Small-scale Power Level Evaluation

A noteworthy observation from literature is that the passive wind energy systems are mostly rated for < 1.5 kW in [17–21], and are rated at a sub 5 kW power level in [22] and [23]. Therefore, a 15 kW uncontrolled passive wind energy system is investigated in this chapter. The aim is thus to answer the research sub-question:

5. How does the uncontrolled passive system compare at different power levels in the small-scale power region?

Furthermore, up until this point the effect that the resistance R_c has on the passive wind energy system has not been discussed in detail. With R_c being the combined resistance of the brush-slip-rings in the nacelle and the transmission cable, shown as Z_c in Fig. 6.1. The resistance R_c is taken into account in Chapters 3, 4 and 5 as part of the total per phase equivalent resistance as in (3.1.17). However, in this chapter the effect that R_c has on the power matching and system performance is analysed in detail.

6.1 15 kW Wind Generator Design

For the 15 kW wind generator design, it is assumed that the results in Chapters 4 and 5 are well founded and that the same topology NO-PMSG and C-PMVG will be the best suited topologies for the 15 kW passive wind energy system. The NO-PMSG then is a 45-42 slot-pole machine, and has a surface mounted PM rotor and semi-closed stator slots. The C-PMVG has a magnetic gearing ratio of $G_r = 8$, with $p_s = 5$, $Q_s = 45$ and $p_r = 40$.

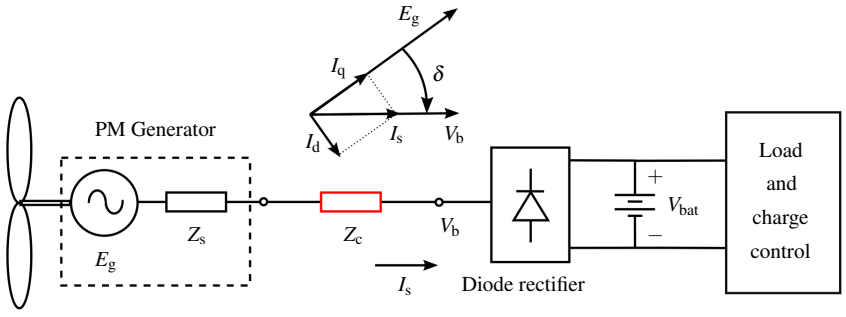

Figure 6.1: Single line diagram of the passive wind generator system highlighting the combined resistance of the brush-slip-rings in the nacelle and the transmission cable.

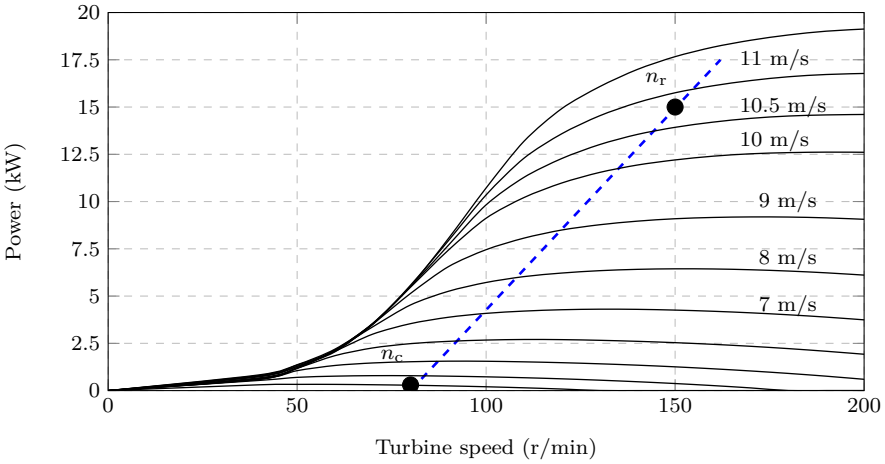

Figure 6.2: Wind turbine power versus speed curves with 15 kW wind generator specifications.

Table 6.1: Summary of specified operating points.

	n_c	n_r
Wind speed	3 m/s	10.8 m/s
Turbine speed	80 r/min	150 r/min
Generated power, P_g	0 kW	15 kW
Battery storage/dc voltage, V_{dc}	220 V	

6.1.1 Specifications

The wind turbine power versus speed curves for the wind turbine shown in Fig. 2.8(b), are shown in Fig. 6.2. Also shown in Fig. 6.2 are the desired operating points for the cut-in speed and at the rated speed. The 15 kW system's specifications are summarised in Table 6.1. The wind generator is connected via the diode bridge rectifier to a 220 V battery storage unit or dc-bus.

6.1.2 Design and Optimisation

The same design optimisation process as in Chapters 3 and 5 are followed for the PMSG and PMVG respectively. The multi-objective functions are

$$\min_{\mathbf{X}_1} \mathbf{F}(\mathbf{X}_1) = \min_{\mathbf{X}_n} \begin{bmatrix} M_{\text{active}}(\mathbf{X}_1) \\ M_{\text{PM}}(\mathbf{X}_1) \\ Z_{\text{ext}}(\mathbf{X}_1) \end{bmatrix} \quad \text{and} \quad \min_{\mathbf{X}_1} \mathbf{F}(\mathbf{X}_1) = \min_{\mathbf{X}_1} \begin{bmatrix} M_{\text{active}}(\mathbf{X}_1) \\ M_{\text{PM}}(\mathbf{X}_1) \end{bmatrix} \tag{6.1.1}$$

for the respective generator technologies. The performance constraints are given by

$$\mathbf{U} = \begin{bmatrix} P_g \\ \eta \\ J_{\text{rms}} \end{bmatrix} = \begin{bmatrix} 15 \text{ kW} \\ \geq 94\% \\ \leq 5 \text{ A/mm}^2 \end{bmatrix}. \tag{6.1.2}$$

Both generators have the same rotor and stator structure. Therefore, the dimensional vector $\mathbf{X}_1$ in (6.1.1) is the same as in (5.3.3), with the dimensions defined in Fig. 5.4. To maintain a realistic optimisation search space, parameterised geometry is used and four geometric boundaries are imposed: the outer diameter is limited to that of the

wind turbine's nacelle, with $d_o < 655$ mm; to maintain structural integrity, the rotor- and stator yoke heights have to be $h_{ry}, h_{sy} > 7$ mm; as a precaution for demagnetisation and for manufacturing ease the minimum allowed PM height is $h_m > 3.5$ mm. For all of the solutions the height of the mechanical air gap is kept constant at $g_{air} = 2$ mm.

6.1.3 Design Results Evaluation

The Pareto front design optimisation results for the PMSG and PMVG are shown in Fig. 6.3. For the PMVG solutions, all of the solutions meet the desired *natural* impedance matching requirement. However, the constraint on P_g is the limiting factor. All of the PMVG Pareto front solutions in Fig. 6.3 converged to η and J_{rms} values that were at a slight offset to their maximum or minimum allowed values. The PMSG solutions where the PMSGs match *naturally* with the wind turbine are also indicated in Fig. 6.3. The PMSG's Pareto front in Fig. 6.3 mimics that of the 4.2 kW Pareto front results in Fig. 4.8, with some of the PMSG solutions requiring external impedance matching.

Two generators are selected from the respective Pareto fronts, as indicated in Fig. 6.3, and their performance results are summarised in Table 6.2. It is shown in Table 6.2 that both wind generators meet the power matching specifications with $P_g \approx 15$ kW at n_r for both. The other performance constraints in (6.1.2) are also met. The PMSG's efficiency is slightly below 94 %, however it is still deemed acceptable. The FEA torque quality

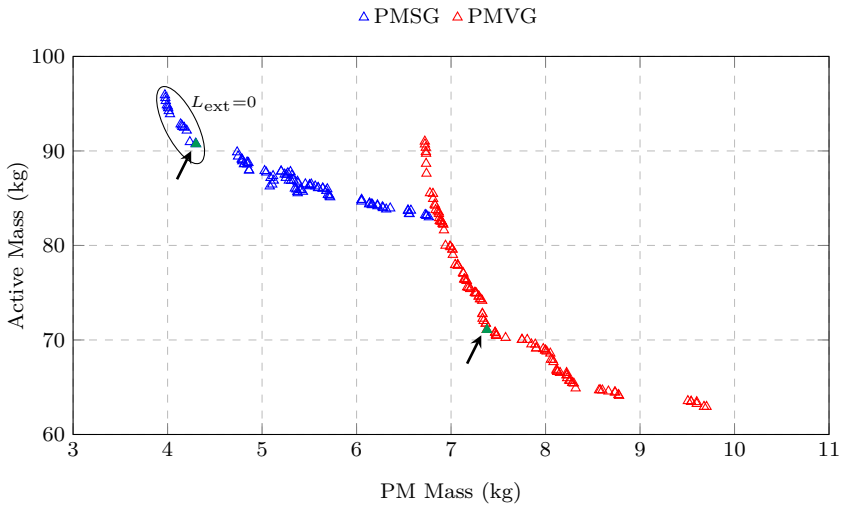

Figure 6.3: Multi-objective optimisation Pareto front results.

Table 6.2: Comparison of selected front solutions.

Generator	PMSG	PMVG
M_{PM} (kg)	4.30	7.38
M_{active} (kg)	90.73	71.08
P_g (kW)	15.17	14.76
η (%)	93.6	96.4
J_{rms} (A/mm^2)	3.9	4.2
d_o (mm)	636	630
l_{Fe} (mm)	88	169
ΔT_{cog} (%)	0.2	0.22
ΔT_r (%)	2.94	0.44

Table 6.3: 2D versus 3D FEA comparison at n_r.

Generator	PMSG		PMVG	
	2D	3D	2D	3D
T_g (Nm)	965.7	994.0	939.4	946.9
η (%)	93.6	93.7	96.0	95.8
P_{Fe} at n_r, (W)	102.4	116.3	165.8	196.7
P_{Fe} at n_c, (W)	75.0	75.4	157.8	131.6

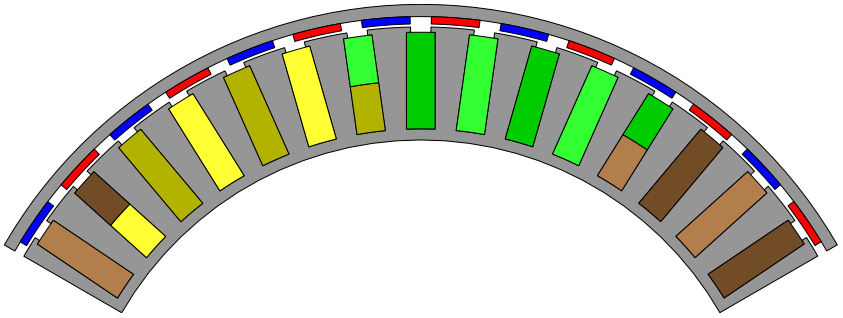

(a) PMSG

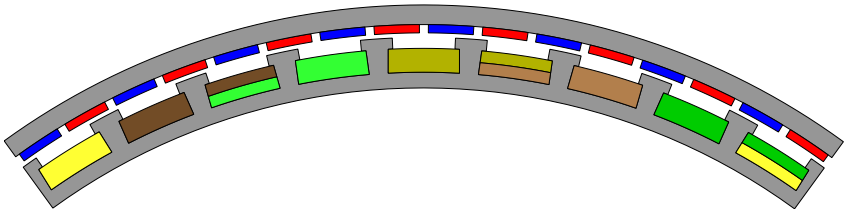

(b) PMVG

Figure 6.4: Partial cross-sections of the 15 kW wind generators (not to scale).

results are also given in Table 6.2. It is shown that both generators have exceptionally low cogging torque ΔT_{cog} and very low torque ripple at rated load ΔT_r. Partial cross-sections of the PMSG and PMVG are shown in Figs. 6.4(a) and (b) respectively.

To validate the 2D FEA designs and optimisation results in Fig. 6.3, both generators in Table 6.2 are also solved using 3D FEA. The 3D FEA results are compared in Table 6.3. It is shown in the comparison that the 2D and 3D FEA results correlate well for both the PMSG and the PMVG. Thereby, validating the respective 15 kW wind generator designs.

6.2 Power Level Comparison

In this section, the system performance of the 4.2 kW and 15 kW passive wind energy systems are compared and evaluated using the optimum designed wind generators in Chapters 4, 5 and Section 6.1.

6.2.1 System Efficiency

Because the passive-yaw wind turbines in Fig. 2.8 have a full degree of yaw-rotation, brush-slip-rings are required for power transmission. The resistance value of these brush-slip-rings is typically between 0.2 Ω and 0.3 Ω.[1] Furthermore, the transmission cable from

[1]These values are from measurements taken on different brush-slip-rings in the laboratory.

the tower to the battery storage will also have a resistance value that depends on the total distance between the two points. This could typically be anything from 50 to 100 m. Therefore, to make the designs in the preceding chapters more realistic, the combined resistance of the brush-slip-rings and transmission cable is estimated as $R_c = 0.3\ \Omega$. This of course results in additional transmission losses to the system that can be calculated as

$$P_{trans} = 3R_c I_{rms}^2, \tag{6.2.1}$$

with the total system efficiency being calculated as

$$\begin{aligned} \eta_{system} &= \eta - \frac{P_{trans}}{P_g + P_{Fe}} \\ &= \frac{P_{bat}}{P_g + P_{Fe}}. \end{aligned} \tag{6.2.2}$$

The power into the battery energy storage or dc-bus, P_{bat}, is shown in Fig. 6.5 for both the 4.2 kW and 15 kW PMSG passive wind energy systems. For reference, the system efficiency versus turbine speed is also shown in Fig. 6.6 for both the PMSGs and

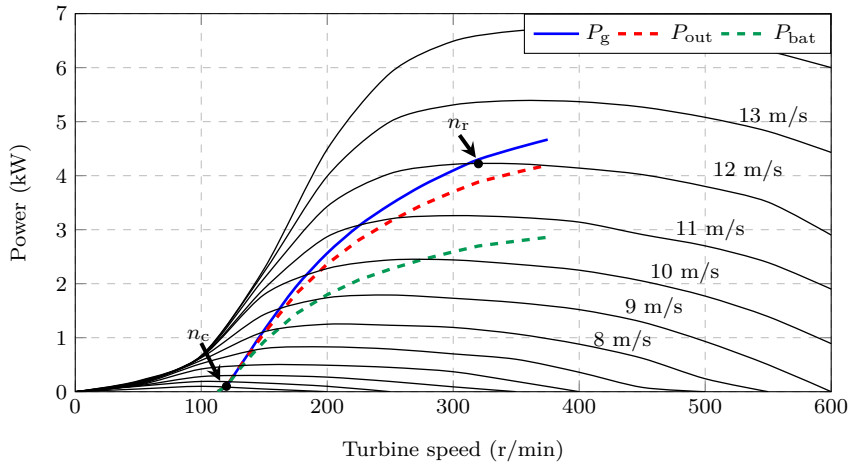

(a) 4.2 kW PMSG

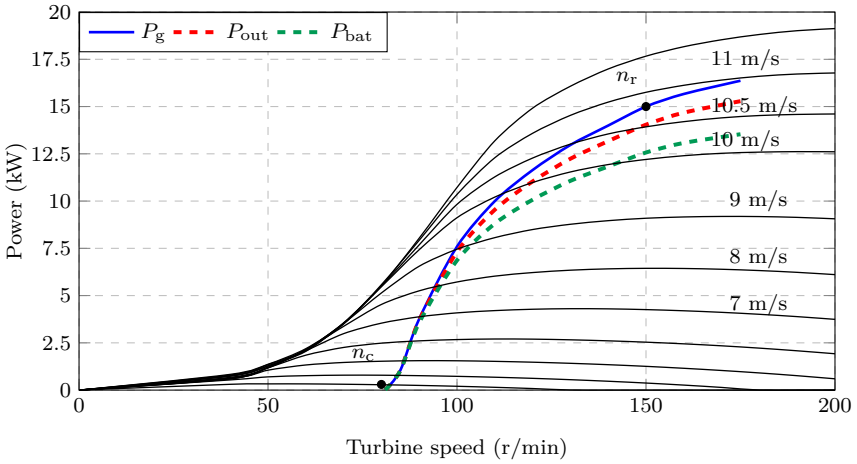

(b) 15 kW PMSG

Figure 6.5: Power matching of the PMSGs at different power levels, showing generator input and output power as well as power delivered to the battery storage.

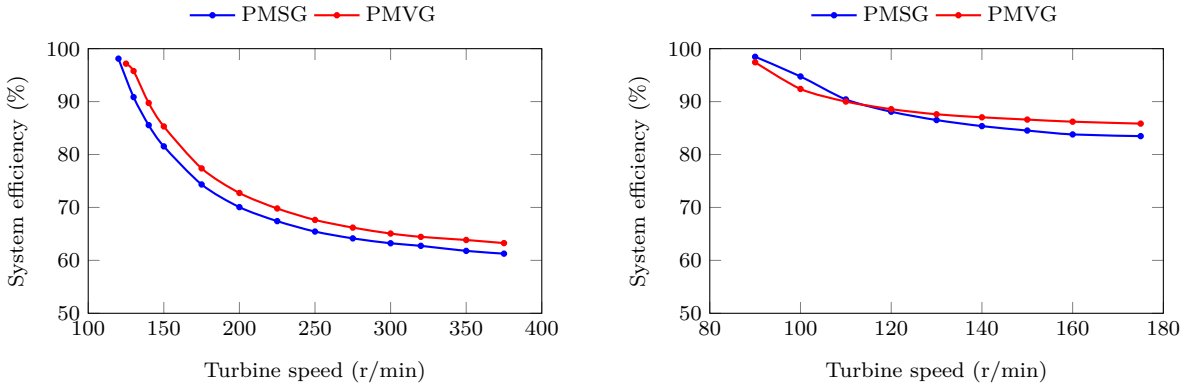

(a) 4.2 kW **(b)** 15 kW

Figure 6.6: System efficiency versus turbine speed at different power levels, with different optimum PM wind generators.

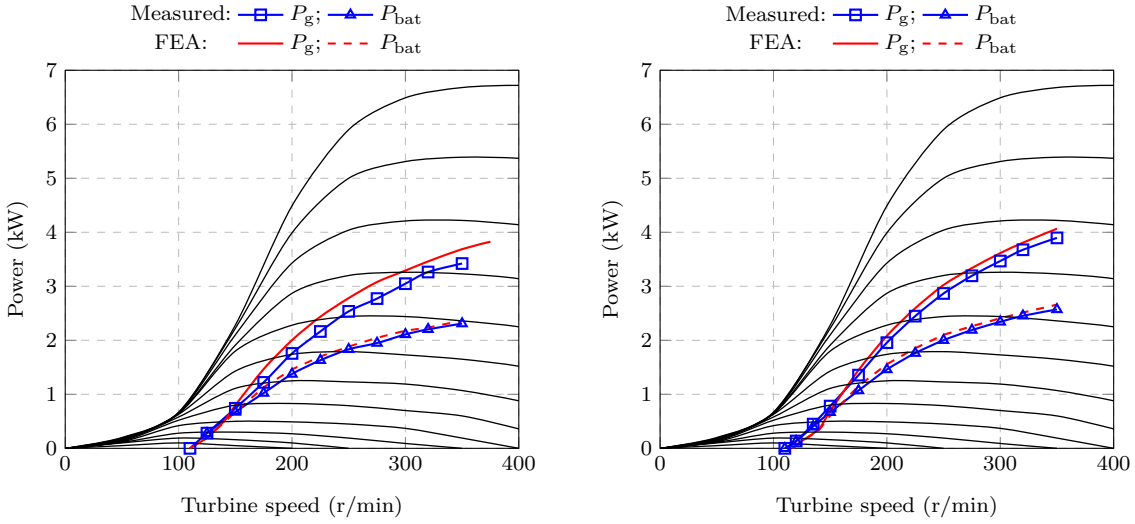

(a) PMSG prototype **(b)** PMVG prototype

Figure 6.7: Measured system efficiency in Chapters 4 and 5 for the respective PMSG and PMVG prototypes.

PMVGs. It is shown in Fig. 6.6(a) that the transmission losses in the 4.2 kW system are quite substantial and result in a low system efficiency of 63% and 65% at n_r for the PMSG and PMVG respectively. This is due to the 4.2 kW passive system resembling that of a low-voltage high-current system, with the fixed load side battery voltage in this case being 48 V. Naturally, as the fixed load side voltage increases, e.g. with an increase in the system's power rating, the transmission losses become less significant and the passive wind energy system becomes more efficient. Such is the case, as is shown in Figs. 6.5(b) and 6.6(b) for the 15 kW passive wind energy system. The system efficiency at n_r for the 15 kW system, is 84% and 87% for the PMSG and PMVG respectively.

The results presented in Fig. 6.5(a) and Fig. 6.6(b) for the 4.2 kW system may seem discouraging. However, it is important to be mindful of the motivation for using the passive wind energy system and that it is for rural applications. Moreover, the power matching and system efficiency at lower wind speeds are still desirable since the passive system will mostly operate at these lower wind speeds. For additional validation, the

measured P_g and P_{bat} for the PMSG and PMVG prototypes in Chapters 4 and 5 are shown in Fig. 6.7. It is shown in Fig. 6.7 that the measured results correlate with the FEA predicted P_g and P_{bat}.

6.2.2 Sensitivity Analysis

As previously stated, the combined resistance of the brush-slip-rings and transmission cable is estimated to be $R_c = 0.3\ \Omega$, which is for a worst case scenario. To show the effect that R_c has on the passive system's power matching, the power matching results for the 4.2 kW and 15 kW PMSGs are shown in Fig. 6.8 with R_c a parameter. It is shown in Fig. 6.8 that the generated power, P_g, and the power into the battery, P_{bat}, are relatively insensitive to variations of R_c, especially for the 15 kW passive system. Of course, if the actual value of R_c is known beforehand, this can be taken into account in the design process. However, in the comparison in Fig. 6.8 it is shown that the effect is almost negligible.

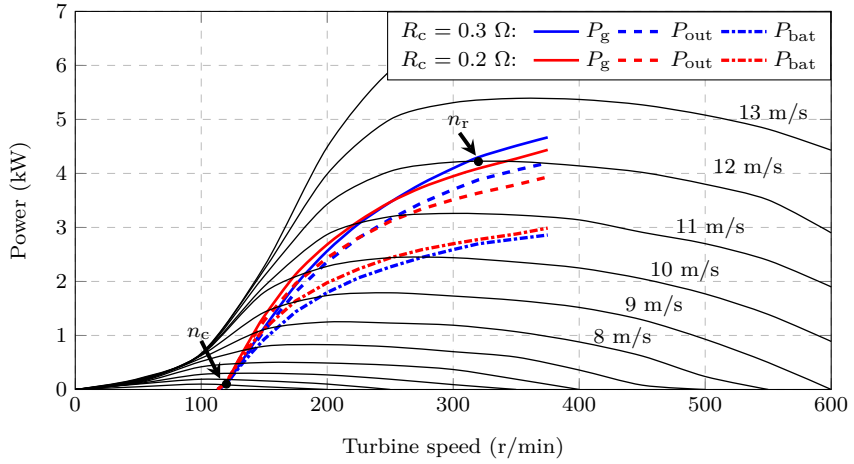

(a) 4.2 kW PMSG

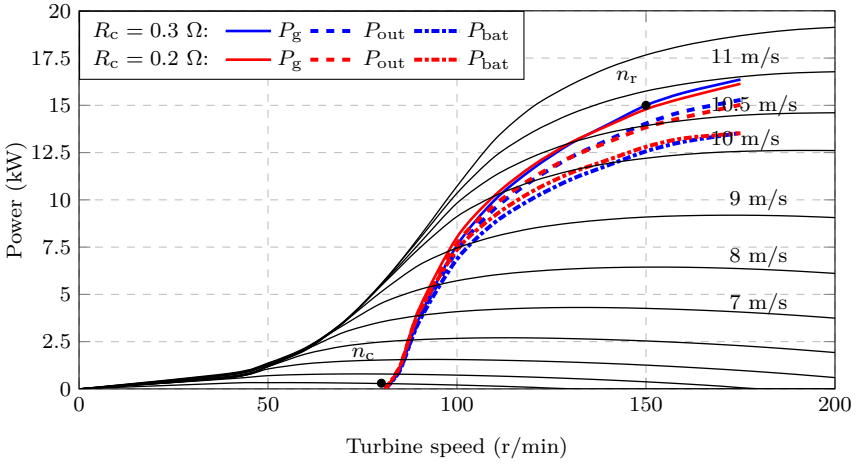

(b) 15 kW PMSG

Figure 6.8: Power matching of the PMSGs at different power levels with R_c a parameter.

6.3 Chapter Summary

In this chapter the passive system is investigated at different power levels. The FEA design results of a PMSG and PMVG for the 15 kW passive system are presented. Subsequently the system's performance at the 4.2 kW and 15 kW power levels are compared:
- It is shown that the resistance, R_c, can have a significant effect on the system's performance in terms of the power delivered to the battery energy storage, especially for the 4.2 kW passive system. Contrary to the norm in literature, where passive systems are only used at a sub 5 kW power level, it is shown that the passive system is actually well suited for higher power levels.
- In reality, the resistance R_c may vary due to the distance between the tower and the battery energy storage system. It is shown that the power matching, and ultimately the system efficiency, is insensitive to this variation and can be considered negligible.

Part 2

Controlled Wind Generator Systems

Chapter 7

DC-DC Converter Wind Generator System

In the DC-DC converter system the PM generator is connected to the battery energy storage via an uncontrolled diode bridge rectifier and a DC-DC converter, as shown in Fig. 7.1. Due to the diode bridge rectifier the generator phase current and terminal voltage will be in phase, i.e. operate at a unity displacement power factor [26] (same as the uncontrolled passive system). However, for the DC-DC converter system the terminal voltage is controlled through gain scheduling and a pre-calculated duty cycle lookup table, as in [35] and [36] for MPPT. Therefore, as with any other controlled wind generator system, it is desired that the load angle, δ, be reduced to increase torque production. Thus, contrary to the passive system, a large internal synchronous impedance is undesired for the DC-DC converter connected wind generator system.

In the context of this dissertation, the design of a PM generator for a controlled DC-DC converter system must be further investigated. Hence the research sub-question:

6. What is the optimal wind generator technology for the DC-DC controlled wind energy system?

For this application only PMSGs are considered. The PMVG is wholly discarded due to its inherent large synchronous reactance. The chapter layout is then as follows: First, the machine selection is discussed. The machine goodness factors are then deduced as a method to evaluate the design results. Thereafter a solution method for solving the PMSG's performance is proposed. Finally the design and optimisation results are evaluated.

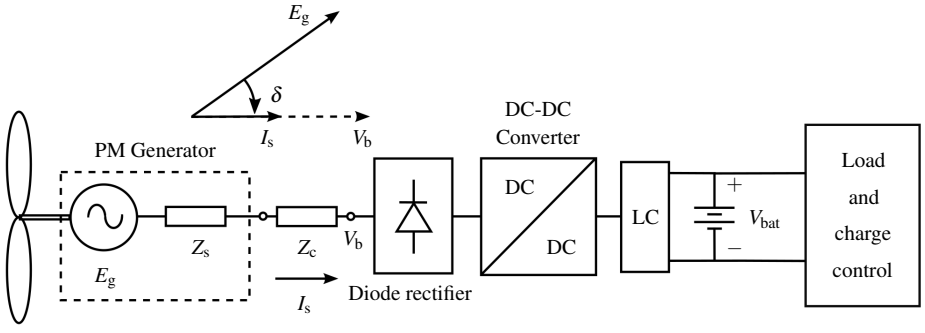

Figure 7.1: Single line diagram of the DC-DC converter wind energy system.

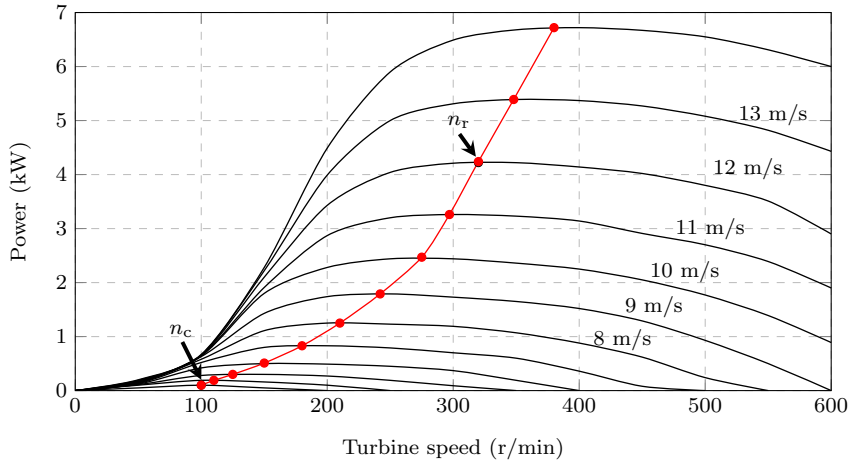

Figure 7.2: Wind turbine power versus turbine speed curves with wind speed a parameter.

Table 7.1: Summary of specified operating points.

	n_c	n_r
Wind speed	3 m/s	12 m/s
Turbine speed	100 r/min	320 r/min
Generated power, P_g	0 kW	4.2 kW
Battery storage voltage, V_{bat}	48 V	

7.1 System Specifications

The wind turbine power versus speed curves, and the specified power matching with the wind turbine for the PMSG, are shown in Fig. 7.2. The system specifications and desired operating points are summarised in Table 7.1. Note here that because a DC-DC buck step-down converter is used, the 48 V battery voltage only determines where the generator cuts in and starts generating power. Ideally, the duty cycle is calculated so that the generator's terminal voltage at the ac-side of the diode bridge rectifier, at rated speed n_r, is relatively high so that the system is a high voltage low current system. This is done to minimise transmission losses in the system.

7.2 Machine Selection

Both NO-PMSGs and O-PMSGs are considered for the DC-DC converter system. In Chapters 3 and 4, only NO-PMSGs were considered because of their tendency for having a higher synchronous reactance due to their high differential harmonic leakage flux coefficient, τ_d, and their shorter end-winding lengths. However, in this case, the typically lower τ_d-value of O-PMSGs might be advantageous. O-PMSGs do however have longer end-winding lengths that increase copper losses and copper mass.

As in Chapter 4.2, the harmonic analysis of Appendix A is done for the possible machine slot-pole combinations. The calculated working harmonic winding factors, k_w, and τ_d-values for 28-pole PMSGs are given in Fig. 7.3, with the number of stator slots as a parameter. Note that the O-PMSG in Fig. 7.3 with the 84-28 combination is that of an integral winding, i.e. $q = 1$, and is discarded due to its poor torque quality. From Fig. 7.3, the most suited O-PMSGs are those with slot-pole combinations of 54-28, 78-28

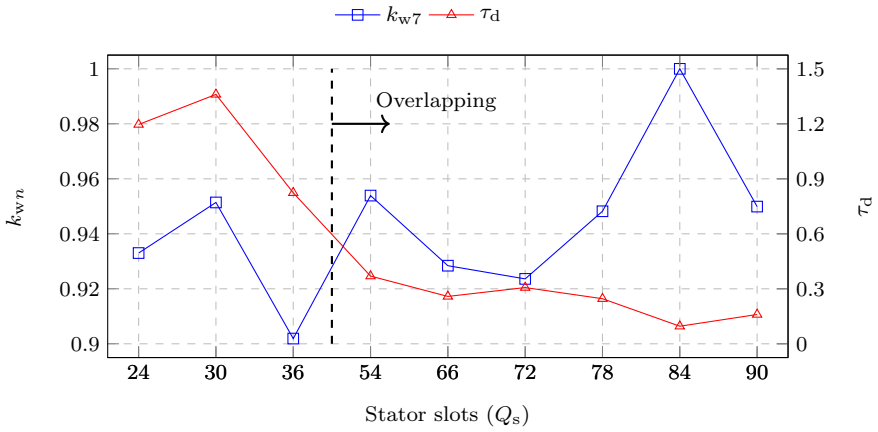

Figure 7.3: Winding factor and stator differential harmonic leakage flux coefficient for 28-pole PMSGs versus stator slot number.

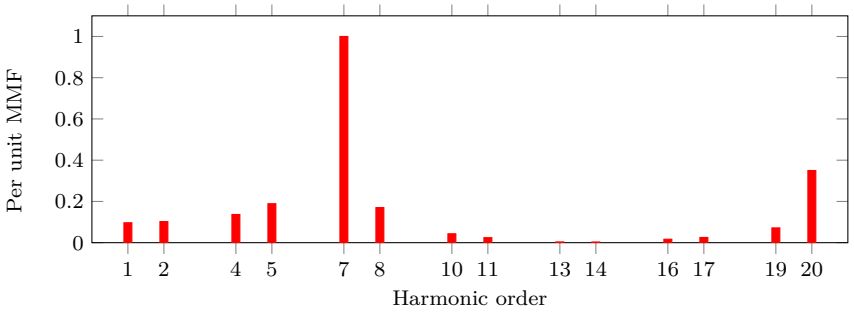

(a) 54-28 slot-pole

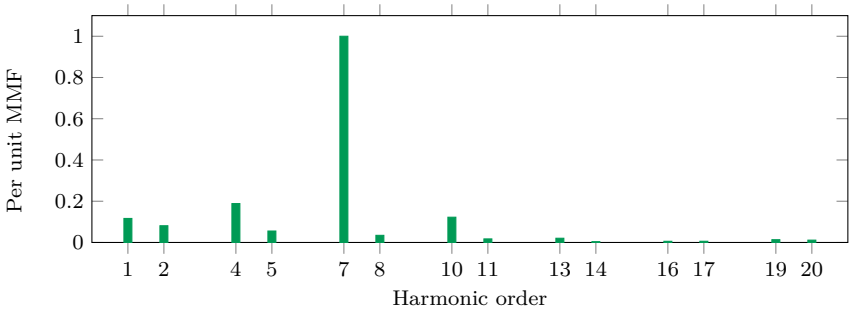

(b) 90-28 slot-pole

Figure 7.4: Per unit MMF harmonic content of potential O-PMSGs.

and 90-28. The O-PMSG with a 90-28 slot-pole combination is seemingly the best, with a high winding factor of $k_w = 0.9499$ and with $\tau_d = 0.16$. However, there is some doubt whether a machine with this many slots is practical to manufacture; given the relatively small diameter of the wind generators, the slot dimensions might be too small. Therefore, the 54-28 O-PMSG is also investigated. As shown in Fig. 7.3, this generator has a winding factor of $k_w = 0.9539$ and differential harmonic leakage flux coefficient of $\tau_d = 0.369$. The per unit MMF harmonic content of the 90-28 and 54-28 O-PMSGs are shown in Fig. 7.4.

As in Chapters 3 and 4, the 30-28 slot-pole NO-PMSG is also considered for the DC-DC converter system. Compared to the aforementioned O-PMSGs, this machine has a high τ_d-value with $\tau_d = 1.4$. It is also shown in Fig. 7.3 that the higher τ_d-values of

NO-PMSGs hold true in general when compared to O-PMSGs. The latter suggests that the O-PMSGs might be better suited for this application.

7.3 Machine Goodness Factors

In this section the goodness (e.g. as in [98]) of the surface mounted PMSG with the generator connected to a diode rectifier load is considered. Through approximation in analytical calculations, expressions for the goodness of the machine's performance is derived in terms of the relevant machine parameters. This is done to better interpret the design optimisation results later presented in this chapter. Through these goodness factors it is possible to better understand the trade-off between the machine's relative end-winding length, l_e, and the load angle, δ, due to the machine's internal synchronous inductance. Thus, theoretically comparing the use of O-PMSGs with NO-PMSGs for this application.

7.3.1 Torque equation

With the PMSG connected to a diode rectifier, the generator operates at unity displacement power factor. Hence the load angle δ is also the angle between the current space phasor and the induced back EMF voltage space phasor. Furthermore it is assumed that $L_d = L_q$. From this the torque equation for the generator can be expressed as

$$T = \frac{3}{2} p_p \lambda_{PM} I_q = \frac{3}{2} p_p \lambda_{PM} \hat{I} \cos\delta. \tag{7.3.1}$$

The flux linkage λ_{PM} and current $\hat{I}$ in (7.3.1) can be expressed as

$$\lambda_{PM} = \left(\frac{k_w N_{ph}}{p} \right) d_i l_{Fe} \hat{B} \tag{7.3.2}$$

and

$$\hat{I} = \hat{J} A_{Cu} \left(\frac{qp}{N_{ph}} \right). \tag{7.3.3}$$

Substituting λ_{PM} and $\hat{I}$ of (7.3.2) and (7.3.3) into (7.3.1) results in

$$T = \frac{3}{2} k_w \hat{J} \hat{B} q p_p A_{Cu} d_i l_{Fe} \cos\delta. \tag{7.3.4}$$

The copper area in (7.3.4) can be approximated by

$$A_{Cu} \approx \frac{\pi k_{Cu} \sigma_s}{Q_s} d_i h_s, \tag{7.3.5}$$

where σ_s is the slot width to slot pitch ratio factor in the middle of the slot. By replacing A_{cu} in (7.3.4) with (7.3.5), the torque is approximated as

$$T \approx \frac{3}{2} \pi k_w k_{Cu} \sigma_s \hat{J} \hat{B} \left(\frac{q p_p}{Q_s} \right) h_s d_i^2 l_{Fe} \cos\delta. \tag{7.3.6}$$

7.3.2 Load Angle and Inductances

It is possible to get an approximation for δ from (7.3.4) and (7.3.6) by temporarily ignoring the stator resistance voltage drop and expressing the generator power as

$$\begin{aligned} P_{\mathrm{g}} &= \frac{3V_{\mathrm{s}}E_{\mathrm{s}}}{X_{\mathrm{s}}}\sin\delta = \frac{3E_{\mathrm{s}}^2}{2\omega_{\mathrm{e}}L_{\mathrm{s}}}\sin 2\delta \quad [V_{\mathrm{s}} = E_{\mathrm{s}}\cos\delta] \\ \rightarrow \delta &= \frac{1}{2}\arcsin\left(\frac{2P_{\mathrm{gFL}}\omega_{\mathrm{eFL}}L_{\mathrm{s}}}{3E_{\mathrm{sFL}}^2}\right), \end{aligned} \tag{7.3.7}$$

where the subscript "FL" denotes full load values that are known. Once more, as in (3.1.3), the synchronous inductance L_{s} in (7.3.7) is given by

$$L_{\mathrm{s}} = L_{\mathrm{m}}(1+\tau_{\mathrm{d}}) + L_{\mathrm{sl}} + L_{\mathrm{e}}. \tag{7.3.8}$$

The slot leakage inductance L_{sl}, given in (3.1.9), can for now be approximated as

$$L_{\mathrm{sl}} \approx \frac{4m}{Q_{\mathrm{s}}}\mu_0 l_{\mathrm{Fe}} N_{\mathrm{ph}}^2 \Lambda_{\mathrm{uv}} \rightarrow \Lambda_{\mathrm{uv}} \approx \frac{h_{\mathrm{s}}}{3b_{\mathrm{s}}}. \tag{7.3.9}$$

It is shown in equations (7.3.7) to (7.3.9) that a large τ_{d}, a large slot height h_{s}, and a small slot width b_{s} increase both L_{s} and δ, and subsequently $\cos\delta$ is decreased.

7.3.3 Goodness Factors

For wind generators in small-scale applications the copper losses in the windings will dominate all other losses in the machine. Hence, the first goodness factor of the generator is the torque per generator copper losses. The copper losses can be expressed as

$$P_{\mathrm{cu}} = 3\hat{J}^2 q p_{\mathrm{p}} A_{\mathrm{Cu}} \rho_{\mathrm{t}} (l_{\mathrm{Fe}} + l_{\mathrm{e}}) \tag{7.3.10}$$

From (7.3.4) and (7.3.10), the torque per copper losses in the generator can be expressed as

$$\frac{T}{P_{\mathrm{cu}}} = \left(\frac{k_{\mathrm{w}}\hat{B}}{2\hat{J}\rho_{\mathrm{t}}}\right)\frac{d_{\mathrm{i}}\cos\delta}{1+\frac{l_{\mathrm{e}}}{l_{\mathrm{Fe}}}} = K_1\left(\frac{d_{\mathrm{i}}\cos\delta}{1+\frac{l_{\mathrm{e}}}{l_{\mathrm{Fe}}}}\right). \tag{7.3.11}$$

Here it is shown that a large air gap diameter and a small power angle improves the torque per copper losses, while the end winding length penalises it, as is expected.

The second goodness factor of the generator is the torque per generator volume. The generator volume can be approximated as

$$V_{\mathrm{PMSG}} \approx \frac{\pi}{4} d_{\mathrm{i}}^2 l_{\mathrm{Fe}}. \tag{7.3.12}$$

From (7.3.6) and (7.3.12) the torque per generator volume can be expressed as

$$\frac{T}{V_{\mathrm{PMSG}}} \approx 6k_{\mathrm{w}}k_{\mathrm{Cu}}\sigma_{\mathrm{s}}\hat{J}\hat{B}\left(\frac{qp_{\mathrm{p}}}{Q_{\mathrm{s}}}\right)\cos\delta = K_2(h_{\mathrm{s}}\cos\delta). \tag{7.3.13}$$

It is interesting to note that in (7.3.13) a larger slot height h_{s} improves the torque per generator volume.

Another generator goodness factor is the torque per generator mass. The generator mass can be approximated as

$$M_{\text{PMSG}} \approx \rho\pi d_{\text{i}} l_{\text{Fe}}(2h_{\text{y}} + h_{\text{s}} + h_{\text{m}}). \tag{7.3.14}$$

The yoke heights of the stator and rotor stacks are assumed to be equal. From (7.3.6) and (7.3.14) the torque per generator mass can be expressed as

$$\begin{aligned}\frac{T}{M_{\text{PMSG}}} &\approx \frac{3}{2\rho} k_{\text{w}} k_{\text{Cu}} \sigma_{\text{s}} \hat{J}\hat{B} \left(\frac{qp_{\text{p}}}{Q_{\text{s}}}\right) \frac{h_{\text{s}} d_{\text{i}} \cos\delta}{2h_{\text{y}} + h_{\text{s}} + h_{\text{m}}} \\ &= K_3 \left(\frac{d_{\text{i}} \cos\delta}{1 + \frac{2h_{\text{y}} + h_{\text{m}}}{h_{\text{s}}}}\right).\end{aligned} \tag{7.3.15}$$

As with the torque per copper losses, the torque per generator mass benefits from a large air gap diameter and a small power angle δ. Furthermore, the torque per generator mass benefits from a large slot height as in the case of the torque per generator volume. It also benefits from smaller yoke heights.

To summarise: d_{i}, $\cos\delta$, h_{s} and $l_{\text{e}}/l_{\text{Fe}}$ are important variables in the goodness of the PMSG. In order to maximise the generator's goodness, the first three variables must be large and the fourth one small. Note that a large h_{s} and small b_{s} are bad for $\cos\delta$. However, the $\cos\delta$ function varies relatively little if δ is small. Machines with high number of slots, Q_{s}, have relatively small b_{s}-values, which increases L_{s}. It is important here to consider both b_{s} and τ_{d} and its combined effect on L_{s}. A final note on the machine goodness factors is that the quality of the generated torque can also be considered as part of the goodness of a machine. Hence, per unit torque ripple or the LCM(Q_{s}, p)-value can also be a goodness factor.

7.4 Static FEA Solution Method

The PMSG in the DC-DC converter system is connected to the DC-DC buck step down converter via an uncontrolled diode bridge rectifier. Therefore, as with the passive system, the current-loading of the PMSG at a certain speed is unknown. To calculate the generator performance at rated speed, the PMSG's terminal voltage and load angle are solved iteratively using multiple static FEA solutions, as explained in the following subsections.

The equivalent modelling of the PMSG and the PMSG's performance calculations are the same as in Chapter 3.2. (L_{ext} is of course omitted form the dq-circuits.)

7.4.1 Rewriting Steady-state Equations

The steady-state dq-equations of the PMSG need to be rewritten in order to solve the unknowns that are necessary to calculate the PMSG performance. Equations (3.2.1) and (3.2.2) are rewritten by substituting the dq-values for voltage and current with their equivalent RMS values from (3.2.5). Then, by rewriting (3.2.1) and (3.2.2) in terms of V_{rms}, it gives

$$V_{\text{rms}} = \frac{-\sqrt{2} I_{\text{rms}}(R_{\text{st}} \cos\delta + \omega_{\text{e}}(L_{\text{d}} + L_{\text{e}}) \sin\delta) + \omega_{\text{e}} \lambda_{\text{PM}}}{\sqrt{2}\cos\delta} \tag{7.4.1}$$

and

$$V_{\text{rms}} = \frac{-\sqrt{2} I_{\text{rms}}(R_{\text{st}} \sin\delta - \omega_{\text{e}}(L_{\text{d}} + L_{\text{e}}) \cos\delta)}{\sqrt{2}\sin\delta} \tag{7.4.2}$$

Equations (7.4.1) and (7.4.2) are used to numerically solve δ and V_{rms}.

7.4.2 Phase Current Calculation

The method for solving the unknowns in the system is similar to that of Chapter 3.3: If the value of I_{rms} in (7.4.1) and (7.4.2) is known, then the PMSG's static FEA solutions can be used to evaluate its performance at the rated speed. By choosing three values for I_{rms} (I_1, I_2, I_3) and calculating the PMSG's performance for these three values, a second degree polynomial of the Newton form in (3.3.3) can be determined in terms of the generated power P_{g} and I_{rms}. The second degree polynomial of (3.3.3) is thus rewritten as

$$P_{\text{g}}(I_{\text{rms}}) = c_1 + c_2(I_{\text{rms}} - I_1) + c_3(I_{\text{rms}} - I_1)(I_{\text{rms}} - I_2). \tag{7.4.3}$$

Using the three generated power values $P_{\text{g}}(I_1)$, $P_{\text{g}}(I_2)$, $P_{\text{g}}(I_3)$, and their corresponding current values I_1, I_2, I_3, the coefficients in (7.4.3) are calculated as

$$\begin{aligned} c_1 &= P_{\text{g}}(I_1), \\ c_2 &= \frac{P_{\text{g}}(I_1) - P_{\text{g}}(I_2)}{I_1 - I_2}, \\ c_3 &= \frac{c_2}{I_1 - I_3} - \frac{P_{\text{g}}(I_2) - P_{\text{g}}(I_3)}{(I_2 - I_3)(I_1 - I_3)}. \end{aligned} \tag{7.4.4}$$

An example of the calculated second degree polynomial is illustrated in Fig. 7.5(b). I_{rms} is calculated by substituting the rated generator power at rated speed into (7.4.3), i.e. $P_{\text{g}}(I_{\text{rms}})$. For the solution to be valid, the values for I_1 and I_3 have to bracket the solution value of I_{rms}. Knowing the maximum allowed current density specification ($J_{\text{rms}} < 5$ A/mm^2), the values for I_1, I_2 and I_3 are then estimated accordingly so that the corresponding RMS current density for I_2 is $J_2 = 4$ A/mm^2. Values for I_1 and I_3 are then chosen such that $I_1 < I_{\text{rms}} < I_3$ (or $J_1 = 2 < J_2 = 4 < J_3 = 6$).

The rest of the solution method is then the same as shown in Fig. 3.10, but instead of substituting in L_{ext}, values for I_{rms} are used to solve V_{rms} and δ.

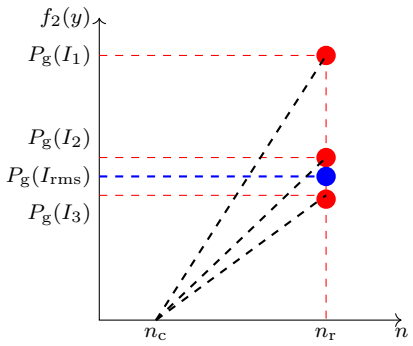

(a) Generated power, calculated at rated speed, with I_1,I_2 and I_3 added to the system. Collectively this brackets $P_{\text{g}}(I_{\text{rms}})$ and ensures accuracy.

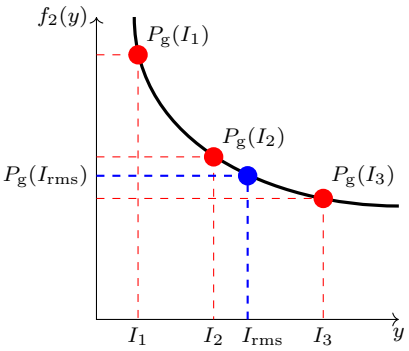

(b) Second degree polynomial curve fitting through three power points, from which I_{rms} is calculated knowing the rated power $P_{\text{g}}(I_{\text{rms}})$.

Figure 7.5: Visual representation of the phase current solution method.

7.5 Design Optimisation

For the design optimisation the NSGA-II algorithm is used with 2D static FEA solutions. The multi-objective function is then

$$\min_{\mathbf{X}_1} \mathbf{F}(\mathbf{X}_1) = \min_{\mathbf{X}_1} \begin{bmatrix} M_{\text{active}}(\mathbf{X}_1) \\ M_{\text{PM}}(\mathbf{X}_1) \end{bmatrix}, \tag{7.5.1}$$

and the performance of the solutions are subject to the design constraints given by

$$\mathbf{U} = \begin{bmatrix} P_{\text{g}} \\ \eta \\ J_{\text{rms}} \end{bmatrix} = \begin{bmatrix} 4.2 \text{ kW} \\ \geq 90\% \\ \leq 5 \text{ A/mm}^2 \end{bmatrix}. \tag{7.5.2}$$

The active mass, M_{active}, is calculated as in (4.5.2) where the end-winding mass is also taken into account. The dimensional vector $\mathbf{X}_1$ in (7.5.1) is the same as in (5.3.3), with the dimensions defined in Fig. 5.4. The generators are then also subject to the same geometric boundaries imposed in previous chapters for the 4.2 kW wind turbine.

7.6 Design Results and Evaluation

In the following subsections, the optimisation results of the O-PMSGs and NO-PMSG are evaluated.

7.6.1 Pareto Front Results

The Pareto front results for the respective PMSGs are given in Fig. 7.6. Also indicated in Fig. 7.6, are the optimal PMSGs for each slot-pole combination. The summarised performance results of the selected PMSGs are given in Table 7.2.

For the 54-28 and 90-28 O-PMSGs, both the Pareto fronts in Fig. 7.6 show that there is almost no difference between these two in terms of the generator's active mass, M_{active}, and PM mass, M_{PM}. It is also shown in Fig. 7.6 that the NO-PMSG's Pareto front solutions use less active material mass, but use slightly more PM material than the O-PMSGs.

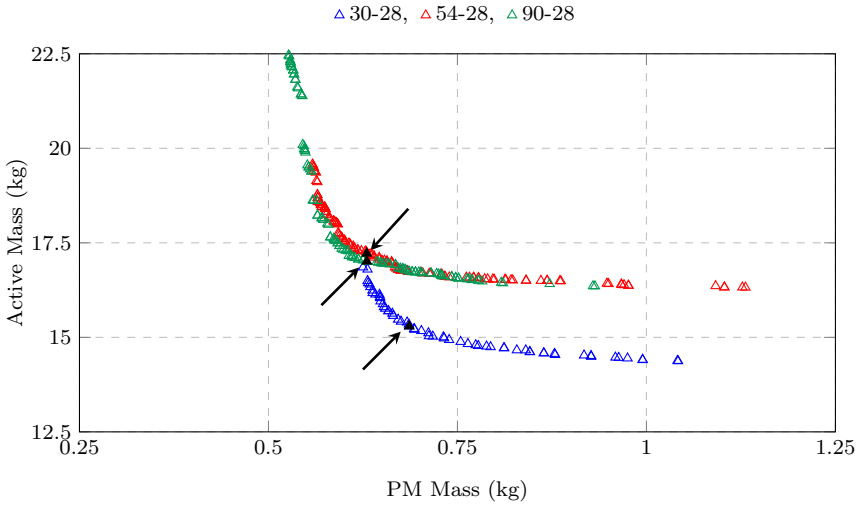

Figure 7.6: Pareto front optimisation results.

Table 7.2: Comparison of selected Pareto front solutions.

Generator	Non-overlapping	Overlapping		**Ratio**
	30-28	54-28	90-28	30:54:90
M_{PM} (kg)	0.69	0.63	0.63	1 : 0.91 : 0.91
M_{active} (kg)	15.29	17.22	17.01	1 : 1.13 : 1.11
P_{g} (kW)	4.20	4.20	4.21	
η (%)	92.0	89.5	89.9	
J_{rms} (A/mm^2)	5.03	5.0	5.0	
d_{o} (mm)	376	395	399	1 : 1.05 : 1.06
l_{Fe} (mm)	34	41	36	1 : 1.21 : 1.06
Machine goodness factors				
-Torque per copper losses	0.105	0.102	0.098	1 : 0.97 : 0.93
-Torque per volume	0.027	0.024	0.027	1 : 0.89 : 1
-Torque per mass	0.198	0.222	0.225	1 : 1.12 : 1.14
$l_{\text{e}}/l_{\text{Fe}}$	1.81	2.42	2.61	1 : 1.34 : 1.44
d_{i} (mm)	354	375	377	1 : 1.06 : 1.06
$\cos\delta$	0.831	0.929	0.936	1 : 1.12 : 1.13
h_{s} (mm)	33.1	26.1	28.6	1 : 0.79 : 0.86
b_{s} (mm)	19.5	11.9	6.8	1 : 0.61 : 0.35
ΔT_{cog} (%)	1.15	2.15	0.39	1 : 1.81 : 0.34
ΔT_{ripple} (%)	5.03	3.55	4.12	1 : 0.71 : 0.82
LCM(Q_{s}, p)	420	756	1260	

For the optimum generator selections in Table 7.2, the NO-PMSG uses $\approx 9.5\%$ more PM material and $\approx 11.2\%$ less active material. The NO-PMSG in Table 7.2 does have a higher efficiency than the specified minimum in (7.5.2). All of the NO-PMSG Pareto front solutions in Fig. 7.6 converged at the maximum allowed current density J_{rms} and at the specified generated power P_{g}, with a higher efficiency η than the specified minimum. Partial cross-sections of the PMSGs are shown in Fig. 7.7.

The values of the theoretical machine goodness factors, as derived in Section 7.3, for the respective PMSGs are also given in Table 7.2. In terms of a direct comparison, it is shown in Table 7.2 that the NO-PMSG is better in terms of the torque per copper losses, whereas the O-PMSGs are better in terms of torque per mass. Ultimately, the goodness factors of the optimum PMSGs in Table 7.2 amount to a near equal "machine goodness".

The important variables in Section 7.3 that indicate the goodness of the PMSG, are also given in Table 7.2 for the different PMSGs. As previously shown in (7.3.11), in terms of the torque per copper losses, the PMSGs are penalised by a large end-winding length l_{e}. It is shown in Table 7.2 that the $l_{\text{e}}/l_{\text{Fe}}$-values for the O-PMSGs are substantially greater than that of the NO-PMSG. Therefore, as predicted in (7.3.11), the optimisation algorithm finds solutions for the O-PMSGs that have a larger d_{i} than the NO-PMSG. One would assume that the optimisation algorithm might find solutions with a larger l_{Fe} for the O-PMSGs, as this would effectively decrease the ratio of $l_{\text{e}}/l_{\text{Fe}}$ and improve the torque per copper losses. However, by increasing the axial length of the generator a substantial amount of material mass is added. With one of the objectives in (7.5.1) being to minimise M_{PM}, it makes sense that the newer generations in the optimisation algorithm rather converge to an increased d_{i}. It would also seem that the generator's end-winding length in this instance outweighs the effect of $\cos\delta$.

In terms of the torque per generator volume, the deduced goodness factor in (7.3.13)

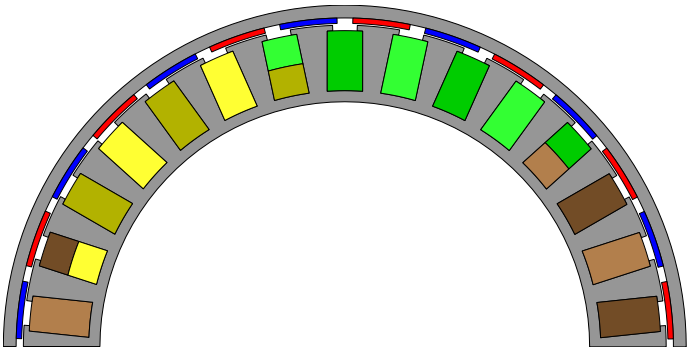

(a) 30-28 slot-pole

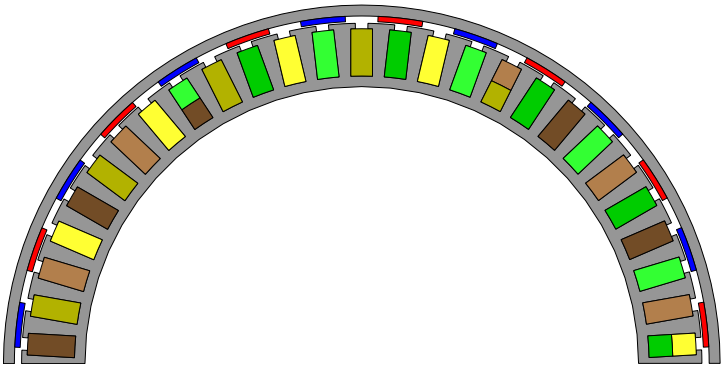

(b) 54-28 slot-pole

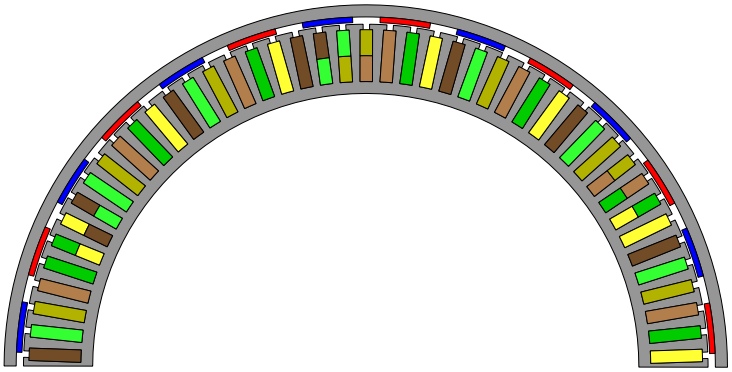

(c) 90-28 slot-pole

Figure 7.7: Partial cross-sections of the optimised NO-PMSG and O-PMSGs.

shows that a larger h_s and $\cos\delta$ would improve this. Therefore, considering that the O-PMSGs' $\cos\delta$-values are much higher than the NO-PMSG's value in Table 7.2, the NO-PMSG has a larger slot height h_s than the respective O-PMSGs. As with the torque per generator volume, the torque per generator mass improves with a larger h_s and $\cos\delta$. The torque per generator mass also improves with a large d_i, as shown in (7.3.15). The relevant values in Table 7.2 then accounts for why the O-PMSGs are competitive in terms of the generator's active mass, M_{active}. However, the goodness factor in (7.3.15) does not take into consideration the copper mass of the end-windings. As shown in Table 7.2 with l_e/l_{Fe}, the two O-PMSGs' end-winding copper mass is much greater than the NO-PMSG's. Therefore, it can be concluded that the effect of the generator's end-windings will have a greater influence on M_{active} than the generator's internal synchronous inductance ($\cos\delta$). However, it is shown in Fig. 7.6 and Table 7.2 that the O-PMSGs have a lower PM mass, M_{PM}, than the NO-PMSG. Minimising M_{PM} is the other objective in the design

optimisation's multi-objective function given by (7.5.1). Thus, it would seem that the O-PMSGs better utilise the PM material in the generator as a result of having a larger $\cos\delta$-value than the NO-PMSG.

7.6.2 Torque Quality

The FE predicted torque quality results are given in Table 7.2. The predicted cogging torque and torque ripple waveforms are also shown in Fig. 7.8.

It is shown that all three of the selected PMSGs have desirable torque quality. The 90-28 O-PMSG in particular has a very low cogging torque, whereas the 54-28 O-PMSG has the lowest torque ripple. Although the NO-PMSG's torque ripple is slightly above 5%, it is still deemed acceptable.

7.6.3 2D FEA versus 3D FEA

To validate the 2D FEA solutions and the optimisation results, the performance of the NO-PMSG and the respective O-PMSGs in Table 7.2 are also solved using 3D FEA. The generated torque and generator efficiency results at the rated operating point, n_r, are summarised and compared in Table 7.3. It is shown in Table 7.3 that the generated torque values compare well and validate the design optimisation results. The efficiency results in Table 7.3 also compare well, with the slight differences being attributed to the core loss

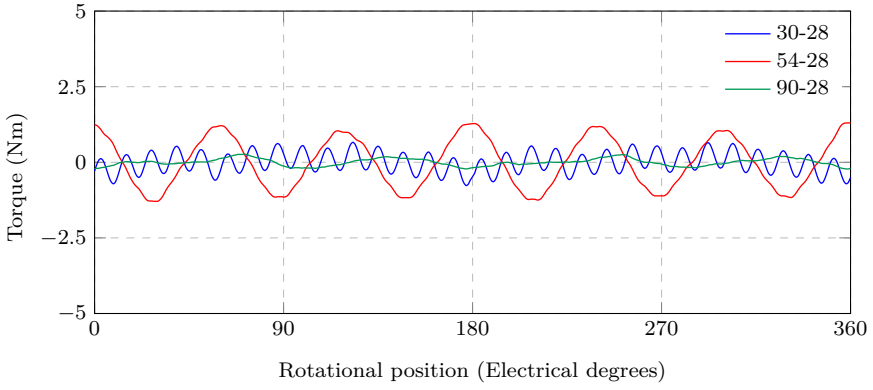

(a) Cogging torque, ΔT_{cog}

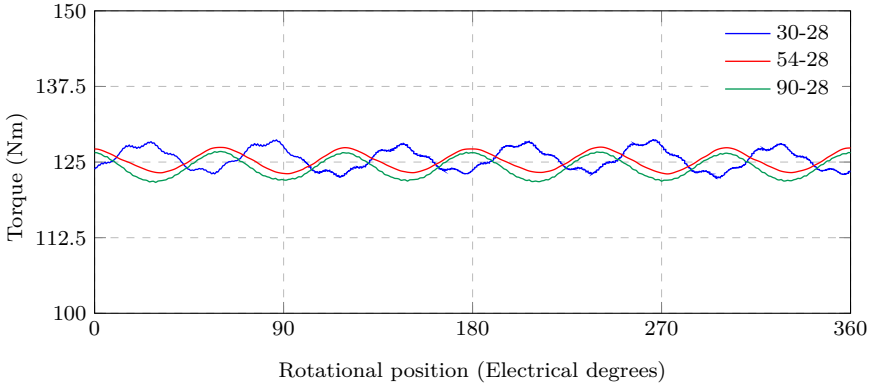

(b) Torque ripple, ΔT_r

Figure 7.8: FE predicted cogging torque and torque ripple of the PMSGs.

Table 7.3: 2D versus 3D FEA comparison at n_r.

Generator	30-28		54-28		90-28	
	2D	3D	2D	3D	2D	3D
T_g (Nm)	125.4	124.7	125.3	124.5	125.5	124.2
η (%)	92.0	92.1	89.5	89.1	89.8	89.3
P_{Fe} at n_r, (W)	41.5	35.6	29.1	46.8	31.2	49.7
P_{Fe} at n_c, (W)	10.5	9.9	10.8	11.9	13.2	11.7

P_{Fe} calculations at n_r. Furthermore, the calculated core losses P_{Fe} at n_c correlate well, and indicate that all of the PMSGs will have low rotational losses up to the generator's start up speed.

7.7 Chapter Summary

In this chapter PMSGs with overlapping and non-overlapping windings are compared for their use in a DC-DC controlled wind generator system. Essentially, the comparison is done to investigate the trade-off when using a generator with a larger internal synchronous inductance versus a generator with a long end-winding length:
- The results presented in this chapter indicate that there is very little trade-off between the respective PMSGs. Both the NO-PMSG and the respective O-PMSGs meet the desired performance criteria and have excellent torque quality. The optimum NO-PMSG uses less active material, however has more PM material than the O-PMSGs.
- Ultimately, a cost comparison between the respective generators is needed for a conclusive outcome. This comparison is done in Chapter 9. For the comparison with the NO-PMSG in Chapter 9, the 54-28 O-PMSG is used.

Chapter 8

Active Synchronous Rectifier Controlled Wind Generator System

In this chapter, the design results of an optimised 4.2 kW and 15 kW NO-PMSG[1], for the actively controlled system shown in Fig. 8.1, are given. The design of PMSGs for maximum power matching in this system are standard and uncomplicated. Unlike the uncontrolled passive and the DC-DC controlled wind generator systems, no current solution method is necessary; the generator current is controlled by the active synchronous rectifier by means of only q-axis current according to MPP tracking. Therefore, only the results of the optimised NO-PMSGs are discussed. The aim is to have two active synchronous rectifier controlled wind generator designs for the comparison between the different wind generator systems in the next chapter. Thus the work done in this chapter relates to the research sub-question:

7. What are the trade-offs from a generator perspective when using the different wind generator systems?

8.1 Design Optimisation and Results

The system specifications for the 4.2 kW active synchronous rectifier controlled wind generator are the same as for the 4.2 kW DC-DC controlled wind generator in Chapter 7.

[1]Based on the results in Chapter 7, it is only necessary to consider either the NO-PMSG or O-PMSG.

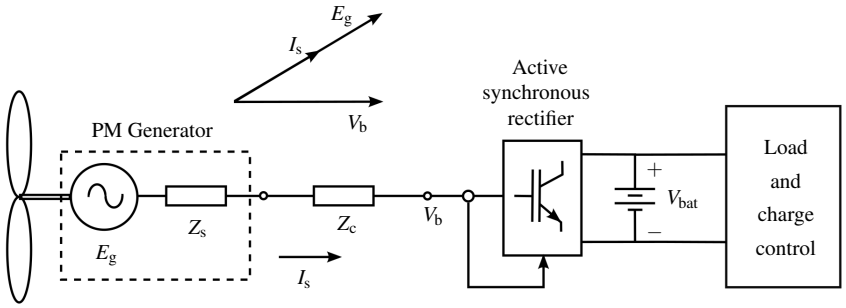

Figure 8.1: Single line diagram of the active synchronous rectifier controlled wind energy system.

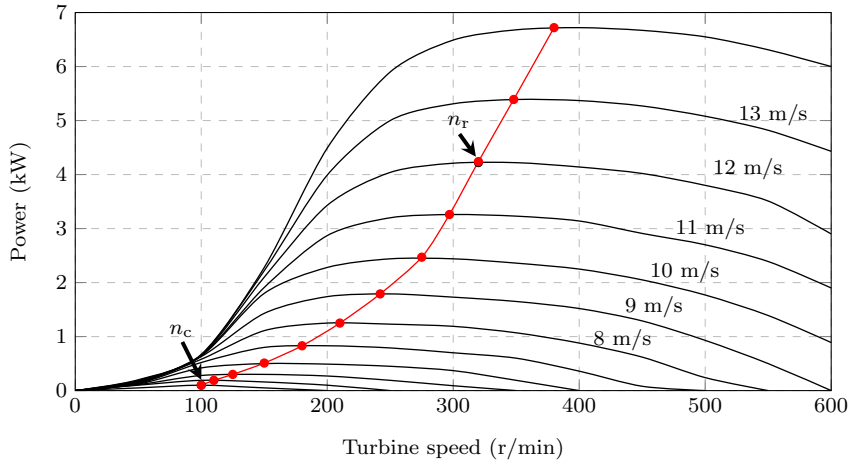

(a) 4.2 kW

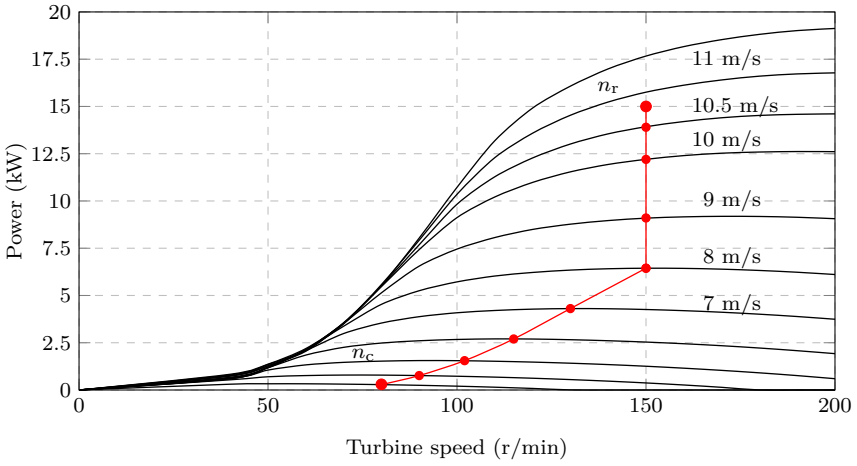

(b) 15 kW

Figure 8.2: Wind turbine power versus turbine speed curves with wind speed a parameter.

Table 8.1: Summary of specified operating points.

	4.2 kW		**15 kW**	
Operating point	n_c	n_r	n_c	n_r
Wind speed	3 m/s	12 m/s	3 m/s	10.8 m/s
Turbine speed	100 r/min	320 r/min	80 r/min	150 r/min
Generated power, P_g	0 kW	4.2 kW	0 kW	15 kW
Battery storage/dc voltage, V_{dc}	48 V		220 V	

These specification are given in Table 8.1, and the wind turbine power versus turbine speed curves are shown in Fig. 8.2(a).

The specified operating points for the 15 kW NO-PMSG are indicated on the wind turbine power versus turbine speed curves in Fig. 8.2(b). The 15 kW system's specifications are also summarised in Table 8.1. Note here that the rated operating point is limited at a maximum turbine speed of 150 r/min. This is based on the specifications from the turbine manufacturer, which state that the turbine should not be operated at turbine speeds much higher than 150 r/min.

8.1.1 Design Optimisation

For the design optimisation the NSGA-II algorithm is used with 2D FEA solutions to solve the generator performance. The multi-objective function and performance constraints for the 4.2 kW system are that of (7.5.1) and (7.5.2) respectively. For the 4.2 kW generator, the 30-28 slot-pole surface mounted PMSG with non-overlapping windings is used. For the 15 kW system, the multi-objective function is that of (6.1.1), without the objective to minimise Z_{ext}. The performance constraints are that of (6.1.2). The 15 kW wind generator has a 45-42 slot-pole combination and is also a surface mounted PMSG with non-overlapping windings. The same geometric boundaries that are outlined in Chapters 4.5.3 and 6.1.2 are imposed for the respective 4.2 kW and 15 kW designs.

8.1.2 Pareto Front Results

The Pareto front results for the active synchronous rectifier controlled PMSGs are shown Fig. 8.3. Also indicated in Fig. 8.3 are the selected optimum PMSGs. The performance

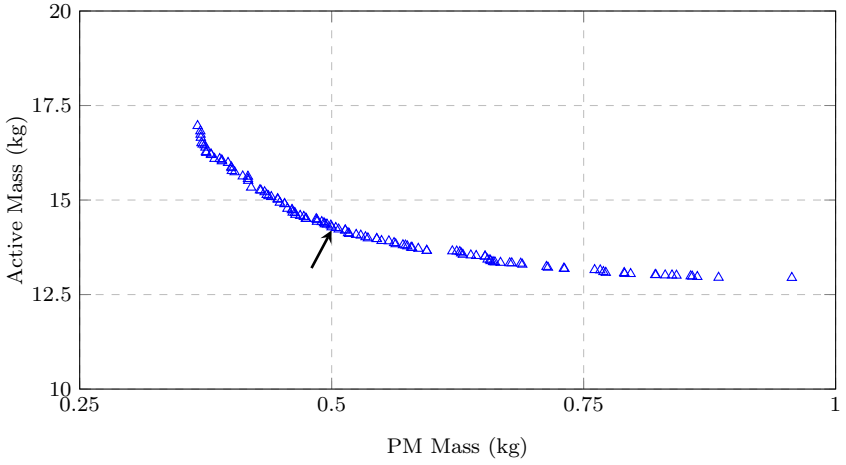

(a) 4.2 kW

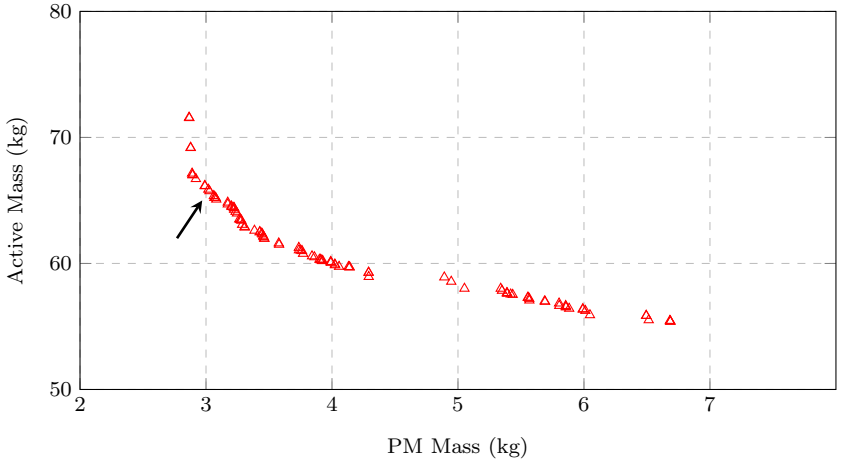

(b) 15 kW

Figure 8.3: Pareto front optimisation results for the active synchronous rectifier controlled NO-PMSGs.

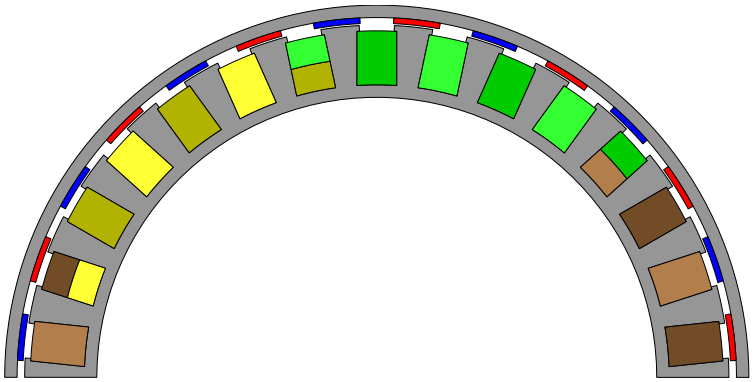

(a) 4.2 kW

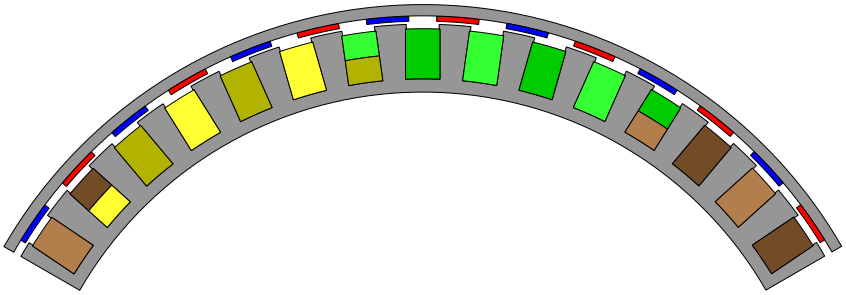

(b) 15 kW

Figure 8.4: Partial cross sections of the optimised active synchronous rectifier controlled NO-PMSGs (not to scale).

Table 8.2: Selected Pareto front solutions.

Parameter	**4.2 kW**	**15 kW**
M_{PM} (kg)	0.50	3.0
M_{active} (kg)	14.27	66.14
P_{g} (kW)	4.20	15.0
η (%)	91.6	93.0
J_{rms} (A/mm^2)	5.0	5.0
d_{o} (mm)	394	640
l_{fe} (mm)	35	97
ΔT_{cog} (%)	0.34	0.26
ΔT_{r} (%)	3.54	5.38

results of the respective PMSGs are summarised in Table 8.2. The partial cross sections of the PMSGs are shown in Fig. 8.4.

It is shown in Table 8.2 that both PMSGs meet the desired performance criteria and have excellent torque quality. The 15 kW PMSG's efficiency is below the design constraint, but is still deemed acceptable. The FE predicted cogging torque and torque ripple results are also shown in Fig. 8.5. It should be noted that no optimisation steps were taken to reduce the torque ripple, ΔT_{r}, of either of the PMSGs. Therefore, if necessary, the 15 kW PMSG's torque ripple can be further reduced. However, for the purpose of this chapter, the torque quality is deemed acceptable. To validate the 2D FEA design results, the PMSGs are also solved using 3D FEA. The 2D and 3D FEA results are compared in Table 8.3 and show good comparison, thereby validating the 2D FEA results.

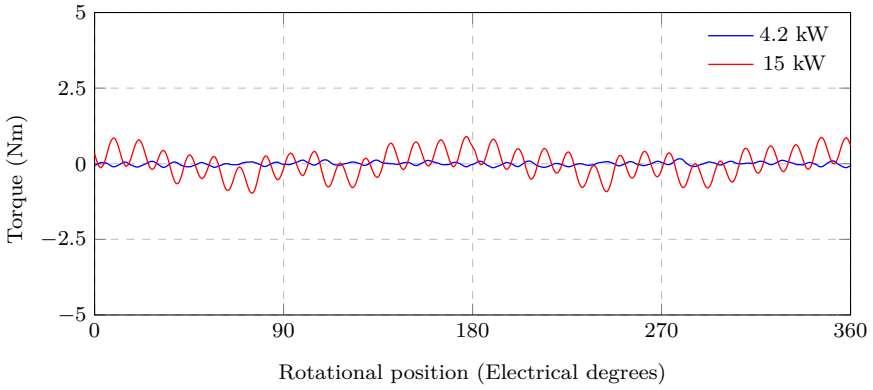

(a) Cogging torque, ΔT_{cog}

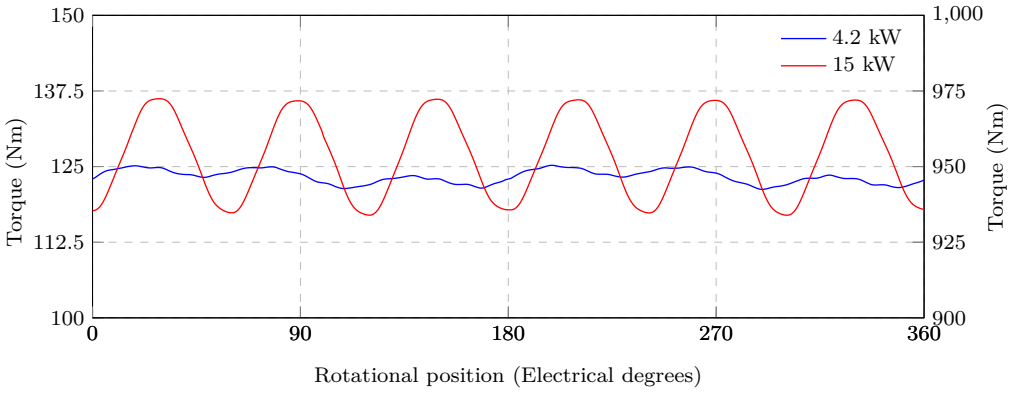

(b) Torque ripple, ΔT_{r}

Figure 8.5: FE predicted cogging torque and full load torque ripple.

Table 8.3: 2D versus 3D FEA comparison at n_{r}.

	4.2 kW		**15 kW**	
	2D	3D	2D	3D
T_{g} (Nm)	125.3	123.5	955.0	957.5
η (%)	91.5	91.7	93.0	93.0
P_{Fe} at n_{r}, (W)	27.9	40.5	85.6	98.2
P_{Fe} at n_{c}, (W)	2.1	7.5	28.7	30.2

8.2 Chapter Summary

In this chapter a brief discussion on the design and results of two optimised NO-PMSGs for a 4.2 kW and 15 kW active synchronous rectifier controlled wind generator system are given. The purpose of this chapter is merely to obtain two optimised generators for the comparison done in the next chapter, where the generators for the different systems are compared.

Chapter 9

Generator and System Comparison

In this chapter the optimum generators from Chapters 4 to 8 are compared. Thus, the aim of this chapter is to address the research sub-question:

7. What are the trade-offs from a generator perspective when using the different wind energy systems?

Subsequently, research sub-questions 4 and 5 are also re-addressed, i.e. comparing the NO-PMSG to the PMVG for the passive system, as well as the the O-PMSG and NO-PMSG for the DC-DC converter system. For reference, the respective wind generator Pareto front results for the different 4.2 kW wind energy systems are shown in Fig. 9.1. Also indicated in Fig. 9.1 are the selected optimum generator designs.

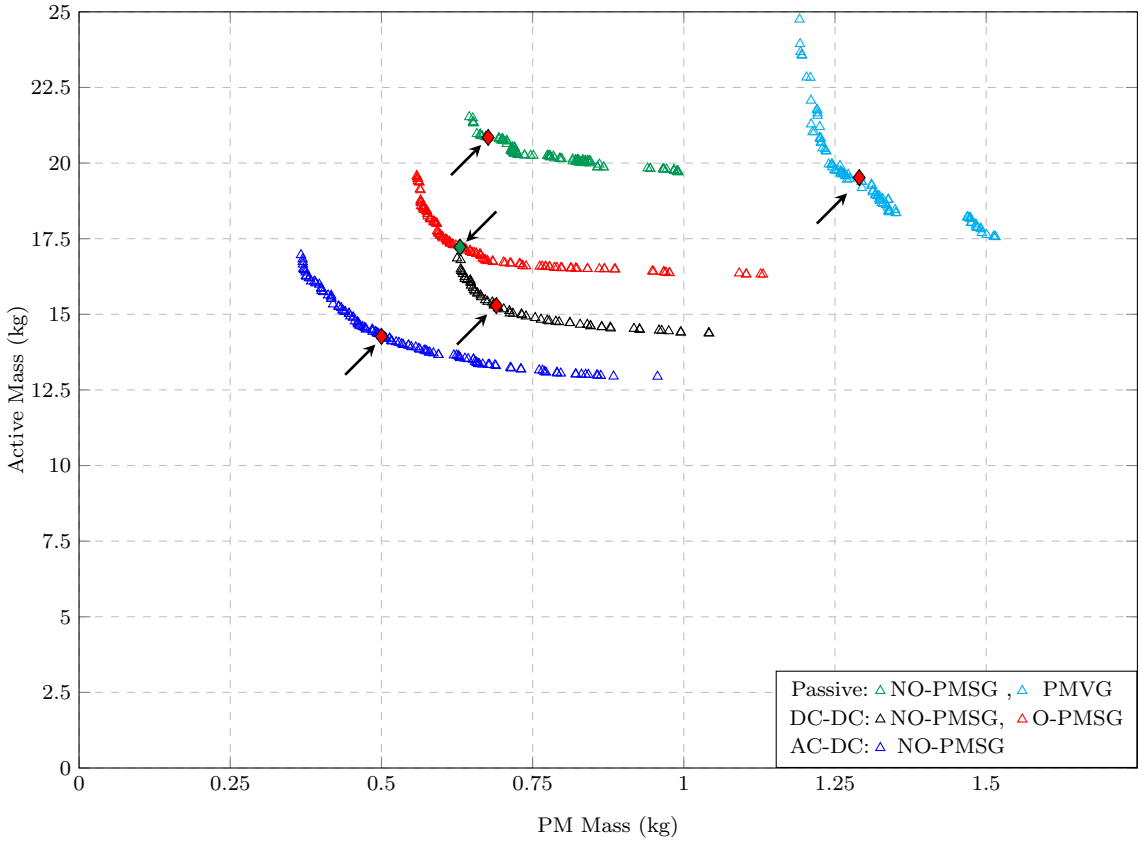

Figure 9.1: Pareto front results comparison for the different 4.2 kW wind energy systems.

9.1 Material Cost Comparison

It is shown in the Pareto front of Fig. 9.1 that the uncontrolled generators for the passive system have a larger active mass than the generators for the controlled systems, as is expected. An estimated per unit material cost breakdown of the optimum generators in Fig. 9.1 is given in Table 9.1. Note that Table 9.1 does not include structural or labour costs, but only the estimated mass-production active material cost. A visual representation of the generator active mass and the estimated per unit cost calculation from Table 9.1 is shown in Fig. 9.2.

For the passive system, it is interesting to note that even though the PMVG is much lighter than the NO-PMSG, that the NO-PMSG's material cost is 26.9% less. The difference in cost can mainly be attributed to the difference in the amount of PM material used. Furthermore, it is shown in Table 9.1 that for both generators the amount PM material contributes to more than half of the total material cost. This outcome emphasises the importance of minimising the generator's PM mass and also highlights how dependent the total material cost is on the volatile price of rare earth PM material. To illustrate this dependency on the price of rare earth material, the cost calculation, as done in Table 9.1,

Table 9.1: Breakdown of estimated per unit active material cost for the 4.2 kW wind generators. (Most expensive generator is taken as base value.)

	Passive		**DC-DC**		**AC-DC**
Generator	NO-PMSG	PMVG	O-PMSG	NO-PMSG	NO-PMSG
Generator active material					
-Iron mass (kg)	11.57	11.98	7.60	8.25	7.02
-PM mass (kg)	0.68	1.29	0.69	0.63	0.50
-Copper mass (kg)	8.60	6.27	7.00	8.34	6.74
Total active mass, M_{active}	21.33	19.48	15.29	17.22	14.27
Active material cost					
-Iron core material ($2.50/kg)	0.095	0.098	0.068	0.062	0.058
-PM material ($164.05/kg)[a]	0.371	0.709	0.346	0.377	0.275
-Copper material ($9.36/kg)[a]	0.265	0.193	0.257	0.215	0.207
Total cost	0.731	1.000	0.671	0.654	0.540

[a] material cost obtained from [12]

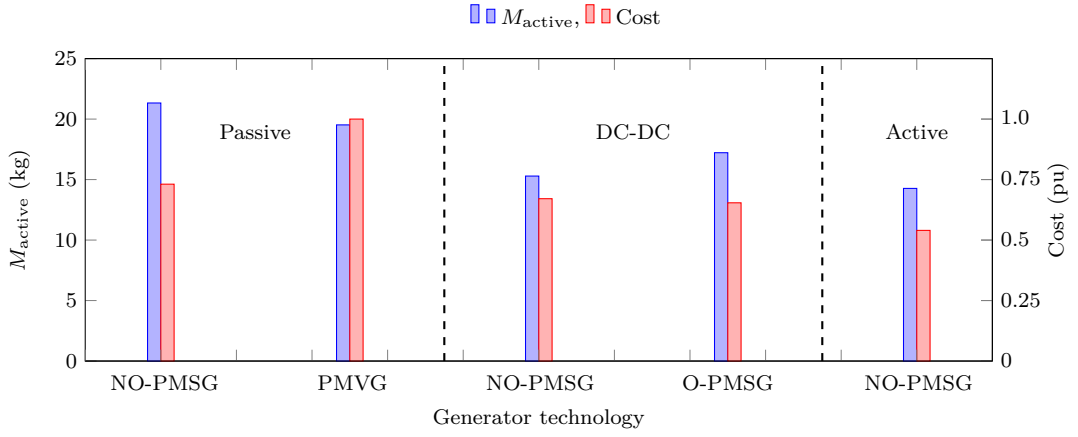

Figure 9.2: Visual comparison of the generator active mass and the total estimated per unit material cost in Table 9.1.

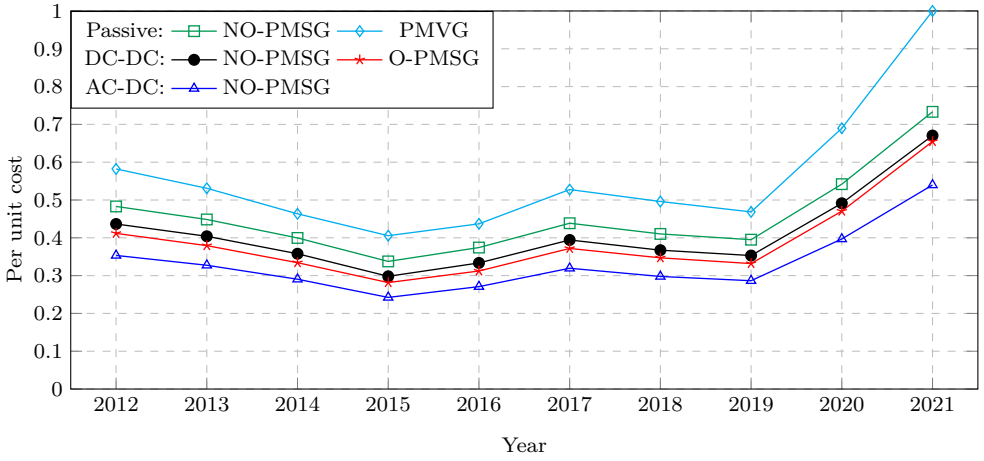

(a) Relative to the PMVG's current cost in 2021.

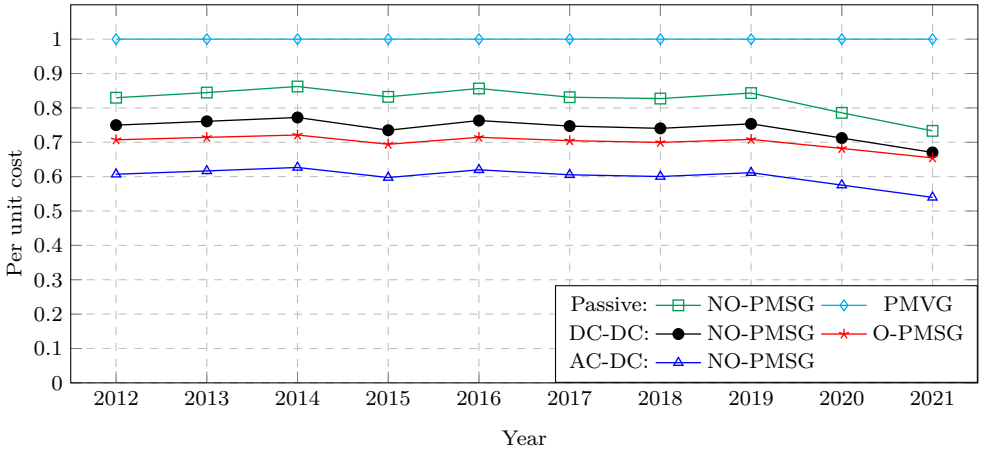

(b) Relative to the PMVG over time.

Figure 9.3: Estimated per unit material cost comparison over time.

is shown for the time period between 2012 and 2021 in Fig. 9.3. In Fig. 9.3(a) it is shown that for the passive system the NO-PMSG is more cost effective when compared to the PMVG, and that this is the case over an extended period of time. However, in Fig. 9.3(b) it is shown that in the last two years the PMVG's active material has become $\approx 10\%$ more expensive than the PMSG's. The same applies for the PMVG when compared to the generators for the controlled wind generator systems. The PMVG is consistently 15-40% more expensive than the rest of the generators over time, and even worse in 2021.

As shown in Table 9.1 and Fig. 9.2, there is not much difference in total generator active mass between the NO-PMSG and O-PMSG for the DC-DC converter system. However, it is interesting that the material cost comparison has the same result as for the passive system. Although the NO-PMSG is the lighter generator, it has more PM material which makes it the more expensive choice. However, the difference in the estimated material cost is a mere 2.5% and can therefore be considered negligible. It should also be noted that the NO-PMSG for the passive system is quite competitive compared to both of the DC-DC converter system's generators in terms of cost, as shown in Table 9.1 and Fig. 9.3.

The active synchronous rectifier controlled wind generator in Table 9.1 is the superior choice in terms of the estimated material cost. This is not an unexpected outcome, since the generator is controlled to have only q-axis current. The results in Table 9.1 and

Fig. 9.3 show that the active material cost of the generators for the DC-DC converter system are ≈ 22% more expensive. The passive system's NO-PMSG is shown to be 35% more expensive, which is not bad considering that the passive system's NO-PMSG is uncontrolled. However, it is shown in Table 9.1 that the PMVG is almost double as expensive in terms of the active material cost.

The estimated material cost comparison is also done for the 15 kW wind generators, as discussed in the following sections.

9.2 Passive System: NO-PMSG versus PMVG

In Chapter 5 the PMVG is investigated as an alternative wind generator technology for the uncontrolled passive wind generator system. Moreover, it is found that PMVGs are well suited for the passive system. Consider the direct comparison of the optimum PMSGs and PMVGs for the 4.2 kW and 15 kW systems in Table 9.2:

It is shown that at both power levels the PMVGs use less active material. However, in both cases the PMVGs are the more expensive generator choice in terms of estimated material cost. This is due to the PMVGs using more PM material and is on average 25% more expensive for both the 4.2 kW and 15 kW system.

It is shown in Table 9.2 that the PMVGs do have better torque quality compared to the PMSGs. However, the PMSGs' torque quality are not undesirable and very close to that of the corresponding PMVGs. The open circuit losses up to n_c, which are predominantly core losses P_{Fe}, are also important. The wind turbine has to overcome these losses at cut-in speed. Hence, the core losses at n_c need to be as low as possible. It is shown in Table 9.2 that the PMSGs have lower core losses at n_c compared to the PMVGs.

Thus, from the above comparison it can be concluded that even though PMVGs are very attractive wind generators for the passive system, the conventional NO-PMSG is still the superior generator choice for this application.

9.3 DC-DC System: NO-PMSG versus O-PMSG

In Chapter 7, the wind generator design for the controlled DC-DC converter wind energy system is investigated. Ultimately, PMSGs with overlapping and non-overlapping windings were investigated to determine which is better suited, i.e. a generator with a long end-winding length and small internal synchronous inductance or a generator with short end-windings and a larger internal synchronous inductance.

It is shown in Table 9.3 that there is essentially no trade-off between the NO-PMSG and the O-PMSG. The results indicate that both factors have an equal effect. The NO-

Table 9.2: Generator comparison for the uncontrolled passive wind generator system.

	4.2 kW		15 kW	
Generator	NO-PMSG	PMVG	NO-PMSG	PMVG
M_{active} (kg)	21.33	19.48	90.73	71.08
M_{PM} (kg)	0.68	1.29	4.30	7.38
Active material cost (pu)	0.731	1.0	0.757	1.0
ΔT_{cog} (%)	1.5	1.1	0.20	0.22
ΔT_r (%)	4.9	1.3	2.94	0.44
P_{Fe} at n_c (W)	13.9	23.3	75.0	157.8

Table 9.3: Generator comparison for the controlled DC-DC connected wind generator system.

Generator	NO-PMSG	O-PMSG (54-28)
M_{active} (kg)	15.29	17.22
M_{PM} (kg)	0.69	0.63
Active material cost (pu)	0.671	0.654
ΔT_{cog} (%)	1.15	2.15
ΔT_{r} (%)	5.03	3.55
P_{Fe} at n_{c} (W)	10.5	10.8

PMSG is the slightly lighter generator, but uses more PM material which results in the O-PMSG being slightly less expensive in terms of active material costs. Furthermore, it is shown in Table 9.3 that the torque quality is the same, as well as the cores losses at n_{c}. This is also the case if the 90-28 O-PMSG in Chapter 7 is used in the comparison.

9.4 System Cost

In this section the system cost is estimated for each of the respective wind energy systems. Where relevant, the optimum generator is used as determined in the previous sections. For this comparison it is assumed that the wind turbine tower structure is fixed and therefore only the generators, the front-end rectifier components and power electronic converters are considered. The transmission cable and battery storage will be the same for all systems and are therefore not taken into account.

The estimated per unit system costs are given in Table 9.4. For both the 4.2 kW and 15 kW wind turbines the passive system's NO-PMSG is the most expensive generator and is taken as the base value. For the power electronic converters it is assumed that the cost is 70 \$/kW, and is based on what is used in [99] and on industry averages in South Africa. In Table 9.4 it is shown that although the uncontrolled passive wind energy systems have more expensive generators, that the estimated per unit system cost is still lower than that of the controlled wind energy systems. For the 4.2 kW power level this is shown to be at least 65% and at the 15 kW power level this is shown to be 22% when compared to the active synchronous rectifier controlled system. The per unit values in Table 9.4 are of course mere estimates. Nonetheless, these per unit values do give more perspective as to why the passive system is so attractive for rural and standalone applications.

A 20 year levelised cost of energy (LCOE) calculation would be an even better technique to evaluate the system cost. However, due to a lack of data for installation and O&M costs, an LCOE is not done and is included in the recommendations for future work

Table 9.4: Estimated per unit system component cost. (Most expensive generator is taken as base value.)

System	**4.2 kW**			**15 kW**	
	Passive	**DC-DC**	**AC-DC**	**Passive**	**AC-DC**
Generator	NO-PMSG	O-PMSG	NO-PMSG	NO-PMSG	NO-PMSG
PM generator	1.0	0.91	0.73	1.0	0.57
Diode rectifier	0.05	0.05	-	0.05	-
DC-DC converter	-	0.97	-	-	-
Active rectifier	-	-	0.97	-	0.70
Total system cost	1.05	1.93	1.70	1.05	1.27

in Chapter 10. The annual power capture from the wind turbine is of course another determining factor, and is discussed in the next section.

9.5 Annual Energy Production

To compare the annual energy production (AEP) of the uncontrolled passive- and controlled active synchronous rectifier wind energy systems[1], two different wind sites are used as case studies. The Weibull distributions for wind site 1 and wind site 2 are both shown in Fig. 9.4. Both wind site examples are from [37], and it is shown in Fig. 9.4 that wind site 1 has a better annual energy production capability compared to wind site 2. Only the optimal generators in Table 9.4 are considered for the AEP comparison.

To calculate the AEP for each wind generator-system combination, the generated power at each wind speed is multiplied by the annual wind speed distributions in Fig. 9.4. The generated power is obtained from each of the respective generators' power matching curves with the relevant 4.2 kW or 15 kW wind turbine. The results for the 4.2 kW systems are shown in Fig. 9.5 and the 15 kW systems' results are shown in Fig. 9.6. Also shown in Figs. 9.5 and 9.6 are the sub-system AEPs, i.e. the annual energy production into the battery energy storage P_{bat}. The predicted sub-system AEP for the passive system is calculated using (6.2.2), taking the losses in the transmission cable and brush-slip-rings into account. For the active synchronous rectifier controlled system's sub-system AEP, the transmission losses are also accounted for and the efficiency of the synchronous rectifier is taken as 96% [37]. It is assumed that the synchronous rectifier's efficiency is constant for all wind speeds. The AEP results in Figs. 9.5 and 9.6 are as expected, with the active synchronous rectifier controlled system being better in terms of AEP performance due to using MPPT. However, it is also shown that the passive system is not that much worse.

For comparison, the respective wind site per annum capacity factors for each system are calculated and summarised in Table 9.5. The capacity factor is calculated as

$$C_{\text{f}} = \frac{\text{AEP}_{\text{tot}}}{\text{AEP}_{\text{max}}}, \tag{9.5.1}$$

where AEP_{tot} is the total annual energy produced in kWh, calculated from the AEP results in Figs. 9.5 and 9.6, and AEP_{max} is the potential maximum annual energy production

[1]The controlled DC-DC converter system will have an identical turbine power capture to the active synchronous rectifier system due to MPPT. As shown in Table 9.4, the DC-DC converter system is also more expensive. Therefore only the active synchronous rectifier system is used in the comparison.

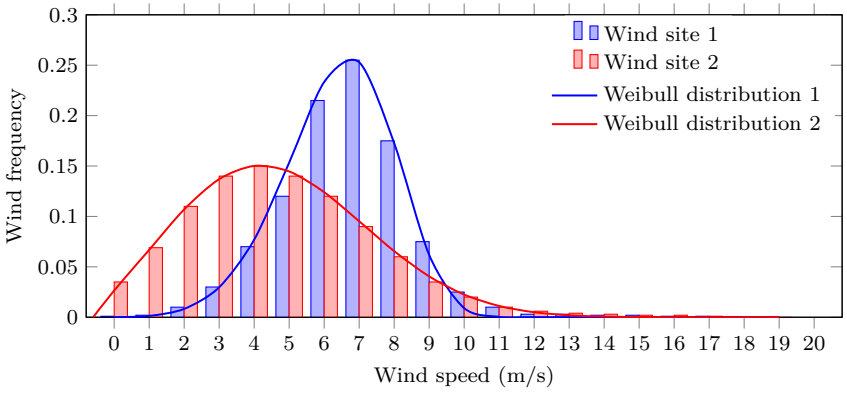

Figure 9.4: Weibull wind distribution at two different wind sites [37].

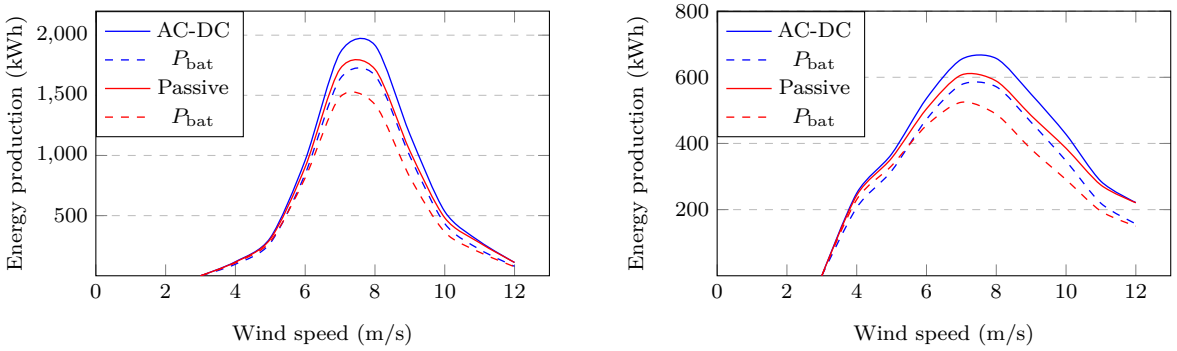

(a) Wind site 1 **(b)** Wind site 2

Figure 9.5: Predicted energy production of the 4.2 kW uncontrolled passive- and active synchronous controlled wind energy system with wind speed a parameter.

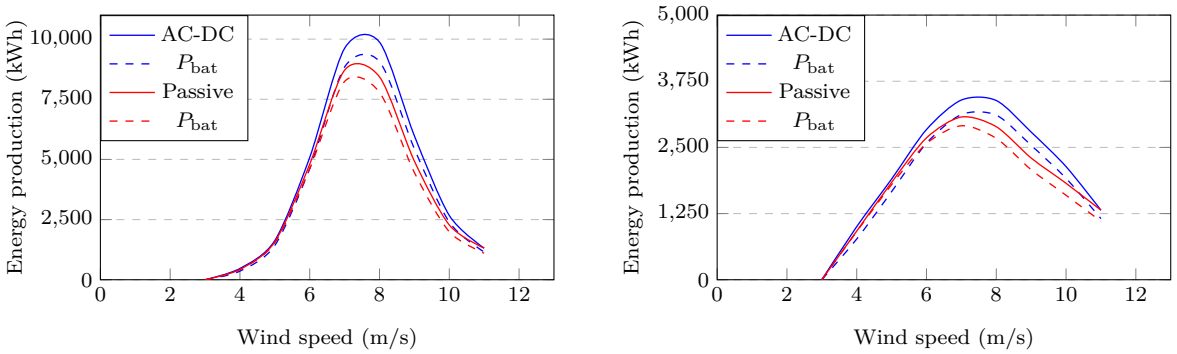

(a) Wind site 1 **(b)** Wind site 2

Figure 9.6: Predicted annual energy production for the 15 kW uncontrolled passive- and active synchronous controlled wind energy system with wind speed a parameter.

Table 9.5: Comparison of wind site capacity factors.

	4.2 kW			**15 kW**		
	Passive	**AC-DC**	**Ratio**	**Passive**	**AC-DC**	**Ratio**
Turbine capacity factor (%)						
-Wind site 1	18.1	19.8	0.917 : 1	24.7	27.9	0.886 : 1
-Wind site 2	10.0	10.7	0.928 : 1	12.8	14.3	0.897 : 1
Sub-system capacity factor (%)						
-Wind site 1	15.2	17.0	0.892 : 1	23.0	25.3	0.905 : 1
-Wind site 2	8.6	9.4	0.917 : 1	11.9	12.8	0.928 : 1
Overall efficiency (%)						
-Wind site 1	77.0	86.2		82.3	90.9	
-Wind site 2	80.1	87.4		83.3	89.8	

calculated with the rated power of either 4.2 kW or 15 kW. It is shown in Table 9.5 that the turbine capacity factor of the 4.2 kW passive system is 91.7% that of the active synchronous rectifier controlled system's capacity factor for wind site 1 and 92.8% for wind site 2. For the 15 kW systems, the passive system's turbine capacity factor is 88.6% that of the active synchronous rectifier controlled system's capacity factor for wind site 1 and 89.7% for wind site 2. Similarly, the sub-system capacity factor, C_{fs}, can also be calculated with (9.5.1) using the P_{bat} results in Figs. 9.5 and 9.6. The sub-system capacity factors are given in Table 9.5 and are used to calculate the overall per annum efficiency, also given in Table 9.5.

Finally, the per unit annual sub-system energy production per cost is calculated by dividing the overall system efficiency in Table 9.5 by the estimated per unit system component cost in Table 9.4. The results are given in Table 9.6. It is shown in Table 9.6 that the 4.2 kW passive system's energy production per cost is between 44-48% more than the active synchronous rectifier controlled system's energy production per cost. For the 15 kW systems, the energy production per cost is shown to be between 9.5-12% more than that of the active synchronous rectifier system. Although the results in Table 9.6 are based off of estimated values, the comparison shows that the uncontrolled passive system is truly a competitive alternative to the controlled wind generator systems. Moreover, it is important to note that the AEP results in Figs. 9.5 and 9.6 do not take downtime due to system failure into account, nor do the cost calculations in Table 9.6 take into account O&M costs. Both of the aforementioned factors will be in favour of the passive system since the risk of electric failure is almost zero.

Table 9.6: Per unit annual sub-system energy production per cost.

	4.2 kW			**15 kW**		
	Passive	**AC-DC**	**Ratio**	**Passive**	**AC-DC**	**Ratio**
Wind site 1	0.733	0.507	1.445 : 1	0.784	0.716	1.095 : 1
Wind site 2	0.763	0.514	1.484 : 1	0.794	0.707	1.122 : 1

9.6 Chapter Summary

In this chapter the cost of the generators, that are specifically designed for each of the wind energy systems in Fig. 1.1, are estimated based on their amount of active material. The active material cost estimation is then used to compare these generators, as well as the total system cost. Subsequently a cost comparison between the PMSG and PMVG for the passive system is done and also between the NO-PMSG and O-PMSG for the DC-DC converter system. Finally, an estimated per unit annual sub-system energy production cost comparison is done between the uncontrolled passive and active synchronous rectifier controlled system using two wind site case studies. To summarise, the outcomes of the comparisons are as follows:

- It is found that the PMVG for the passive system is the most expensive generator. Not only compared to the conventional NO-PMSG that is designed for the passive system, but also compared to the other PMSGs for the controlled systems. Furthermore, it is shown that rare earth PM material is the main contributor to generator cost, and in the case of the PMVG it is detrimental to the outcome.

- It is also shown that for the DC-DC converter system there is nothing to be gained from using PMSGs with either overlapping or non-overlapping windings. The predicted advantages of using either generator type are found to result in an equal outcome.
- It is shown through estimated system costs and annual energy production case studies, that at both 4.2 kW and 15 kW the passive system is the most cost-effective system. Thereby highlighting its advantage for being used in rural and standalone applications.

Chapter 10

Conclusions and Recommendations

This chapter contains the conclusions on wind generator design for small-scale wind energy systems. The conclusions are listed under the relevant research sub-questions, so as to finally answer the main research question of this dissertation. Thereafter, the major contributions that are specific to the work done in this dissertation are stipulated. Recommendations and additional comments for future research are then offered in the last section of this chapter.

10.1 Research Sub-questions

10.1.1 Part 1: Uncontrolled Passive Wind Energy System

1. **Are analytical methods to calculate the external inductance for external impedance matching sufficient or is there a more accurate solution method?**

The first research sub-question is then dealt with in Chapter 3. Therein, an analytical method and a proposed solution method, that uses static FEA to calculate the necessary external inductance, are compared. It is shown that the analytical method to calculate the necessary external inductance is inaccurate when applied to iron-cored PMSGs and can lead to a significant error in power matching with the wind turbine. The proposed solution method on the other hand is shown to be accurate and relatively inexpensive in terms of the total computational time. The accuracy of the proposed static FEA solution method and the improved power matching are confirmed by measured results.

2. **To what extent can external impedance matching be applied in small-scale passive wind energy systems to improve power matching?**

It is shown in Chapter 3 that the external impedance matching method can be used effectively to improve power matching between the wind generator and the wind turbine with 4.2 kW and 12.5 kW case studies. For the 12.5 kW case study, the refurbishment of an existing 15 kW wind generator is investigated for the passive system. It is shown that with external impedance matching, and the solution method to calculate the external inductance, that the existing generator can be effectively recycled. Furthermore, this can be applied to any existing wind generator with a sufficient rated power and wind turbine.

It is also shown that external impedance matching with the proposed solution method can be incorporated into the design optimisation of the wind generator. Although this is

not investigated in detail, it is evident that external impedance matching can be included in wind site-specific design optimisation, maximising annual wind energy harvesting and minimising generator and external inductance sizes.

3. **Can PMSGs be designed for a *natural* impedance matching with the wind turbine? (i.e. there is no external inductance)**

Although external impedance matching can be used effectively, the additional component to the system is unwanted. Therefore, different PMSG structural topologies are considered in Chapter 4 for the design process. The results in Chapter 4 conclude that the answer to the research sub-question is: Yes, PMSGs can be designed for a *natural* impedance matching with the wind turbine.

It is shown that merely using a stator structure with semi-closed slots is sufficient for increasing the PMSG's internal synchronous reactance to have a natural impedance matching with the wind turbine. Embedding the PMs in the rotor is also effective in this regard. However, the PMSG topology with a surface mounted PM rotor and semi-closed stator slots is shown to have better torque quality, and is the most cost-effective option.

4. **What are the alternative PM wind generator technologies, other than the widely used PMSG, and are there any benefits to using these technologies instead?**

Permanent magnet Vernier generators are identified as an alternative candidate for the passive system. Since this is an unknown application for PMVGs, a comprehensive design of different conventional and split-tooth PMVGs are done in Chapter 5.

It is shown that PMVGs are excellently suited for passive wind generator systems. The inherently high internal reactance of PMVGs, which is typically considered to be its main drawback, is found to be advantageous for this application. In terms of the optimal topology, it is found that conventional PMVGs with overlapping windings are superior to split-tooth PMVGs. Furthermore, careful consideration should be taken for the PMVG selection; it is shown that PMVGs with certain magnetic gear ratios are unsuited. The PMVG with $G_r = 8$ is a very attractive generator choice. This PMVG has excellent power matching and performance results, and near ideal torque quality.

However, it is shown with the estimated cost evaluation done in Chapter 9 that PMVGs are approximately 25% more expensive than PMSGs. This is due to PMVGs having a greater amount of rare earth PM material. Therefore, it is still more beneficial to use PMSGs for uncontrolled passive wind energy systems.

5. **How does the uncontrolled passive system compare at different power levels in the small-scale power region?**

A noteworthy observation from literature is that the passive wind energy systems are mostly rated for sub 5 kW power level systems. To evaluate the passive system at higher power levels, 15 kW uncontrolled passive wind energy systems are investigated in Chapter 6, and are evaluated alongside the 4.2 kW passive system. It is shown that the combined resistance of the brush-slip-rings in the turbine's yaw mechanism and the transmission cable can have a significant effect on the system's performance in terms of the power delivered to the battery energy storage, especially for the 4.2 kW passive system. Contrary to the norm in literature, where passive systems are only used at a sub 5 kW power level, it is shown that the passive system is also suited for higher power levels, or where the system resembles a high voltage low current system.

10.1.2 Part 2: Controlled Wind Energy Systems

6. **What is the optimal wind generator technology for the DC-DC controlled wind energy system?**

In Chapter 7, using a PMSG with a non-overlapping winding or a PMSG with an overlapping winding is investigated for the controlled DC-DC converter wind energy system. Essentially, the comparison is done to investigate the trade-off when using a generator with a larger internal synchronous inductance versus a generator with a long end-winding length. It is shown in Chapter 7 that there is very little trade-off between the respective PMSGs. Of the investigated slot-pole combinations, both the NO-PMSG and the respective O-PMSGs meet the desired performance criteria and have excellent torque quality. The optimum NO-PMSG uses less active material, however has more PM material than the O-PMSGs. A cost comparison between the respective generators is done in Chapter 9, where it is shown that the NO-PMSG is slightly more expensive. However, neither the NO-PMSG or O-PMSG has a distinct advantage over the other, indicating that there is essentially no trade-off and that either generator can be used for the controlled DC-DC converter wind energy system.

7. **What are the trade-offs from a generator perspective when using the different wind energy systems?**

To fully address this research sub-question in the dissertation, wind generators are specifically designed for each of the respective wind energy systems with the objective to minimise the active material mass and the PM mass. This is done to collectively minimise the top-tower mass and the overall generator cost. These objectives were identified in Chapter 1 as critical design aspects that must be addressed to make small-scale wind energy more competitive.

For both the 4.2 kW and 15 kW wind turbines it is shown in the design optimisation results that the uncontrolled passive system's wind generators are the heaviest, while the generators for the active synchronous rectifier controlled system use the least amount of active material. By comparison, the 4.2 kW passive system's NO-PMSG and PMVG are 50% and 36% heavier than the active synchronous rectifier controlled system's NO-PMSG. The DC-DC converter system's generators are between 7% and 20% heavier than the active synchronous rectifier controlled system's NO-PMSG. Similarly, the 15 kW passive system's NO-PMSG and PMVG are 37% and 7.5% heavier than the active synchronous rectifier controlled wind generator.

A similar trend is shown in the optimum generator active material cost comparison done in Chapter 9. For the 4.2 kW systems, the passive system's NO-PMSG is 35% more expensive than the active synchronous rectifier controlled system's NO-PMSG. For the 15 kW systems, the difference in generator active material cost is 43%.

All of the wind generators are optimised for the same design constraints and therefore have a similar performance and torque quality. However, the controlled wind generators have better power matching with the wind turbine due to MPPT being used. Nonetheless, it is shown in Chapter 9 that the uncontrolled passive systems still achieve a good capacity factor and sub-system capacity factor when compared to the active synchronous rectifier controlled system. The difference in capacity factor is less that 10% for the 4.2 kW systems, and less than 12% for the 15 kW systems. This is a remarkable result in terms of the generator trade-off, given that the passive system's generators are designed for a natural impedance matching, i.e. no method of control is used to match the

generated power with the available power from the wind turbine. Moreover, it is shown that the passive system is the most cost-effective system when taking the converters of the controlled wind energy systems into account. Ultimately, it is shown that the passive systems are superior in terms of the estimated annual sub-system energy production per cost, although somewhat overestimated in the study because labour and other costs regarding the generator were ignored. The 4.2 kW passive system's energy production per cost is between 44-48% more than the active synchronous rectifier controlled system's energy production per cost. For the 15 kW systems, the energy production per cost is shown to be between 9.5-12% more than that of the active synchronous rectifier system. Thereby, confirming that the passive system is the most cost-competitive system.

10.2 Main Research Question

Can wind generators in small-scale uncontrolled passive wind energy systems be designed to make the system more competitive, and which properties make it a better alternative for the small-scale wind energy industry?

By critically evaluating the results presented in this dissertation, and answering the preceding research sub-questions, it is concluded that wind generators in small-scale uncontrolled passive wind energy systems can be designed to make the system more competitive:
- It is shown that wind generators for the uncontrolled passive system can be designed for a natural impedance matching without requiring any external inductance connected between the wind generator and the battery energy storage. Moreover, the optimised wind generators achieve good power matching with the wind turbine at lower wind speeds, while still matching with the maximum available power from the wind turbine at the rated operating point. Ultimately, it is shown that the annual energy production for the uncontrolled passive system is competitive when compared to the controlled wind energy systems that use MPPT. Therefore, the design- and solution methods presented in this dissertation for improved power matching are deemed effective.
- The optimised wind generators for the passive system are heavier and more expensive than the wind generators that are optimised for the controlled wind energy systems. However, when comparing the different front-end rectifier connected systems in terms of the estimated annual sub-system energy production per cost, it is shown that the uncontrolled passive system is the most cost-effective system. A 20 year levelised cost of energy calculation is not done in this dissertation. However, the result will favour the passive system even more. Therefore, considering the passive system's installation costs, the system's reliability, and the system performance, it is concluded that uncontrolled passive wind energy systems should be the preferred choice for small-scale wind energy systems that are deployed in rural locations for standalone application.

10.3 Contributions

Firstly, it should be pointed out that the existing literature on generator design for small-scale uncontrolled passive wind energy systems is very limited. The design methodology for these generators are also deemed insufficient by the author, since they do not guarantee satisfactory power matching with the wind turbine. Given the aforementioned shortcomings, significant strides are made in improving the design of wind generator technology

for uncontrolled passive wind energy systems in this dissertation. The main contributions of this dissertation are summarised as follows:

1. In the global context for small-scale wind energy systems, reinstallations and the refurbishment of system components are very relevant. Therefore, the external impedance matching method and proposed solution method (to accurately calculate the necessary external inductance) are a significant contribution, and offer a cost-effective alternative for the small-scale wind energy industry.

2. It is shown that conventional PMSGs can be designed for a natural impedance matching to have good power matching with the available power from the wind turbine. In doing so, a well founded argument can now be made to use the uncontrolled passive system instead of the standard actively controlled wind energy systems; the passive system is geographically independent, and more cost-effective.

3. Using a PM Vernier generator in an uncontrolled passive wind energy system is a new and unknown concept. The PMVG design and built prototype presented in this dissertation is a definite contribution to literature. It is shown in this dissertation that PMVGs are well suited for this application and can have desirable performance. Even if the PMVGs in this dissertation are found to be more expensive than the conventional PMSG, there are topologies that can potentially reduce the amount of PM material. More is said on this in the recommendations for future work.

4. Up until now, uncontrolled passive systems have only been investigated at sub 5 kW power levels. Although it is a minor contribution, it is shown in this dissertation that uncontrolled passive systems are feasible for higher power levels (< 20 kW).

10.4 Recommendations for Future Work

10.4.1 New PMs for Prototypes

The optimised PMSG and PMVG prototypes in Chapters 4 and 5 did not have the desired power matching due to the manufacturing tolerances of the PMs. However, it is shown in Chapters 4 and 5 that the prototypes' results can be accounted for, and that the FEA designs are accurate. Therefore, the existing PMs of the prototypes should be replaced with new PMs where the manufacturing tolerances are taken into account; both prototypes have a uniform and large enough air gap so that slightly thicker PMs will not hinder the rotational freedom of the machine.

Both prototypes will then have the desired power matching with the wind turbine and an overall improved generator performance. These prototypes can then be used for further scientific experiments and data logging, as explained in the next recommendation.

10.4.2 Levelised Cost of Energy

As mentioned in Chapter 9, a good method for comparing and determining the viability of renewable energy systems is to do a 20 year levelised cost of energy (LCOE) calculation. The levelised cost of energy is typically calculated as

$$\text{LCOE} = \frac{\text{ICC} + \text{O\&M}}{\text{AEP}_{\text{net}}}, \tag{10.4.1}$$

where ICC is the installed capital cost, O&M is the yearly operation and maintenance cost and AEP_{net} is the net annual energy production per year (kWh).

In this dissertation, the 20 year LCOE is not done due to a lack of data concerning the ICC and O&M costs. It is recommended that this be further investigated. Especially the LCOE for the uncontrolled passive wind energy systems, since no such study has been done in literature. Moreover, the renewed PMSG and PMVG prototypes for the passive system, as explained in the previous recommendation, can be mounted onto the existing 4.2 kW wind turbine shown in Fig. 2.8(a). This practical setup can then be used to obtain field measurements at the actual wind site. The outcome of such a study will be a significant contribution and will provide invaluable measured results.

Furthermore, comparing the in depth LCOE calculations for the various front-end rectifier connected wind energy systems should also be done in a comparative study. Thereby, obtaining a holistic picture of the cost for small-scale wind energy systems.

10.4.3 Consequent-pole Generators

Machines with consequent-pole PM rotors are not considered in this dissertation due to the machine topology's inherent sensitivity regarding torque quality (and due to the limited time in which the dissertation must be completed). As mentioned, good torque quality is paramount for small-scale wind generators, specifically a low cogging torque. However, it is shown in this dissertation that rare earth PM material contributes substantially to the generator's active material cost. The cost of PM material is also very volatile.

Using a PMSG or PMVG with a consequent-pole PM rotor can potentially reduce the amount of PM material by a substantial amount. Therefore, based on the results presented in this dissertation, it is justifiable to consider consequent-pole PM generators for small-scale wind generators. It is thus recommended that the design of consequent-pole PMSGs and PMVGs be done for the uncontrolled passive wind energy system shown in Fig. 1.1(a). However, methods to reduce the generator's cogging torque should be of the utmost importance in the proposed investigation.

Appendices

Appendix A

Harmonic Analysis

In this appendix, the harmonic analysis of non-overlapping and overlapping windings are described. The harmonic analysis is used throughout the dissertation to evaluate the harmonic content of different generators, and to calculate their differential harmonic leakage flux coefficients. Subsequently, simple formulae to calculate the machines' winding factors are also given. The non-overlapping winding harmonic analysis is adapted from [100], and the overlapping winding harmonic analysis is adapted from [101] and [102].

A.1 Non-overlapping winding

A.1.1 Winding Parameters and Definitions

For the first part of the non-overlapping winding's analysis, some of the machine and winding parameters are defined:
The number of stator coils is given by

$$N_{\text{sc}} = \frac{Q_{\text{s}} N_{\text{L}}}{2}, \tag{A.1.1}$$

where N_{L} is the number of coil layers in a slot. Here, $N_{\text{L}} = 1$ denotes a single layer winding and $N_{\text{L}} = 2$ is for a double layer winding.
The number of machine sections that repeat within a machine are calculated using the greatest common divisor between the number of stator pole pairs, p_{s}, and the number of stator coils, N_{sc}.

$$M_{\text{s}} = \text{GCD}(p_{\text{s}}, N_{\text{sc}}) \tag{A.1.2}$$

The number of winding sections that repeat throughout the machine itself is then determined by

$$W_{\text{s}} = \text{GCD}(2p_{\text{s}}, N_{\text{sc}}). \tag{A.1.3}$$

The periodicity of the machine, τ_{per}, is determined by dividing the number of repeating winding sections, W_{s}, by the number of machine sections, M_{s}. If $\tau_{\text{per}} = 1$ the machine has positive periodicity and if $\tau_{\text{per}} = 2$ the machine has negative periodicity.

$$\tau_{\text{per}} = \frac{W_{\text{s}}}{M_{\text{s}}} \tag{A.1.4}$$

The number of coils distributed in a coil phase group are determined by

$$u = \frac{N_{\text{sc}}}{mW_{\text{s}}} = \frac{N_{\text{sc}}}{3W_{\text{s}}}. \tag{A.1.5}$$

The u-coil flux linkage and induced voltage space phasors of the $\nu_{\text{s}}^{\text{th}}$ order harmonic are phase-displaced by the electric angle

$$\delta_{\text{s}} = \begin{Bmatrix} 2\theta_{\text{s}} & N_{\text{L}} = 1 \\ \theta_{\text{s}} + \frac{\pi}{|\nu_{\text{s}}|} & N_{\text{L}} = 2 \end{Bmatrix}, \tag{A.1.6}$$

where θ_{s} is the average electrical slot pitch angle given by

$$\theta_{\text{s}} = \frac{2\pi M_{\text{s}}}{Q_{\text{s}}}. \tag{A.1.7}$$

A.1.2 Stator Armature Winding MMF Harmonics

As derived in [100], the ν^{th} order MMF spacial harmonic for a phase group of u coils is expressed as

$$F_{\text{ph}\nu} = A_\nu i \cos\left(\nu(\theta - \alpha_\nu)\right) \tag{A.1.8}$$

where A_ν is the ν^{th} order machine constant given by

$$A_\nu = \frac{2\tau_{\text{per}} u N_{\text{s}}}{\pi|\nu|} k_{\text{w}\nu}. \tag{A.1.9}$$

In (A.1.9), $k_{\text{w}\nu}$ is the ν^{th} order winding factor given by

$$k_{\text{w}\nu} = k_{\text{p}\nu} k_{\text{d}\nu}, \tag{A.1.10}$$

where $k_{\text{p}\nu}$ and $k_{\text{d}\nu}$ are the ν^{th} order coil pitch factor and distribution factor given by

$$k_{\text{p}\nu} = \sin\left(\frac{|\nu|\theta_{\text{s}}}{2}\right) \tag{A.1.11}$$

and

$$k_{\text{d}\nu} = \frac{\sin(|\nu| u \delta_{\text{s}}/2)}{u \sin(|\nu|\delta_{\text{s}}/2)} \tag{A.1.12}$$

respectively. The angle α_ν in (A.1.8) is given by

$$\alpha_\nu = (u-1)\frac{\delta_\nu}{2}. \tag{A.1.13}$$

Thus, the ν^{th} order 3-phase winding MMF harmonic is given by

$$F_\nu = A_\nu \left[i_{\text{a}} \cos(\theta - \alpha_\nu) + i_{\text{b}} \cos(\theta - \alpha_\nu - \frac{2\pi}{3}) + i_{\text{c}} \cos(\theta - \alpha_\nu + \frac{2\pi}{3}) \right]. \tag{A.1.14}$$

Subsequently, if the phase currents are

$$[i_{\text{abc}}] = \begin{bmatrix} I \sin(\omega_{\text{e}} t) \\ I \sin(\omega_{\text{e}} t - \frac{2\pi}{3}) \\ I \sin(\omega_{\text{e}} t + \frac{2\pi}{3}) \end{bmatrix}, \tag{A.1.15}$$

where I is the peak phase current, F_ν is expressed as

$$F_\nu = \frac{3A_\nu I}{2z} \sin\left[\omega_e t + \nu(\theta - \alpha_\nu)\right]. \tag{A.1.16}$$

The order of the MMF harmonics in (A.1.16) are described by the series

$$\nu = 3\tau_{per}k - 1, \quad k \in \mathbb{Z}. \tag{A.1.17}$$

Thus, the order of the MMF harmonics are given in (A.1.18), with the sign of the harmonic order indicating the direction of the travelling wave.

$$\nu = \begin{Bmatrix} -1, & 2, & -4, & 5, & -7, & 8, & -10, & 11... & \tau_{per} = 1 \\ -1, & & & 5, & -7, & & & 11... & \tau_{per} = 2 \end{Bmatrix} \tag{A.1.18}$$

A.2 Overlapping windings

For the overlapping windings, the classical harmonic analysis is used as in [101] and [102]. The ν^{th} order MMF space harmonic for a phase is given by

$$F_{ph\nu} = A_\nu i \cos(\nu\theta), \tag{A.2.1}$$

where the ν^{th} order machine constant is given by

$$A_\nu = \frac{2k_{w\nu}N_s}{\pi p_s \nu}. \tag{A.2.2}$$

The winding factor is calculated as

$$k_{w\nu} = k_{p\nu}k_{d\nu}, \tag{A.2.3}$$

where $k_{p\nu}$ is the coil pitch factor and $k_{d\nu}$ is the distribution factor. The ν^{th} order coil pitch factor is calculated using

$$k_{p\nu} = \sin\left(\nu\frac{\pi c_p}{2mq}\right), \tag{A.2.4}$$

where c_p is the coil pitch in terms of the number of slots. The ν^{th} order distribution factor is calculated using

$$k_{d\nu} = \frac{\sin\left(\nu\frac{\sigma}{2}\right)}{q\sin\left(\nu\frac{\sigma}{2q}\right)}, \tag{A.2.5}$$

where σ is the electrical angle of a phase-band in radians given by

$$\sigma = q\left(\frac{2\pi p_s}{Q_s}\right). \tag{A.2.6}$$

The MMF for the 3-phase winding is thus given by

$$F_\nu = \frac{3A_\nu I}{2z} \sin\left[\omega_e t - \nu\theta\right]. \tag{A.2.7}$$

Appendix B

Tables for End-winding Constants

The values for k_2 in (3.1.13) can be found in the lookup tables, Tables B.1 and B.2 in this appendix, and are from [80]. In Tables B.1 and B.2, $a = r_c$ as defined in Fig. 3.5(b) and $c = h_s$ as defined in Fig. 3.4. For K_1, $b = b_{sc}$ and for K_2, $b = 2b_{sc}$. If $c/b \leq 1$ then Table B.1 should be used. If $b/c \leq 1$ then Table B.2 should be used.

Table B.1: Lookup table for k_2 [80].

c/b	c/2a					c/b
	0.05	0.10	0.15	0.20	0.25	
0.00	0.0325	0.0633	0.0925	0.1200	0.1458	0.00
0.05	0.0316	0.0621	0.0911	0.1186	0.1445	0.05
0.10	0.0308	0.0608	0.0896	0.1170	0.1428	0.10
0.15	0.0300	0.0594	0.0879	0.1151	0.1409	0.15
0.20	0.0293	0.0581	0.0861	0.1131	0.1388	0.20
0.25	0.0286	0.0569	0.0843	0.1109	0.1365	0.25
0.30	0.0280	0.0557	0.0826	0.1085	0.1342	0.30
0.35	0.0274	0.0546	0.0810	0.1069	0.1319	0.35
0.40	0.0269	0.0535	0.0796	0.1051	0.1297	0.40
0.45	0.0264	0.0525	0.0782	0.1033	0.1276	0.45
0.50	0.0259	0.0516	0.0769	0.1016	0.1256	0.50
0.55	0.0254	0.0507	0.0755	0.0999	0.1236	0.55
0.60	0.0250	0.0498	0.0742	0.0982	0.1216	0.60
0.65	0.0246	0.0490	0.0730	0.0966	0.1197	0.65
0.70	0.0242	0.0482	0.0719	0.0952	0.1179	0.70
0.75	0.0238	0.0474	0.0708	0.0937	0.1161	0.75
0.80	0.0234	0.0467	0.0697	0.0923	0.1144	0.80
0.85	0.0230	0.0460	0.0687	0.0910	0.1128	0.85
0.90	0.0227	0.0453	0.0677	0.0897	0.1113	0.90
0.95	0.0224	0.0447	0.0667	0.0884	0.1097	0.95
1.00	0.0221	0.0441	0.0658	0.0872	0.1082	1.00
	0.30	0.35	0.40	0.45	0.50	
0.00	0.1700	0.1925	0.2133	0.2325	0.2500	0.00
0.05	0.1687	0.1913	0.2123	0.2317	0.2494	0.05
0.10	0.1671	0.1898	0.2109	0.2304	0.2484	0.10
0.15	0.1651	0.1879	0.2091	0.2288	0.2470	0.15
0.20	0.1630	0.1858	0.2071	0.2270	0.2453	0.20
0.25	0.1607	0.1835	0.2048	0.2248	0.2432	0.25
0.30	0.1583	0.1810	0.2024	0.2224	0.2410	0.30
0.35	0.1558	0.1785	0.1999	0.2199	0.2386	0.35
0.40	0.1533	0.1759	0.1973	0.2174	0.2361	0.40
0.45	0.1510	0.1732	0.1945	0.2146	0.2335	0.45
0.50	0.1487	0.1706	0.1916	0.2118	0.2308	0.50
0.55	0.1464	0.1682	0.1890	0.2091	0.2280	0.55
0.60	0.1442	0.1658	0.1866	0.2065	0.2252	0.60
0.65	0.1421	0.1635	0.1842	0.2039	0.2225	0.65
0.70	0.1400	0.1613	0.1818	0.2014	0.2199	0.70
0.75	0.1380	0.1591	0.1794	0.1988	0.2173	0.75
0.80	0.1360	0.1569	0.1770	0.1963	0.2147	0.80
0.85	0.1341	0.1548	0.1747	0.1939	0.2121	0.85
0.90	0.1323	0.1527	0.1725	0.1915	0.2096	0.90
0.95	0.1305	0.1507	0.1704	0.1892	0.2071	0.95
1.00	0.1288	0.1489	0.1683	0.1869	0.2047	1.00
	0.55	0.60	0.65	0.70	0.75	
0.00	0.2658	0.2800	0.2925	0.3033	0.3125	0.00
0.05	0.2655	0.2800	0.2928	0.3040	0.3135	0.05
0.10	0.2648	0.2795	0.2926	0.3040	0.3138	0.10
0.15	0.2636	0.2786	0.2920	0.3037	0.3139	0.15
0.20	0.2621	0.2773	0.2910	0.3031	0.3136	0.20
0.25	0.2603	0.2758	0.2897	0.3021	0.3129	0.25
0.30	0.2582	0.2739	0.2881	0.3007	0.3118	0.30
0.35	0.2559	0.2718	0.2862	0.2991	0.3104	0.35
0.40	0.2535	0.2695	0.2841	0.2972	0.3088	0.40
0.45	0.2509	0.2671	0.2818	0.2951	0.3070	0.45
0.50	0.2483	0.2645	0.2794	0.2929	0.3050	0.50
0.55	0.2456	0.2619	0.2769	0.2906	0.3028	0.55
0.60	0.2428	0.2592	0.2743	0.2881	0.3005	0.60
0.65	0.2400	0.2564	0.2716	0.2856	0.2981	0.65
0.70	0.2373	0.2536	0.2689	0.2830	0.2957	0.70
0.75	0.2346	0.2509	0.2662	0.2804	0.2932	0.75
0.80	0.2320	0.2483	0.2636	0.2777	0.2906	0.80
0.85	0.2294	0.2456	0.2609	0.2750	0.2880	0.85
0.90	0.2268	0.2430	0.2582	0.2724	0.2855	0.90
0.95	0.2242	0.2404	0.2556	0.2698	0.2829	0.95
1.00	0.2217	0.2378	0.2530	0.2672	0.2804	1.00
	0.80	0.85	0.90	0.95	1.00	
0.00	0.3200	0.3258	0.3300	0.3325	0.3333	0.00
0.05	0.3213	0.3275	0.3321	0.3351	0.3363	0.05
0.10	0.3221	0.3287	0.3337	0.3371	0.3388	0.10
0.15	0.3225	0.3294	0.3349	0.3386	0.3408	0.15
0.20	0.3225	0.3298	0.3356	0.3397	0.3423	0.20
0.25	0.3221	0.3298	0.3359	0.3404	0.3434	0.25
0.30	0.3213	0.3294	0.3359	0.3408	0.3441	0.30
0.35	0.3202	0.3286	0.3355	0.3407	0.3445	0.35
0.40	0.3189	0.3276	0.3347	0.3403	0.3445	0.40
0.45	0.3173	0.3263	0.3337	0.3397	0.3442	0.45
0.50	0.3156	0.3248	0.3326	0.3389	0.3436	0.50
0.55	0.3137	0.3231	0.3311	0.3377	0.3428	0.55
0.60	0.3116	0.3213	0.3295	0.3363	0.3417	0.60
0.65	0.3093	0.3192	0.3277	0.3348	0.3404	0.65
0.70	0.3070	0.3171	0.3258	0.3331	0.3390	0.70
0.75	0.3046	0.3149	0.3238	0.3313	0.3375	0.75
0.80	0.3022	0.3126	0.3217	0.3294	0.3358	0.80
0.85	0.2998	0.3103	0.3195	0.3274	0.3340	0.85
0.90	0.2973	0.3079	0.3172	0.3253	0.3321	0.90
0.95	0.2949	0.3055	0.3149	0.3231	0.3301	0.95
1.00	0.2929	0.3031	0.3126	0.3209	0.3281	1.00

Table B.2: Lookup table for k_2 [80].

c/b	c/2a					c/b
	0.05	0.10	0.15	0.20	0.25	
0.00	0.0325	0.0633	0.0925	0.1200	0.1458	0.00
0.05	0.0316	0.0621	0.0911	0.1186	0.1445	0.05
0.10	0.0308	0.0608	0.0896	0.1170	0.1428	0.10
0.15	0.0300	0.0594	0.0879	0.1151	0.1409	0.15
0.20	0.0293	0.0581	0.0861	0.1131	0.1388	0.20
0.25	0.0286	0.0569	0.0843	0.1109	0.1365	0.25
0.30	0.0280	0.0557	0.0826	0.1085	0.1342	0.30
0.35	0.0274	0.0546	0.0810	0.1069	0.1319	0.35
0.40	0.0269	0.0535	0.0796	0.1051	0.1297	0.40
0.45	0.0264	0.0525	0.0782	0.1033	0.1276	0.45
0.50	0.0259	0.0516	0.0769	0.1016	0.1256	0.50
0.55	0.0254	0.0507	0.0755	0.0999	0.1236	0.55
0.60	0.0250	0.0498	0.0742	0.0982	0.1216	0.60
0.65	0.0246	0.0490	0.0730	0.0966	0.1197	0.65
0.70	0.0242	0.0482	0.0719	0.0952	0.1179	0.70
0.75	0.0238	0.0474	0.0708	0.0937	0.1161	0.75
0.80	0.0234	0.0467	0.0697	0.0923	0.1144	0.80
0.85	0.0230	0.0460	0.0687	0.0910	0.1128	0.85
0.90	0.0227	0.0453	0.0677	0.0897	0.1113	0.90
0.95	0.0224	0.0447	0.0667	0.0884	0.1097	0.95
1.00	0.0221	0.0441	0.0658	0.0872	0.1082	1.00
	0.30	0.35	0.40	0.45	0.50	
0.00	0.1700	0.1925	0.2133	0.2325	0.2500	0.00
0.05	0.1687	0.1913	0.2123	0.2317	0.2494	0.05
0.10	0.1671	0.1898	0.2109	0.2304	0.2484	0.10
0.15	0.1651	0.1879	0.2091	0.2288	0.2470	0.15
0.20	0.1630	0.1858	0.2071	0.2270	0.2453	0.20
0.25	0.1607	0.1835	0.2048	0.2248	0.2432	0.25
0.30	0.1583	0.1810	0.2024	0.2224	0.2410	0.30
0.35	0.1558	0.1785	0.1999	0.2199	0.2386	0.35
0.40	0.1533	0.1759	0.1973	0.2174	0.2361	0.40
0.45	0.1510	0.1732	0.1945	0.2146	0.2335	0.45
0.50	0.1487	0.1706	0.1916	0.2118	0.2308	0.50
0.55	0.1464	0.1682	0.1890	0.2091	0.2280	0.55
0.60	0.1442	0.1658	0.1866	0.2065	0.2252	0.60
0.65	0.1421	0.1635	0.1842	0.2039	0.2225	0.65
0.70	0.1400	0.1613	0.1818	0.2014	0.2199	0.70
0.75	0.1380	0.1591	0.1794	0.1988	0.2173	0.75
0.80	0.1360	0.1569	0.1770	0.1963	0.2147	0.80
0.85	0.1341	0.1548	0.1747	0.1939	0.2121	0.85
0.90	0.1323	0.1527	0.1725	0.1915	0.2096	0.90
0.95	0.1305	0.1507	0.1704	0.1892	0.2071	0.95
1.00	0.1288	0.1489	0.1683	0.1869	0.2047	1.00
	0.55	0.60	0.65	0.70	0.75	
0.00	0.2658	0.2800	0.2925	0.3033	0.3125	0.00
0.05	0.2655	0.2800	0.2928	0.3040	0.3135	0.05
0.10	0.2648	0.2795	0.2926	0.3040	0.3138	0.10
0.15	0.2636	0.2786	0.2920	0.3037	0.3139	0.15
0.20	0.2621	0.2773	0.2910	0.3031	0.3136	0.20
0.25	0.2603	0.2758	0.2897	0.3021	0.3129	0.25
0.30	0.2582	0.2739	0.2881	0.3007	0.3118	0.30
0.35	0.2559	0.2718	0.2862	0.2991	0.3104	0.35
0.40	0.2535	0.2695	0.2841	0.2972	0.3088	0.40
0.45	0.2509	0.2671	0.2818	0.2951	0.3070	0.45
0.50	0.2483	0.2645	0.2794	0.2929	0.3050	0.50
0.55	0.2456	0.2619	0.2769	0.2906	0.3028	0.55
0.60	0.2428	0.2592	0.2743	0.2881	0.3005	0.60
0.65	0.2400	0.2564	0.2716	0.2856	0.2981	0.65
0.70	0.2373	0.2536	0.2689	0.2830	0.2957	0.70
0.75	0.2346	0.2509	0.2662	0.2804	0.2932	0.75
0.80	0.2320	0.2483	0.2636	0.2777	0.2906	0.80
0.85	0.2294	0.2456	0.2609	0.2750	0.2880	0.85
0.90	0.2268	0.2430	0.2582	0.2724	0.2855	0.90
0.95	0.2242	0.2404	0.2556	0.2698	0.2829	0.95
1.00	0.2217	0.2378	0.2530	0.2672	0.2804	1.00
	0.80	0.85	0.90	0.95	1.00	
0.00	0.3200	0.3258	0.3300	0.3325	0.3333	0.00
0.05	0.3213	0.3275	0.3321	0.3351	0.3363	0.05
0.10	0.3221	0.3287	0.3337	0.3371	0.3388	0.10
0.15	0.3225	0.3294	0.3349	0.3386	0.3408	0.15
0.20	0.3225	0.3298	0.3356	0.3397	0.3423	0.20
0.25	0.3221	0.3298	0.3359	0.3404	0.3434	0.25
0.30	0.3213	0.3294	0.3359	0.3408	0.3441	0.30
0.35	0.3202	0.3286	0.3355	0.3407	0.3445	0.35
0.40	0.3189	0.3276	0.3347	0.3403	0.3445	0.40
0.45	0.3173	0.3263	0.3337	0.3397	0.3442	0.45
0.50	0.3156	0.3248	0.3326	0.3389	0.3436	0.50
0.55	0.3137	0.3231	0.3311	0.3377	0.3428	0.55
0.60	0.3116	0.3213	0.3295	0.3363	0.3417	0.60
0.65	0.3093	0.3192	0.3277	0.3348	0.3404	0.65
0.70	0.3070	0.3171	0.3258	0.3331	0.3390	0.70
0.75	0.3046	0.3149	0.3238	0.3313	0.3375	0.75
0.80	0.3022	0.3126	0.3217	0.3294	0.3358	0.80
0.85	0.2998	0.3103	0.3195	0.3274	0.3340	0.85
0.90	0.2973	0.3079	0.3172	0.3253	0.3321	0.90
0.95	0.2949	0.3055	0.3149	0.3231	0.3301	0.95
1.00	0.2929	0.3031	0.3126	0.3209	0.3281	1.00

Appendix C

Vernier Machine Principle

PM Vernier generators are investigated in Chapter 5 for the uncontrolled passive wind generator system. However, there are still eluding fundamentals of the Vernier machine's operation that require more clarity for readers that are not familiar with this technology. In this appendix, an in depth analytical explanation of the vernier machine's working principle is given. The bulk of this appendix consists of work from [40], a technical report by the author, and is mainly adapted from [88] and [103]. The aim of this chapter is to theoretically present the basic working principle of harmonic coupling, and to show how flux modulation is utilised in Vernier machines.

C.1 Vernier Machines Working Principle

For the theoretical explanation, a surface mounted PM Vernier machine structure is used. To simplify the analytical analysis, the machine's geometry is linearised as shown in Fig. C.1. The conventional Vernier machine topology is used, where the stator teeth act as the modulator. Open slots are used and the stator winding is a double layer distributed winding (overlapping winding).

The relevant mechanical angles on the stator and rotor in Fig. C.1 are defined as follows: $\theta_f = 0$ is the reference position on the stator and taken in the middle of a stator slot, $\theta_s = 0$ is the armature winding's positive magnetic axis for phase A (i.e. flux is in the direction from the rotor to the stator), $\theta_r = 0$ is at the center of a particular PM

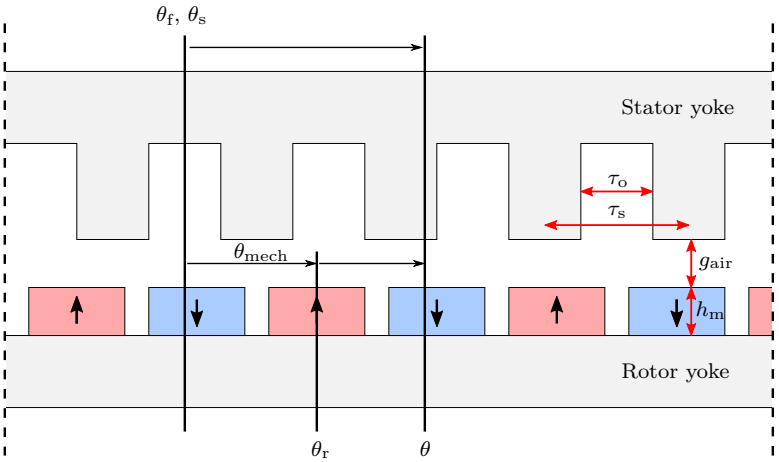

Figure C.1: Linearised geometry of a typical surface mounted PM Vernier machine. (Adapted from [55] and [88])

pole with the PM magnetised in the direction of the stator. Subsequently, the mechanical rotor position is defined as $\theta_{\text{mech}} = \theta_{\text{f}} - \theta_{\text{r}}$.

Other relevant dimensions defined in Fig. C.1 are the air gap length g_{air}, the height of the magnet h_{m}, the slot-pitch τ_{o}, and the slot-opening pitch τ_{s}.

C.1.1 Flux Modulation in the Air gap

Understanding the flux modulation effect taking place in Vernier machines is an integral part of understanding how harmonic coupling is utilised to produce torque. This concept can seem abstract, because it is very different from typical AC machines with a single working harmonic. Therefore, in this subsection, the flux modulation effect is first considered separately from the harmonic coupling that is taking place.

C.1.1.1 Air gap Flux Distribution due to the PM Rotor

For a surface mounted PM rotor, with uniformly magnetised PMs, the magnetisation vector in the airgap is given by

$$\vec{M} = \vec{M}_{\text{r}}\vec{r} + \vec{M}_{\theta}\vec{\theta}. \tag{C.1.1}$$

The magnetisation vector in (C.1.1) is given in polar coordinates, consisting of a radial and tangential component. However, because the surface mounted PMs are magnetised only in the radial direction, the magnetisation vector will be perpendicular to the curvature of the PMs surface. It is therefore accurate to assume that the tangential component in (C.1.1) is zero, i.e $\vec{M}_{\theta}\vec{\theta} = 0$. The radial component in (C.1.1) is given by

$$\vec{M_{r,n}} = \frac{4}{n\pi}\frac{B_{\text{r}}}{\mu_0}\sin\left(\sigma_{\text{m}}\frac{n\pi}{2}\right), \qquad \text{with} \quad n = 1, 3, 5, 7..., \tag{C.1.2}$$

where B_{r} is the remanent flux density, μ_0 is the permeability of a vacuum and σ_{m} is the ratio of a PM's pitch to the pole pitch.

To simplify the analysis of the airgap flux distribution due to the PMs, the linearised geometry in Fig. C.1 is now approximated to be that given in Fig. C.2. In Fig. C.2, the stator is slotless and the relative permeability of the ferromagnetic material in the rotor and stator yokes are assumed to be infinite. Also shown in Fig. C.2, is the resultant

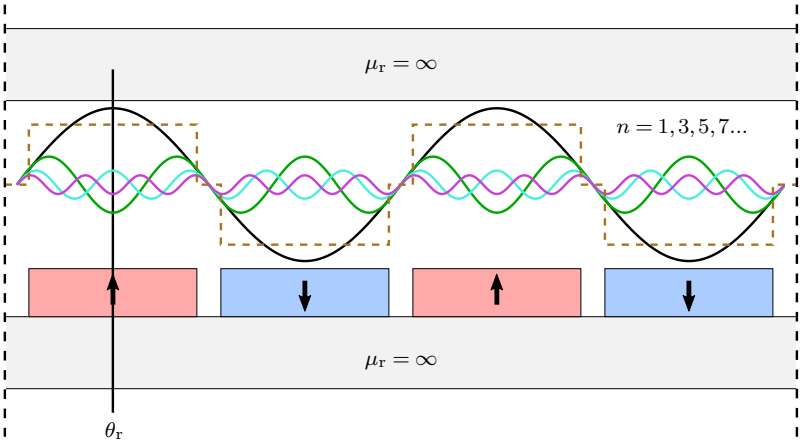

Figure C.2: Linearised approximation of the MMF harmonic waveforms in a uniform air gap for radially magnetised surface mounted PMs. (Adapted from [55])

quasi-square wave MMF distribution. The resulting air gap MMF due the PMs is given by

$$F_{\mathrm{PM}}(\theta,\theta_{\mathrm{r}}) \approx \sum_{n=1,3,5\ldots}^{\infty} \vec{M_{r,n}} \frac{h_{\mathrm{m}}}{\mu_{\mathrm{r(PM)}}} \cos(np_{\mathrm{r}}(\theta-\theta_{\mathrm{r}})). \tag{C.1.3}$$

The relationship between the mechanical speed of the PM rotor and the equivalent electrical frequency is given by

$$\omega_{\mathrm{e}} = p_{\mathrm{r}} \frac{d}{dt}\theta_{\mathrm{r}} = p_{\mathrm{r}}\omega_{\mathrm{r}}. \tag{C.1.4}$$

Hence, the air gap MMF due to the PM rotor can be rewritten as a function of time:

$$\begin{aligned} F_{\mathrm{PM}}(\theta,t) &\approx \sum_{n=1,3,5\ldots}^{\infty} \vec{M_{r,n}} \frac{h_{\mathrm{m}}}{\mu_{\mathrm{r(PM)}}} \cos(np_{\mathrm{r}}(\theta-\omega_{\mathrm{r}}t)) \\ &\approx \sum_{n=1,3,5\ldots}^{\infty} \vec{M_{r,n}} \frac{h_{\mathrm{m}}}{\mu_{\mathrm{r(PM)}}} \cos(n(p_{\mathrm{r}}\theta-\omega_{\mathrm{e}}t)) \end{aligned} \tag{C.1.5}$$

Equation (C.1.5) is still dependent on the ratio σ_{m}, and is a function of the higher order harmonics that are present, as shown in Fig. C.2. In [103], the effect of σ_{m} was investigated. It is shown in [103] that certain higher order harmonics can be eliminated by adjusting σ_{m}. Therefore, to further simplify the analysis, it is only necessary to take into account the first order harmonic. Equation (C.1.5) is now rewritten as

$$F_{\mathrm{PM}}(\theta,t) \approx F_{\mathrm{PM1}} \cos(p_{\mathrm{r}}(\theta-\omega_{\mathrm{r}}t)) \tag{C.1.6}$$

where

$$\begin{aligned} F_{\mathrm{PM1}} &= \vec{M_{r,1}} \frac{h_{\mathrm{m}}}{\mu_{\mathrm{r(PM)}}} \\ &= \frac{4}{\pi} \frac{B_{\mathrm{r}} h_{\mathrm{m}}}{\mu_0 \mu_{\mathrm{r(PM)}}} \sin\left(\sigma_{\mathrm{m}} \frac{\pi}{2}\right). \end{aligned} \tag{C.1.7}$$

C.1.1.2 Air gap Permeance due to the Slotted Stator

The linearised PM Vernier machine in Fig. C.1 has open stator slots which significantly influences the magnetic air gap permeance. The stator teeth not only act as a flux path but also act as a flux modulator which introduces higher order harmonics in the air gap permeance. The flux modulator angle, θ_{f}, is taken in the middle of the slot as shown in Fig. C.1, which in this case corresponds to the positive magnetic axis of the armature winding. If it is assumed that the rotor surface is smooth and that the relative permeability of the iron regions are infinite, the permeance function can be described as in [104] with the Fourier series

$$\Lambda(\theta,\theta_{\mathrm{f}}) \cong \Lambda_0 - \sum_{v=1,3,5\ldots}^{\infty} \Lambda_v \cos(vQ_{\mathrm{s}}(\theta-\theta_{\mathrm{f}}). \tag{C.1.8}$$

In (C.1.8), Λ_0 is the average permeance and Λ_v is the v^{th} harmonic's magnitude given by

$$\Lambda_0 = \frac{\mu_0}{g'_{\mathrm{air}}} \left(1 - 1.6\beta \frac{\tau_{\mathrm{o}}}{\tau_{\mathrm{s}}}\right) \tag{C.1.9}$$

and

$$\Lambda_v = \frac{\mu_0}{v g'_{\text{air}}} \frac{2\beta}{\pi} \left[\frac{0.78125}{0.78125 - 2\left(\frac{v\tau_\text{o}}{\tau_\text{s}}\right)^2} \right] \sin\left(1.6 v\pi \frac{\tau_\text{o}}{\tau_\text{s}}\right) \tag{C.1.10}$$

respectively. In (C.1.9) and (C.1.10), the equivalent air gap length, g'_{air}, is given by

$$g'_{\text{air}} = g_{\text{air}} + \frac{h_\text{m}}{\mu_{\text{r(PM)}}}, \tag{C.1.11}$$

and the coefficient β is given by

$$\beta = \frac{1}{2} - \frac{1}{2\sqrt{1 + \left(\frac{\tau_\text{o}}{2g'_{\text{air}}}\right)^2}}. \tag{C.1.12}$$

In the above equations of (C.1.8)-(C.1.12), it is shown that the air gap permeance is a function of the slot-opening to air gap ratio $\frac{\tau_\text{o}}{g'_{\text{air}}}$ and the slot-opening to slot-pitch ratio $\frac{\tau_\text{o}}{\tau_\text{s}}$. Both τ_o and τ_s are defined in Fig. C.1. It is shown in [103] that for $\frac{\tau_\text{o}}{\tau_\text{s}} > 0.5$, that the higher order harmonics in (C.1.8) are negligible. Therefore, only Λ_0 and Λ_1 are further considered since $\frac{\tau_\text{o}}{\tau_\text{s}}$ is typically > 0.5. Hence, equation (C.1.8) can be approximated as

$$\Lambda(\theta, \theta_\text{f}) \approx \Lambda_0 - \Lambda_1 \cos(Q_\text{s}(\theta - \theta_\text{f})) \tag{C.1.13}$$

and rewritten as a time varying function, given by

$$\Lambda(\theta, t) \approx \Lambda_0 - \Lambda_1 \cos(Q_\text{s}(\theta - \omega_\text{f} t)). \tag{C.1.14}$$

C.1.1.3 Air gap Flux Density

The air gap flux density can be obtained by multiplying the air gap MMF due to the rotor PMs, with the air gap permeance function that results from the stator slotting:

$$\begin{aligned} B_\text{g}(\theta, t) &= F_{\text{PM}}(\theta, t) \times \Lambda(\theta, t) \\ &= [F_{\text{PM1}} \cos(p_\text{r}(\theta - \omega_\text{r} t))] \times [\Lambda_0 - \Lambda_1 \cos(Q_\text{s}(\theta - \omega_\text{f} t)] \end{aligned} \tag{C.1.15}$$

Since the modulator is attached to the stator, i.e. the stator teeth, the mechanical rotational speed of the modulator is $\omega_\text{f} = 0$. Thus, the air gap flux density in (C.1.15) can be determined using the trigonometric identity: $\cos X \cos Y = \frac{1}{2}(\cos(X - Y) + \cos(X + Y))$, and is given as

$$\begin{aligned} B_g(\theta, t) &= [F_{\text{PM1}} \cos(p_\text{r}(\theta - \omega_\text{r} t))] \times [\Lambda_0 - \Lambda_1 \cos(Q_\text{s}\theta)] \\ &= \Lambda_0 F_{\text{PM1}} \cos(p_\text{r}\theta - p_\text{r}\omega_\text{r} t) \\ &- \frac{1}{2}\Lambda_1 F_{\text{PM1}} \left[\cos((Q_\text{s} + p_\text{r})\theta - p_\text{r}\omega_\text{r} t) + \cos((Q_\text{s} - p_\text{r})\theta + p_\text{r}\omega_\text{r} t)\right]. \end{aligned} \tag{C.1.16}$$

Note here that the order of the modulated spatial harmonics coincide with that predicted by the right hand side of the equation

$$p_\text{s} = \underbrace{Q_\text{s} \pm p_\text{r}} \tag{C.1.17}$$

for choosing the pole numbers and number of stator slots of the Vernier machine. Equation (C.1.16) thus clearly shows the modulation effect of the air gap flux due to the stator slots, and the spatial harmonics present in the air gap flux density.

C.1.1.4 Flux Modulation Example

To demonstrate the flux modulation effect with an example, the harmonic content of the air gap flux density is investigated using LD-PEM[1].

Consider the conventional Vernier machine in Fig. C.3. This particular Vernier machine has a harmonic coupling factor of $G_r = 5$, the number of stator slots is $Q_s = 48$ and the machine has $p_r = 40$ rotor pole pairs. According to the relationship in (C.1.17) the resulting number of stator pole pairs on the armature winding should be $p_s = 8$, but for this example we are only interested in the flux modulation taking place in the air gap due to the PMs on the rotor and the stator teeth.

First, the stator core of the machine is taken as solid, without any stator slots, as shown in Fig. C.4. The induction spectrum from the LD-PEM field calculation is also shown in Fig. C.4. The only harmonic present in the induction spectrum is the rotor's working harmonic at 40. Which is as expected due to the 80 rotor poles (40 pole pairs).

Next, the stator slots are now added to the machine's geometry. Once more the field calculation is done. In Fig. C.4 it is shown that there are now additional harmonics present in the air gap flux density. By closer inspection it is observed that the additional harmonics in Fig. C.4 are of the order $kQ_s \pm p_r$. Thus, the equation for the normalised harmonic orders in the air gap distribution due to the stator slots is given by

$$\nu = k\frac{Q_s}{p_r} \pm 1. \tag{C.1.18}$$

By rewriting equation (C.1.18) with $k = 1$ as

$$\nu p_r = Q_s \pm p_r, \tag{C.1.19}$$

it becomes more clear that these harmonics can be attributed to the modulation effect of the stator teeth. Note that (C.1.19) is also equal to the vernier machine relation in (C.1.17), and therefore

$$p_s = \nu p_r = Q_s \pm p_r. \tag{C.1.20}$$

[1]LD-PEM is the in-house FEA package used at Siemens Mobility GmbH.

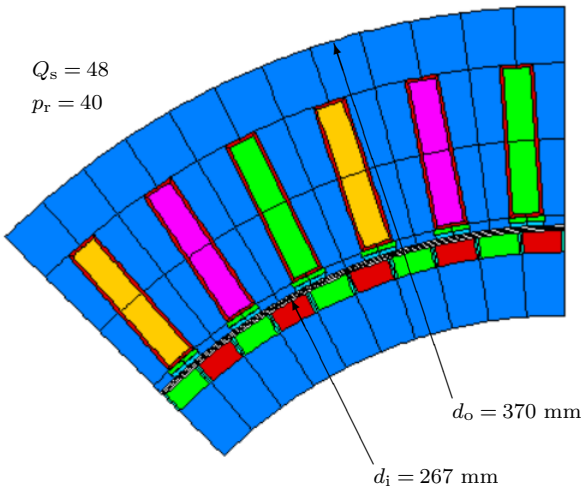

Figure C.3: Example surface mounted PM machine in LD-PEM.

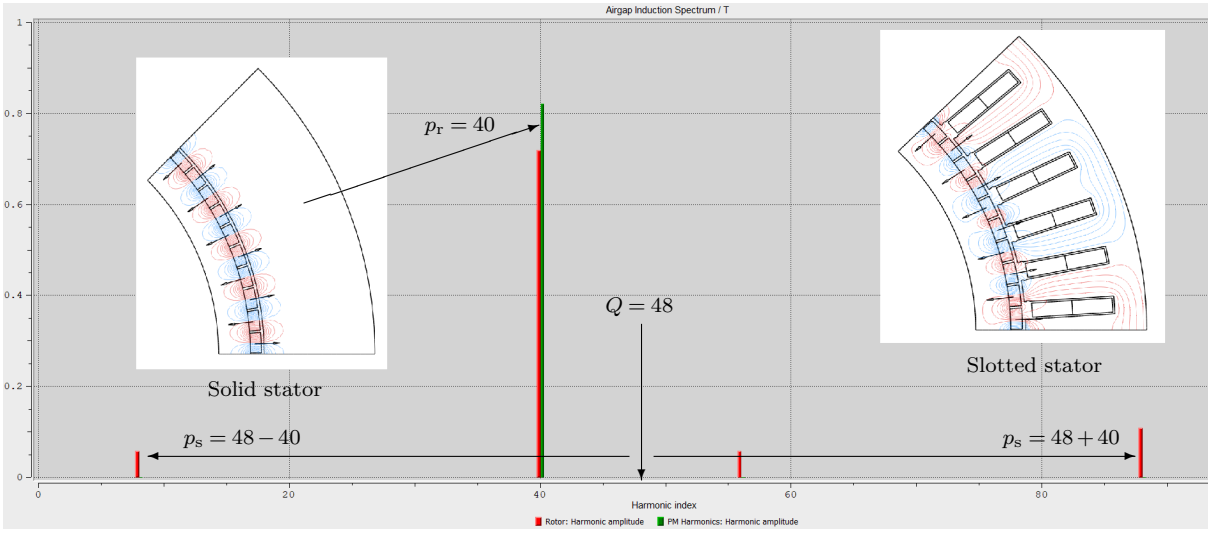

Figure C.4: Experimental LD-PEM case studies of the air gap flux density harmonic content to illustrate the flux modulation effect.

Note here already, that the lower order modulated harmonic at $p_s = Q_s - p_r = 8$, will rotate in the opposite direction of the working harmonic as seen from (C.1.16).

C.1.2 Armature Winding Selection

Having theoretically established the air gap flux-modulation effect in the previous subsection, it is still unclear how the Vernier machine produces torque. From general machine theory, we know that *torque is produced when the rotor and stator fields have equal synchronous speed and the same spatial harmonic content.* For typical synchronous machines this implies that the rotor and the stator have the same number of pole pairs. For Vernier machines, equation (C.1.19) already hints toward explaining machine selection as a result of the flux-modulation effect, but it is still unclear how harmonic coupling is utilised. Most of literature simply states that the armature winding should be selected accordingly, however, this statement requires a bit more clarity for understanding the Vernier machine's working principle.

C.1.2.1 Armature Winding MMF and Harmonic Content

Consider a standard overlapping winding. For simplification, the winding is also assumed to be an integral winding with $q = 1$. Therefore, from Appendix A, we know that the order of the armature winding's higher order MMF harmonics are given by the series

$$\nu = 6k - 1 \qquad \{k = 1, 2, 3...\}. \tag{C.1.21}$$

Thus, the only harmonics that are present are of the order $\nu = 1, 5, 7, 11...$ Subsequently, the rotating air gap MMF due to the armature currents can be expressed as

$$F(\theta_e, t) = \frac{3}{2} F_1 \left[\sum_{\nu=1,7,13...}^{\infty} \frac{k_{w\nu}}{\nu} \cos(\nu\theta_e - \omega_e t) + \sum_{\nu=5,11,17...}^{\infty} \frac{k_{w\nu}}{\nu} \cos(\nu\theta_e + \omega_e t) \right], \tag{C.1.22}$$

using cosine terms. Note, that for the Vernier machine the only higher order harmonic content that is of interest, are the terms that will have the same order as the terms in

(C.1.16) for the air gap flux density. This is because these are the harmonics that will interact and produce useful torque.

The harmonics in (C.1.22) are normalised to the working harmonic, whereas the harmonics in (C.1.16) are not. Therefore, (C.1.21) is multiplied with the number of stator pole pairs and rewritten as

$$\begin{aligned} p_{\mathrm{s}}\nu &= 6kp_{\mathrm{s}} \pm p_{\mathrm{s}} \\ &= 6k\left(\frac{Q_{\mathrm{s}}}{2mq}\right) \pm p_{\mathrm{s}} \qquad \{k = 1, 2, 3...\} \\ &= kQ_{\mathrm{s}} \pm p_{\mathrm{s}}. \end{aligned} \tag{C.1.23}$$

The armature winding MMF in (C.1.22), is therefore also rewritten as

$$F(\theta, t) = \frac{3}{2}F_1\left[\sum_{\nu=1,7,13...}^{\infty}\frac{k_{\mathrm{w}\nu}}{\nu}\cos(\nu p_{\mathrm{s}}\theta - \omega_{\mathrm{e}}t) + \sum_{\nu=5,11,17...}^{\infty}\frac{k_{\mathrm{w}\nu}}{\nu}\cos(\nu p_{\mathrm{s}}\theta + \omega_{\mathrm{e}}t)\right]. \tag{C.1.24}$$

Furthermore, because we previously assumed that the machine has a number of slots per pole per phase of $q = 1$, it is only necessary to consider the fundamental and first order harmonics[2] in (C.1.24). Therefore, the armature winding's MMF in (C.1.24) is rewritten as

$$\begin{aligned} F(\theta, t) = &\frac{3}{2}F_1 k_{\mathrm{w}1}\cos(p_{\mathrm{s}}\theta - \omega_{\mathrm{e}}t) \\ &+ \frac{3}{2}F_1 k_{\mathrm{w}5}\frac{1}{\frac{Q_{\mathrm{s}}}{p_{\mathrm{s}}} - 1}\cos((Q_{\mathrm{s}} - p_{\mathrm{s}})\theta + \omega_{\mathrm{e}}t) \\ &- \frac{3}{2}F_1 k_{\mathrm{w}7}\frac{1}{\frac{Q_{\mathrm{s}}}{p_{\mathrm{s}}} + 1}\cos((Q_{\mathrm{s}} + p_{\mathrm{s}})\theta - \omega_{\mathrm{e}}t), \end{aligned} \tag{C.1.25}$$

with $k = 1$.

C.1.2.2 Harmonic Coupling

Once more, consider the air gap flux density due to the rotor PMs and the modulated harmonics due to stator slotting as derived in Section C.1.1.3:

$$\begin{aligned} B_{\mathrm{g}}(\theta, t) &\approx [F_{\mathrm{PM}1}\cos(p_{\mathrm{r}}(\theta - \omega_{\mathrm{r}}t)] \times [\Lambda_0 - \Lambda_1\cos(Q_{\mathrm{s}}\theta)] \\ &= \Lambda_0 F_{\mathrm{PM}1}\cos(p_{\mathrm{r}}\theta - p_{\mathrm{r}}\omega_{\mathrm{r}}t) \\ &- \frac{1}{2}\Lambda_1 F_{\mathrm{PM}1}\cos((Q_{\mathrm{s}} + p_{\mathrm{r}})\theta - p_{\mathrm{r}}\omega_{\mathrm{r}}t) \\ &- \frac{1}{2}\Lambda_1 F_{\mathrm{PM}1}\cos((Q_{\mathrm{s}} - p_{\mathrm{r}})\theta + p_{\mathrm{r}}\omega_{\mathrm{r}}t) \end{aligned} \tag{C.1.26}$$

It is shown that there are three spatial harmonic components that are of interest. The only way in which these components will interact with the harmonic components of the armature winding MMF is if they have the same spatial harmonic content and synchronous rotational speed in the same direction. Therefore, also consider the armature winding MMF in (C.1.25), that can be rewritten as

[2]There are higher order harmonics that will also "couple" and contribute to useful torque production, but for this explanation they are assumed to be negligible. For machines with $q = 1.5$, $q = 2...$ the same concept still applies, only the stator MMF harmonics will be of a higher order e.g. at $k = 2$ or $k = 3$.

$$\begin{aligned} F(\theta,t) = &\frac{3}{2}F_1 k_{w1}\cos((Q_s - p_r)\theta - \omega_e t) \\ &+ \frac{3}{2}F_1 k_{w5}\frac{1}{\frac{Q_s}{p_s}-1}\cos(p_r\theta + \omega_e t) \\ &- \frac{3}{2}F_1 k_{w7}\frac{1}{\frac{Q_s}{p_s}+1}\cos((2Q_s - p_r)\theta - \omega_e t), \end{aligned} \tag{C.1.27}$$

knowing that machine selection is based on (C.1.17) where $p_s = Q_s - p_r$. Upon comparing the terms in (C.1.26) and (C.1.27), it is observed that the following terms have similar spatial components:

(i) $\Lambda_0 F_{PM1}\cos(p_r\theta - p_r\omega_r t) \Leftrightarrow \frac{3}{2}F_1 k_{w5}\frac{1}{\frac{Q_s}{p_s}-1}\cos(p_r\theta + \omega_e t)$

(ii) $\frac{1}{2}\Lambda_1 F_{PM1}\cos((Q_s - p_r)\theta + p_r\omega_r t) \Leftrightarrow \frac{3}{2}F_1 k_{w1}\cos((Q_s - p_r)\theta - \omega_e t)$

The above shows the harmonic coupling taking place in the Vernier machine, where (i) the working harmonic of the PM rotor will couple with the $5p_s$ higher order harmonic of the armature winding MMF, and (ii) the lower order modulated harmonic of the rotor PMs will couple with the armature winding MMF's working harmonic (p_s).

The other condition for useful torque to be produced, is that the above "coupling" terms should have the same synchronous rotational speed. It is noticed that the terms with the same spatial harmonic content have opposite rotational directions (refer to the signs in front of $p_r\omega_r$ and ω_e). This means that for harmonic coupling to take place, the rotor and the stator fields would have to rotate in the opposite direction. One way to visualise this, is that if the armature MMF rotates in a clockwise direction, the rotor must mechanically rotate anti-clockwise for harmonic coupling to take place. Furthermore, it is observed from (C.1.26) and (C.1.27) that the electrical rotational speed is determined by the rotor pole pairs p_r, i.e. $p_r\omega_r = \omega_e$.

C.1.2.3 Vernier Machine Principle Example

To demonstrate the harmonic coupling effect with an example, the harmonic content of the air gap flux density is once more investigated using LD-PEM. The same conventional Vernier machine in Fig. C.3 is used for this example, with $p_s = 8$, $Q_s = 48$ and $p_r = 40$.

The flux modulation effect due to stator slotting was already demonstrated with the LD-PEM field calculation in Section C.4. These same results, with no armature currents flowing, are once more plotted in Fig. C.5.

Next, the rotor is taken as a solid yoke and the armature winding is set so that $p_s = 8$ and $q = 1$. An arbitrary q-axis current is assigned to the winding and the field calculation is done in LD-PEM. The resulting induction spectrum of the armature winding is then also plotted in Fig. C.5. It is shown that the spatial content of the armature winding's MMF and the air gap flux density harmonics coincide with that predicted in the analytical analysis. The armature winding's working harmonic at $p_s = 8$ will couple with the PM rotor's modulated harmonic at $Q_s - p_r = 8$. Additionally, the PM rotor's working harmonic at $p_r = 40$ will couple with the armature winding's higher order harmonic. As is, these harmonics that are of the same order will have opposite rotational direction. However, as stated previously, the rotor has to mechanically rotate in the opposite direction.

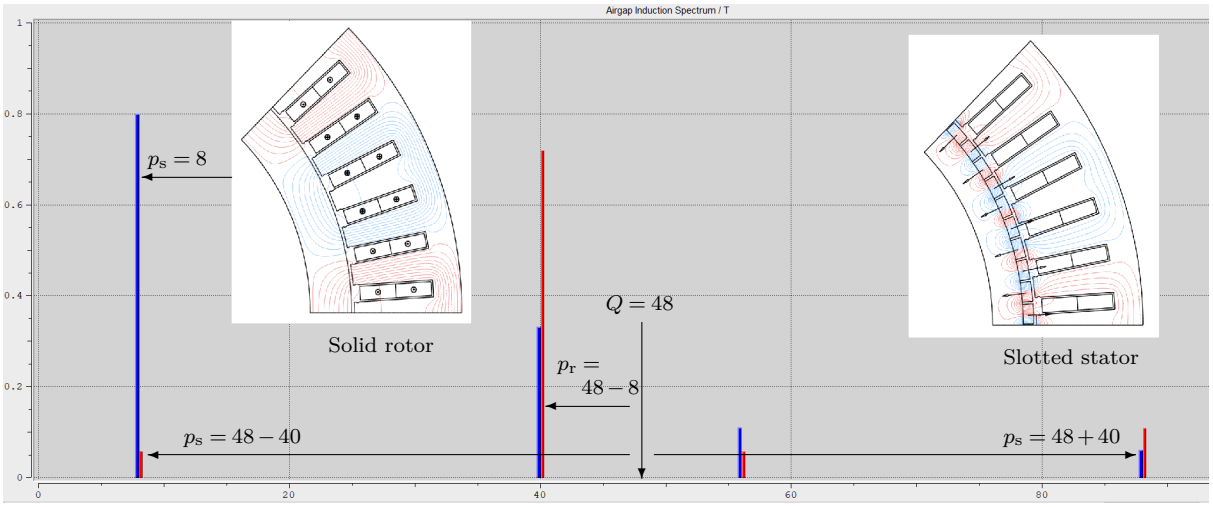

Figure C.5: Experimental LD-PEM case studies of the air gap flux density harmonic content to illustrate the harmonic coupling.

It is also shown in Fig. C.5 that there are additional higher order spatial harmonics that will also contribute to torque production through harmonic coupling. The total contribution of these harmonics compared to the working and first order harmonics are however considered negligible in the preceding theoretical analysis.

Appendix D

Cogging Torque Minimisation Technique

When designing PM wind generators for small-scale wind energy systems, it is imperative that the generator has good torque quality. Good torque quality implies that the generator has:

1. Low cogging torque, i.e. the generator's peak to peak torque at no-load (no current) conditions is low.

2. Low load torque ripple, i.e. the variation in peak to peak torque at the rated-load operating speed is low.

For small-scale wind generators the load torque ripple at higher turbine speeds is not such a great concern. Therefore, in this appendix, the focus is on reducing or minimising PM wind generator cogging torque. The majority of the work presented in this appendix is from the conference paper [105].

There are various techniques to reduce cogging torque; such as skewing, pole shifting, adding auxiliary slots to the stator teeth etc. However, the issues with the aforementioned techniques are that they can complicate the manufacturing process if the machine's cogging torque is very sensitive to manufacturing tolerances and can also significantly affect the machine's performance. Alternatively, in [106], it is shown that the cogging torque can be reduced by varying certain dimensional parameters of the machine. This technique to minimise cogging torque was also shown to be very effective in [107]. However, the approach to implementing this method as used in [106] and [107] is computationally expensive and requires a lot of self evaluation of the objective and constraints.

A less computationally expensive cogging torque minimisation method is presented in this appendix that uses single parameter variation of the relevant generator dimensions in a coordinate descent method, that streamlines the design for a low generator cogging torque. To illustrate its effectiveness, the coordinate descent method is used to minimise the cogging torque of two machines that were designed in [96] and that were subsequently rejected due to their poor cogging torque. The work presented in this appendix then ultimately functions as a useful tool in the broader design approach for PM wind generators used in small-scale wind energy systems.

D.1 Wind Generator Case Studies

The two wind generators from [96] that are considered for the case studies were both designed for the uncontrolled passive wind generator system shown in Fig. 1.1(a). Both wind generators are PM Vernier generators. Some of the relevant PMVG design detail from [96] are given in Table D.1. The partial cross sections of the respective PMVGs are shown in Fig. D.1.

The PMVGs in Table D.1 were selected in [96] for gearing ratios of $G_r = 5$ and $G_r = 11$ respectively, with the number of rotor pole pairs constrained by the maximum allowed operating frequency as in Chapter 5. Both PMVGs in Table D.1 were optimised for the design objectives and system constraints, as explained in [96]. However, both machines have an undesirably large cogging torque, ΔT_{cog}, which makes them unsuited for small-scale wind turbines. Therefore, these machines provide excellent case studies for this cogging torque minimisation method. The cogging torques of both machines are shown in Fig. D.2 for a mechanical rotation of 360 electrical degrees.

Table D.1: PMVG parameters from [96].

PMVG	$G_r = 5$	$G_r = 11$
Stator pole pairs, p_s	4	2
Stator slots, Q_s	24	24
PM rotor pole pairs, p_r	20	22
Active mass, M_{active} (kg)	17.09	19.88
PM mass, M_{PM} (kg)	1.26	1.73
P_g (kW)	4.10	4.12
η (%)	91.1	95.9
J_{rms} (A/mm^2)	4.94	1.90
Cogging torque, ΔT_{cog} (%)	17.9	5.1
LCM (Q,$2p_r$)	120	264

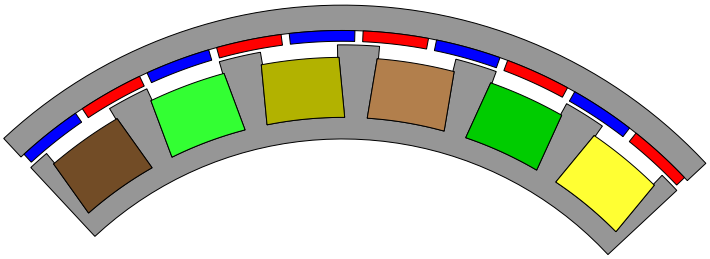

(a) $G_r = 5$

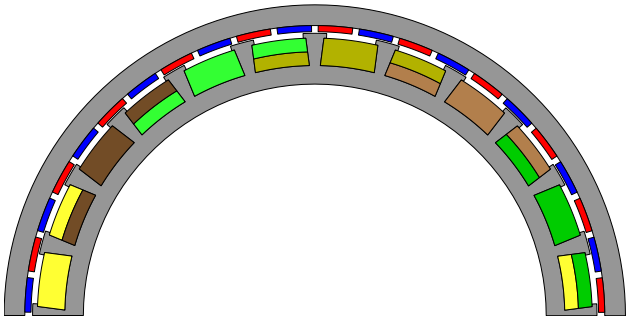

(b) $G_r = 11$

Figure D.1: Partial cross sections of the respective PMVGs [96]. (Not to scale)

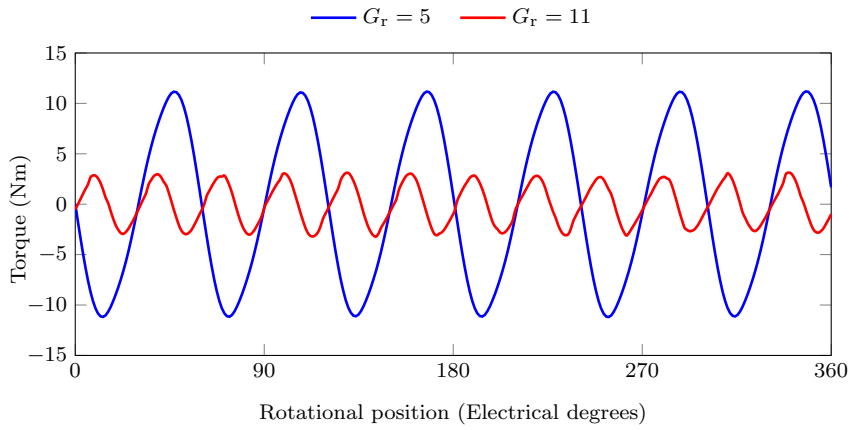

Figure D.2: FE predicted cogging torque, ΔT_{cog}, for the machines in Table D.1

Cogging torque is the no-load torque that results from the interaction between the rotor PMs' harmonics and the air gap permeance harmonics due to the slotting of the machine's stator. Therefore, machine selection also plays an important role and can be used to predict whether a machine will inherently have a low cogging torque and be insensitive to manufacturing imperfections. One such an indicator that is used throughout this dissertation is the least common multiple (LCM) between the number of slots, Q, and the number of poles, $2p$. Generally, the larger the machine's LCM(Q,$2p$) is, the better its cogging torque qualities. The LCMs of the two PMVGs are given in Table D.1. Although the LCM-value does not directly relate to the amplitude of the cogging torque, this index correlates with the cogging torque results in Table D.1 and Fig D.2. The PMVG with $G_r = 5$ has a cogging torque of $\Delta\tau = 17.9\%$ and the PMVG with $G_r = 11$ has a cogging torque of $\Delta\tau = 5.1\%$. Nonetheless, both PMVGs still have desirable performance and whether the cogging torque can be sufficiently reduced needs to be investigated.

D.2 Cogging Torque Minimisation

The cogging torque can be calculated as

$$\Delta\tau = \Delta T_{cog} = \frac{\Delta T_{no\text{-}load}}{T_g}, \tag{D.2.1}$$

where $\Delta T_{no\text{-}load}$ is the peak to peak torque at no-load and T_g is the generated torque at the specified operating point. The alternative notation for cogging torque, $\Delta\tau$, is used in this appendix to simplify subscripts in the following sections.

D.2.1 Multiple and Single Parameter Variation

As shown in [106] and [107], the relevant dimensions that affect the machine's cogging torque are

$$\mathbf{X} = \begin{bmatrix} \sigma_m & \sigma_t & h_{yr} & h_{ys} \end{bmatrix}^T, \tag{D.2.2}$$

which are defined in Fig. D.3. Here, σ_m is the magnet pitch to pole pitch ratio given by

$$\sigma_m = \frac{\theta_m}{\theta_p}, \tag{D.2.3}$$

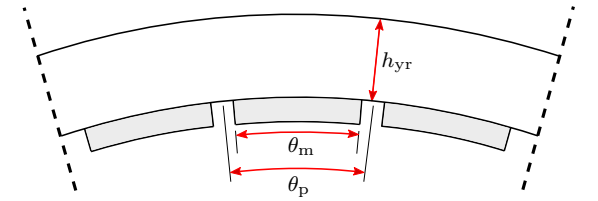

(a) Rotor

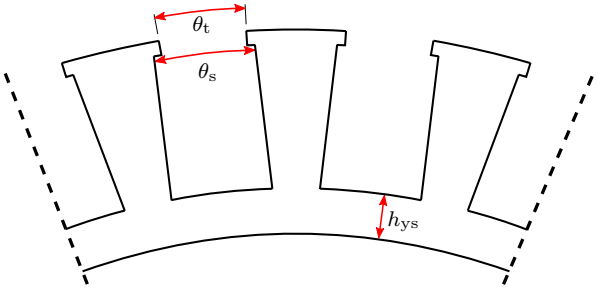

(b) Stator

Figure D.3: Dimensions for cogging torque minimisation.

where

$$\theta_m = \frac{2\pi}{2p_r}; \tag{D.2.4}$$

σ_t is the slot tooth opening pitch to the slot pitch ratio given by

$$\sigma_t = \frac{\theta_t}{\theta_s}; \tag{D.2.5}$$

h_{yr} and h_{ys} are the respective rotor- and stator yoke heights.

Multiple and single parameter variation of the dimensions in (D.2.2) can be done to minimise the cogging torque as in [106] and [107]. Such an analysis has been done for both PMVGs in Table D.1. The static FEA calculated cogging torque versus σ_m and σ_t are shown in Figs. D.4(a) and (b) for the respective PMVGs.

To minimise the cogging torque, new corresponding values for σ_m and σ_t can be selected from the results in Fig. D.4. However, for this method to be effective, relatively small dimensional increments for both σ_m and σ_t are required over a large search space. This method then quickly becomes computationally expensive, with the number of required solutions being $m \times n = 399$ in Fig. D.4. Thereafter, to further minimise the cogging torque, h_{yr} and h_{ys} also need to be varied. Another issue with this approach is that after changing the relevant dimensions, there is no guarantee that the performance constraints of the machine are still met and still needs to be verified independently.

D.2.2 Coordinate Descent Method

Although the method of multiple and single parameter variation that is described in the previous subsection works, it is too computationally expensive. The cogging torque minimisation method needs to be streamlined for it to be more practical in the design process.

The coordinate descent method is essentially the first step in Powell's non-gradient method [108], and has been shown in [95] to be very fast for minimising or maximising

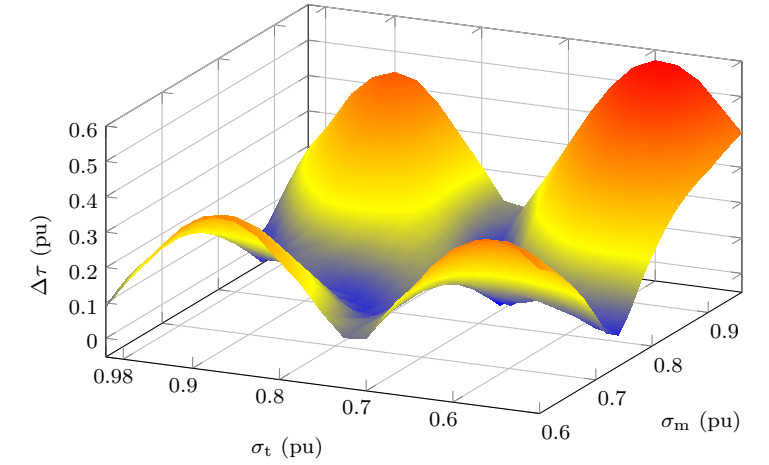

(a) $G_r = 5$

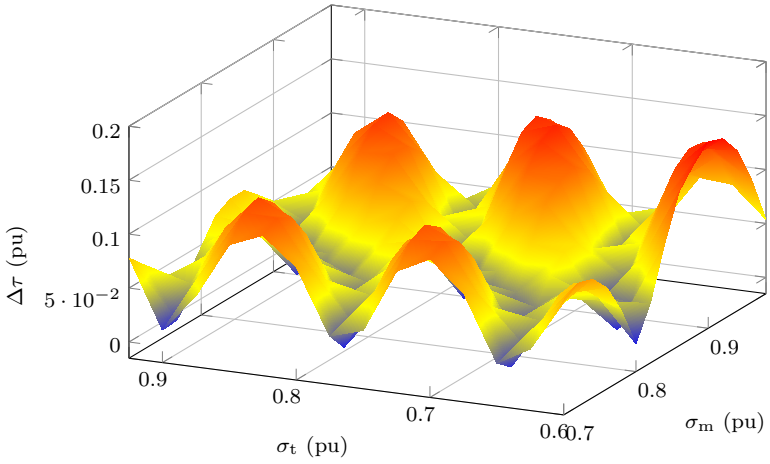

(b) $G_r = 11$

Figure D.4: Cogging torque profiles for the respective PMVGs, where σ_t and σ_m are parameters.

performance parameters of electrical machines. Hence, to minimise generator cogging torque, the coordinate descent method is implemented as follows:

The objective function to minimise the generator's cogging torque is given by

$$\min_{\mathbf{X}} \mathbf{F}(\mathbf{X}) = \min_{\mathbf{X}} \left[\Delta\tau(\mathbf{X})\right], \tag{D.2.6}$$

where $\mathbf{X}$ is the dimensional array in (D.2.2). Instead of $m \times n$ solutions as in Fig. D.4, only single parameter variation of one dimension of (D.2.2) is done at an instance. An example of this method is shown for the magnet pitch to pole pitch ratio, σ_m, in Fig. D.5.

1. First, the starting point is set to the cogging torque calculated with the initial machine dimensions, i.e. $\Delta\tau_0$.

2. The relevant dimension in (D.2.2), σ_m in this example, is then increased by a discreet value, δ. A new cogging torque is then calculated and the result is then used to determine the direction that minimises the cogging torque. Thus determining whether the new σ_m should be at $\sigma_m - \delta$ or $\sigma_m + \delta$.

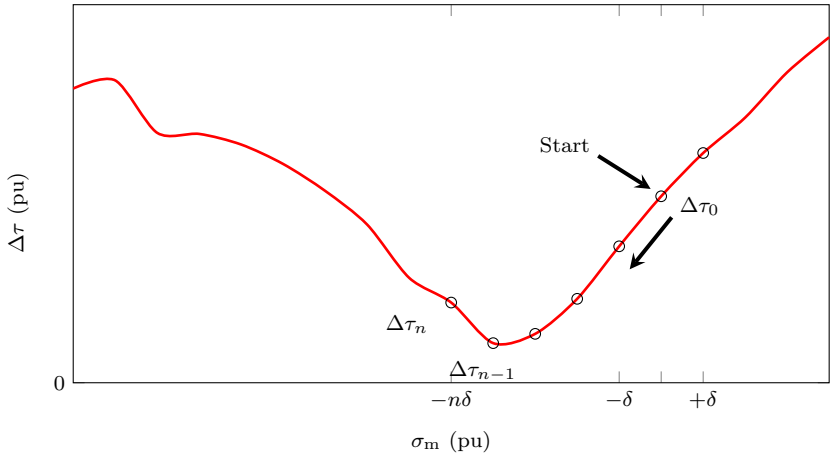

Figure D.5: Discrete single parameter variation to minimise cogging torque.

3. Thereafter, the cogging torque is calculated for each new $\sigma_{\mathrm{m}n} = \sigma_{\mathrm{m}} \pm n\delta$ until $\Delta\tau_n > \Delta\tau_{n-1}$, i.e. an absolute or local minimum has been surpassed. All this of course, within the machine's dimensional boundaries.

4. Knowing that a minimum cogging torque lies between $\Delta\tau_n$, $\Delta\tau_{n-1}$ and $\Delta\tau_{n-2}$, and that these values and their corresponding dimensions bracket the minimum solution, a second degree polynomial of the form

$$f_2(y) = c_1 + c_2(y - y_1) + c_3(y - y_1)(y - y_2) \tag{D.2.7}$$

can be obtained. The polynomial in (D.2.7) can be rewritten in terms of $\Delta\tau$ and σ_{m} as

$$\Delta\tau(\sigma_{\mathrm{m}}) = c_1 + c_2(\sigma_{\mathrm{m}} - \sigma_{\mathrm{m}(n-1)}) + c_3(\sigma_{\mathrm{m}} - \sigma_{\mathrm{m}(n-1)})(\sigma_{\mathrm{m}} - \sigma_{\mathrm{m}n}), \tag{D.2.8}$$

with the coefficients c_1, c_2 and c_3 being equal to

$$c_1 = \Delta\tau_{n-2}, \quad c_2 = \frac{\Delta\tau_{n-2} - \Delta\tau_{n-1}}{\sigma_{\mathrm{m}(n-2)} - \sigma_{\mathrm{m}(n-1)}} \text{ and}$$
$$c_3 = \frac{c_2}{\sigma_{\mathrm{m}(n-2)} - \sigma_{\mathrm{m}n}} - \frac{\Delta\tau_{n-1} - \Delta\tau_n}{(\sigma_{\mathrm{m}(n-1)} - \sigma_{\mathrm{m}n})(\sigma_{\mathrm{m}(n-2)} - \sigma_{\mathrm{m}n})}. \tag{D.2.9}$$

5. Using (D.2.8) and (D.2.9), the minimum cogging torque can be calculated using

$$\Delta\tau_{min} = \frac{1}{2}\left(\sigma_{\mathrm{m}(n-1)} + \sigma_{\mathrm{m}n} - \frac{c_2}{c_3}\right), \tag{D.2.10}$$

and subsequently the new value for σ_{m} is determined.

6. Steps 1 to 5 are then repeated for σ_{t}, h_{yr} and h_{ys} to complete the first iteration.

7. This process is then repeated for each iteration until the cogging torque, $\Delta\tau$, converges to a minimum value.

D.3 Cogging Torque Minimisation Results

The minimised cogging torque results using the coordinate descent method in Section D.2.2 are summarised in Table D.2. It is shown that for both cases the cogging torque can be minimised using the coordinate descent method. Moreover, for the PMVG with $G_r = 5$ the cogging torque is significantly reduced from $\Delta\tau = 17.1\%$ to $\Delta\tau = 2.1\%$. The cogging torque of both PMVGs, before and after the cogging torque minimisation, are shown in Fig. D.6.

In terms of computational time, the coordinate descent method is very fast to converge to a minimum with both the $G_r = 5$ and $G_r = 11$ PMVGs taking only three iterations to converge to a minimum. The number of solutions and the total computational time are also given in Table D.2. This is a significant improvement on the number of FEA solutions and computational time required for the alternative method in Section D.2.1.

The cogging torques versus the number of iterations are shown in Fig. D.7 for both machines. Here it is shown that the percentage cogging torque of the $G_r = 5$ PMVG drops tremendously, from 17.1% to below 5% within only one (the first) iteration. This shows a powerful characteristic of the coordinate descent method in the first iteration of the minimisation; an aspect also found in [95]. After the first iteration, there is a slow reduction with each iteration to the minimum, as also shown by [95]. It is interesting in this case that during the slow reduction iterations, only the rotor yoke height, h_{yr}, was adjusted to minimise the cogging torque and is shown in Fig. D.8. In the case of the $G_r = 11$ PMVG, the reduction in cogging torque with the iterations was slow from the start. The reason being that this machine already has a relatively low cogging torque.

The quite huge reduction in cogging torque, however, substantially increases the $G_r = 5$ PMVG's active mass, M_{active}, as can be seen in Table D.2, and the trade-off for a very low cogging torque becomes unwanted. Further shown in Table D.2, is that the generated power at the rated operating point, P_g, is the only other constraint that is significantly affected by the changed dimensions. However, the overall performance is still acceptable considering the large reduction in cogging torque.

For the PMVG with $G_r = 11$ the generator cogging torque is reduced, as is shown in Table D.2 and Fig. D.6. However, the PMVG's performance is undesired, with P_g falling

Table D.2: Coordinate descent method results.

PMVG	$G_r = 5$		$G_r = 11$	
	Before	After	Before	After
Cogging torque, $\Delta\tau$ (%)	17.9	2.1	5.1	1.1
Iterations		3		3
Solutions		61		59
Time (s)		1173.7		5810.4
σ_m (pu)	0.89	0.83	0.81	0.79
σ_t (pu)	0.97	0.98	0.90	0.91
h_{yr} (mm)	7.08	12.54	12.9	17.7
h_{ys} (mm)	6.00	6.56	11.1	10.6
Active mass, M_{active} (kg)	17.09	20.05	19.88	22.03
PM mass, M_{PM} (kg)	1.26	1.18	1.73	1.64
P_g (kW)	4.10	3.97	4.12	3.52
η (%)	91.1	91.1	95.9	95.4
J (A/mm^2)	4.94	4.85	1.90	1.95

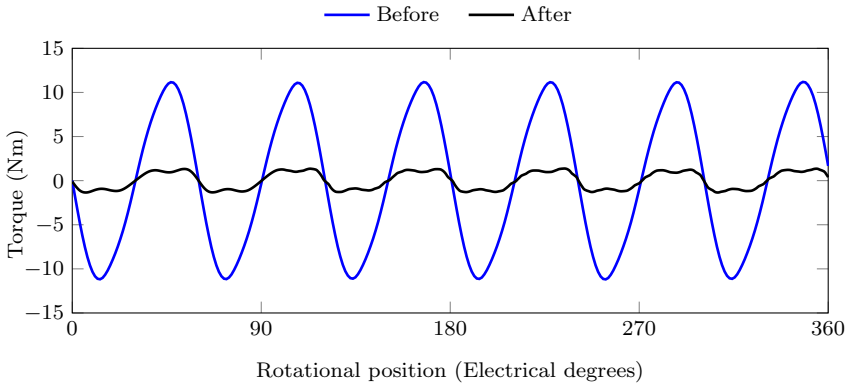

(a) $G_r = 5$

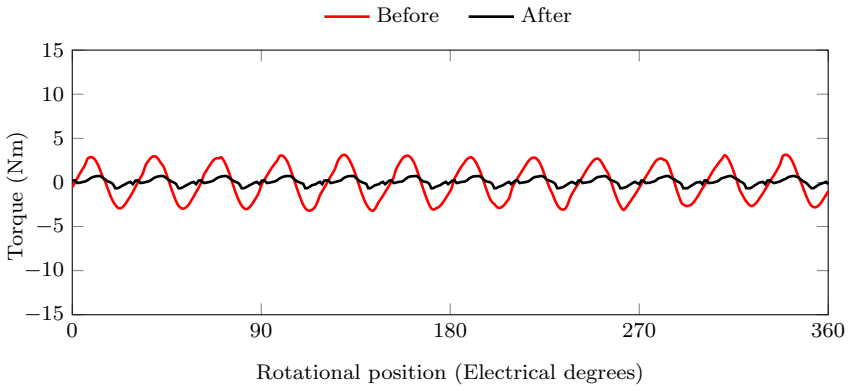

(b) $G_r = 11$

Figure D.6: FE predicted cogging torque, ΔT_{cog}.

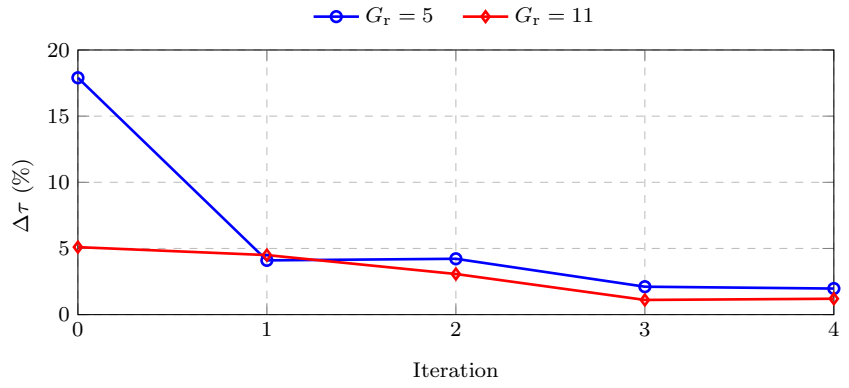

Figure D.7: Generator cogging torque minimisation using coordinate descent method.

from 4.12 kW to 3.52 kW. This is the case already after the first iteration and further minimisation of the cogging torque only results in even worse generator performance. In this case, for the PMVG with $G_r = 11$, reducing the cogging torque is not an option as it will compromise the performance constraints.

All of the static FEA solutions were performed on a 3.20 GHz Intel(R) Core i7 CPU with 32 GB RAM.

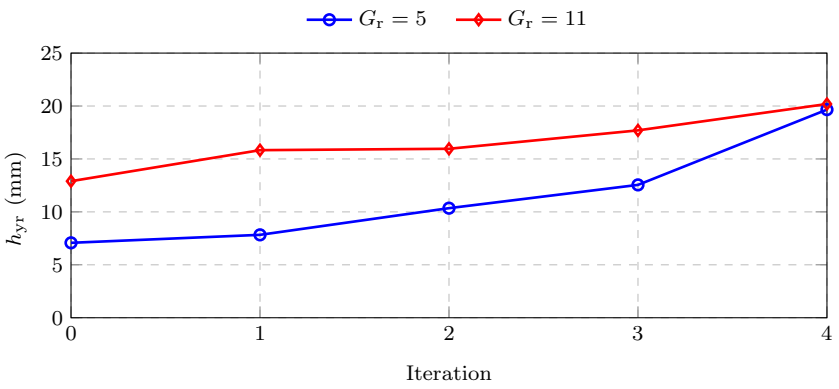

Figure D.8: Change in rotor yoke height.

D.4 Discussion

Undesired generator cogging torque in small-scale wind energy systems is a critical design issue, since this can lead to the wind turbine failing to start-up at low wind speeds. In this appendix, an accurate and computationally efficient method to minimise cogging torque is proposed.

Two cases are investigated for PM Vernier generators with undesired cogging torque. It is found that the coordinate descent method is effective in minimising the generators' cogging torque. Moreover, the coordinate descent method is found to be extremely fast in comparison to an alternative method of multiple and single parameter variation.

The coordinate descent method is easy to implement and to integrate in the design process for small-scale wind generators. This cogging torque minimisation technique, can then function as a useful and computationally efficient design tool.

Appendix E

Prototype Manufacturing and Assembly

In this appendix, additional pictures of the manufacturing and assembly process for the prototypes from Chapters 3, 4 and 5 are given. All of the prototypes were assembled in the Electrical Machines Laboratory with the help of the workshop staff from the Department of Electrical & Electronic Engineering, at Stellenbosch University.

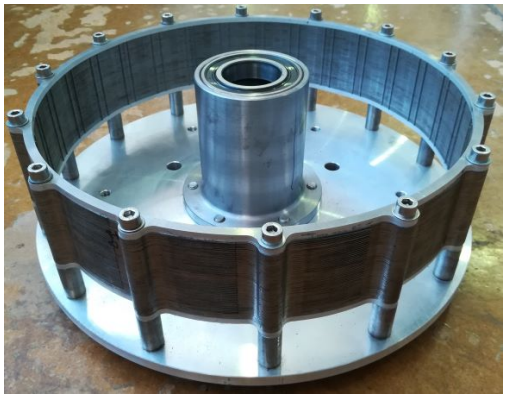

(a) Rotor lamination stack

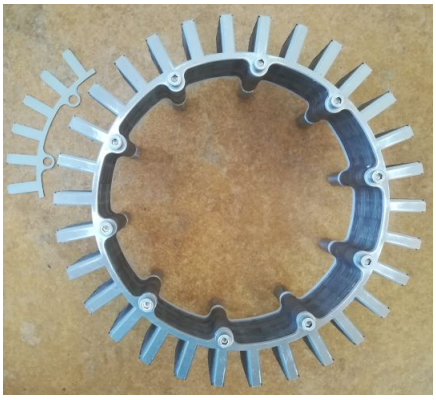

(b) Stator lamination stacking

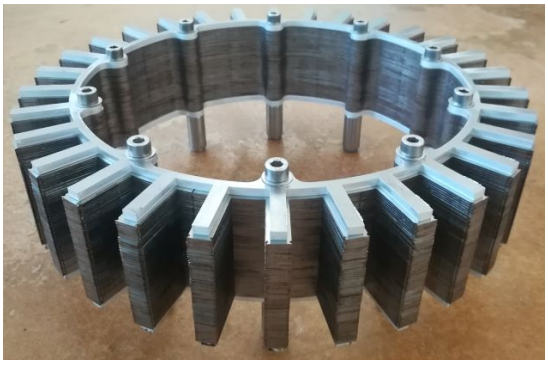

(c) Stator lamination stack

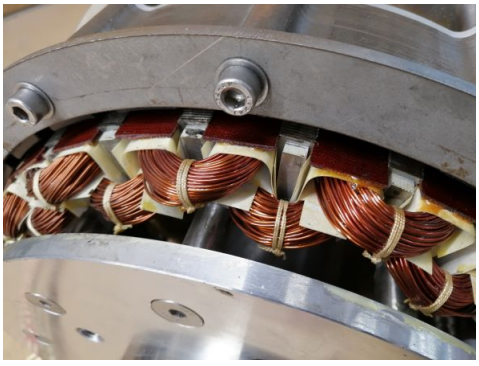

(d) Non-overlapping stator winding

Figure E.1: PMSG prototype manufacturing process (Chapter 3).

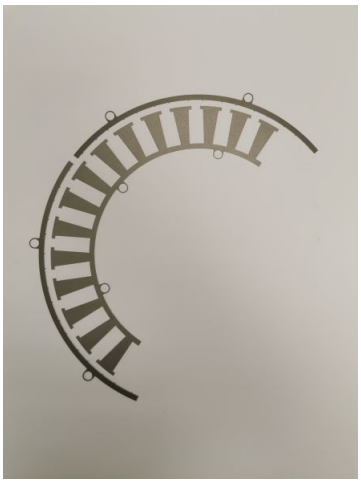

(a) Lamination segments

(b) Stator lamination stacking

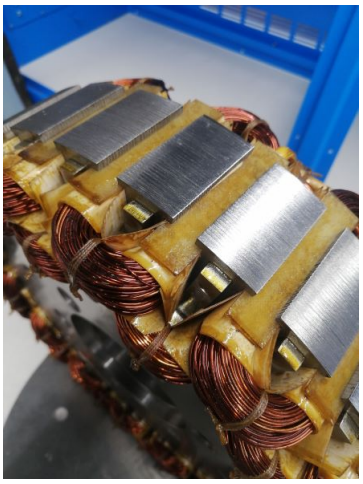

(c) Stator with windings

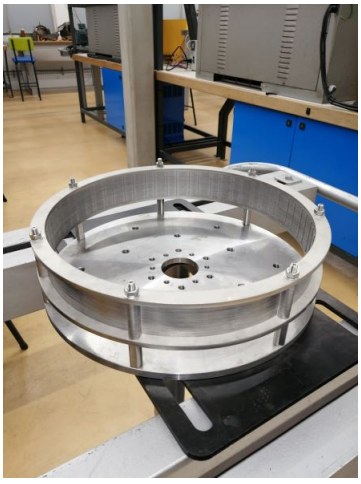

(d) Rotor lamination stacking

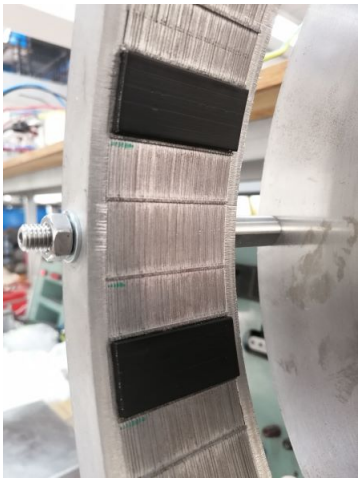

(e) Apply PMs

(f) PM rotor

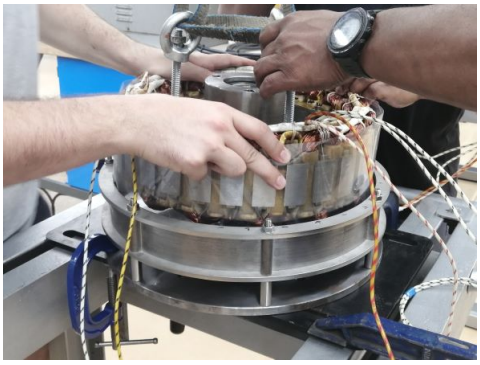

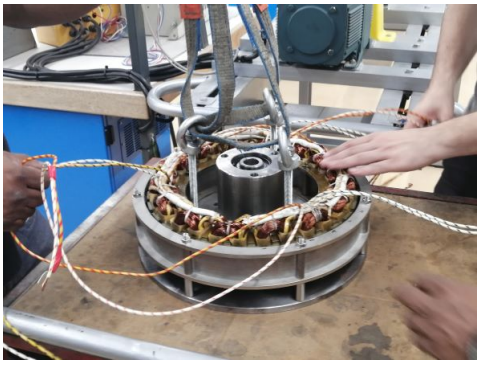

(g) Full PMSG assembly

Figure E.2: PMSG prototype manufacturing process (Chapter 4).

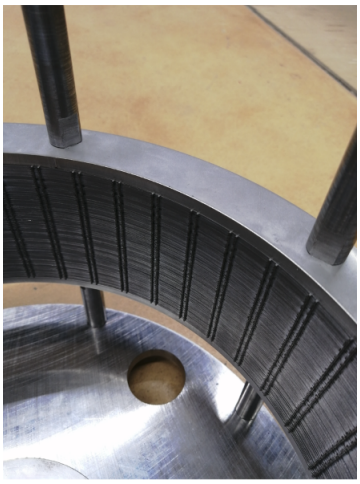

(a) Rotor lamination tracks

(b) Apply PMs

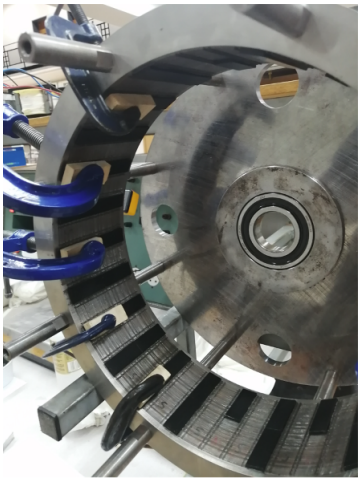

(c) Apply PMs

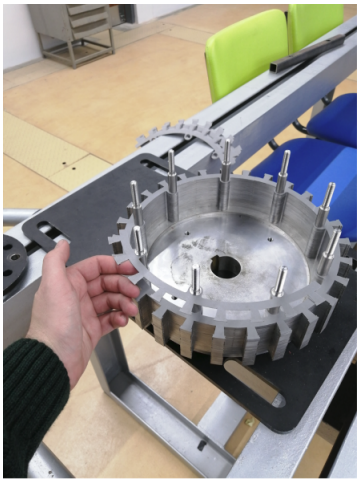

(d) Stator lamination stacking

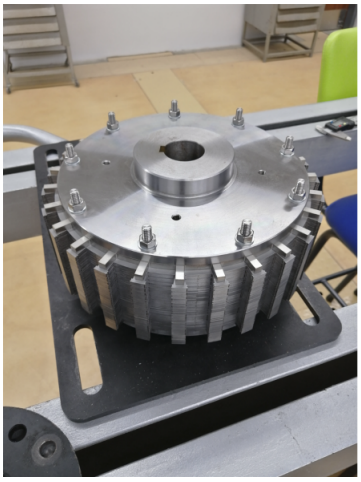

(e) Full stator stack

(f) Stator slots

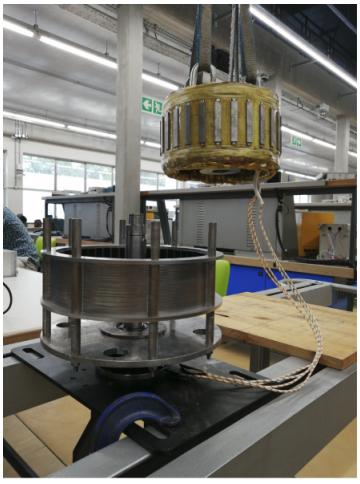

(g) Full PMVG assembly

Figure E.3: PMVG prototype manufacturing process (Chapter 5).

Appendix F

Additional Design Data

Additional design data for the wind generators that are evaluated in Chapters 3 to 8 are given in this appendix.

Table F.1: Design detail for the PMSGs in Table 6.2.

Conventional	G_1	G_2	G_3
d_{o}, (mm)	384.0	655.0	360.8
h_{yr}, (mm)	6.9	7.2	5.3
h_{m}, (mm)	6.2	6.0	3.0
θ_{m} (deg)	9.0	5.7	9.4
h_{hs}, (mm)	3.0	3.0	3.0
h_{s}, (mm)	35.1	39.3	44.1
b_{t}, (mm)	14.0	21.4	11.2
h_{ys}, (mm)	6.1	8.0	5.6
l_{Fe}, (mm)	71.0	120.0	53.4
f_{e} (Hz)	74.67	50.0	74.67
N_{ph}	130	304	220
Steel	M19-29 Ga	M19-29 Ga	M19-29 Ga
K_{f}	0.95	0.95	0.95

Table F.2: Design detail for the PMSGs in Table 4.4.

Open slot	S-PMSG	E-PMSG	SP-PMSG
d_{o}, (mm)	375.5	374.7	382.9
h_{yr}, (mm)	7.1	7.0	1.0
h_{m}, (mm)	4.5	3.0	-
h_{m}, (mm)	-	-	13.3
θ_{m} (deg)	8.5	9.3	-
b_{m} (mm)	-	-	9.1
h_{hs}, (mm)	3.0	3.0	3.0
h_{s}, (mm)	49.1	43.3	48.5
b_{t}, (mm)	12.2	12.8	11.6
h_{ys}, (mm)	6.1	7.1	6.0
l_{Fe}, (mm)	40.0	47.4	36.2
f_{e} (Hz)	74.67	74.67	74.67
N_{ph}	260	230	260
Steel	M400-50A	M400-50A	M400-50A
K_{f}	0.95	0.95	1.0

Semi-closed slot	S-PMSG	E-PMSG	SP-PMSG
d_{o}, (mm)	375.6	376.3	384.3
h_{yr}, (mm)	6.2	7.4	1.0
h_{m}, (mm)	3.3	3.0	-
h_{m}, (mm)	-	-	12.6
θ_{m} (deg)	6.8	8.8	-
b_{m}, (mm)	-	-	8.8
h_{hs}, (mm)	3.8	3.1	3.1
h_{s}, (mm)	41.5	37.3	47.7
b_{o}, (mm)	10.5	12.7	15.9
b_{s}, (mm)	17.5	19.4	16.9
h_{ys}, (mm)	6.0	6.1	7.7
l_{Fe}, (mm)	48.5	47.6	42.4
f_{e} (Hz)	74.67	74.67	74.67
N_{ph}	200	200	220
Steel	M400-50A	M400-50A	M400-50A
K_{f}	0.95	0.95	1.0

Table F.3: Design detail for the PMVGs in Table 5.2.

Conventional	$G_r = 5$	$G_r = 8$	$G_r = 11$
d_o, (mm)	335.6	314.0	275.6
h_{yr}, (mm)	6.9	9.2	9.4
h_m, (mm)	3.0	3.0	3.1
θ_m (deg)	5.6	5.7	6.6
h_{hs}, (mm)	3.0	3.25	3.0
h_s, (mm)	14.8	10.0	10.0
b_o, (mm)	20.4	20.7	21.6
b_s, (mm)	22.5	22.7	23.4
h_{ys}, (mm)	6.2	9.0	9.9
l_{Fe}, (mm)	61.3	82.0	108.6
f_e (Hz)	133.33	128.0	117.33
N_{ph}	90	54	40
Steel	M400-50A	M400-50A	M400-50A
K_f	0.92	0.92	0.92

Split-tooth	$G_r = 5$	$G_r = 8$	$G_r = 11$
d_o, (mm)	360.2	342.9	-
h_{yr}, (mm)	7.0	9.9	-
h_m, (mm)	3.1	3.0	-
θ_m (deg)	5.4	6.5	-
w_{at}, (mm)	13.0	12.0	-
w_{st}, (mm)	27.1	33.7	-
α_1, (mm)	8.8	13.6	-
α_2, (mm)	3.0	3.0	-
α_3, (mm)	7.1	5.1	-
h_s, (mm)	7.4	6.8	-
h_{ys}, (mm)	6.2	8.8	-
l_{Fe}, (mm)	75.7	92.3	-
f_e (Hz)	133.33	128.0	-
N_{ph}	80	48	-
Steel	M400-50A	M400-50A	-
K_f	0.92	0.92	-

Table F.4: Design detail for the 15 kW PMSG and PMVG in Table 6.2.

Generator	PMSG	PMVG
d_{o}, (mm)	636.2	629.6
h_{yr}, (mm)	8.1	8.7
h_{m}, (mm)	4.9	3.65
θ_{m} (deg)	6.0	3.76
h_{hs}, (mm)	3.5	4.8
h_{s}, (mm)	63.9	10.5
b_{o}, (mm)	13.4	27.4
b_{s}, (mm)	18.9	31.4
h_{ys}, (mm)	7.4	7.0
l_{Fe}, (mm)	88.0	168.8
f_{e} (Hz)	52.5	100
N_{ph}	360	105
Steel	M400-50A	M400-50A
K_{f}	0.95	0.92

Table F.5: Design detail for the PMSGs in Table 7.2.

Slot-Pole	30-28	54-28	90-28
d_{o}, (mm)	376.4	395.0	398.7
h_{yr}, (mm)	7.1	6.0	6.7
h_{m}, (mm)	3.0	3.0	3.0
θ_{m} (deg)	10.1	7.43	8.3
h_{hs}, (mm)	3.0	3.0	3.0
h_{s}, (mm)	33.1	26.1	28.6
b_{o}, (mm)	13.4	6.9	3.5
b_{s}, (mm)	19.5	11.9	6.8
h_{ys}, (mm)	6.1	6.0	6.6
l_{Fe}, (mm)	34.5	40.6	35.8
f_{e} (Hz)	74.67	74.67	74.67
N_{ph}	760	738	780
Steel	M400-50A	M400-50A	M400-50A
K_{f}	0.95	0.95	0.95

Table F.6: Design detail for the PMSGs in Table 8.2.

Generator	4.2 kW	15 kW
d_{o}, (mm)	393.8	639.8
h_{yr}, (mm)	6.6	7.5
h_{m}, (mm)	3.0	3.5
θ_{m} (deg)	7.5	5.2
h_{hs}, (mm)	3.0	3.0
h_{s}, (mm)	28.6	33.2
b_{o}, (mm)	18.3	21.6
b_{s}, (mm)	21.0	22.8
h_{ys}, (mm)	6.6	8.8
l_{Fe}, (mm)	35.1	96.8
f_{e} (Hz)	74.67	52.5
N_{ph}	210	375
Steel	M400-50A	M400-50A
K_{f}	0.95	0.95

List of References

[1] L. Hermanus and L. Scholtz, "Small-scale renewable energy technologies in East Africa: An overview," WWF South Africa, Cape Town, South Africa, Tech. Rep., 2018. [Online]. Available: www.wwf.org.za/report/small_scale_re_localisation

[2] D. Fitzgerald and U. Terblanche, "Potential East African localisation of small-scale renewable energy manufacture," Centre for Renewable and Sustainable Energy Studies (CRSES), Stellenbosch, South Africa, Tech. Rep., 2020. [Online]. Available: https://www.crses.sun.ac.za/files/research/publications/technical-reports/WWF%20East%20Africa%20Localisation%20of%20RE%20Manufacture_rev3.pdf

[3] E. I. Baring-Gould, R. W. Preus, R. Wills, D. Davis, K. R. Jackson, and S. Dana, "Competitiveness improvement project informational workshop," National Renewable Energy Laboratory (NREL), Golden, Colorado, United States, Tech. Rep., 2020. [Online]. Available: https://www.osti.gov/biblio/1605088

[4] A. C. Orrell, K. Kazimierczuk, and L. Sheridan, "Distributed wind market report: 2021 edition," Pacific Northwest National Laboratory (PNNL), Richland, WA (United States), Tech. Rep., 2021.

[5] J. O. Dabiri, J. R. Greer, J. R. Koseff, P. Moin, and J. Peng, "A new approach to wind energy: opportunities and challenges," in *AIP conference proceedings*, vol. 1652, no. 1. American Institute of Physics, 2015, pp. 51–57.

[6] A. C. Orrell, N. A. F. Foster, J. S. Homer, and S. L. Morris, "2015 Distributed wind market report," Pacific Northwest National Laboratory (PNNL), Richland, WA (United States), Tech. Rep., 2016.

[7] G. Van Kuik, J. Peinke, R. Nijssen, D. Lekou, J. Mann, J. N. Sørensen, C. Ferreira, J.-W. van Wingerden, D. Schlipf, P. Gebraad *et al.*, "Long-term research challenges in wind energy–a research agenda by the European Academy of Wind Energy," *Wind energy science*, vol. 1, no. 1, pp. 1–39, 2016.

[8] S. Zhou and P. Yang, "Risk management in distributed wind energy implementing analytic hierarchy process," *Renewable Energy*, vol. 150, pp. 616–623, 2020.

[9] W. Liang and W. Liu, "Key technologies analysis of small scale non-grid-connected wind turbines: A review," in *2010 World Non-Grid-Connected Wind Power and Energy Conference*, Nov 2010, pp. 1–6.

[10] Z. Alnasir and M. Kazerani, "An analytical literature review of stand-alone wind energy conversion systems from generator viewpoint," *Renewable and Sustainable Energy Reviews*, vol. 28, pp. 597–615, 2013.

[11] S. O. Ani, "Low cost small wind turbine generators for developing countries," Ph.D. dissertation, Electrical Sustainable Energy, Delft University of Technology, 2013.

[12] TradingEconomics. (2021. [Online], Dec. 1,). [Online]. Available: https://tradingeconomics.com/

[13] M. Arifujjaman, M. T. Iqbal, and J. E. Quaicoe, "Reliability analysis of grid connected small wind turbine power electronics," *Applied Energy*, vol. 86, no. 9, pp. 1617 – 1623, 2009.

[14] J. Carroll, A. McDonald, and D. McMillan, "Reliability comparison of wind turbines with DFIG and PMG drive trains," *IEEE Transactions on Energy Conversion*, vol. 30, no. 2, pp. 663–670, 2015.

[15] H. Chen, Y. Zuo, K. T. Chau, W. Zhao, and C. H. T. Lee, "Modern electric machines and drives for wind power generation: A review of opportunities and challenges," *IET Renewable Power Generation*, 2021.

[16] S. O. Ani, H. Polinder, and J. A. Ferreira, "Comparison of energy yield of small wind turbines in low wind speed areas," *IEEE Transactions on Sustainable Energy*, vol. 4, no. 1, pp. 42–49, Jan 2013.

[17] J. G. Aredjodoun, P. K. Chetangny, S. Houndedako, A. Vianou, D. Chamagne, and C. Espanet, "Optimal adaptation of the wind rotor to the permanent magnets synchronous generator of a small passive wind turbine," in *2019 IEEE PES/IAS PowerAfrica*. IEEE, 2019, pp. 164–169.

[18] B. Sareni, A. Abdelli, X. Roboam, and D. H. Tran, "Model simplification and optimization of a passive wind turbine generator," *Renewable Energy*, vol. 34, no. 12, pp. 2640–2650, 2009.

[19] D. H. Tran, B. Sareni, X. Roboam, and C. Espanet, "Integrated optimal design of a passive wind turbine system: An experimental validation," *IEEE Transactions on Sustainable Energy*, vol. 1, no. 1, pp. 48–56, April 2010.

[20] D. H. Tran, B. Sareni, X. Roboam, E. Bru, and A. De Andrade, "Robust design of a passive wind turbine system," *COMPEL-The international journal for computation and mathematics in electrical and electronic engineering*, vol. 31, no. 3, pp. 932–944, 2012.

[21] H. Z. Agrebi, N. Benhadj, M. Chaieb, F. Sher, R. Amami, R. Neji, and N. Mansfield, "Integrated optimal design of permanent magnet synchronous generator for smart wind turbine using genetic algorithm," *Energies*, vol. 14, no. 15, 2021. [Online]. Available: https://www.mdpi.com/1996-1073/14/15/4642

[22] F. G. Rossouw and M. J. Kamper, "Use of air-cored axial flux permanent magnet generator in direct battery charging wind energy systems," in *2007 7th International Conference on Power Electronics and Drive Systems*. IEEE, 2007, pp. 1102–1107.

[23] J. A. Stegmann and M. J. Kamper, "Design aspects of double-sided rotor radial flux air-cored permanent-magnet wind generator," *IEEE Transactions on Industry Applications*, vol. 47, no. 2, pp. 767–778, March 2011.

[24] S. O. Ani, H. Polinder, and J. A. Ferreira, "Small wind power generation using automotive alternator," *Renewable Energy*, vol. 66, pp. 185–195, 2014.

[25] J. S. Artal-Sevil, R. Dufo, J. A. DomÃnguez, and J. L. Bernal-AgustÃn, "Small wind turbines in smart grids. Transformation of electrical machines in permanent magnet synchronous generators," in *2018 Thirteenth International Conference on Ecological Vehicles and Renewable Energies (EVER)*, April 2018, pp. 1–8.

[26] N. Mohan, T. M. Undeland, and W. P. Robbins, *Power electronics: converters, applications, and design*. John Wiley & Sons, 2003.

[27] M. J. Kamper, C. Africa, C. J. J. Labuschagne, and L. P. Mdakane, "Line reactance criteria for minimizing line current harmonic content in diode rectifier connected wind generator systems," in *2020 International SAUPEC/RobMech/PRASA Conference*, 2020, pp. 1–6.

[28] Yuanye Xia, K. H. Ahmed, and B. W. Williams, "Different torque ripple reduction methods for wind energy conversion systems using diode rectifier and boost converter," in *2011 IEEE International Electric Machines Drives Conference (IEMDC)*, May 2011, pp. 729–734.

[29] S. Li, T. A. Haskew, and L. Xu, "Conventional and novel control designs for direct driven PMSG wind turbines," *Electric Power Systems Research*, vol. 80, no. 3, pp. 328–338, 2010.

[30] M. A. Abdullah, A. H. M. Yatim, C. W. Tan, and R. Saidur, "A review of maximum power point tracking algorithms for wind energy systems," *Renewable and sustainable energy reviews*, vol. 16, no. 5, pp. 3220–3227, 2012.

[31] R. Kot, M. Rolak, and M. Malinowski, "Comparison of maximum peak power tracking algorithms for a small wind turbine," *Mathematics and Computers in Simulation*, vol. 91, pp. 29–40, 2013.

[32] W. T. Villet and M. J. Kamper, "Position sensorless control of a reluctance synchronous wind generator drive with an LC inverter filter," *Electric Power Components and Systems*, vol. 43, no. 8-10, pp. 1051–1061, 2015.

[33] M. Ragheb, "Modern wind generators," University of Illinois at Urbana–Champaign, Tech. Rep., 2014. [Online]. Available: https://mragheb.com/NPRE%20475%20Wind%20Power%20Systems/Modern20Wind%20Generators.pdf

[34] T. Kanda, L. P. Mdakane, C. J. J. Labuschagne, and M. J. Kamper, "Dynamics of maximum power point wind energy battery charging systems," in *2019 Southern African Universities Power Engineering Conference/Robotics and Mechatronics/Pattern Recognition Association of South Africa (SAUPEC/RobMech/PRASA)*, 2019, pp. 576–581.

[35] L. P. Mdakane and M. J. Kamper, "Simple robust MPPT control for wind energy dc-grid connected systems," in *IECON 2019 - 45th Annual Conference of the IEEE Industrial Electronics Society*, vol. 1, 2019, pp. 2495–2500.

[36] L. P. Mdakane, "Geared PM wind generator and MPPT control for dc-grid wind energy system," Master's thesis, Department of Electrical & Electronic Engineering, Stellenbosch University, 2020.

[37] J. A. Stegmann and M. J. Kamper, "Economic and efficiency evaluation of different battery charging wind generator systems," in *Southern African Universities Power Engineering Conference (SAUPEC), Johannesburg, South Africa*, 2010.

[38] S. Gerber. (2021. [Online], Dec. 1,) SEMFEM (Stellenbosch Electrical Machines Finite Element Method). [Online]. Available: http://www0.sun.ac.za/semfem/v3/index.html#

[39] C. J. J. Labuschagne and M. J. Kamper, "Wind generator impedance matching in small-scale passive wind energy systems," *IEEE Access*, vol. 9, pp. 22 558–22 568, 2021.

[40] C. J. J. Labuschagne, "Permanent magnet vernier machines: Design and feasibility study for railway traction applications," Siemens Mobility GmbH, R&D Motors and Generators, Nuremberg, Germany, Tech. Rep., 2020.

[41] T. M. Jahns, "The expanding role of PM machines in direct-drive applications," in *2011 International Conference on Electrical Machines and Systems*, 2011, pp. 1–6.

[42] H. Li and Z. Chen, "Overview of different wind generator systems and their comparisons," *IET Renewable Power Generation*, vol. 2, no. 2, pp. 123–138, 2008.

[43] M. Dubois, H. Polinder, and J. Ferreira, "Comparison of generator topologies for direct-drive wind turbines," *Proceedings of the 2000 NORPIE*, pp. 22–26, 2000.

[44] A. Cavagnino, M. Lazzari, F. Profumo, and A. Tenconi, "A comparison between the axial flux and the radial flux structures for PM synchronous motors," *IEEE transactions on industry applications*, vol. 38, no. 6, pp. 1517–1524, 2002.

[45] M. J. Kamper, J. H. Potgieter, J. A. Stegmann, and P. Bouwer, "Comparison of air-cored and iron-cored non-overlap winding radial flux permanent magnet direct drive wind generators," in *2011 IEEE Energy Conversion Congress and Exposition*, 2011, pp. 1620–1627.

[46] M. Chirca, S. Breban, C. Oprea, and M. Radulescu, "Analysis of innovative design variations for double-sided coreless-stator axial-flux permanent-magnet generators in micro-wind power applications," in *2014 International Conference on Electrical Machines (ICEM)*, 2014, pp. 385–389.

[47] G. De Donato, F. G. Capponi, G. A. Rivellini, and F. Caricchi, "Integral-slot versus fractional-slot concentrated-winding axial-flux permanent-magnet machines: comparative design, fea, and experimental tests," *IEEE Transactions on Industry Applications*, vol. 48, no. 5, pp. 1487–1495, 2012.

[48] J. J. Germishuizen and M. J. Kamper, "Classification of symmetrical non-overlapping three-phase windings," in *The XIX International Conference on Electrical Machines - ICEM 2010*, 2010, pp. 1–6.

[49] A. M. El-Refaie, "Fractional-slot concentrated-windings synchronous permanent magnet machines: Opportunities and challenges," *IEEE Transactions on industrial Electronics*, vol. 57, no. 1, pp. 107–121, 2009.

[50] A. M. EL-Refaie, "Fractional-slot concentrated-windings synchronous permanent magnet machines: Opportunities and challenges," *IEEE Transactions on Industrial Electronics*, vol. 57, no. 1, pp. 107–121, 2010.

[51] N. Bianchi and E. Fornasiero, "Impact of MMF space harmonic on rotor losses in fractional-slot permanent-magnet machines," *IEEE Transactions on energy conversion*, vol. 24, no. 2, pp. 323–328, 2009.

[52] N. Bianchi, S. Bolognani, and E. Fornasiero, "An overview of rotor losses determination in three-phase fractional-slot PM machines," *IEEE Transactions on Industry Applications*, vol. 46, no. 6, pp. 2338–2345, 2010.

[53] F. Magnussen and H. Lendenmann, "Parasitic effects in PM machines with concentrated windings," *IEEE transactions on industry applications*, vol. 43, no. 5, pp. 1223–1232, 2007.

[54] B. Kim, "Design method of a direct-drive permanent magnet Vernier generator for a wind turbine system," *IEEE Transactions on Industry Applications*, vol. 55, no. 5, pp. 4665–4675, 2019.

[55] P. M. Tlali, R. Wang, S. Gerber, C. D. Botha, and M. J. Kamper, "Design and performance comparison of Vernier and conventional PM synchronous wind generators," *IEEE Transactions on Industry Applications*, vol. 56, no. 3, pp. 2570–2579, 2020.

[56] D. K. K. Padinharu, G. J. Li, Z. Q. Zhu, R. Clark, A. S. Thomas, and Z. Azar, "System-level investigation of multi-MW direct-drive wind power PM Vernier generators," *IEEE Access*, vol. 8, pp. 191 433–191 446, 2020.

[57] F. Wu and A. M. El-Refaie, "Permanent magnet Vernier machine: a review," *IET Electric Power Applications*, vol. 13, no. 2, pp. 127–137, 2019.

[58] D. Li, R. Qu, and T. A. Lipo, "High-power-factor Vernier permanent-magnet machines," *IEEE Transactions on Industry Applications*, vol. 50, no. 6, pp. 3664–3674, 2014.

[59] W. Li, T. W. Ching, and K. T. Chau, "A hybrid-excited Vernier permanent magnet machine using homopolar topology," *IEEE Transactions on Magnetics*, vol. 53, no. 11, pp. 1–7, 2017.

[60] S.-U. Chung, J.-W. Kim, Y.-D. Chun, B.-C. Woo, and D.-K. Hong, "Fractional slot concentrated winding PMSM with consequent pole rotor for a low-speed direct drive: Reduction of rare earth permanent magnet," *IEEE Transactions on energy conversion*, vol. 30, no. 1, pp. 103–109, 2014.

[61] J. Qi, Z. Zhu, L. Yan, G. Jewell, C. Gan, Y. Ren, S. Brockway, and C. Hilton, "Suppression of torque ripple for consequent pole PM machine by asymmetric pole shaping method," in *2021 IEEE International Electric Machines & Drives Conference (IEMDC)*. IEEE, 2021, pp. 1–7.

[62] G. H. Zhang, K. Wang, and J. Li, "Torque ripple suppression of consequent-pole permanent magnet machine by magnet shifting," in *2019 22nd International Conference on Electrical Machines and Systems (ICEMS)*. IEEE, 2019, pp. 1–6.

[63] "State of Renewable Energy in South Africa," Department of Energy in South Africa, Tech. Rep., 2016.

[64] (2021. [Online], Dec. 1,) Wind Atlas for South Africa. [Online]. Available: http://wasadata.csir.co.za/wasa1/WASAData

[65] (2021. [Online], Dec. 10,) Access to electricity, rural (% of rural population). [Online]. Available: https://data.worldbank.org/indicator/EG.ELC.ACCS.RU.ZS?end=2019&name_desc=false&start=1996&view=map&year=2019

[66] O. Rodriguez-Hernandez, M. Martinez, C. Lopez-Villalobos, H. Garcia, and R. Campos-Amezcua, "Techno-economic feasibility study of small wind turbines in the Valley of Mexico metropolitan area," *Energies*, vol. 12, no. 5, 2019. [Online]. Available: https://www.mdpi.com/1996-1073/12/5/890

[67] M. Gough, M. Lotfi, R. Castro, A. Madhlopa, A. Khan, and J. P. Catalão, "Urban wind resource assessment: a case study on Cape Town," *Energies*, vol. 12, no. 8, p. 1479, 2019.

[68] N. Goudarzi, K. Mohammadi, A. St Pé, R. Delgado, and W. Zhu, "Wind resource assessment and economic viability of conventional and unconventional small wind turbines: A case study of Maryland," *Energies*, vol. 13, no. 22, p. 5874, 2020.

[69] Y. Yang, S. Bremner, C. Menictas, and M. Kay, "Battery energy storage system size determination in renewable energy systems: A review," *Renewable and Sustainable Energy Reviews*, vol. 91, pp. 109–125, 2018.

[70] X. Tan, Q. Li, and H. Wang, "Advances and trends of energy storage technology in microgrid," *International Journal of Electrical Power & Energy Systems*, vol. 44, no. 1, pp. 179–191, 2013.

[71] D. Kumar, F. Zare, and A. Ghosh, "DC microgrid technology: system architectures, AC grid interfaces, grounding schemes, power quality, communication networks, applications, and standardizations aspects," *IEEE Access*, vol. 5, pp. 12 230–12 256, 2017.

[72] G. M. Masters, *Renewable and efficient electric power systems*. John Wiley & Sons, 2013.

[73] A. P. Schaffarczyk, *Introduction to wind turbine aerodynamics*. Springer Nature, 2020.

[74] J. A. Stegmann, "Design and analysis aspects of radial flux air-cored permanent magnet wind generator system for direct battery charging applications," Master's thesis, Department of Electrical & Electronic Engineering, Stellenbosch University, 2010.

[75] P. Enrici, I. Meny, and D. Matt, "Conceptual study of Vernier generator and rectifier association for low power wind energy systems," *Energies*, vol. 14, no. 3, p. 666, 2021.

[76] B. Heller and V. Hamata, *Harmonic field effects in induction machines*. Elsevier Science & Technology, 1977.

[77] C. Madariaga, W. Jara, J. A. Tapia, J. Pyrhönen, P. Lindh, and J. A. Riedemann, "Closed-form solution for the slot leakage inductance of tooth-coil-winding permanent magnet machines," *IEEE Transactions on Energy Conversion*, vol. 34, no. 3, pp. 1572–1580, Sep. 2019.

[78] J. Pyrhönen, T. Jokinen, and V. Hrabovcova, *Design of rotating electrical machines*. John Wiley & Sons, 2013.

[79] J. H. J. Potgieter and M. J. Kamper, "Calculation methods and effects of end-winding inductance and permanent-magnet end flux on performance prediction of nonoverlap winding permanent-magnet machines," *IEEE Transactions on Industry Applications*, vol. 50, no. 4, pp. 2458–2466, July 2014.

[80] F. W. Grover, *Inductance calculations: working formulas and tables*. Courier Corporation, 2004.

[81] J. H. J. Potgieter and M. J. Kamper, "Design optimization of directly grid-connected PM machines for wind energy applications," *IEEE Transactions on Industry Applications*, vol. 51, no. 4, pp. 2949–2958, 2015.

[82] Z. Q. Zhu and D. Howe, "Influence of design parameters on cogging torque in permanent magnet machines," *IEEE Transactions on Energy Conversion*, vol. 15, no. 4, pp. 407–412, 2000.

[83] M. Chirca, C. Oprea, P.-D. Teodosescu, and S. Breban, "Optimal design of a radial flux spoke-type interior rotor permanent magnet generator for micro-wind turbine applications," in *2016 International Conference on Applied and Theoretical Electricity (ICATE)*. IEEE, 2016, pp. 1–5.

[84] C. J. J. Labuschagne and M. J. Kamper, "Evaluation of PM rotor topologies for impedance matching of small-scale passive dc-connected wind generator systems," in *2020 International Conference on Electrical Machines (ICEM)*, vol. 1. IEEE, 2020, pp. 1896–1902.

[85] ——, "Performance and cost comparison of conventional and Vernier PM wind generators for small-scale uncontrolled passive wind energy systems," in *2021 IEEE Energy Conversion Congress and Exposition (ECCE)*, 2021, pp. 4591–4597.

[86] K. Deb, A. Pratap, S. Agarwal, and T. Meyarivan, "A fast and elitist multiobjective genetic algorithm: NSGA-II," *IEEE Transactions on Evolutionary Computation*, vol. 6, no. 2, pp. 182–197, 2002.

[87] J. H. J. Potgieter and M. J. Kamper, "Torque and voltage quality in design optimization of low-cost non-overlap single layer winding permanent magnet wind generator," *IEEE Transactions on Industrial Electronics*, vol. 59, no. 5, pp. 2147–2156, 2012.

[88] A. Toba and T. A. Lipo, "Generic torque-maximizing design methodology of surface permanent-magnet Vernier machine," *IEEE Transactions on Industry Applications*, vol. 36, no. 6, pp. 1539–1546, 2000.

[89] B. Kim, "Investigation on slot–pole combinations of a PM Vernier motor with fractional–slot concentrated winding configurations," *Energies*, vol. 10, no. 9, 2017.

[90] D. Li, T. Zou, R. Qu, and D. Jiang, "Analysis of fractional-slot concentrated winding PM Vernier machines with regular open-slot stators," *IEEE Transactions on Industry Applications*, vol. 54, no. 2, pp. 1320–1330, 2018.

[91] P. M. Tlali and R.-J. Wang, "PM Vernier machine for utility scale wind generator applications: Design and evaluation," in *2020 International Conference on Electrical Machines (ICEM)*, vol. 1, 2020, pp. 2637–2643.

[92] C. Gong and F. Deng, "Design and optimization of a high-torque-density low-torque-ripple Vernier machine using ferrite magnets for direct-drive applications," *IEEE Transactions on Industrial Electronics*, pp. 1–1, 2021.

[93] J. F. Gieras, *Permanent magnet motor technology: design and applications*. CRC press, 2002.

[94] E. Howard, "Design optimisation of reluctance synchronous machine: a motor and generator study," Ph.D. dissertation, Department of Electrical & Electronic Engineering, Stellenbosch University, 2017.

[95] M. J. Kamper, "Design optimisation of cageless flux barrier rotor reluctance synchronous machine," Ph.D. dissertation, Department of Electrical & Electronic Engineering, Stellenbosch University, 1996.

[96] C. J. J. Labuschagne and M. J. Kamper, "Permanent magnet Vernier generator design for a small-scale passive wind generator system," in *2021 IEEE International Electric Machines & Drives Conference (IEMDC)*, 2021, pp. 1–7.

[97] L. Wu, R. Qu, D. Li, and Y. Gao, "Influence of pole ratio and winding pole numbers on performance and optimal design parameters of surface permanent-magnet Vernier machines," *IEEE Transactions on Industry Applications*, vol. 51, no. 5, pp. 3707–3715, 2015.

[98] E. R. Laithwaite, "The goodness of a machine," *Proceedings of the Institution of Electrical Engineers*, vol. 112, no. 3, pp. 538–541, March 1965.

[99] T. D. Strous, U. Shipurkar, H. Polinder, and J. A. Ferreira, "Comparing the brushless DFIM to other generator systems for wind turbine drive-trains," in *Journal of Physics: Conference Series*, vol. 753, no. 11. IOP Publishing, 2016, p. 112014.

[100] A. J. Rix, "Design, comparison and experimental evaluation of non-overlap winding radial flux permanent magnet hub drives for electric vehicles," Ph.D. dissertation, Department of Electrical & Electronic Engineering, Stellenbosch University, 2011.

[101] M. Liwschitz-Garik and C. C. Whipple, *Alternating-current machines*. van Nostrand, 1961.

[102] M. J. Kamper, "Die ontwerp-kriteria en ontwikkeling van 'n ontwerpprogram vir kourotor-induksiemotors vir gebruik in die belastingsgebied," Master's thesis, Department of Electrical & Electronic Engineering, Stellenbosch University, 1987.

[103] P. M. Tlali, "Design and performance evaluation of a permanent magnet Vernier machine for wind turbine generator applications," Ph.D. dissertation, Department of Electrical & Electronic Engineering, Stellenbosch University, 2019.

[104] B. Kim and T. A. Lipo, "Operation and design principles of a PM Vernier motor," *IEEE Transactions on Industry Applications*, vol. 6, no. 50, pp. 3656–3663, 2014.

[105] C. J. J. Labuschagne and M. J. Kamper, "Coordinate descent method to minimise cogging torque in small-scale wind generators," in *2021 Southern African Sustainability Conference (SASEC)*, 2021, pp. 182–187.

[106] J. H. Potgieter and M. J. Kamper, "Cogging torque sensitivity in design optimisation of low cost non-overlap winding PM wind generator," in *The XIX International Conference on Electrical Machines - ICEM 2010*, 2010, pp. 1–6.

[107] C. J. J. Labuschagne and M. J. Kamper, "Design optimisation and comparison of fractional-slot overlap and non-overlap winding direct-drive PM wind generators for dc-connected applications," in *2019 IEEE Energy Conversion Congress and Exposition (ECCE)*, 2019, pp. 724–731.

[108] M. J. D. Powell, "An efficient method for finding the minimum of a function of several variables without calculating derivatives," *The Computer Journal*, vol. 7, no. 2, pp. 155–162, 1964.